POROUS LADDER POLYMER NETWORKS:

DESIGN, SYNTHESIS, AND PROPERTIES

A Dissertation

by

SAI CHE

Submitted to the Office of Graduate and Professional Studies of
Texas A&M University
in partial fulfillment of the requirements for the degree of

DOCTOR OF PHILOSOPHY

Chair of Committee,	Lei Fang
Committee Members,	Karen L. Wooley
	Michael Nippe
	Jaime Grunlan
Head of Department,	Simon W. North

August 2020

Major Subject: Chemistry

ABSTRACT

This dissertation describes the research on the design, synthesis and properties of porous ladder polymer networks (PLANs), which can be defined as porous organic polymers featuring full ladder type backbone. Porous Organic Polymers (POPs) are a class of permanently porous materials whose entire organic framework is crosslinked by covalent bonds. The high porosity, structural diversity, and thermal/chemical stability of POPs render them promising candidates in gas adsorption, catalyst, sensors, *etc*. Meanwhile, ladder polymers with fused-ring rigid backbones have demonstrated various unique properties that are not accessible on conventional polymers with non-fused backbones. In the past decade, numerous efforts have been devoted to incorporate fully-fused ladder-type constitution into POPs, affording the so-called PLANs. Advancements of this field in the past decade lead to the development of exciting PLAN materials embracing advantages from both worlds of POPs and ladder polymers. These synergistic properties include but are not limited to: (1) extraordinary stability in terms of chemical constitution and porosity; (2) low entropy backbones that favor gas adsorption process; and (3) extended pi-conjugation for better charge transport.

This dissertation begins with an introduction of the development of PLAN constructed from a variety of geometry topologies and synthetic strategies. The reported synthetic strategies as well as the corresponding properties of PLAN are identified and discussed. Then the perspectives on the promising future direction of this field are presented.

Firstly, we describe the synthesis of an example of truxene-based PLAN through Suzuki crosslinking followed by ring-closing olefin metathesis ladderization. Thermodynamically controlled ring-fusing step allowed for the formation of complete ladder type backbone with minimal backbone defects. This crosslinking followed by ladderizaion method offers a universal strategy of introducing ladder-type backbone into porous system heterogeneously.

Secondly, we present the proof of concept of using a ladder-type backbone in POP to achieve more entropically favorable methane adsorption, based on the PLAN described previously. Thermodynamic investigation revealed a significantly smaller entropy penalty of PLAN upon high-pressure methane uptake compared to its non-ladder-type counterpart. This entropic approach can serve as a new general strategy to further enhance methane storage capacity of porous materials.

Thirdly, we present a new synthetic approach to porous graphitic carbon, which can also be viewed as a subclass of PLANs. Bottom-up synthesis of PGC was achieved through a one-pot reaction involving crosslinking and graphitization. The framework was crosslinked by MSA-mediated aldol triple condensation reaction, while the pre-organized aromatic moieties allowed for cyclodehydrogenation to complete the graphitic structure. This PGC material is equipped with regulated ultramicropores with facile graphitization process, allowing for its application in electrocatalysis and chemiresistive sensing.

The main purpose of the work presented in this dissertation is to (1) establish efficient and versatile strategies to PLAN construction and (2) understand the fundamental correlation between ladder-type backbone and their application-relevant properties.

Building up on this work and the rapid development by others in this field, promising applications of PLANs in energy storage, gas separation, highly selective and sensitive sensors, and electrocatalysis are anticipated.

DEDICATION

Hang Che

Tianru Yue

ACKNOWLEDGEMENTS

First and foremost, I would like to thank my advisor, Prof. Lei Fang, for his enlighten, guidance, and encouragement through my entire graduate study. He not only gave me precious intellectual instructions, but also set a good example of being a professional researcher. I could not have imagined having a better advisor and mentor for my graduate study.

Besides my advisor, I would like to thank my committees: Prof. Karen L. Wooley, Prof. Michael Nippe, and Prof. Jaime Grunlan, for their insightful comments and encouragement, but also for the hard question which incented me to widen my research from various perspectives.

I also thank my group members for the inspiring discussions, constant encouragement, and all the fun we have had together. They are Dr. Yang Zou, Dr. Zi-Hao Guo, Dr. Congzhi Zhu, Dr. Jongbok Lee, Dr Tianyu Yuan, Dr. Alex J. Kalin, Dr. Chenxu Wang, Xiaozhou Ji, Mariela Vazquez, Anthony U. Mu, Bailey K. Phillips, Che-Hsuan Chang, Yirui Cao, Bo-Ji Peng, Chenxuan Li, Octavio Miranda, Guvanch Gurbandurdyyev, and Mingwan Leng. I would also thank the undergraduate students who worked with me. They are Dylan Cole and Jessica Glynn.

I would like to thank my collaborators, including Prof. Hong-Cai Zhou, Prof. Sarbajit Banerjee, Professor Mohammed Al-Hashimi. Special acknowledgement goes to Prof. Hong-Cai Zhou and his group. Their expertise in porous materials is essential to my graduate research.

Last but not the least, I would like to thank my parents for their love and support throughout my life. Thank you both for giving me strength to chase my dreams.

CONTRIBUTORS AND FUNDING SOURCES

Contributors

This work was supervised by a dissertation committee consisting of Professor Lei Fang (chair of committee), Professor Karen L. Wooley, and Professor Michael Nippe of the Department of Chemistry, and Professor Jaime Grunlan of the Department of Mechanical Engineering.

The TGAs depicted in Chapter II and IV were conducted by Dr. Chenxu Wang. The DRIFTS and SEM images depicted in Chapter II were conducted by Jia-Luo Li. XPS depicted in Chapter II were conducted by Xiaozhou Ji. High-pressure methane adsorption depicted in Chapter III were conducted by Dr. Jiangdong Pang.

All other work described in the dissertation was completed by the student independently.

Funding Sources

Graduate study was supported by *Qatar National Priority Research Program* (*NPRP9-160-2-088* and *NPRP10-0111-170152)*, Welch (A-1898), *TAMU College of Science Strategic Transformative Research Program*.

NOMENCLATURE

ANG	Adsorbed Natural Gas
BET	Brunauer–Emmett–Teller
BPO	Benzoyl Peroxide
DMF	N,N-dimethylformamide
DMSO	Dimethyl Sulfoxide
DRIFTS	Diffuse Reflectance Infrared Fourier Transform Spectroscopy
MS	Mass Spectroscopy
NLDFT	Nonlocal Density Functional Theory
NMR	Nuclear Magnetic Resonance
PLAN	Porous Ladder Polymer Network
PPN	Porous Polymer Network
PXRD	Powder X-Ray Diffraction
RCM	Ring-closing Olefin Metathesis
SEM	Scanning Electron Microscopy
TGA	Thermogravimetric Analysis
THF	Tetrahydrofuran
XPS	X-ray Photoelectron Spectroscopy

TABLE OF CONTENTS

Page

LIST OF FIGURES

Page

LIST OF TABLES

CHAPTER I

INTRODUCTION

1.1 Introduction of Porous Ladder Polymer Networks

The past few decades have seen a thriving development of bottom-up synthesized porous organic materials with facile functionalization and precise structural tunability. These materials include those referred as covalent-organic frameworks (COFs),[1-7] porous aromatic frameworks (PAFs),[8-12] conjugated microporous polymers (CMPs),[13-17] porous polymer networks (PPNs),[18-24] porous organic polymers (POPs),[25-28] hyper crosslinked polymers (HCPs),[29-37] and polymers of intrinsic microporosity (PIMs).[38-45] To avoid confusion, we use the general term POPs in this dissertation to represent all the bottom-up synthesized, non-small molecule microporous organic materials . The microporosity of certain POPs can reach an extremely high level, with BET surface area over 6000 m^2 g^{-1}.[20] The covalently linked frameworks of POPs, especially those synthesized through kinetically-controlled bond formation, usually exhibit excellent thermal and chemical stability hence can survive harsh conditions for post-modification or application.[9, 21, 46, 47] Furthermore, the composition of only light elements renders POPs low cost, low density, and the potential to possess ultra-high gravimetric porosity.[8, 11, 20, 48, 49] The diverse backbone structures and remarkable stability allow for pre- or post-functionalization of POPs so that their pore structures and chemical constitutions can be tuned in a facile manner.[47, 50, 51] Overall, these features make POPs a highly promising class of materials

for many distinctive applications that require robustness, porosity, light weight, and unique structural tunability.

Ladder polymers are multi-strand polymers whose backbones are constituted by periodically repeated rings, with adjacent rings fused to one another by sharing two or more atoms.[52] This type of constitution restricts free torsional motion of the polymer backbone, leading to rigid conformation and remarkable thermal and chemical stability.[53-56] In addition, the rigid backbone of non-conjugated ladder polymers with structural "kinks" can facilitate the formation of micropores without collapsing in the solid state, as demonstrated by the class of polymers referred as "polymers of intrinsic microporosity".[38] For conjugated ladder polymers whose backbones are mainly composed of π-conjugated repeating units, persistent coplanar conformation extends the delocalization of the π molecular orbitals while the rigid conformation minimizes the reorganization energy required for electron transfer.[57-60] These properties can facilitate fast intra-chain charge transport,[61] long exciton diffusion length,[62] and strong intermolecular electronic coupling[63] in conjugated ladder polymers. For the past several decades, remarkable efforts and progresses have been made to construct ladder polymers through either one-step ring-fusing polymerization or stepwise polymerization-ladderization approaches.[64-68] The term "ladderization" is defined here as the annulation of a polymer chain into a fully fused ladder-type constitution. Although it still remains challenging to achieve defect-free ladder-type backbones and good solubility on ladder polymers,[56, 64, 69-71] the unique fundamental chemistry and advanced materials applications of conjugated ladder polymers has gained intensive research attentions. The investigations of ladder polymers

in applications such as gas separation,[72-74] organic light emitting diodes,[75] and organic field effect transistors[76] have emerged rapidly.

The integration of the structural features of POPs with that of ladder polymer has been an intriguing approach to develop unprecedented new materials possessing the advantages of both worlds. Significant advances have been achieved towards this goal in the past decade, affording a number of highly porous, crosslinked organic polymer networks featuring fully ladder-type backbones. This class of materials are defined as "porous ladder polymer networks" in the following text. In principle, these materials embrace the advantages from both POPs and ladder polymers, affording synergistic properties such as: (1) extraordinary chemical and thermal stability in terms of chemical constitution and porous topology; (2) rigid backbones that favor gas adsorption processes in an entropic manner; and (3) extended π-conjugation for better transport of quasi particles such as charges and excitons throughout the network. These enable the promising application of porous ladder polymer networks as the next-generation materials for a number of exciting topics such as energy storage, gas separation, highly selective and sensitive sensors, and electrocatalysis. In the meantime, more strict requirements are also imposed from both worlds of POPs and ladder polymers, leading to challenges on multiple fronts. In this introduction, we summarize and discuss the recent research progresses made on bottom-up synthesized porous ladder polymer networks, including design principles, synthetic strategies, and their corresponding exotic properties. Outlook on the challenges and future development of this field is also provided at the end of this introduction.

1.2 Design and Synthesis

So far, a wide variety of fused hydrocarbon or fused heterocycle building blocks, equipped with various functional groups, have been successfully employed into the construction of porous ladder polymer network backbones. The combination of the numerous geometric options and various choices of the building blocks renders an enormous structural parameter space of possible porous ladder polymer network materials with great diversity in terms of their potential properties and functions.

The general synthetic design of porous ladder polymer networks involves the design principles for both POPs and ladder polymers. From the perspective of POPs, the backbones are generally constructed from either crosslinking linear polymer chains,[77, 78] or direct polymerization of rigid monomers containing more than two functional groups. In either case, the polymer chain must extend in more than two directions at some point during the step-growth process, so that a fully crosslinked porous network can be constructed when the reaction conversion of the functional groups is higher than the theoretical gel point.[79] POPs can be made crystalline if synthesized through thermodynamically-controlled reversible reactions, such as boroxine formation[80] and Schiff-base reaction[81]. In most other cases, POPs are amorphous and synthesized through kinetically-controlled reactions, such as Yamamoto reaction,[8, 18, 20, 22, 48, 80] Suzuki cross-coupling,[81] Sonagashira reaction,[15] oxidative coupling,[82] Buchwald-Hartwig coupling,[83] aromatization triple condensation,[84-86] Friedel-Crafts reaction,[87-89] Scholl oxidation,[90] etc. These diverse synthetic methods afforded a large library of POPs with diverse backbone

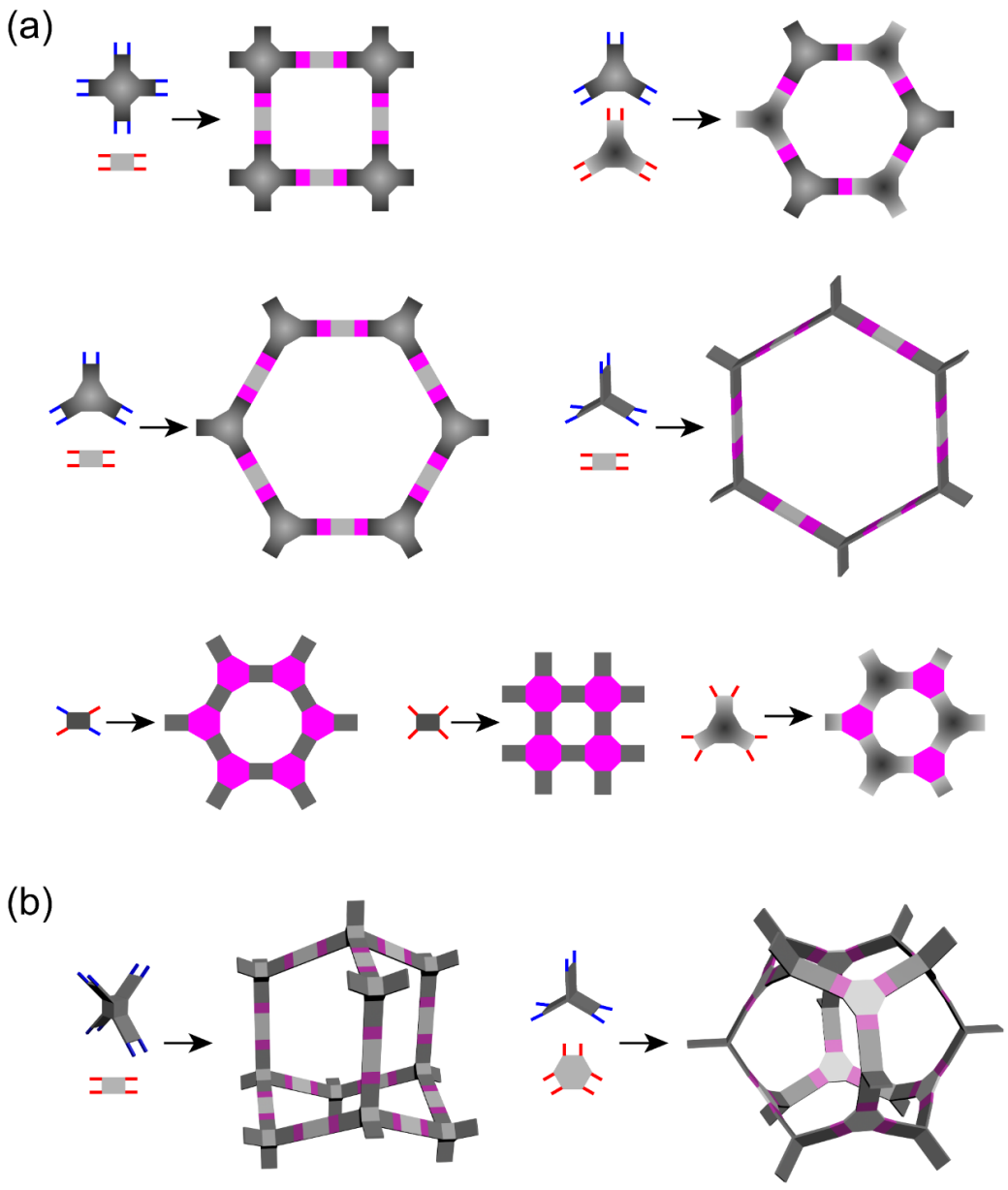

Figure 1.1. Graphical illustration of reported topological diagrams of porous ladder polymer networks.
(a) 2D porous ladder polymer networks
(b) 3D porous ladder polymer networks

structures. In order to persist high porosities, the building blocks are usually rigid, and the growth directions should be geometrically diverged.[3, 13, 14] From the perspective of

ladder polymer backbone, at least two strands of bonds should be formed for each growth direction so that the fused ladder-type constitution is ensured throughout the network. This goal can be achieved by a ring-fusing reaction that forms the multiple strands of bonds while crosslinking the material in one-pot, or by a stepwise approach involving the crosslinking through the formation of one strand of bonds, followed by ladderization.[69, 70, 91-93] Both strategies require the presence of more than one reactive site on each growth direction.

By integrating the design principles for POPs and ladder polymers, a number of extended 2D and 3D porous ladder polymer networks with various topologies and geometries have been constructed as summarized in **Figure 1.1**. It is noteworthy that only the ideal structure of each topology is shown here for the demonstration of the model. In real life, the structures often deviate more or less from these ideal ones due to the presence of defect formed in the cross-linking reactions or annulation reactions. The most commonly seen geometry is layered two-dimensional network with either hexagonal or tetragonal channels (**Figure 1.1a**). Topologically, an ideal 2D porous ladder polymer network structure usually consists of 2D layered sheets with either hexagonal or tetragonal channels, which are constructed by connecting building blocks that extend in multiple directions (nodes) in a confined 2D space. Such a node can either come from a multi-functional monomer, or be generated during a multi-component condensation reaction. There has been study showing that coplanar ladder-type backbone with rigidity and strong directionality facilitates efficient stacking and thus two-dimensional growth.[94] It is noteworthy that the growth of many 2D porous ladder polymer networks, especially the

amorphous ones, are not strictly confined in 2D and could extend in 3D due to defects during the polymerization. In this introduction, they are categorized as 2D networks instead of 3D ones on account of the intrinsically different manners of structural extension and network growth between 2D and intrinsic 3D porous ladder polymer networks.

Compared to the large number of reported 2D structures, a few 3D extended porous ladder polymer networks have been also reported, though the design of the monomer structure and crosslinking chemistry still remains challenging (**Figure 1.1b**). 3D porous ladder polymer networks are potentially more isotropic in terms of its properties, such as conductivity and mass transport pathways, compared to the anisotropic 2D structures. It is also more likely to achieve an ultrahigh surface area by a 3D porous network. Most non-ladder type 3D POPs are constructed from moieties with three-dimensional growth directions, usually in tetrahedral geometry. However, such a tetrahedral moiety is often extended through single-stranded bonds of a sp^3 hybridized unit, such as tetrahedral carbon or adamantane group, and cannot be used to construct a fully fused ladder-type structure. Cyclooctatetraene and triptycene represent the rare cases of fully-fused building blocks that can extend the ladder-type backbone in 3D. Nevertheless, the synthesis of highly porous 3D porous ladder polymer networks still require deliberate structural design and synthetic efforts.

In terms of synthesis methodology, the special structural features of porous ladder polymer networks impose strict requirements on the reactions that can be employed in the synthesis. On one hand, the reaction(s) should be highly efficient in order to fully crosslink the network. On the other hand, the reaction(s) must facilitate the formation of more than

one strands of bonds throughout the network to afford a full ladder-type backbone. Despite these demands, bottom-up syntheses of porous ladder polymer networks have been achieved through a wide variety of methods, as shown in **Figure 1.2**. These include both thermodynamically controlled reactions and kinetically controlled reactions. More than ten different types of ladder-type linkages and numerous porous ladder polymer network materials have been reported in the past decade. In the following discussion, these synthetic methods are categorized into (1) ring-fusing condensation between different monomers, (2) ring-fusing self-condensation, and (3) stepwise crosslinking followed by annulation. In this dissertation, all the chemical structures are drawn in a standardized manner so that the structure represents the repeating unit with a correct ratio of different components. The prevalent style of drawing macrocylic pore structures for porous organic polymers are not used here in order to avoid the potential misrepresentation of the real pore structures, which are often not how they are drawn on papers. It is also noteworthy that these structures show only the ideal bond connectivity that extends the network, while the possibility of the presence of structural defects throughout the network should not be excluded.

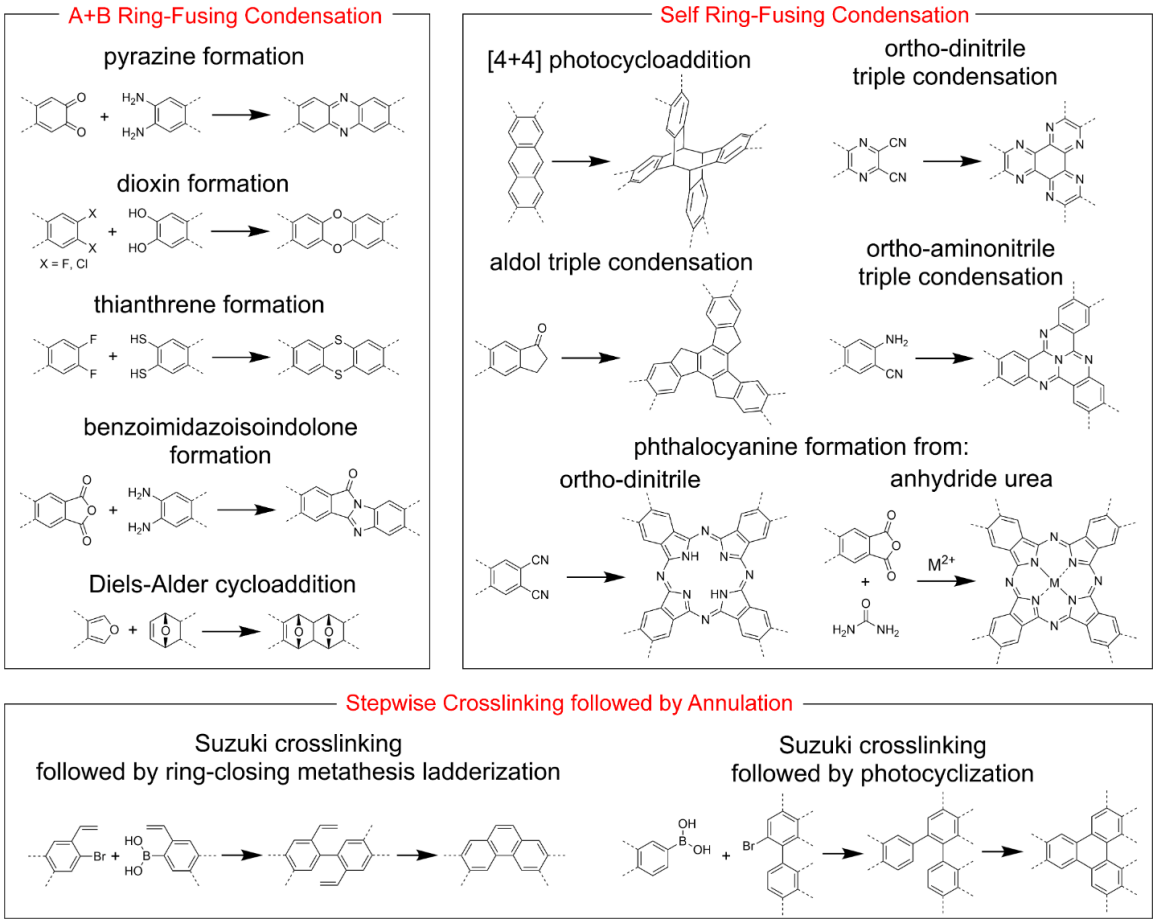

Figure 1.2. Ring-fusing reactions employed in the synthesis of porous ladder polymer networks.

1.2.1 A+B Ring-Fusing Condensation

1.2.1.1 Pyrazine-Fusing

Pyrazine-fusing reaction represents a widely employed, direct ring-fusing crosslinking reaction for porous ladder polymer network synthesis. The condensation of ortho-diamine groups on one monomer and 1,2-diketone moiety from another monomer affords a pyrazine ring as the linkage for a fused, coplanar ladder-type backbone. Pyrazine formation has been one of the most widely employed synthetic strategies for the

construction of porous ladder polymer network, owing to (*i*) the relatively feasible synthesis of 1,2-diketone- and ortho-diamine-functionalized monomers, and (*ii*) the favorable thermodynamic driving force of the formation of aromatic pyrazine unit. This method is versatile in constructing hexagonal 2D, tetragonal 2D, and 3D porous ladder polymer network structures.[95-99] Besides amorphous structures, crystalline porous ladder polymer networks were also reported by using this reaction, indicating the possibility of achieving reversibility on the pyrazine-fusing process under certain conditions.

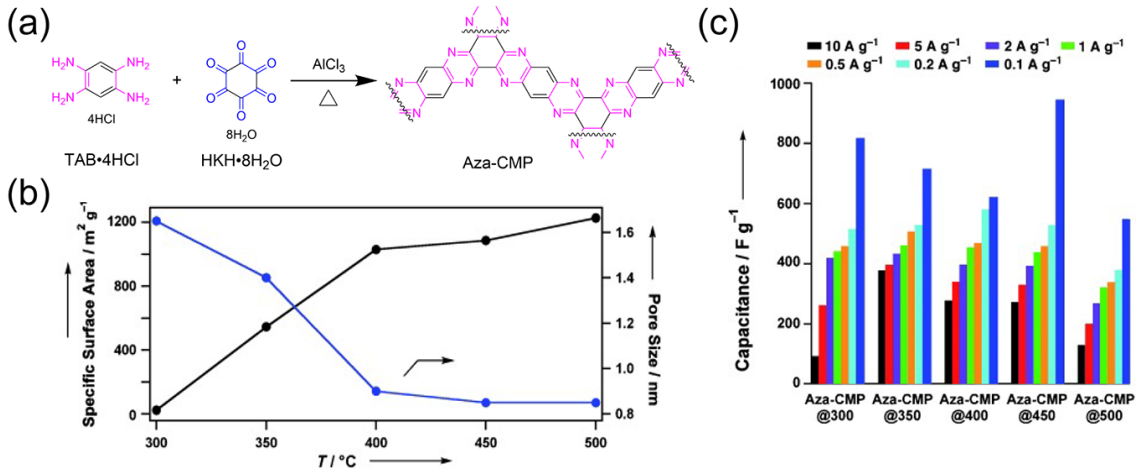

Figure 1.3. Synthesis and properties of Aza-CMP.
(a) Synthetic scheme of Aza-CMP through a pyrazine-fusing crosslinking reaction.
(b) Plot of BET surface areas and pore sizes versus reaction temperatures.
(c) Gravimetric specific capacitance of Aza-CMPs at varying current densities.
Reproduced with permission from Jiang et al.[100] Copyright 2011 Wiley-VCH.

Jiang and co-workers reported[100] the synthesis of an early example of pyrazine-linked porous ladder polymer network (Aza-CMP) in 2011. The network was constructed from imine double condensation reaction between 1,2,4,5-benzenetetramine and

triquinoyl hydrate under ionothermal conditions at elevated temperatures (**Figure 1.3a**). The chemical integrity, especially the formation of the characteristic aromatic C=N units, was characterized by Fourier-transform infrared spectroscopy (FT-IR), solid state ^{13}C cross-polarization/magic angle spinning NMR spectroscopy (^{13}C CP/MAS NMR), and X-ray photoelectron spectroscopy (XPS). No clear peaks in X-ray powder diffraction (PXRD) indicated the amorphous nature of the structure under this synthetic condition. The Brunauer-Emmett-Teller (BET) specific surface areas and pore size distributions measurements showed increased porosity (up to 1227 $m^2 g^{-1}$ at 500 °C) and decreased pore size from 1.65 to 0.9 nm with higher reaction temperatures (**Figure 1.3b**). Aza-CMP demonstrated remarkable supercapacitive energy storage performance with both high capacitance and exceptional stability in charge-discharge cycles (**Figure 1.3c**). This pyrazine-fused backbone not only feature a fully π-conjugated and coplanar ladder-type structure that facilitates electron transport, but also enabled dipolar interaction with electrolyte and accumulation of protons. These characters, together with the intrinsic microporosity, led to large electrostatic interfaces for excellent charge-discharge performance. This work proved the concept of using pyrazine linked porous ladder polymer network in energy storage applications. However, it is worth noting that Mirica and co-workers reported[101] the synthesis of a crystalline porous ladder polymer network aza-COF-2, which had the same designed structure as Aza-CMP, through solvothermal strategies. Although no energy storage performance was reported for direct comparison, critical questions about the reproducibility of the materials remain on how the actual

structures deviated from the seemingly same designed structures and how these differences impacted the properties.

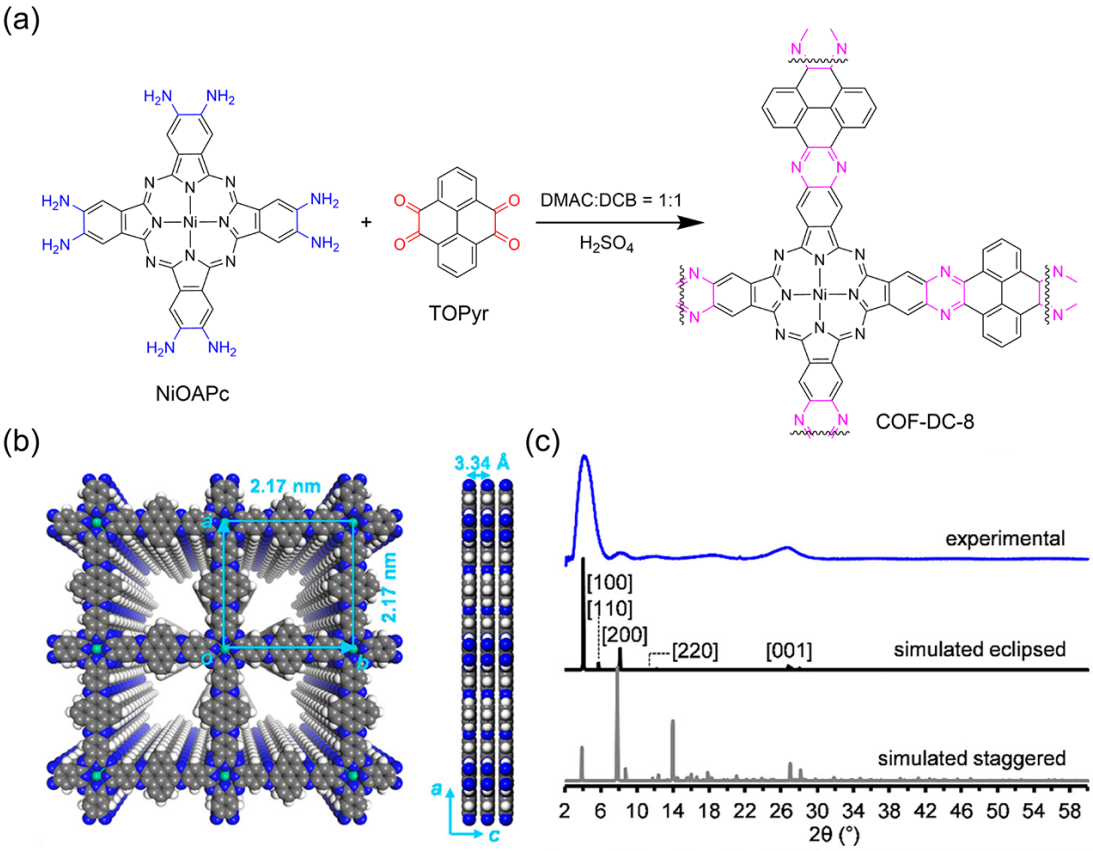

Figure 1.4. Synthesis and characterization of COF-DC-8.
(a) Synthesis of COF-DC-8 through a pyrazine-fusing crosslinking reaction.
(b) Top and side view of 2 × 2 square grids in an eclipsed stacking lattice.
(c) Experimental powder X-ray diffraction of COF-DC-8 and simulated patterns of the eclipsed and staggered stacking structures.

Reproduced with permission from Mirica et al.[102] Copyright 2018 American Chemical Society.

From then on, other pyrazine-linked porous ladder polymer networks have been reported, including several crystalline materials under modified reaction conditions. Mirica and co-workers reported[102] a crystalline structure with tetragonal channels (COF-DC-8) by pyrazine-fusing reaction between an intrinsically planar conjugated phthalocyanine monomer and a pyrene-derived monomer (**Figure 1.4a**). Good crystallinity was achieved under H_2SO_4 catalyzed solvothermal conditions after 10 days. Optimization efforts showed that the use of acid catalysts (such as H_2SO_4, triflic acid, or acetic acid) and relatively low concentration of the monomeric reactants were beneficial for improving crystallinity. Microwave heating significantly reduced the reaction time at the expense of slightly diminished crystallinity. The crystallinity was confirmed by PXRD (**Figure 1.4c**), Scanning electron microscopy (SEM), and High-resolution transmission electron microscopy (HR-TEM). These data were consistent with the structures simulated by density functional theory (DFT) calculations, demonstrating a fully eclipsed stacking model (**Figure 1.4b**). More recently, Feng and co-workers reported[96] similar crystalline pyrazine-linked porous ladder polymer network structures, finding the tert-butyl groups on pyrene largely contributed to the layer-stacking conformation in these 2D COFs. Besides the acidic condition, Liu and co-workers also achieved[103] crystalline pyrazine-fused porous ladder polymer network (PGF-1) under basic aqueous condition (4 M KOH/H_2O). The unusual dynamic character of C=N under such condition benefited the remarkable in-plane order, leading to good crystallinity in the final product.

Pyrazine-fusing reaction has also been employed in the synthesis of 3D porous ladder polymer network structures. A 3D-extending network structure usually give higher

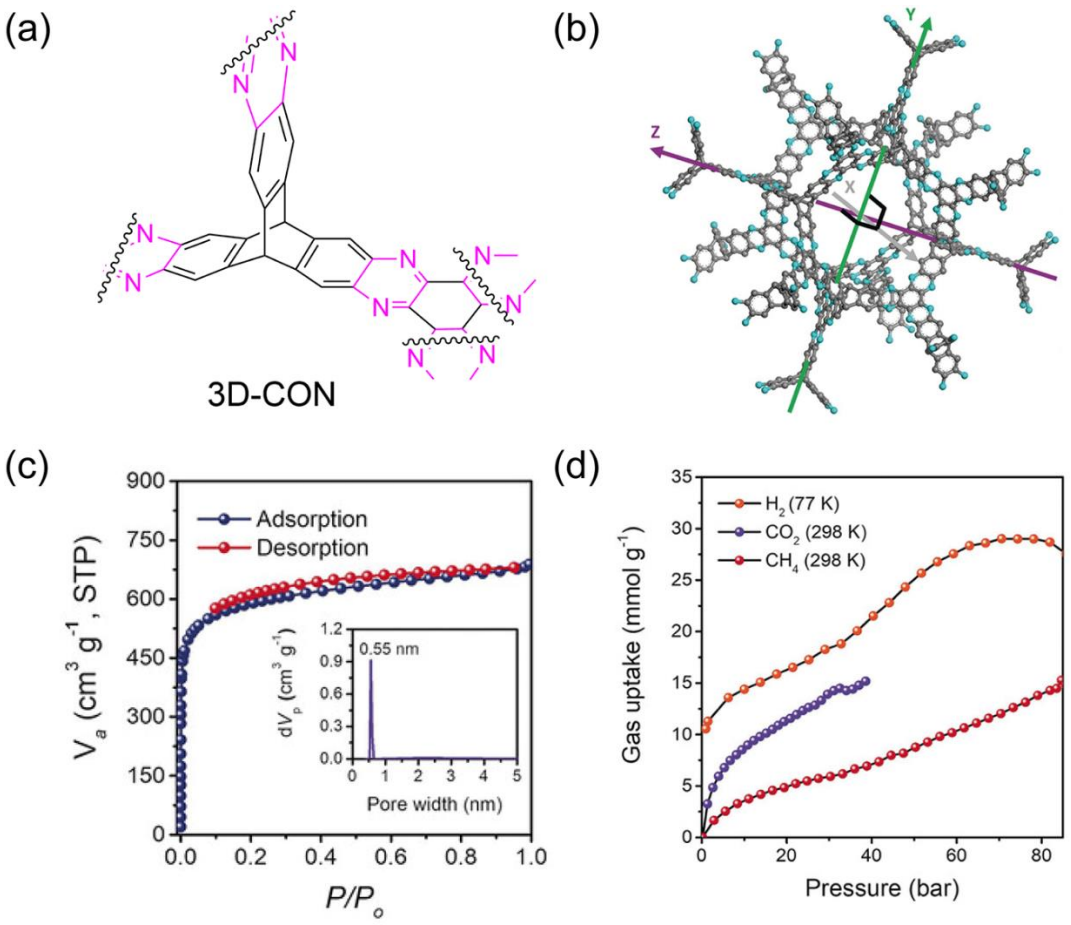

Figure 1.5. Gas adsorption properties of 3D-CON.

(a) Structural formula of the repeating unit of 3D-CON constructed by pyrazine-fusing crosslinking reaction.

(b) Nitrogen adsorption isotherm at 77 K. Inset: pore size distribution from NLDFT calculation.

(c) High-pressure H_2, CH_4, and CO_2 adsorptions.

Reproduced with permission from Baek et al.[105] Copyright 2018 Wiley-VCH.

porosity than a 2D-analogue.[8, 104] Baek and co-workers reported[105] the synthesis of a 3D porous ladder polymer network structure (3D-CON) through double imine condensation between triptycene hexamine and hexaketocyclohexane in a 1:1 stoichiometric ratio, without the introduction of commonly used tetrahedral center for a 3D network (**Figure**

1.5a). The directionality of the linkages extended from these two monomers generated cage-like 3D ladder-type nodes, which further grew into a 3D porous ladder polymer network structure (**Figure 1.5b**). 3D-CON exhibited high BET surface area of 2247 $m^2 g^{-1}$ with dominant microporosity (**Figure 1.5c**). It exhibited good uptake and heat of adsorption on H_2, CH_4, and CO_2 (**Figure 1.5d**). In addition, remarkable thermal stability up to 600 °C was achieved owing to the ladder-type backbone. The combination of this geometry and condensation method offers a promising strategy for building highly porous 3D porous ladder polymer networks.

1.2.1.2 Dioxin-Fusing

Dioxin-fusing through double aromatic nucleophilic substitution reaction has been applied extensively in the syntheses of POPs. McKeown and co-workers reported[106] in 2003 the synthesis of dioxin-linked, crosslinked POP structure using this method. Crosslinked dioxin-derived porous ladder polymer networks have been synthesized[106-113] from monomers such as tridentate hexachlorohexaazatrinaphthylene and cyclotricatechylene derivatives, as well as quadridentate phthalocyanine and calixresorcarene derivatives. Most of the dioxin-fused porous ladder polymer networks reported so far are amorphous, indicating an irreversible nature of this reaction in most of these cases.[114, 115]

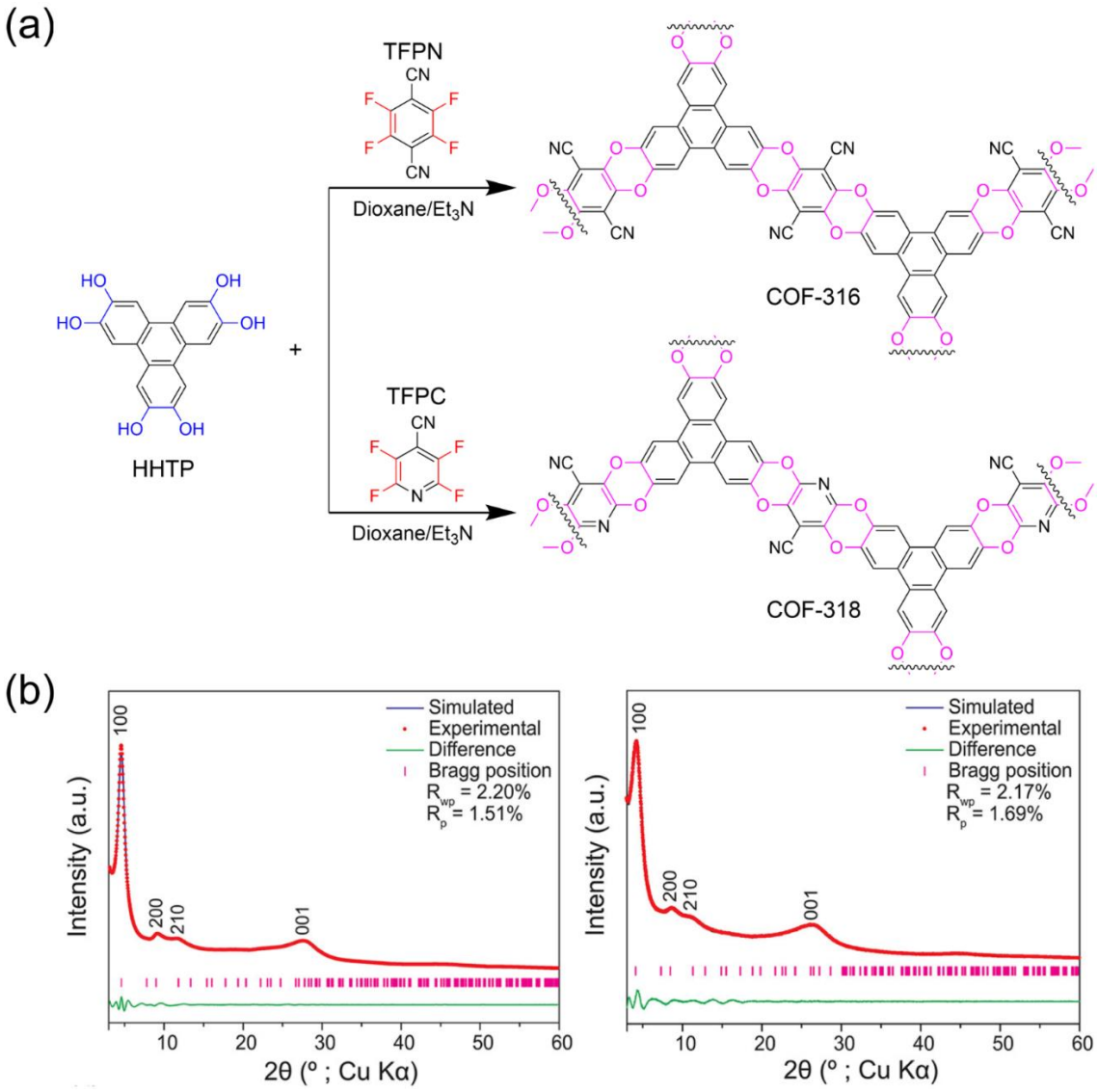

Figure 1.6. Synthesis of COF-316 and -318.

(a) Synthesis of COF-316 and -318 through a dioxin-fusing crosslinking reaction. Note that the backbone is regio-irregular due to the unsymmetrical nature of the cyano-pyridine units, only one arbitrary backbone constitution is shown.

(b) PXRD patterns and Pawley refinement of COF-316 (left) and -318 (right), respectively.

Reproduced with permission from Yaghi et al.[94] Copyright 2018 American Chemical Society.

Recently, Yaghi group and Fang group independently reported[94, 116] crystalline dioxin-fused porous ladder polymer networks, namely COF-316, COF-318, and JUC-505, JUC-506, respectively (**Figure 1.6, 1.17**). Despite slightly different reaction conditions, both materials were synthesized by two consecutive nucleophilic aromatic substitutions between a catechol-like monomer and an ortho-difluoro benzene-derived monomer. The strong electron withdrawing substituents on the center of difluoro benzene monomers are essential to render them reactive. Distinct from other reported crystalline COFs that are most constructed through reversible bond formation, it was proven that the dioxin ring-closing reaction was irreversible during the synthesis of COF-316 and JUC-505, despite their crystalline nature (**Figure 1.6b**). It is hypothesized that the coplanar ladder-type backbone that induced rigidity and strong directionality of the linkage played an important role in facilitating the ordered-growth and ordered-stacking of the network layers. This irreversibly-formed linkage endowed these porous ladder polymer networks with exceptional thermal and chemical stabilities, allowing it to survive certain harsh conditions of application and post-functionalization, including strong acid, base, reductant, and oxidant. The unique combination of crystallinity and stability of dioxin-linked porous ladder polymer networks makes this chemistry promising for a wide variety of applications. On this basis, Lan and co-workers synthesized[117] a series of covalently bonded Z-scheme heterojunctions of COF-318 and inorganic semiconductors (TiO_2, Bi_2WO_6, and α-Fe_2O_3), which demonstrated high efficiency in photocatalytic CO_2 to CO conversion.

1.2.1.3 Thianthrene-Fusing

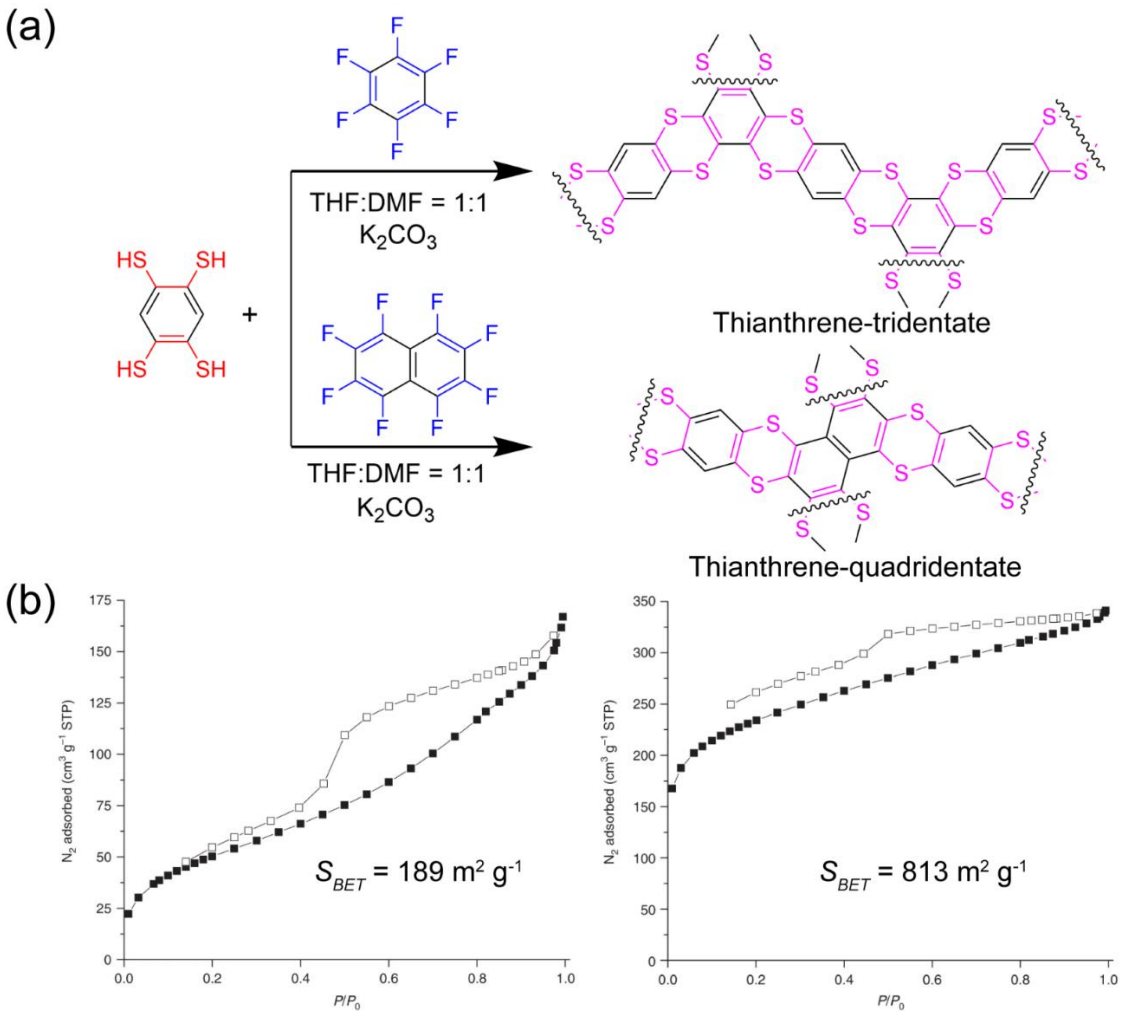

Figure 1.7. Synthesis of porous ladder polymer networks through thianthrene-fusing crosslinking.

(a) Synthesis of porous ladder polymer networks through thianthrene-fusing crosslinking reactions from hexafluorobenzene and octafluoronaphthalene monomers, respectively.

(b) N_2 adsorption-desorption isotherms of Thianthrene-tridentate (left) and Thianthrene-quadridentate (right) at 77 K, respectively.

Reproduced with permission from Swager et al.[118] Copyright 2018 Nature Publishing Group.

Swager and co-workers reported[118] thianthrene linked porous ladder polymer network through double nucleophilic aromatic substitution reaction that is similar to the dioxin-fusing reaction (**Figure 1.7a**). Monomers with three or four directions of extension were applied into the synthesis and afford two insoluble crosslinked porous ladder polymer networks. Among these structures, the one composed of quadridentate nodes (Thianthrene-quadridentate) showed much higher BET surface area (813 m^2 g^{-1}) than that the one with tridentate nodes (Thianthrene-tridentate) (189 m^2 g^{-1}) (**Figure 1.7b**), presumably due to less interpenetration induced by smaller pore size and higher degree of crosslinking as confirmed by the sulfur/fluorine ratio from XPS. Interestingly, none of these reported porous ladder polymer networks were crystalline despite of the dynamic nature of the C—S bonds and reversibility of thianthrene-fusing reaction demonstrated in small molecular model reactions. This counterintuitive result, together with the results of crystalline structures of COF-316, JUC-505, and COF-DC-8 obtained from irreversible reactions, indicate that the crystallinity of porous ladder polymer networks is not solely governed by the reversibility of the bond formation processing. Instead, non-covalent guidance of ordered network growth, such as interlayer stacking, could play an important role in facilitating long-range order in thesynthesis.

1.2.1.4 Benzoimidazoisoindolone-Fusing

Linear benzoimidazobenzophenanthroline ladder polymers (BBL) were first synthesized[66] in the 1960s. BBL polymers have been investigated[119, 120] extensively in the past decades on account of their promising optical and electronic properties. Recently,

Baek and co-workers reported[121] porous ladder polymer network structures 2D-BBL-T-HT and 2D-BBL-H-HT that extend the benzoimidazoisoindolone unit – the characteristic building block in BBL – in multiple directions. It is worth noting that though the chemistry is similar to BBL formation, the constructed linkage in these materials is benzoimidazoisoindolone, not BBL. The linkage was fused by double condensation reaction between an aromatic cyclic anhydride and an ortho-diamine unit in polyphosphoric acid (**Figure 1.8a**). The chemical identities of 2D-BBL-T-HT and 2D-BBL-H-HT were confirmed by ^{13}C CP/MAS NMR, FT-IR, and XPS. Thermogravimetric analysis (TGA) demonstrated an excellent thermal stability with a decomposition temperature as high as 500 °C. These benzoimidazoisoindolone-derived porous ladder polymer networks do not typically show porosity until annealed at high temperatures due to physically trapped small molecules. After annealing at 450 °C for 2 h, the materials reached BET surface areas of 615 and 365 $m^2\ g^{-1}$ for 2D-BBL-T-HT and 2D-BBL-H-HT, respectively. Owing to abundant polar heteroatoms (nitrogen and oxygen) introduced by the benzoimidazoisoindolone linkage, these materials showed strong affinity towards CO_2 molecules, with heats of adsorptions (Q_{st}) as high as 37.80 kJ mol^{-1} and 44.43 kJ mol^{-1} for 2D-BBL-T-HT and 2D-BBL-H-HT, respectively (**Figure 1.8b**). Very recently, Baek and co-workers further achieved[122] the synthesis of a vertical 2D layered porous ladder polymer network with the real BBL linkage (V2D-BBL), through a polycondensation between triptycene hexamine and naphthalenetetracarboxylic dianhydride.

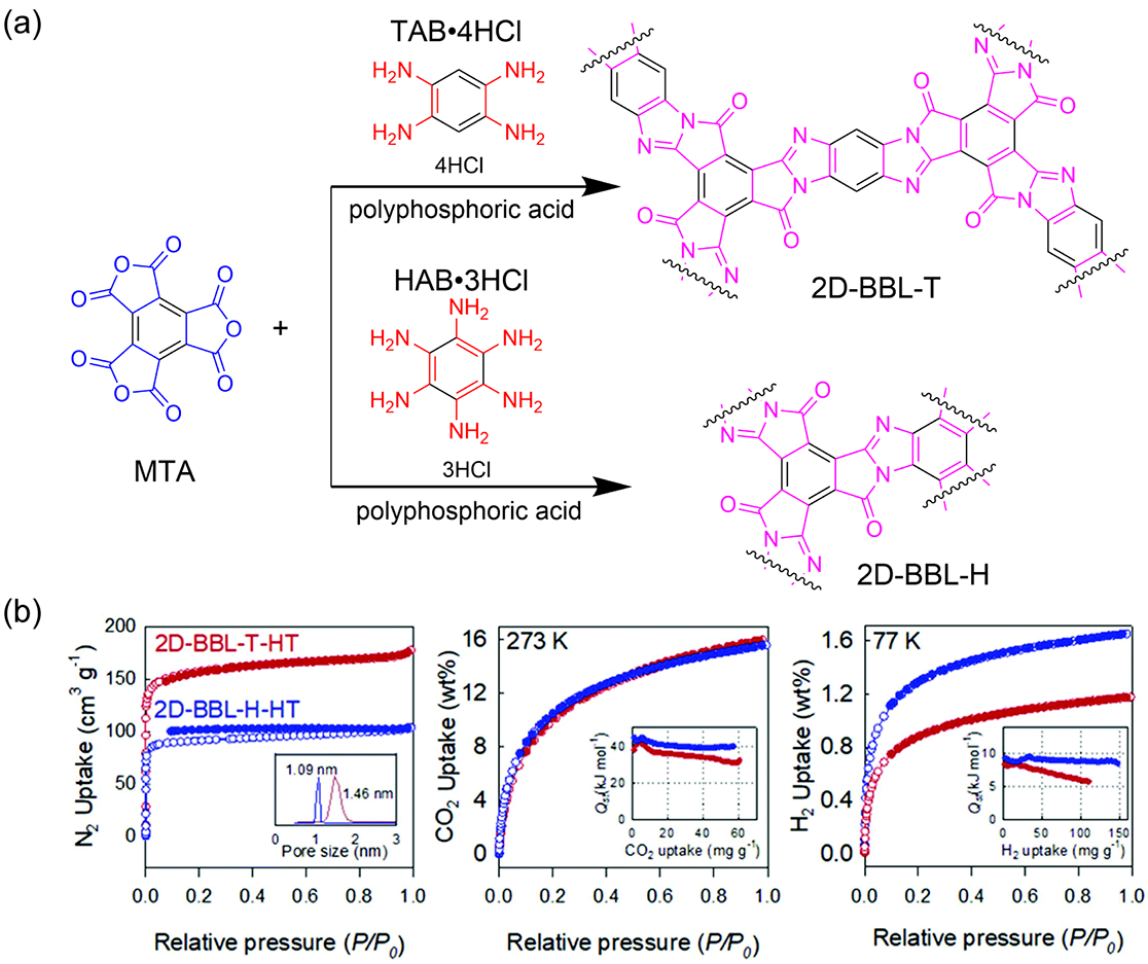

Figure 1.8. Synthesis and gas adsorption properties of 2D-BBL-T and 2D-BBL-H.

(a) Synthesis of 2D-BBL-T and -H through fusing benzoimidazoisoindolone units during crosslinking. Note that the backbone is regio-irregular and only one arbitrary constitution is shown.

(b) Left: N_2 adsorption-desorption isotherms at 77 K. Inset: Pore size distribution calculated from NLDFT. Middle: CO_2 adsorption-desorption isotherms at 273 K. Inset: Q_{st} for CO_2 estimated from isotherms at 273 K and 298 K. Right: H_2 adsorption-desorption isotherms at 77 K. Inset: Q_{st} for H_2 estimated from isotherms at 77 K and 87 K.

Reproduced with permission from Baek et al.[121] Copyright 2019 Royal Society of Chemistry.

1.2.2.1 Topochemical Photocycloaddition

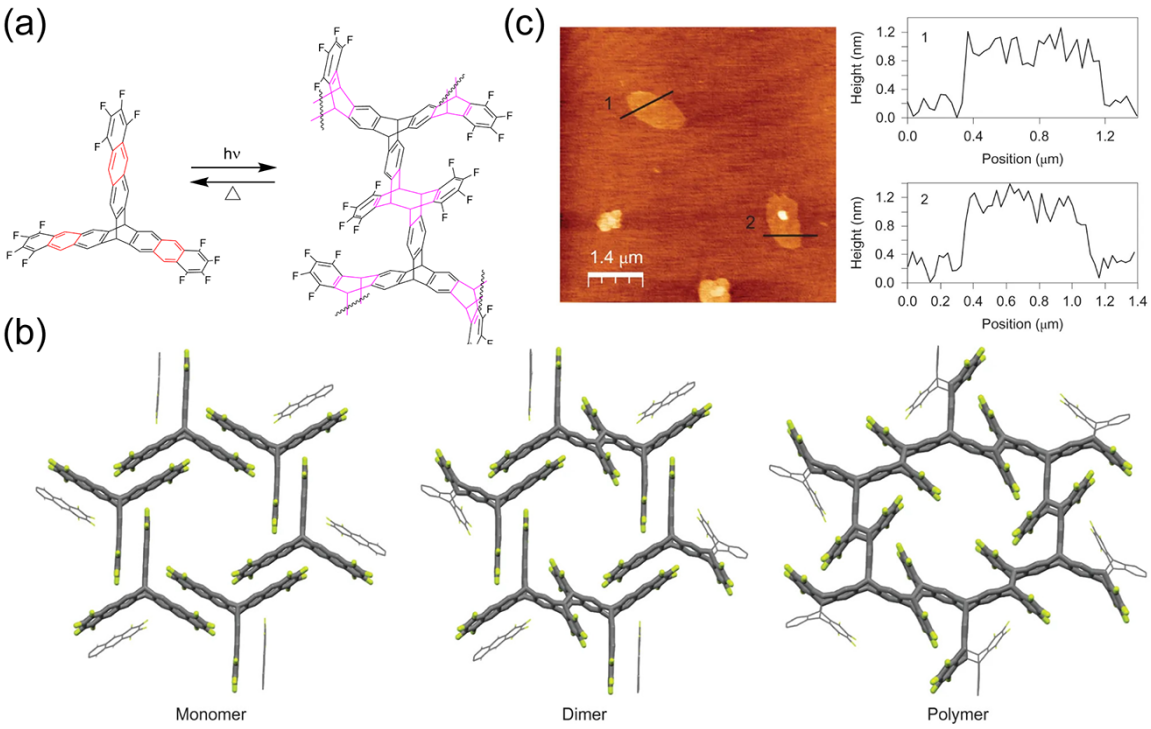

Figure 1.9. Topochemical synthesis and exfoliation of fantrip-derived 2D porous ladder polymer network sheets.

(a) Construction of the 2D porous ladder polymer network structure through a single-crystal-to-single-crystal [4+4] photopolymerization of fluorinated anthracene groups arranged in a triptycene motif.

(b) X-ray crystal structures of the fantrip monomer, dimer, and polymer.

(c) Left: AFM height image of exfoliated monolayers by slow rotation in NMP at 50 °C for 6 days. Right: AFM height profiles recorded along the lines indicated on left.

Reproduced with permission from King et al.[123] Copyright 2014 Nature Publishing Group.

In the early 2010s, the groups of Sakamoto, Schlüter, and King explored[124-127] topochemical self-photopolymerization of monomers to synthesize 2D polymer networks with long range order through crystal-to-crystal transformations. The key feature of this

strategy is the formation of pre-organized closely packed photoreactive precursor in a single crystal phase, which usually containing anthracene units. Subsequent photo irradiation triggers the photopolymerization to afford a 2D polymer network. King and co-workers further expanded[123] the strategy to synthesize a 2D porous ladder polymer network. A triptycene-derived precursor that bears photoreactive fluorinated anthracene unit in each arm was synthesized and pre-organized into a single crystal featuring lamellar packing. The monomer molecules were closely packed in such a manner that each anthracene group located parallelly to another anthracene from an adjacent monomer. The following [4+4] photopolymerization of the 9,10 positions of the anthracene units led to double strands crosslinking across each layer, generating a ladder-type backbone, while maintaining the crystalline nature of the product (**Figure 1.9a, b**). Although no gas adsorption data was reported, the individual crystalline sheets were indeed porous with pore size of ~0.9 nm and pore density of 3.3×10^{13} pores/cm^2. Free-standing single layer 2D porous ladder polymer network sheets were also successful exfoliated with the help of N-Methyl-2-Pyrrolidone solvent, as confirmed by height profile of 0.8 to 1 nm from atomic force microscopy (AFM), corresponding well to the expected thickness of a monolayer (**Figure 9c**).

1.2.2.2 Aldol triple condensation

Aldol triple condensation (ATC) of monofunctional indan-1-one derivatives has been well explored[85, 86, 128-132] in the synthesis of truxene-derived small molecules and POPs under acidic conditions. In this reaction, two aldol reactions take place in between

the —$COCH_2$— groups followed by dehydration, electrocyclic ring-closing, and eventually aromatization, to afford the fused benzene ring in the center with the loss of three equivalents of water. A multifunctional monomer thus can be used to construct a truxene-derived porous ladder polymer network structure. In such a triple condensation cross-linking, each functional group grows into two directions. As a result, efficient cross-linking can be achieved[133-135] even from a bifunctional monomer, with a gel point as low as 50%. Scherf, Thomas and co-workers reported[84] the synthesis of rigid, microporous, truxene-cored porous ladder polymer network structures (Trux-ATC) by ATC reaction from simple bifunctional diketo-s-indacene derived monomers with various Lewis acid catalysts, such as $TiCl_4$, molten $ZnCl_2$, H_2SO_4, or methanesulfonic acid (MSA), *etc* (**Figure 1.10**). These porous ladder polymer networks are amorphous as a result of the irreversible nature of ATC reaction. The chemical identities were confirmed by ^{13}C CP/MAS NMR. Among these materials, tetraketo-s-indacene derived porous ladder polymer network (Trux-ATC-Carbonyl) exhibited the highest BET surface area (1650 $m^2 g^{-1}$), and contained additional carbonyl groups for further functionalization. ATC approach is generally scalable and facile, promising good potential in porous ladder polymer network synthesis.

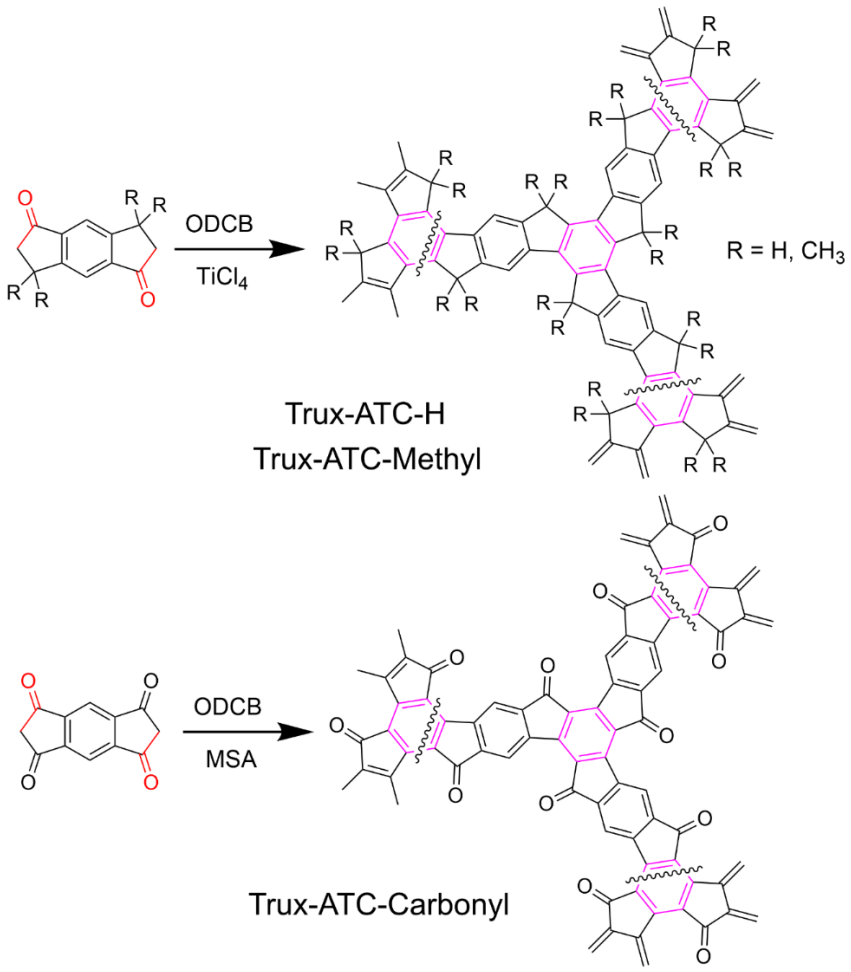

Figure 1.10. Schematic representation for the synthesis of porous ladder polymer networks that are self-crosslinked through an aldol triple condensation reaction. Note that the backbone of the bottom structure is regio-irregular and only one arbitrary constitution is shown.

Reproduced with permission from Scherf et al.[84] Copyright 2010 Royal Society of Chemistry.

1.2.2.3 Ortho-dinitrile triple condensation

Oschatz and co-workers reported[136] a ortho-dinitrile triple condensation strategy to synthesize 2D porous ladder polymer networks from a pre-organized

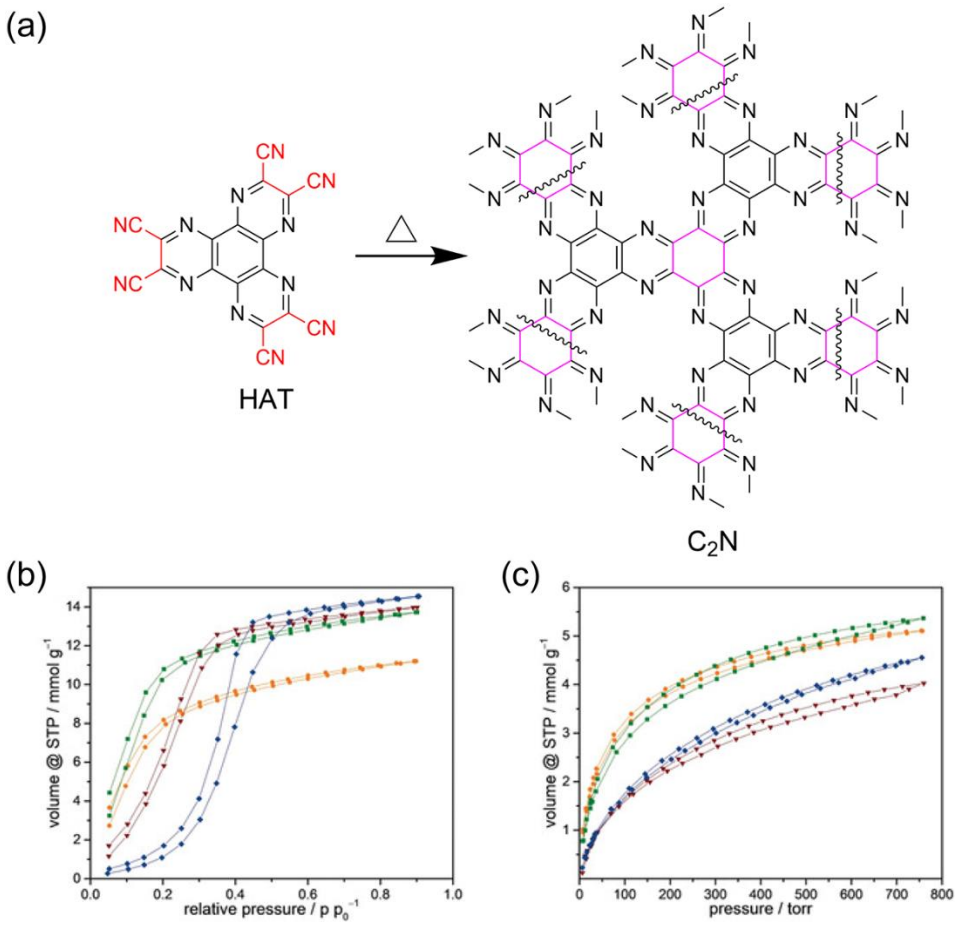

Figure 1.11. Synthesis and gas adsorption properties of C_2N structure.

(a) Self-crosslinking of HAT monomers to afford C_2N through an ortho-dinitrile triple condensation.

(b) Water vapor adsorption isotherms at 298 K of C_2N samples that are carbonized at variable temperatures: 550 °C (orange circles), 700 °C (green squares), 850 °C (wine triangles), 1000 °C (blue diamonds).

(c) Carbon dioxide adsorption isotherms of these samples at 273 K.

Reproduced with permission from Oschatz et al.[136] Copyright 2018 Wiley-VCH.

hexaazatriphenylene (HAT) precursor. Based on the designed reaction scheme, thermal condensation of three ortho-dinitrile pyrazine units took place through the loss of six nitrile groups, to afford a new fused six-membered-ring in the center (**Figure 1.11a**). This

reaction lead to a pyrazine-rich porous ladder polymer network structure C_2N similar (but not identical) to that of Aza-CMP discussed above. The temperature effects on the synthesis of the frameworks was investigated, revealing lower nitrogen contents and increasing micropore volumes with increasing condensation temperatures from 550 °C to 1000 °C. Although the exact chemical identity of the framework was difficult to determine due to its amorphous nature, high nitrogen content was confirmed by elemental analysis, energy dispersive X-ray spectroscopy, and XPS. These pyrazine units provided highly polarizing surface and more specific binding sites for polar small molecules. Combined with the microporosity (600-800 $m^2\ g^{-1}$), these materials demonstrated high H_2O and CO_2 adsorption affinities and capacities (**Figure 1.11b, c**).

1.2.2.4 Ortho-aminonitrile triple condensation

Ruoff and co-workers employed[137] self-triple condensation of bifunctional aromatic ortho-aminonitrile in the synthesis of a series of nitrogen rich, tricycloquinazoline linked porous ladder polymer networks (CQNs). The feasibility of the formation of tricycloquinazoline core was first demonstrated on a small molecular model by triple condensation reaction of 2-aminobenzonitrile under zinc chloride ($ZnCl_2$) catalyzed ionothermal condition. The use of $ZnCl_2$ as catalyst and high temperature are critical for this reaction. This strategy was subsequently applied to synthesize crosslinked CQN by using bifunctional monomers (**Figure 1.12a**). It was found that higher temperatures and larger amount of $ZnCl_2$ facilitated high conversion of the reaction. FT-IR, ^{13}C CP/MAS NMR, and XPS confirmed the formation of the characteristic

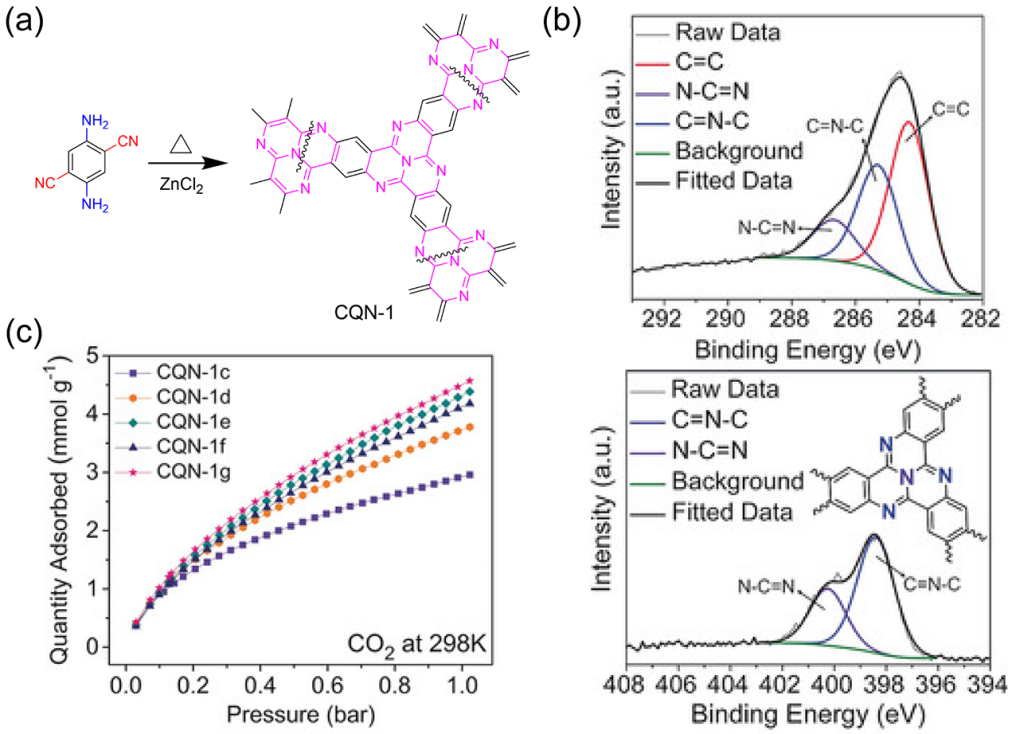

Figure 1.12. Synthesis, characterization, and CO_2 adsorption properties of CQN-1.
(a) Synthesis of CQN-1 constructed by self-crosslinking an ortho-aminonitrile monomer through triple condensation.
(b) High resolution XPS C-1s (top) and N-1s (bottom) spectra of CQN-1.
(c) CO_2 adsorption isotherms of various CQN-1 samples collected up to 1 bar at 273 K.

Reproduced with permission from Ruoff et al.[137] Copyright 2018 Wiley-VCH.

tricycloquinazoline structures (**Figure 1.12b**). CQNs showed excellent thermal stability up to 500 °C, demonstrating the advantage of conjugated ladder-type backbone. Porosity also showed dependency with temperatures and $ZnCl_2$ amount, with highest BET surface area (1870 m^2 g^{-1}) achieved at 400 °C and excessive addition of $ZnCl_2$ (10 equivalents *vs* monomer). CQNs demonstrated a high CO_2 uptake value among reported POPs (4.57 mmol g^{-1} at 298 K and 1 bar, **Figure 1.12c**), which can be attributed to the synergetic effects of high porosities, appropriate pore sizes, and the high nitrogen content (up to 24

wt%) of the materials. The rigid ladder-type backbone of CQNs may also contribute entropically to the CO_2 uptake performance, due to the low initial backbone entropy.

1.2.2.5 Ortho-dinitrile quadruple condensation

McKeown and co-workers reported[107] a porous ladder polymer network constructed by ortho-dinitrile quadruple condensation from a bifunctional monomer. For each growth terminal, four monomers with eight nitrile groups condensed together to form a phthalocyanine macrocycle. This reaction could take place with or without the participation of a metal ion. The resulting porous ladder polymer network possessed active catalytic sites for several important reactions, including methane oxidation, olefin oxidation, and C-C bond formation. Afterwards, Abel, Clair, and co-workers reported the employment of a similar chemistry to construct a porous ladder polymer network structure (poly-FePc) on surface.[138, 139] Firstly, the monomer 1,2,4,5-tetracyanobenzene precursor and Fe were co-evaporated onto atomically clean and well-defined Ag or Au surface, which acted as templates to confine polymerization and generate a true 2D crystalline ordered framework. Subsequently, a metal-directed, on-surface synthesis was conducted in between the monomers (**Figure 1.13a**). This on-surface structure can be directly visualized by *in situ* scanning tunneling microscopy (STM) (**Figure 1.13b, c**). Precise control of 2:1 stoichiometry of monomer:Fe was crucial to obtain the desired porous ladder polymer network structure. Observed pattern from STM matched well with the theoretical 2D lattice from DFT calculations, confirming the covalent formation of the phthalocyanine linkages. It was also demonstrated that this porous ladder

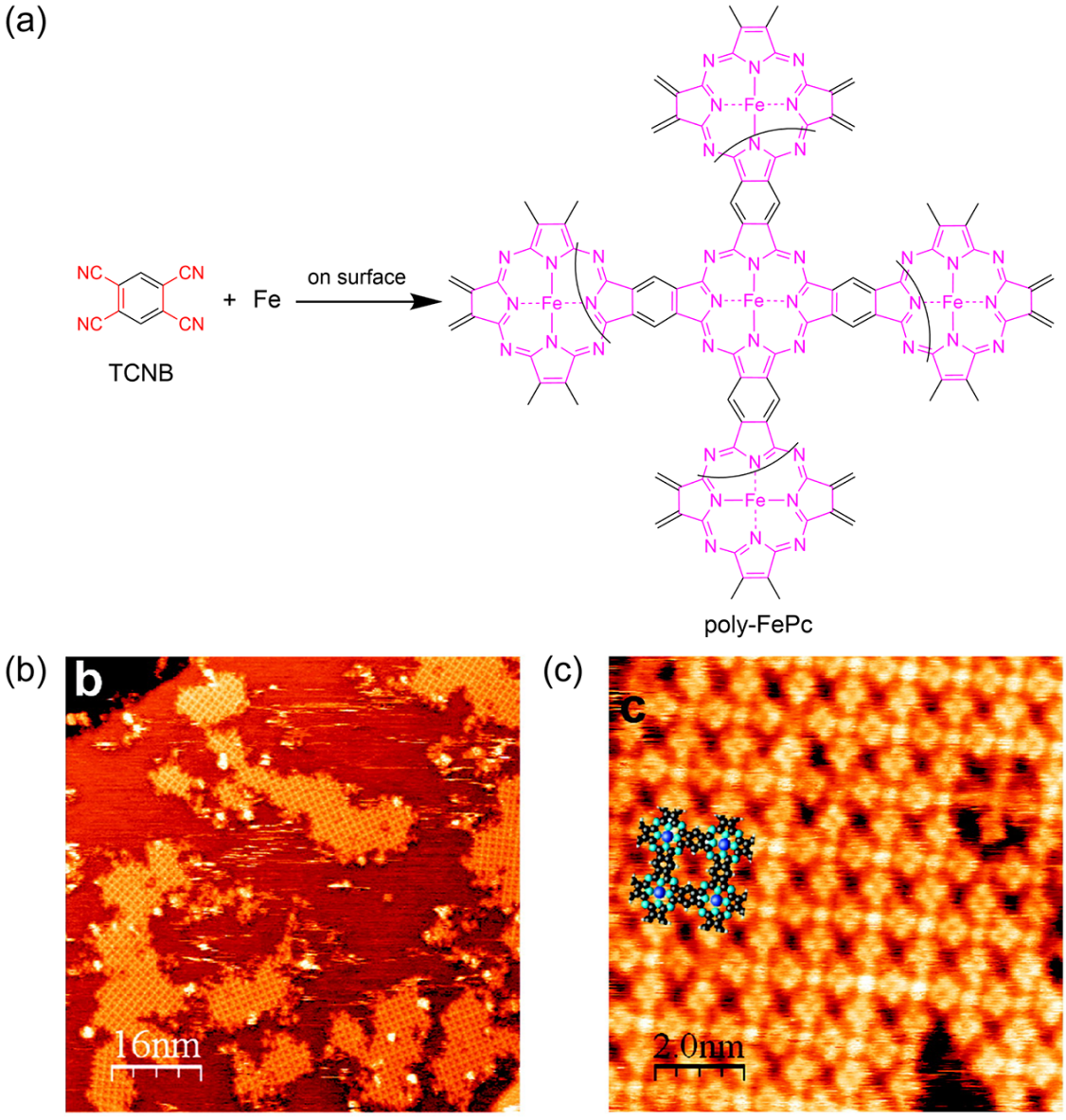

Figure 1.13. Synthesis and characterization of Fe-phthalocyanine 2D porous ladder polymer network.

(a) On-surface synthesis of Fe-phthalocyanine 2D porous ladder polymer network through a quadruple condensation of ortho-dinitrile functionalized monomers.

(b,c) STM images of poly-FePc formed on a Ag(111) surface (square unit cell, 1.15 nm large).

Reproduced with permission from Abel et al.[138] Copyright 2011 American Chemical Society.

polymer network structure could be grown directly on a thin insulating NaCl film, and the organic layer can potentially be transferred to various devices and characterization systems by soft lithography techniques. With the regularly and dispersively distributed transition-metal atoms in the center of phthalocyanine, its intriguing magnetism properties have been reported in several following-up publications. It is noteworthy that in-solution synthesis of similar materials has also been conducted through cross coupling between benzenetetracarboxylic anhydride and urea, although the product structure could not be clearly determined due to its amorphous nature.[140-142]

1.2.3 Diels-Alder cycloaddition

Diels-Alder (DA) cycloaddition reaction has also drawn attention for the purpose of constructing porous ladder polymer networks due to its ability to form two bonds simultaneously in a pristine, catalyst-free manner.[143-145] Coskun and co-workers reported[143, 144] the one-pot synthesis of 2D and 3D porous ladder polymer networks (2D/3D ep-POP) by DA reactions between *anti*-diepoxyanthracene and benzotrifuran or that between *anti*-diepoxyanthracene and cyclooctatetrafuran (**Figure 1.14a**). Promoted by simple heating in DMF solution, a furan unit as the diene and an anthracene unit as the dienophile underwent [4+2] cycloaddition to afford a ladder-type linkage between the monomeric building blocks. The formation of the eight-membered cyclooctatetraene center, with a boat conformation, can served as a true 3D node with ladder-type constitution, extending into an intrinsically 3D porous ladder polymer network structure.

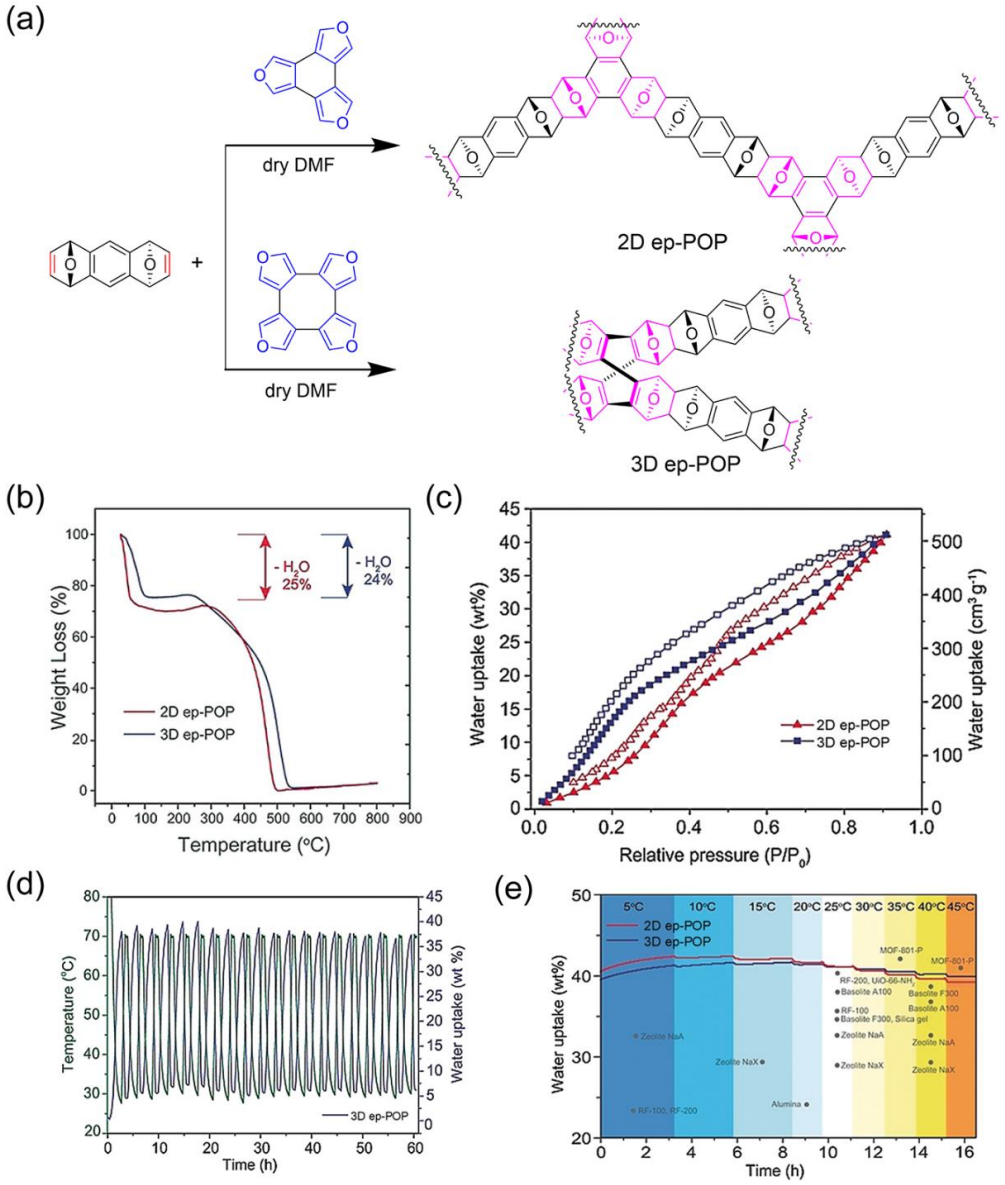

Figure 1.14. Synthesis, characterization, and water adsorption properties of ep-POPs.

(a) Synthesis of 2D and 3D ep-POP through Diels-Alder cycloaddition.
(b) TGAs of ep-POPs under air.
(c) Water adsorption isotherms of 2D and 3D ep-POPs at 298 K.
(d) Cycle performance for water adsorption using 3D ep-POP by the continuous change in the temperature between 30–70 °C at a constant humidity of RH=90%.
(e) Water adsorption experiment of 2D and 3D ep-POPs in the temperature range of 5–45 °C, acquired at RH=90%.

Reproduced with permission from Coskun et al.[143] Copyright 2018 Wiley-VCH.

These ep-POPs were characterized by ^{13}C CP/MAS NMR, XPS, and FT-IR. No distinct crystallinity was observed. BET surface areas of 2D and 3D ep-POPs were 852 and 779 $m^2 g^{-1}$, respectively. Lower porosity of 3D ep-POP was attributed to the presence of interpenetration. With this special monomer design, abundant oxygen atoms were introduced into the, leading to efficient hydrogen-bonding sites for water molecules. Combined with the dominant microporosity, ep-POPs showed high water adsorption capacities up to 39.2–42.4 wt% in a wide temperature range of 5-45 °C (**Figure 1.14e**). More importantly, their isosteric heats of adsorption for water were significantly lower than other commercial adsorbents, allowing for energy-efficient regeneration at temperatures as low as 55 °C. These outstanding properties and performance make ep-POPs promising materials for dehumidification and water capture.

1.2.4 Stepwise crosslinking followed by annulation

Despite the numerous reported examples on direct one-pot construction of porous ladder polymer networks, the scope of suitable reactions is still relatively narrow because the simultaneous demands on (*i*) one-pot formation of multiple strands of bonds and (*ii*) high conversion for crosslinking. Alternatively, porous ladder polymer networks can be constructed through a stepwise approach[17, 145-148]: firstly, cross-linking the network through the formation of a single strand of bonds, and subsequently ladderization of the entire backbone to give the desired structure. This general strategy has been extensively employed[70, 91, 92, 149] in the formation of linear ladder polymers, and allows a much wider

scope of suitable reactions. The major concern associated with the stepwise synthesis is in the second step: because the first step already crosslinked the monomers into an insoluble intermediate, the subsequent ladderization step, which needs to be highly efficient for low defect level, would have to take place in a challenging heterogenous manner.

1.2.4.1 Suzuki crosslinking followed by ring-closing metathesis ladderization

Recently, Fang and co-workers reported[146] a stepwise synthesis of truxene-derived porous ladder polymer network (trux-PLAN) through Suzuki cross-coupling and subsequent heterogeneous ring-closing olefin metathesis (RCM). The backbone of the non-ladder-type intermediate (PPN-Precursor), was first constructed by crosslinking of vinyl-functionalized tridentate truxene monomer and linear phenylene derived monomer. The pre-functionalized vinyl groups on the ortho-positions of coupling sites allowed for the subsequent RCM reaction (**Figure 1.15a**). To ensure the conversion of this heterogeneous annulation, the RCM reaction was conducted for twice to afford trux-PLAN with low level of unannulated defect. This low-defect backbone was confirmed by ^{13}C CP/MAS NMR, with the observation of complete disappearance of the vinyl $=CH_2$ signal in trux-PLAN spectrum (**Figure 1.15b**), even with 99% ^{13}C isotope labeled on the terminal vinyl unit. The remarkably high efficiency of the solid-state RCM ladderization was attributed to (*i*) the strong driving force of aromatization during this

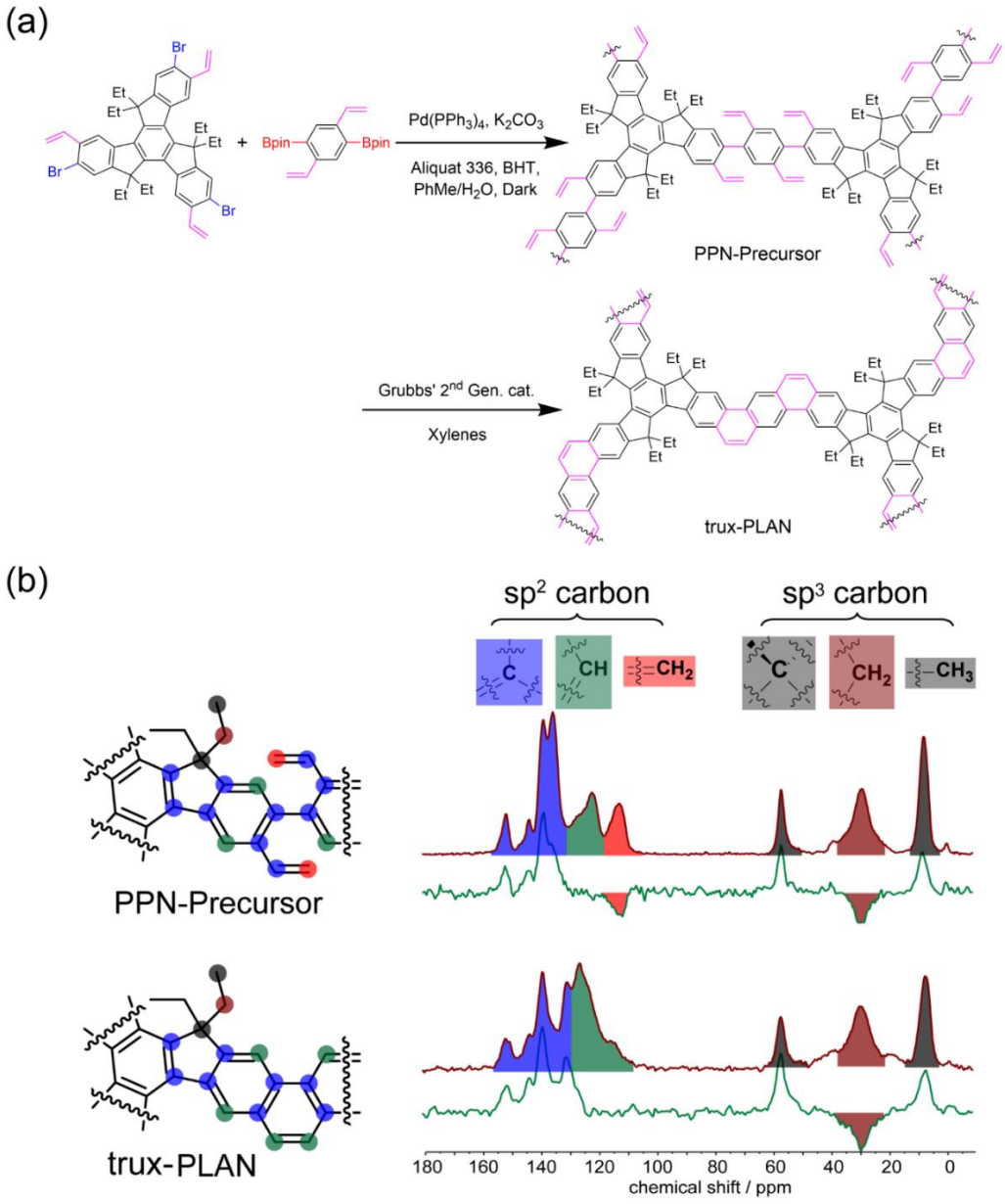

Figure 1.15. Synthesis and characterization of trux-PLAN.

(a) Synthesis of porous ladder polymer network through Suzuki crosslinking followed by ring closing metathesis.

(b) Solid-state CP/MAS ^{13}C NMR spectra of PPN-Precursor and trux-PLAN with color-coded signal assignments. Red represents regular CP/MAS spectra; green represents CPPI spectra.

Reproduced with permission from Fang et al.[146] Copyright 2020 American Chemical Society.

thermodynamically controlled reaction, and (*ii*) the microporosity of the material that allowed for catalytic accessibility of the reacting sites. The resulting trux-PLAN exhibited a high BET surface area of 1542 m^2 g^{-1}, which further increased to 1958 m^2 g^{-1} after treatment of TfOH. The methane storage performance of the trux-PLAN materials was investigated, proving the concept of employing ladder-type backbone in entropically favorable gas adsorption, especially for high temperature applications.

1.2.4.2 Suzuki crosslinking followed by photocyclization

Another example of stepwise construction of porous ladder polymer network was reported[147] by Yang, Roy, Nuckolls and co-workers via Suzuki cross-coupling followed by photocyclization. Similarly, a non-ladder-type POP-Precursor was first constructed by the formation of carbon-carbon single bonds between triptycene and perylene diimide (PDI) units. Low molar mass intermediate was first prepared from a monomer solution with low concentration. Then the resulting fjord-type structure allowed for the following facile photocyclization to complete the ladder-type structure (**Figure 1.16a**). Owing to geometry restrain of triptycene core, the networks extended two dimensionally through triptycene moieties, but vertically aligned backbone adds thickness to the third dimension. As a result, hexagonal crosslinked nanobelt-like porous structures are constructed, where all the faces of ladder-type backbone pointing towards the center of the pores (**Figure 1.16c**). Due to bulkiness of the alkyl chains, the material was not microporous until the removal of these chains at 375 °C. The intrinsic porosity and good thermal stability,

combined with well-developed redox properties of PDI unit, contributed to the high performance as a pseudocapacitor with capacitance as high as 350 F g^{-1} at 0.2 A g^{-1} and excellent stability over 10,000 cycles (**Figure 1.16d**).

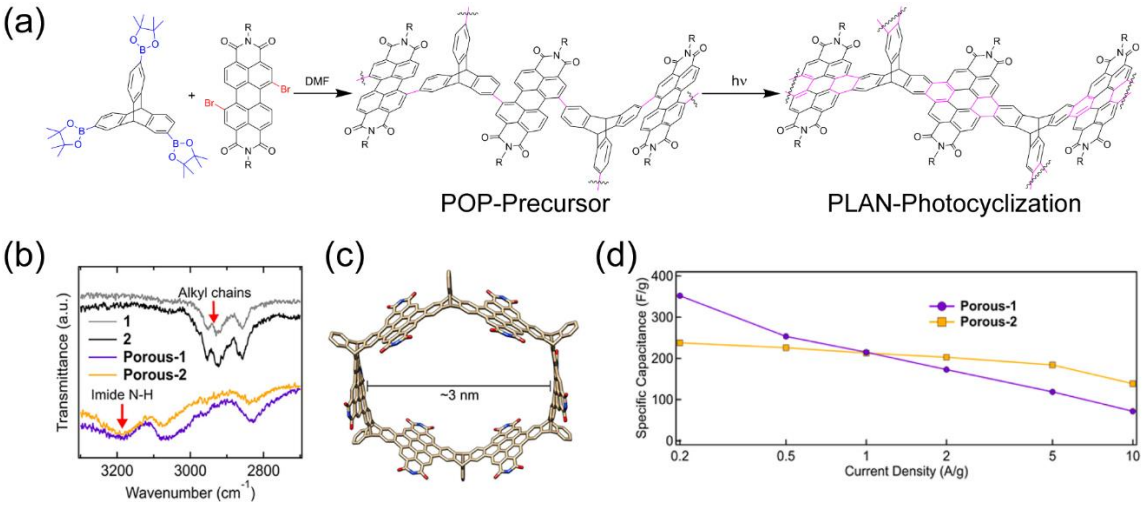

Figure 1.16. Synthesis, characterization, and properties of porous ladder polymer network with macrocyclic pore structure.

(a) Synthesis of porous ladder polymer network through Suzuki crosslinking followed by photocyclization.
(b) IR spectra of the intermediate and the porous ladder polymer network product, as well as dealkylation products of both materials.
(c) DFT-optimized energy minimum structure of a macrocyclic subunit in the porous ladder polymer network.
(d) Gravimetric specific capacitance as a function of current density.

Reproduced with permission from Yang et al.[147] Copyright 2018 American Chemical Society.

1.2.5 Bottom-up Synthesized Porous Graphene

In principle, porous graphene structures can also be considered as porous ladder polymer networks. This topic, however, is not extensively discussed in this dissertation

because of the significantly different synthetic strategies and the presence of a number of recent systematic reviews published on this topic.[150-154] Among these reported examples, several were synthesized in a bottom-up approach or derived from bottom-up synthesized metal-organic frameworks.[155-158] Most of these materials were constructed in a stepwise manner, with high temperature annealing required for the ladderization/graphitization step. Due to complicated reaction pathways during pyrolysis, the exact chemical constitutions of the backbones were usually not clearly characterized. DFT calculations, XPS, and energy dispersive X-ray spectroscopy were often involved in the analysis of the structures. Nevertheless, such strategy provided a facile and general method to construct chemically and thermally robust graphitic porous ladder polymer networks. The graphitic nature after high temperature endowed them good electrical conductivity, enabling wide applications in electrochemical catalysis and energy storage.

1.3 Properties and Applications

1.3.1 Stability

Fused with multiple strands of bonds, the conjugated ladder-type backbone in a porous ladder polymer network often possesses extraordinary thermal and chemical stability, enabling them to survive extremely harsh conditions. Many of the aforementioned literature reports have already demonstrated outstanding stability of the porous ladder polymer networks in harsh thermal and chemical environments. The thermodynamic stability is typically originated from both enthalpic and entropic contributions: Most porous ladder polymer network backbones are composed of

polycyclic aromatic systems that are enthalpically favorable, while the multiple strands of bonds renders it entropically unfavorable to decompose the network backbone. In addition, the rigid nature of ladder-type backbones can prevent collapse of the pores in different environment, ensuring the good morphological stability.

A few porous ladder polymer networks have been subjected to systematic stability tests. For example, Yaghi and co-workers demonstrated[94] the superior stabilities of dioxin-linked COF-316 and COF-318. These materials can survive the treatments of concentrated HCl and NaOH at room temperature, making it possible to post-modify the material with desirable functional groups. Fang, Yan, Valtchev and co-workers further explored[116] stability of the same structure (JUC-505) in broader chemical environments including boiling water, strong acids (12 M HCl, 7 days; 18 M H_2SO_4, 7 days; 40% HF, 7 days), strong bases (14 M NaOH, 7 days; 5 M MeONa in MeOH, 7 days), oxidant (0.1 M $K_2Cr_2O_7$ in concentrated H_2SO_4, 7 days), and reductant (2.4 M $LiAlH_4$ in THF, 7 days), showing almost unaltered characters in FT-IR, PXRD, and N_2 adsorption isotherms (**Figure 1.17**). The ladder-type backbone plays a critical role in endowing the extraordinary stability into these porous ladder polymer network materials. On one hand, the double stranded dioxin linkage and the rest aromatic building blocks contributed to the chemical stability. On the other hand, the porous morphology was stabilized by (*i*) the rigid and crystalline ladder-type backbone with low level of defects, as well as (*ii*) the compact stacking of layers due to the coplanar and rigid nature of the ladder-type backbone.

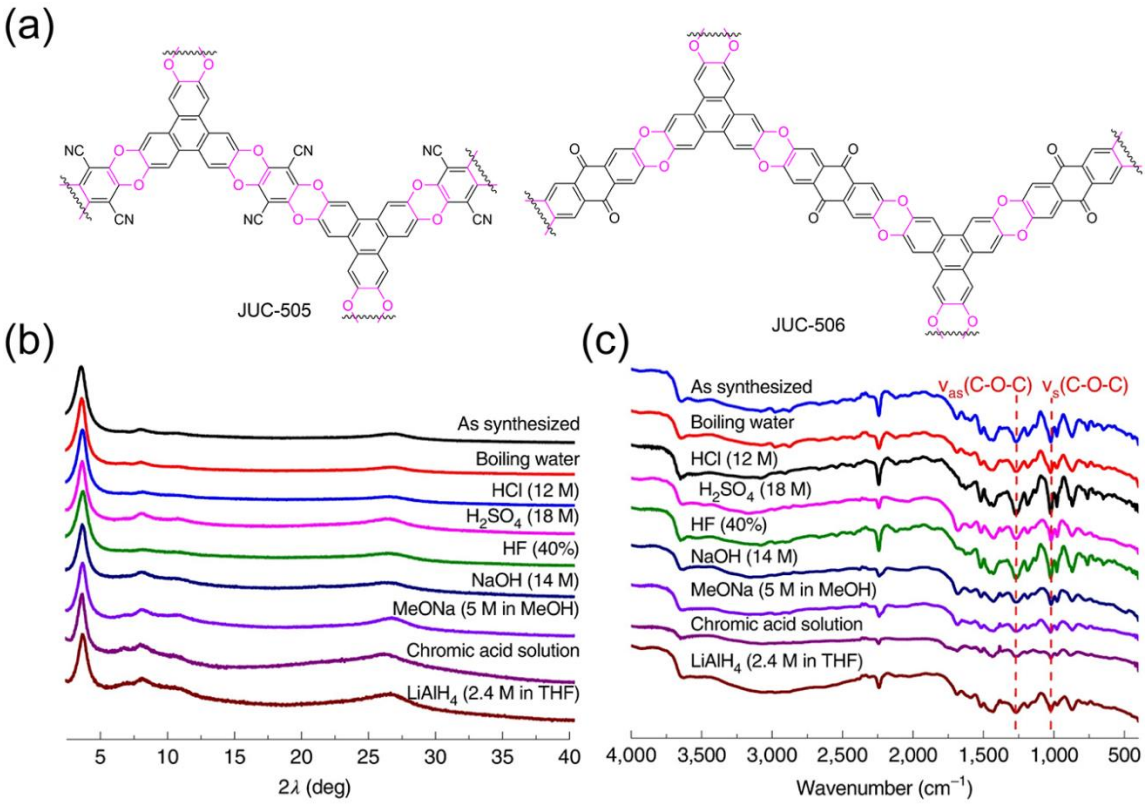

Figure 1.17. Stability tests of JUC-505.

(a) Structural formula of the repeating unit of JUC-505 and -506 constructed by dioxin-fusing crosslinking reactions.

(b,c) PXRD patterns (b) and IR spectra (c) of JUC-505 after treatments under different chemical environments for 1 week, respectively.

Reproduced with permission from Fang et al.[116] Copyright 2019 Nature Publishing Group.

Amorphous POPs constructed through the formation of thermodynamically irreversible bonds typically demonstrate excellent stability. However, the connection points of single stranded bonds in many POPs could still be at risk of structural breakdown. Fang and co-workers introduced a second strand of robust covalent bonds into an amorphous POP by RCM reaction.[146] The error-checking and proof-reading ability of RCM led to highly efficient ring closure and hence backbones with extremely low level

of defects, even in a heterogenous reaction. The resulting trux-PLAN showed high tolerance towards harsh chemical treatments including strong acids (12 M HCl at 80 °C, 7 days; 98% TfOH, 7 days), strong base (14 M NaOH in H_2O/MeOH at 80 °C, 7 days), reductant (50 equiv. $NaBH_4$ in MeOH at 80 °C, 7 days), and oxidant (0.1 M $K_2Cr_2O_7$ in concentrated H_2SO_4). High porosity was preserved after these treatments (**Figure 1.23**). Acid treatments even increased BET surface areas up to 1958 m^2 g^{-1}, likely due to the removal of trace amount of oligomers and other impurities from the micropores.

1.3.2 Conductivity

The urgent demands of energy storage, electrocatalysis, chemical sensing materials have driven[159, 160] significant progress in porous materials with high electrical conductivity. Non-ladder-type POPs, however, rarely show good conductivity as a result of (*i*) the presence of large pore volume and (*ii*) poor through-network charge transport due to torsional disorders caused by the single stranded bond connection. In contrast, the high conductivity of graphene, porous graphene, and graphitized porous carbon illustrates the potential of achieving high conductivity of conjugated porous ladder polymer networks, which share similar structural features. In this context, conjugated porous ladder polymer networks with locked conformation, extended conjugation, ordered packing represent a promising class of materials to integrate electrical conductivity, porosity, and tailored functionalities in a single material.

Pyrazine-linked porous ladder polymer network COF-DC-8 reported by Mirica and co-workers demonstrated[102] an intrinsic bulk electrical conductivity of 2.51×10^{-3} S

m^{-1}, which could be further increased by 3 orders of magnitude with I_2 doping. Through-network charge transport was promoted by the coplanar, rigid, and conjugated backbone, while through-space transport was promoted by eclipse stacking of the embedded metallophthalocyanine units. The ordered crystalline structure also ensured good charge transport over a long range. Moreover, the framework adopted a tetragonal Lieb lattice that was known to benefit through-bond charge delocalization, instead of hexagonal Kagome lattice. The synergistic incorporation of electrical conductivity into the porous framework enabled unique application of the material as an electrical gas vapor sensor.[161] COF-DC-8 was integrated into chemiresistive devices, which exhibited positive resistance responses to reducing gases (NH_3, H_2S) and negative resistance responses to oxidizing gases (NO, NO_2) (**Figure 1.18**), indicating COF-DC-8 behaved as a p-type semiconductor. The high porosity endowed the device ultralow limits of detection at parts-per-billion level.

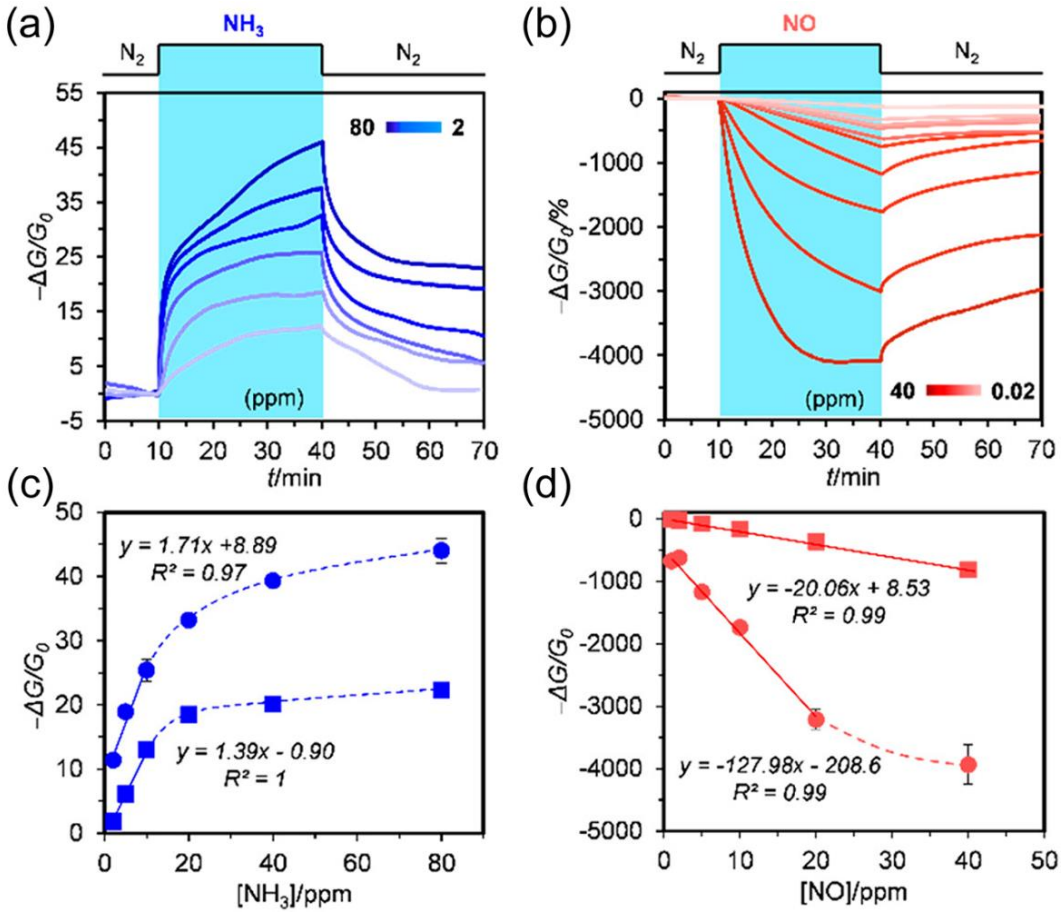

Figure 1.18. Chemiresistive responses of COF-DC-8 integrated devices to gas analytes.

(a) Response to reducing gas NH_3.

(b) Response to oxidizing gas NO.

(c,d) Responses after 1.5 min (squares) and 30 min (circles) exposure versus concentration of NH_3 (c) and NO (d), respectively.

Reproduced with permission from Mirica et al.[102] Copyright 2018 American Chemical Society.

Pyrazine-linked porous ladder polymer network (Aza-CMPs) reported by Jiang and co-workers also exhibited[100] high electrical conductivity and excellent supercapacitive performance. The same set of authors reported another pyrazine-linked network (CS-COF)

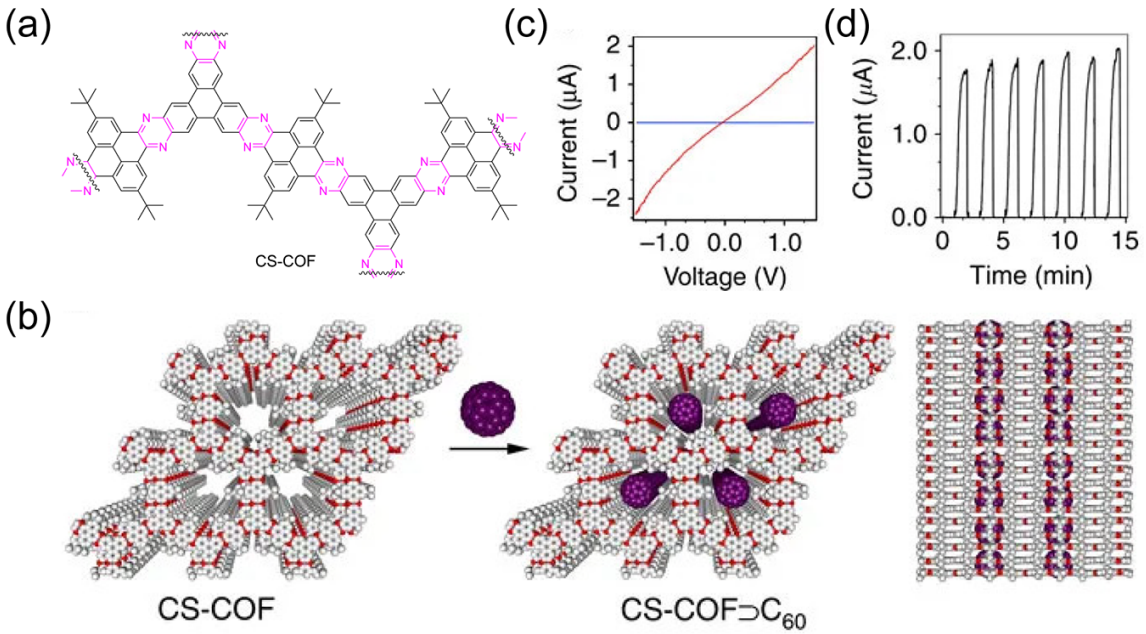

Figure 1.19. Photoconductive properties of CS-COF.
(a) Structural formula of the repeating unit of CS-COF constructed by pyrazine-fusing crosslinking reaction.
(b) Incorporation of C_{60} into the open one-dimensional channels of CS-COF by sublimation to afford CS-COF⊃C_{60}.
(c,d) I–V curve (Blue: dark current; Red: photo current) (c) and photocurrent switching at a bias voltage of 1.5 V with repetitive light on-off actions (d) of a CS-COF⊃C_{60}/PMMA film in air at 25 °C.
Reproduced with permission from Jiang et al.[162] Copyright 2013 Nature Publishing Group.

constructed from double imine condensation reaction between triphenylene and pyrene units (**Figure 1.19a**).[162] CS-COF demonstrated a rapid response to light irradiation with high-rate hole-conducting mobility of 4.2 cm^2 V^{-1} s^{-1}. Furthermore, the rigid channel structure allowed for the accommodation of fullerene molecules in an ordered manner (**Figure 1.19b**). The resulting bicontinuous donor and acceptor columns promoted efficient charge carrier separation and charge transport along the columns. A photoswitch

device was fabricated and showed a high on-off ratio of 5.9×10^7 and multiple rounds of on-off switching without a loss of performance (**Figure 1.19c, d**).

Besides electrical conductivity, porous ladder polymer networks can also be rendered ionically conductive. For example, pyrazine-linked aza-COF-1 and aza-COF-2 exhibited[101] proton conductivities of 10^{-5} and 10^{-3} S cm^{-1} before and after acid doping, respectively. The unique constitution of the nitrogen-containing repeating unit that resembles a phenanthroline moiety benefited the adsorption of water through hydrogen bonding, and facilitated protonation by phosphoric acid (**Figure 1.20a**). The presence of phosphoric acid doping was evidenced by significantly reduced porosity as well as modified mass-loss profile of TGA after acidification. The combination of phenanthroline-like units on the backbone and accessible 1D channels originated from the crystalline porous structure contributed to the observed proton conductivity (**Figure 1.20b**). It was also demonstrated that both the crystal grain size and the ionic charge carrier density were important in governing the ionic conductivity.

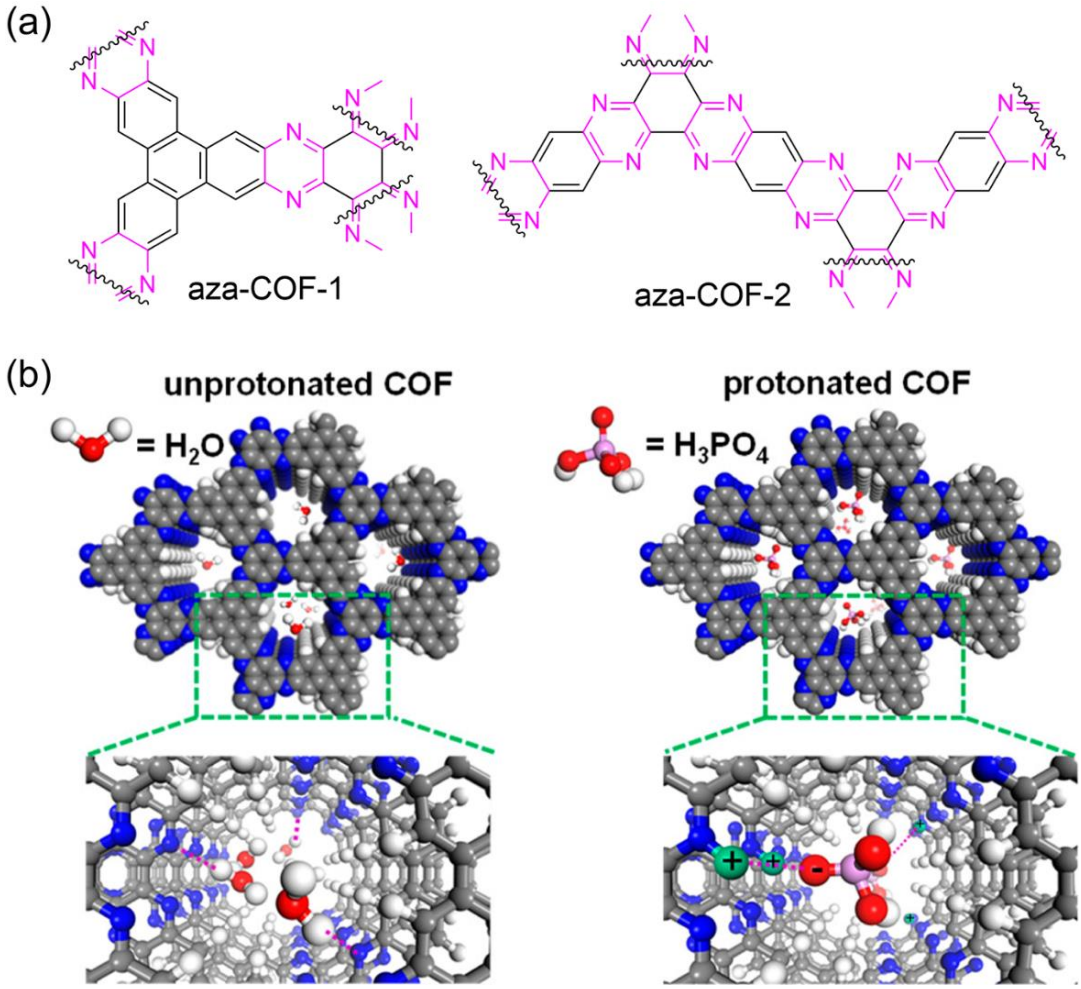

Figure 1.20. Proton conductive properties of aza-COF-1 and -2.

(a) Structural formula of the repeating unit of aza-COF-1 and -2 constructed by pyrazine-fusing crosslinking reactions.

(b) Graphical representation of the proposed proton conduction mechanism in aza-COFs: Left: hydrogen bonding (O−H···N) between N atoms on the wall and water molecules; Right: protonation induced electrostatic interaction between cationic N−H group and anionic dihydrogen phosphate group.

Reproduced with permission from Mirica et al.[101] Copyright 2018 American Chemical Society.

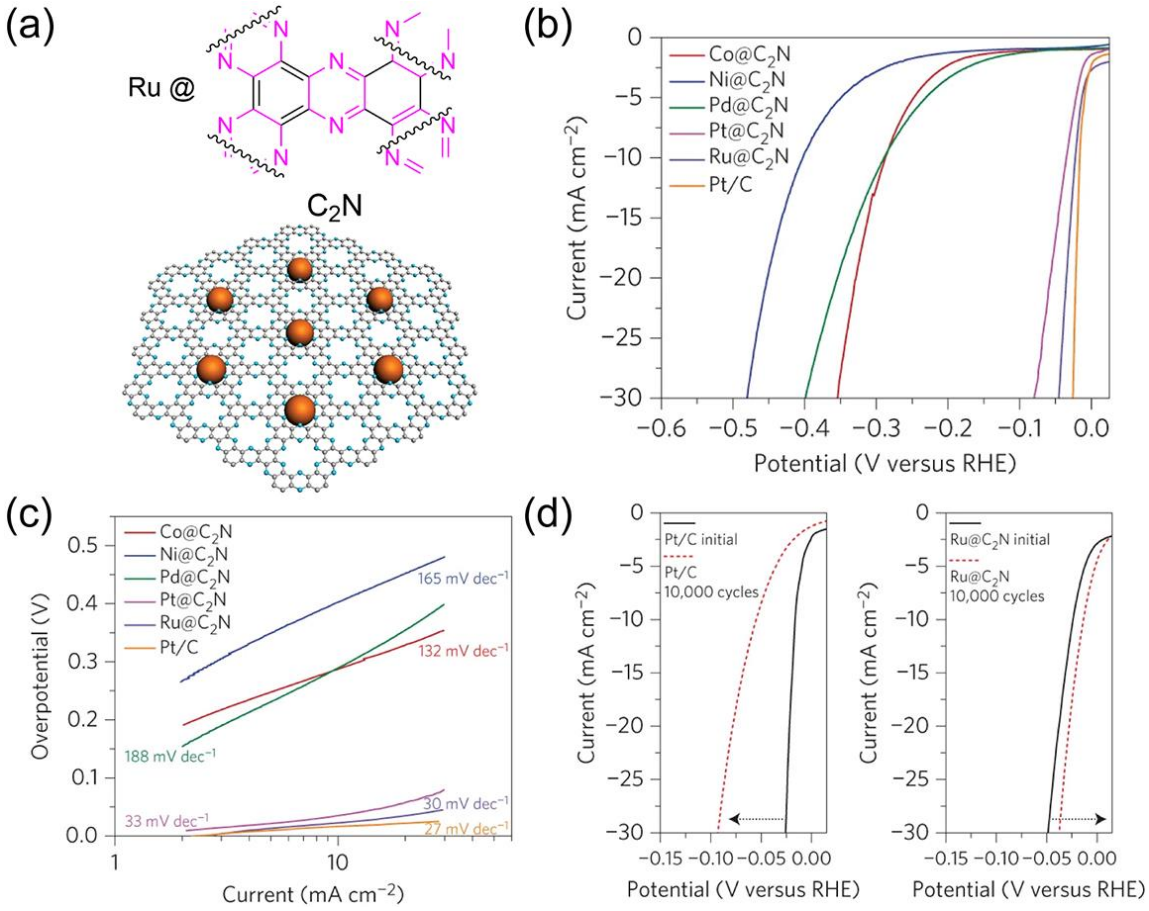

Figure 1.21. HER properties of Ru embedded C_2N.

(a) Structural formula and schematic illustration of the structure of the Ru@C_2N electrocatalyst.

(b) HER polarization curves of Co@C_2N, Ni@C_2N, Pd@C_2N, Pt@C_2N and Pt/C electrocatalysts in 0.5 M H_2SO_4 solution.

(c) Tafel plots obtained from the polarization curves in (c).

(d) The partial polarization curves of Pt/C and Ru@C_2N recorded before and after 10000 potential cycles in 0.5 M H_2SO_4 solution.

Reproduced with permission from Baek et al.[167] Copyright 2017 Nature Publishing Group.

As a subgroup of POPs, most porous ladder polymer networks possess permanent porosity. Combined with the rigidity and superior stability originated from their ladder-

type backbone, the highly porous nature of these materials has been widely exploited[99, 163-166] in applications such as gas adsorption, catalyst encapsulation, and ion sieving, *etc*.

Baek and co-workers reported[167] a hydrogen evolution reaction (HER) catalyst (Ru@C_2N) by incorporating well-defined Ru nanoparticles into a pyrazine-linked porous ladder polymer network (C_2N) (**Figure 1.21a**). The C_2N in this case provided a porous, rigid, and conductive scaffold. During the synthesis of Ru@C_2N, highly dense nitrogen atoms surrounding the pores acted as anchoring sites for Ru ion, contributing to the uniform nucleation and distribution of Ru nanoparticles. In addition, the rigid porous backbone confined the particle growth, leading to the formation of ultrasmall Ru nanoparticles with average diameter of 1.6 ± 0.5 nm, which are evenly distributed between C_2N layers with narrow pore size distributions. As for HER performance, Ru@C_2N electrocatalyst showed overpotential and turnover frequency comparable to those of Pt/C in acidic condition and better performance in basic condition (**Figure 1.21b, c**). Moreover, it demonstrated great electrochemical stability for long-term electrochemical process in wide pH range (**Figure 1.21d**), presumably from the stabilization and confinement of the ladder-type backbone as discussed above.

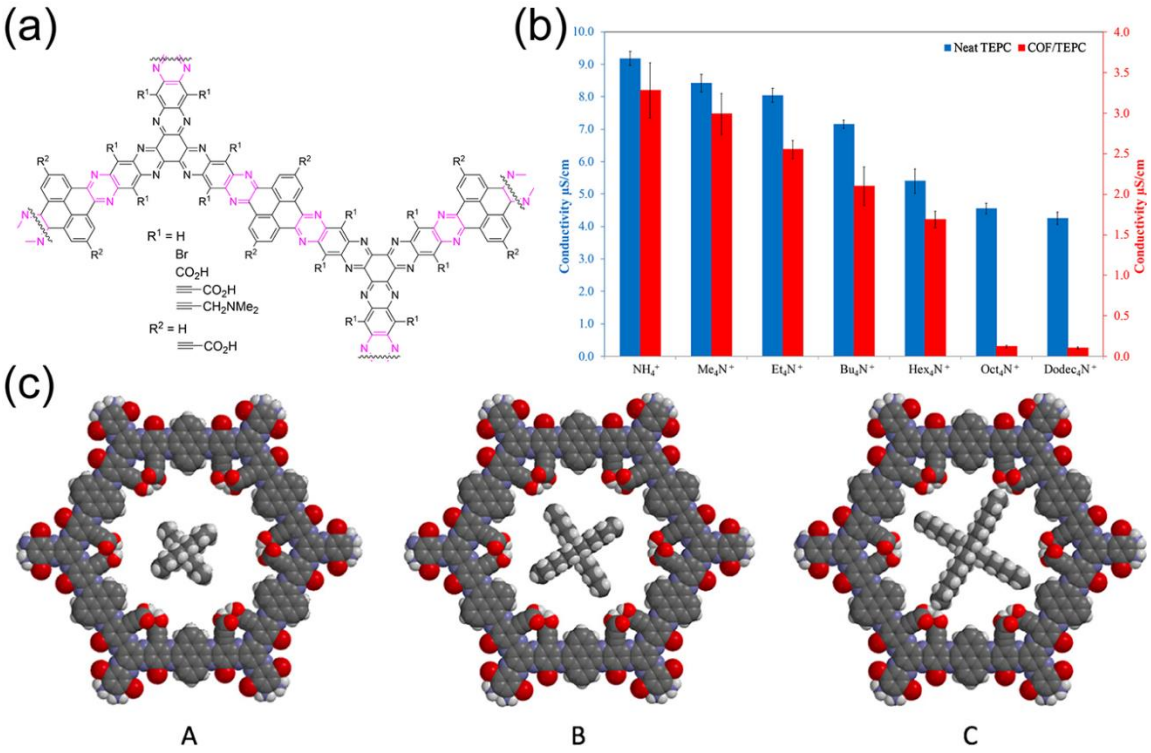

Figure 1.22. Ion sieving properties of porous ladder polymer network towards cations with different sizes.

(a) Structural formula of the repeating unit of porous ladder polymer networks constructed by pyrazine-fusing crosslinking reaction.

(b) Cation transport of COF/TEPC membrane showing rejection of tetraalkyl cations larger than tetrahexyl ammonium.

(c) Space-filling models of a single pore of porous ladder polymer network with Bu_4N^+ (A), Hex_4N^+ (B), and Oct_4N^+ (C) cations inside the pore.

Reproduced with permission from Li-Oakey et al.[168] Copyright 2018 American Chemical Society.

Li-Oakey, Parkinson, Hoberg, and co-workers developed[168] a 2D pyrazine-linked porous ladder polymer network platform for facile modification of the pore sizes and chemical environments (**Figure 1.22a**). The abundant functional groups could be installed by either pre- or post-functionalization, enabling (*i*) the incorporation of various charge

states (neutral, positive, or negative), and (*ii*) the precise regulation of pore sizes by varying the length of the functional groups. The rigid, highly porous, charged hydrophilic structure allowed for a high water flux through a membrane fabricated from the porous ladder polymer network. Moreover, a membrane functionalized by carboxylate groups demonstrated a clear cation size selectivity (**Figure 1.22b, c**). Presumably, membranes with different size rejection thresholds and charge selectivity can be fabricated using the similar synthetic strategy.

1.3.4 Low Entropy Gas Adsorption

Although the intrinsic porous nature of porous ladder polymer networks has enabled various general gas adsorption applications, the special contribution of the rigid ladder-type backbone to gas uptake has not been well explored. With fully locked backbone conformation, a porous ladder polymer network possesses lower initial backbone entropy than its non-ladder-type counterpart. Consequently, it translates to less adsorption entropy penalty after accommodation of gas molecules, thus a more thermodynamically favorable gas uptake process. Recently, Fang and co-workers studied[146] the structure-property relationship between ladder-type backbone and high-pressure methane storage. Trux-PLAN and two traditional POPs (PPN-Precursor and PPN-Ref) were synthesized and characterized for direction comparison. Trux-PLAN demonstrated a high methane uptake per unit surface area that was superior to most other reported porous hydrocarbons and

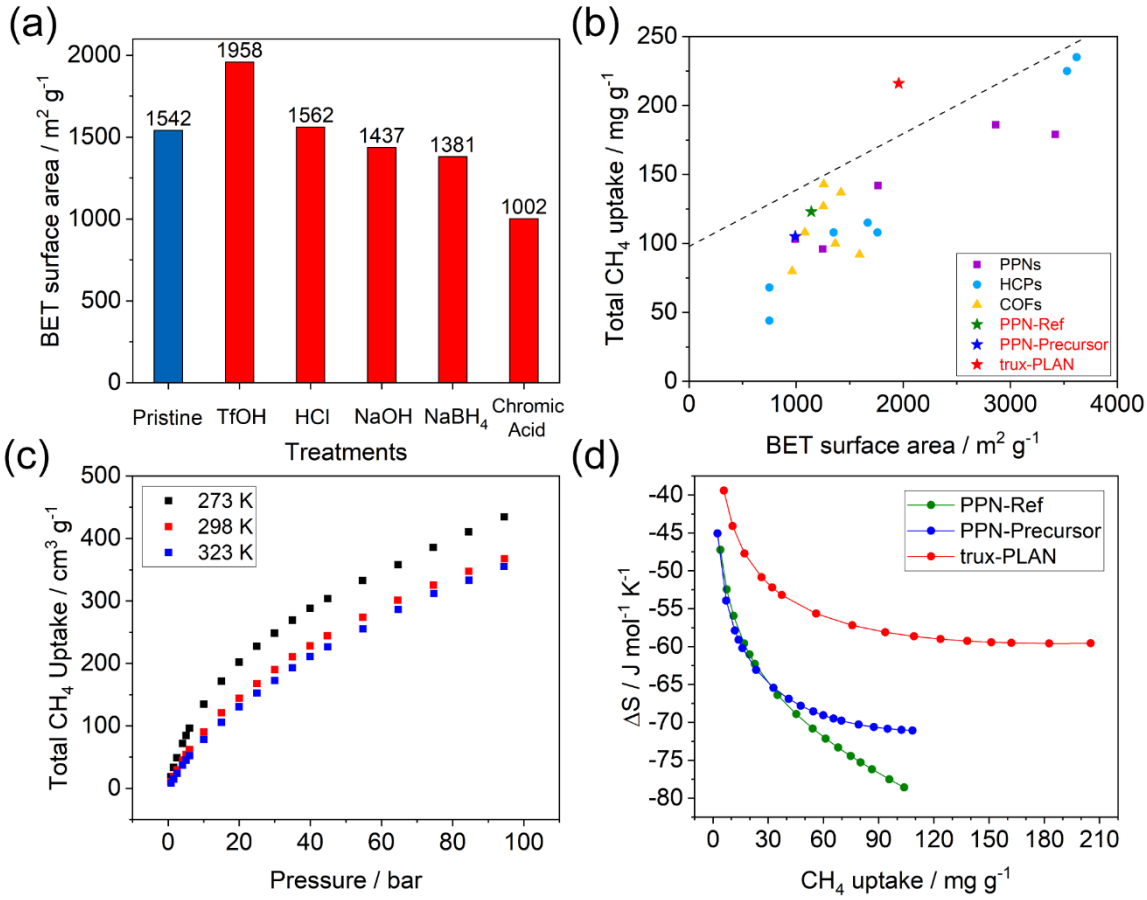

Figure 1.23. Stability and low entropy methane adsorption of porous ladder polymer network.

(a) BET surface area of porous ladder polymer network after treatment of acid (HCl, TfOH), base (NaOH), reducing agent ($NaBH_4$), or oxidant (chromic acid solution).

(b) Plot of total methane uptake (65 bar, 298 K) versus BET surface areas of porous organic polymers without enthalpically favorable interactions with methane, including trux-PLAN, COFs, and porous hydrocarbons.

(c) High pressure CH_4 uptakes of trux-PLAN at 273, 298, and 323 K.

(d) Entropy changes derived from variable-temperature high-pressure methane adsorption isotherms of PPN-Ref, PPN-Precursor, and trux-PLAN.

Reproduced with permission from Fang et al.[146] Copyright 2020 American Chemical Society.

COFs without enthalpically favorable interactions with methane to eliminate enthalpic contributions (**Figure 1.23b**). Trux-PLAN clearly located above the upper bound on the chart, indicating entropy contributed to the superior methane uptake performance. The following thermodynamic investigation under different temperatures revealed a significantly smaller entropy penalty of trux-PLAN (19.8 J mol^{-1} K^{-1} difference compared to PPN-Ref at 100 mg g^{-1} of methane uptake) as a result of the elimination of torsional rotation from single bonds (**Figure 1.23d**). Entropic contribution to high-pressure gas adsorption could impact the overall performance significantly. The favorable entropic approach based on porous ladder polymer network offers a universal strategy to increase the deliverable capacity for various types of gases while mitigating the performance decline in high temperature applications.

1.4 Conclusion and Perspective

In summary, the past decade has seen the happy marriage of the field of POPs and that of ladder polymers, which gave birth to many exciting new materials that possess advantages from both worlds. This introduction summarizes the progresses made on the thriving topics of the design, synthesis, property, and application of porous ladder polymer networks. Despite the significant advancement described in this introduction, a number of critical challenges need to be addressed before the promising potential of porous ladder polymer networks can be fully exploited.

First of all, although most network topologies seen in traditional POPs have been successfully achieved on porous ladder polymer network, 2D networks are still the most

dominant structures. True 3D porous ladder polymer networks with ultrahigh porosity and isotropic transport of charge or mass are rather rare. It is desirable to extend the current synthetic scope to access more general 3D porous ladder polymer networks. A hybrid approach can also be employed by incorporating ladder-type linker into 3D metal-organic frameworks that feature rigid metal-organic nodes, to afford a broader range of 3D ladder polymer-derived porous materials.

Second, despite the various one-step ring-fusing crosslinking or stepwise crosslinking-annulation methods that have been successfully employed in porous ladder polymer network synthesis, it is still challenging to construct them with high efficiency and minimal defects, meanwhile achieving the desired backbone constitution and crystallinity. The long-term challenge on balancing crystallinity and stability faced by the communities of POPs and metal-organic frameworks also applies on the synthesis of porous ladder polymer networks, with added complexity. In addition, the need of constructing multiple strands of bonds on the backbone impose another significant challenge on screening the optimized reaction, because the possibility of structural defect on the backbone could be detrimental for many applications. Meanwhile, it is important to characterize the nature and to quantify the amount of these defects. In this context, more rigorous and sensitive methods to probe defects, such as NMR spectroscopy on ^{13}C isotope labeled samples,[146] are desired for thorough structural and defect characterizations. Moreover, the impacts of structural defects on the properties and functional performances of porous ladder polymer networks, is yet to be established. Such correlations will provide valuable insights to future development of these materials. In this context, new reactions

that fulfill the demands of producing fused-ring structures, with high conversion and potential reversibility are needed for the development of future porous ladder polymer networks.

Last but not least, systematic investigations on the properties and functions of porous ladder polymer networks are still limited so far due to (i) the relatively young age of the research field and unavailability of commercial materials; (ii) and the potential issue of batch-to-batch variation and reproducibility. As a result, the potential of performance of porous ladder polymer network in practical applications are far from been fully exploited. In order to accelerate the discovery of the next champion porous ladder polymer network material, the synthetic and processing challenging associated with these materials need to be addressed. Scalable synthesis of high-quality materials with consistent batch-to-batch reproducibility are desirable for the development of commercially available, reliable supply of porous ladder polymer networks. It is also challenging to process this class of materials into desired forms such as thin films and fibers, due to their insoluble/unmeltable nature and rigid backbone. Methods such as processing followed by *in situ* crosslinking, or exfoliation followed by colloidal processing are promising potential strategies to explore.[169]

Overall, the rapid developments of porous ladder polymer networks have led to exciting breakthroughs in both fundamental science and materials application, offering an attractive platform for various challenging issues. We envision that the demand for advanced porous ladder polymer network materials will become more important than ever

in the near future, presenting tremendous research opportunities that require the collaborative efforts from multiple subjects of science and engineering.

CHAPTER II

RIGID LADDER-TYPE POROUS POLYMER NETWORKS CONSTRUCTED BY RING-CLOSING METATHESIS LADDERIZATION*

2.1 Introduction

Porous Organic Polymers (POPs) is a type of permanent porous materials whose entire framework is constructed by covalent bonds. Their high porosity, structural diversity, and thermal/chemical stability enable them promising candidates in gas adsorption, catalyst, sensors, *etc*. Meanwhile, ladder polymers with fused-ring rigid backbones have emerged and demonstrated various unique properties that are not accessible on conventional flexible or semi-flexible polymers. In the past decade, numerous efforts have been devoted to incorporate fully-fused ladder-type constitution into POPs, affording the so-called porous ladder polymer networks (PLANs). Advancements of this field in the past decade lead to the development of exciting PLAN materials embracing advantages from both worlds of POPs and ladder polymers. These synergistic properties include but are not limited to: (1) extraordinary stability in terms of chemical constitution and porosity; (2) low entropy backbones that favor gas adsorption process; and (3) extended pi-conjugation for better charge transport. These intriguing properties enables the promising application of PLANs as the next-generation materials

*Reprinted with permission from "Rigid Ladder-Type Porous Polymer Networks for Entropically Favorable Gas Adsorption" Che, S.; Pang, J.; Kalin, A. J.; Wang, C.; Ji, X.; Lee, J.; Cole, D.; Li, J.-L.; Tu, X.; Zhang, Q.; Zhou, H.-C.; Fang, L. *ACS Materials Lett.* **2020**, *2*, 49. Copyright 2020 American Chemical Society.

for some of the most exciting topics such as energy storage, gas separation, highly selective and sensitive sensors, and electrocatalysis.

As for synthetic methods, a wide range of reactions have been employed successfully for PLAN constructions. These including pyrazine formation, benzoimidazobenzophenanthroline (BBL) formation, dioxin formation, ortho-aminonitriles triple condensation, hexaazatriphenylene triple condensation, thianthrene formation, Diels-Alder cycloaddition, anthracene photopolymerization, ortho-dinitrile quadruple condensation, and aldol triple condensation, *etc*. Despite the numerous reported examples on direct one-pot construction of PLANs, the scope of reactions suitable for such synthesis is relatively narrow because the demands on one-pot formation of multiple strands of bonds and high conversion for network formation. In contrast, PLANs can be also constructed through a stepwise approach: (1) cross-linking the network through the formation of a single strand of bonds, (2) followed by annulation reaction (or referred as "ladderization") to form the additional strand of bond to fuse the entire backbone. This general strategy has been extensively employed in the formation of linear ladder polymers, and allows a much wider scope of selection of reactions. The major challenge associated with the stepwise synthesis is in the second step: because the first step already afforded an insoluble crosslinked intermediate, the desired high efficiency of the subsequent annulation in a heterogeneous reaction would be challenging to maintain. Therefore, the synthesis of PLAN with minimal backbone defects is still of high demand.

2.2 Structure Design and Synthesis

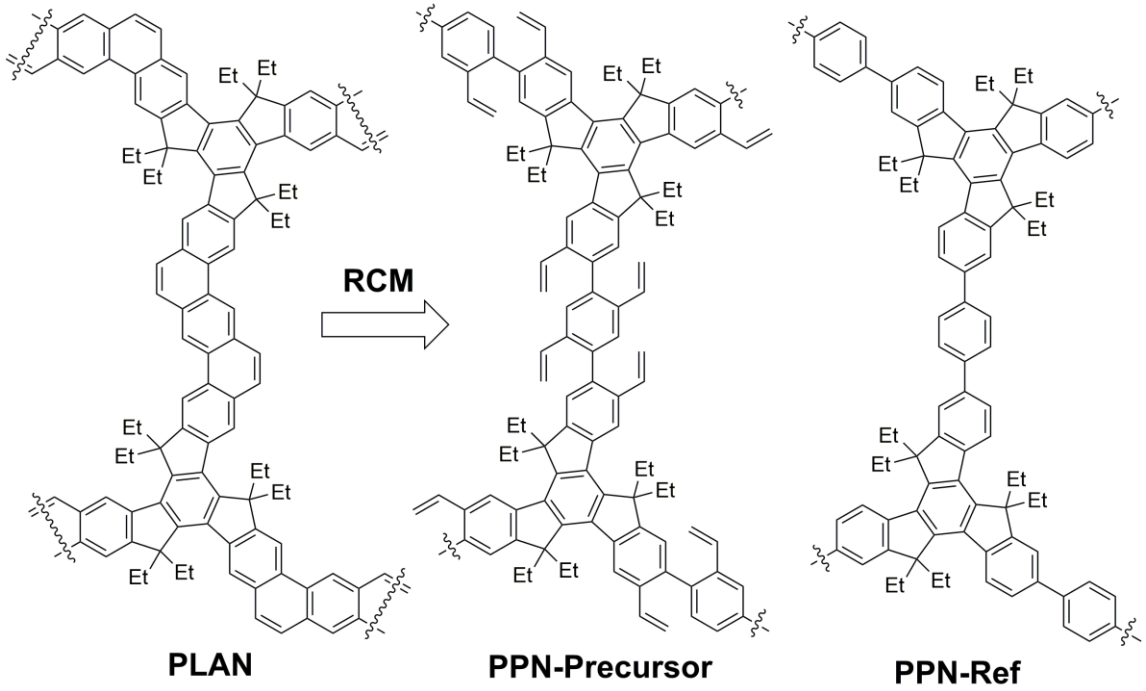

Figure 2.1. Structural formulas of the repeating units of cross-linked porous polymer networks **PLAN**, **PPN-Precursor**, and **PPN-Ref.**
Reproduced with permission from Fang et al.[146] Copyright 2020 American Chemical Society.

The **PLAN** model was designed as a porous organic material constructed from rigid monomers through the kinetic formation of covalent bonds, which can be categorized as a subset of porous polymer networks (PPNs).[18, 20, 24] (**Figure 2.1**) In general, PPNs can be imparted with high porosity and superior thermal and chemical stability,[8, 17, 20, 36, 170, 171] suitable as a model system for methane storage application. Ring closing olefin metathesis (RCM) was selected to construct the ladder-type backbone of PLAN because it typically gives a highly efficient annulation conversion with an extremely low level of defects under thermodynamic control.[64, 93, 172] It has been shown that this reaction can take

place heterogeneously in porous solids.[173] In terms of monomers, a fused-ring, tribromo functionalized truxene derivative and a diboronic ester functionalized linear phenylene derivative were employed to construct the network via Suzuki coupling. These monomers were also functionalized with vinyl groups on the ortho-positions for the RCM reaction. In addition, a reference material PPN-Ref for control study was also designed to possess a non-ladder type backbone while resembling the constitutional structure of PLAN as much as possible. (**Figure 2.1**)

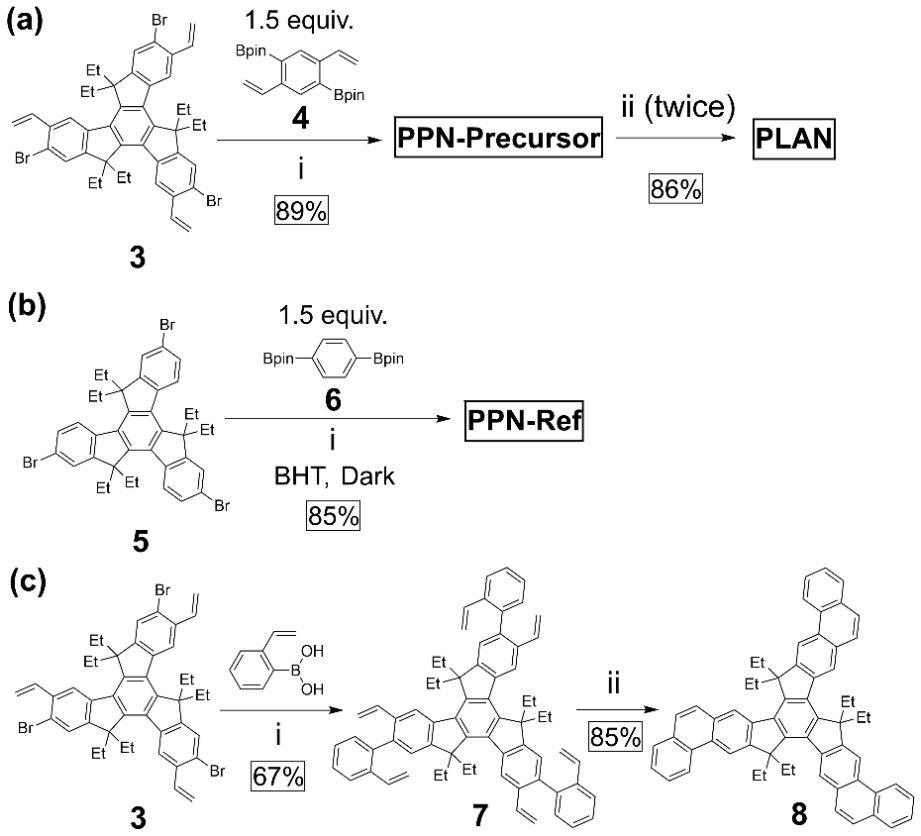

Figure 2.2. Synthesis of (a) **PPN-Precursor** and **PLAN**, (b) **PPN-Ref**, and (c) small molecular model compounds **7** and **8**.
Reaction conditions: (i) $Pd(PPh_3)_4$, K_2CO_3, aliquat 336, BHT, PhMe, H_2O, 100 ^oC, 48 h; (ii) Grubbs Catalyst 2nd Generation, xylenes, 150 ^oC, 6 h.
Reproduced with permission from Fang et al.[146] Copyright 2020 American Chemical Society.

The synthesis of **PLAN** started with the preparation of alkylated truxene, followed by radical bromination. Further hydrolysis and Wittig vinylation afforded the desired tribromo and trivinyl functionalized monomer **3**. Next, Suzuki polymerization of **3** with the diboronic ester functionalized monomer **4** gave the key intermediate network **PPN-Precursor** with pre-organized vinyl groups. (**Figure 2.2a**) Subsequently, it underwent the RCM annulation reaction followed by work-up and washing. To improve the annulation conversion, the RCM reaction and washing process was repeated one more time to afford **PLAN** with ladder-type backbone constitution. **PPN-Ref** was synthesized from a non-vinyl monomer **5** and **6**. (**Figure 2.2b**) Small molecular model compounds **7** and **8** were also synthesized to aid characterization. (**Figure 2.2c**)

2.3 Characterization and Discussion

Solid state cross-polarization magic angle spinning (CP/MAS) ^{13}C NMR spectroscopy was conducted to characterize **PPN-Precursor** and **PLAN**. The observed ^{13}C resonance signals were assigned according to the solution-phase ^{1}H, ^{13}C, HSQC, and HMBC NMR spectra of **7** and **8** (**Figure 2.3, 2.39-2.44**). In addition, cross-polarization editing experiments by polarization-inversion (CPPI) were recorded to clearly identify signals corresponding to the terminal vinyl $=CH_2$ unit and the sp^3 CH_2 carbon as negative peaks.[174] Transformation of the peak patterns from **PPN-Precursor** to **PLAN** agreed well with those observed from **7** to **8**. Particularly, the disappearance of the vinyl $=CH_2$ signal

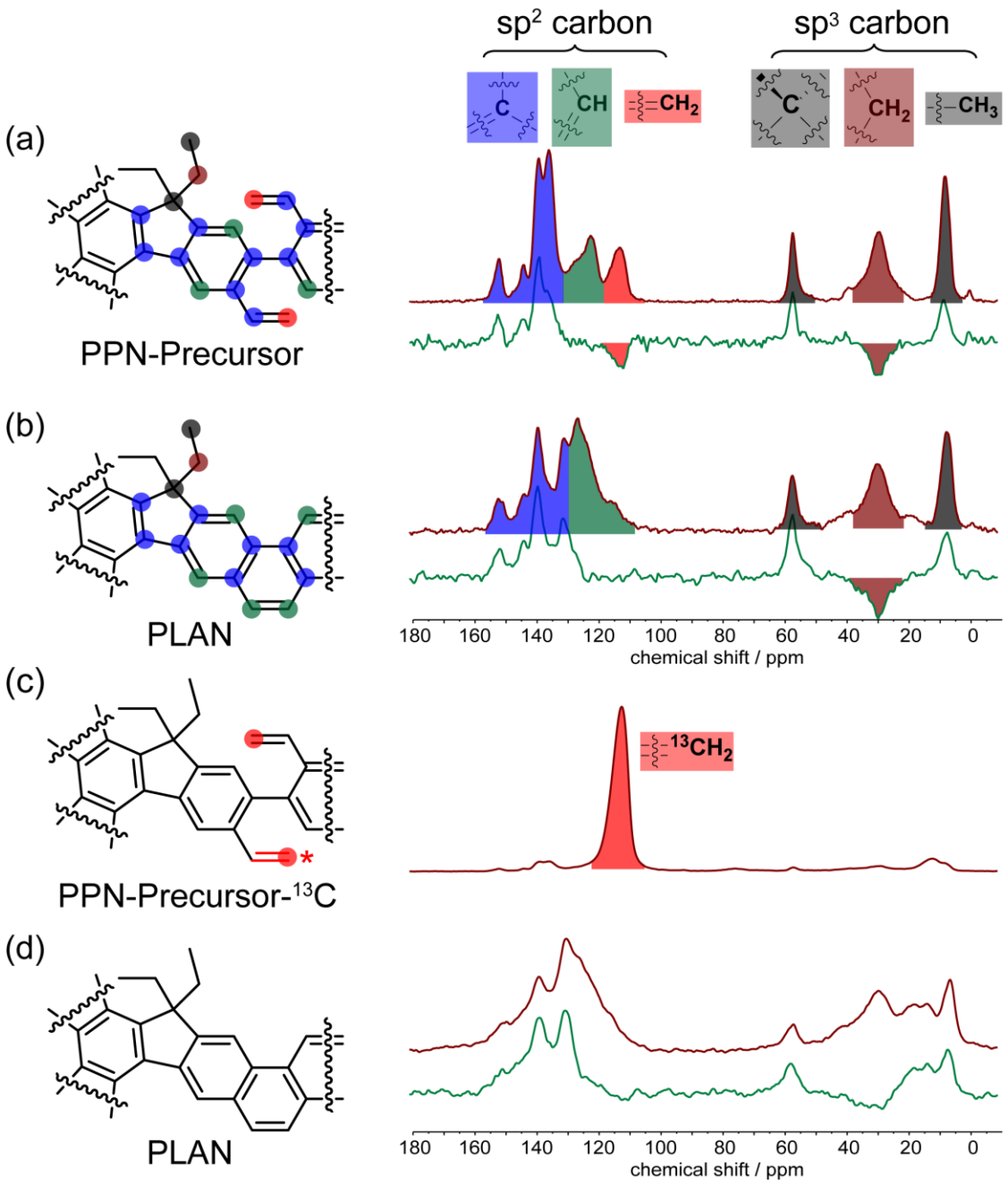

Figure 2.3. Solid state CP/MAS NMR ^{13}C spectra of (a) **PPN-Precursor**, (b) **PLAN**, (c) **PPN-Precursor-^{13}C**, and (d) **PLAN** from PPN-Precursor-^{13}C, with color-coded signal assignments.
Red: regular CP/MAS spectra; Green: CPPI spectra.
Reproduced with permission from Fang et al.[146] Copyright 2020 American Chemical Society.

in **PLAN** spectrum indicated the conversion of the vinyl groups into cyclized aromatic rings. In order to better quantify the conversion of the RCM reaction using a much more sensitive method, **PPN-Precursor-^{13}C** with 99% ^{13}C isotope labeled on the terminal vinyl $=CH_2$ unit was synthesized and demonstrated an intense peak at 112 ppm. After two RCM cycles, the spectrum of the resulting **PLAN** showed no observable $=^{13}CH_2$ signal. This observation confirmed that the conversion of the RCM reaction was over 99%,[64] corroborating its high efficiency even on the backbone of a solid-state material, as long as the porosity of the material allows catalyst access to the vinyl groups.[173]

The porosity of the **PPN-Ref**, **PPN-Precursor**, and **PLAN** was measured by nitrogen adsorption experiments at 77 K, giving Brunauer-Emmett-Teller (BET) surface areas of 1142 $m^2\ g^{-1}$, 992 $m^2\ g^{-1}$, and 1958 $m^2\ g^{-1}$, respectively (**Figure 2.4a**). Similar to other robust porous aromatic materials reported recently,[46, 48, 116] both **PPN-Ref** and **PLAN** demonstrated good stability and retained high porosity after extended treatment in harsh chemical conditions (**Figure 2.4b, 2.16**), including acids (12 M HCl at 80 °C, 7 days; or 98% TfOH, 7 days), base (14 M NaOH in H_2O/MeOH at 80 °C, 7 days), and reducing agent (50 equiv. $NaBH_4$ in MeOH at 80 °C, 7 days). An exception was chromic acid solution (0.1 M $K_2Cr_2O_7$ in concentrated H_2SO_4), which caused **PPN-Ref** to lose its porosity completely. In contrast, **PLAN** still retained a BET surface area over 1000 $m^2\ g^{-1}$ after a 3-day treatment with chromic acid solution, demonstrating its better chemical stability against strong oxidants. It is also noteworthy that treatment with TfOH increased the BET surface area of **PLAN** from 1542 $m^2\ g^{-1}$ to 1958 $m^2\ g^{-1}$ (**Figure 2.4b**) while retaining its structural integrity, evidenced by solid-state NMR spectra (**Figure 2.17**). The

TfOH treatment likely removed impurities trapped inside the pores of **PLAN**, so it was used as a standard procedure in this work to purify the tested materials.

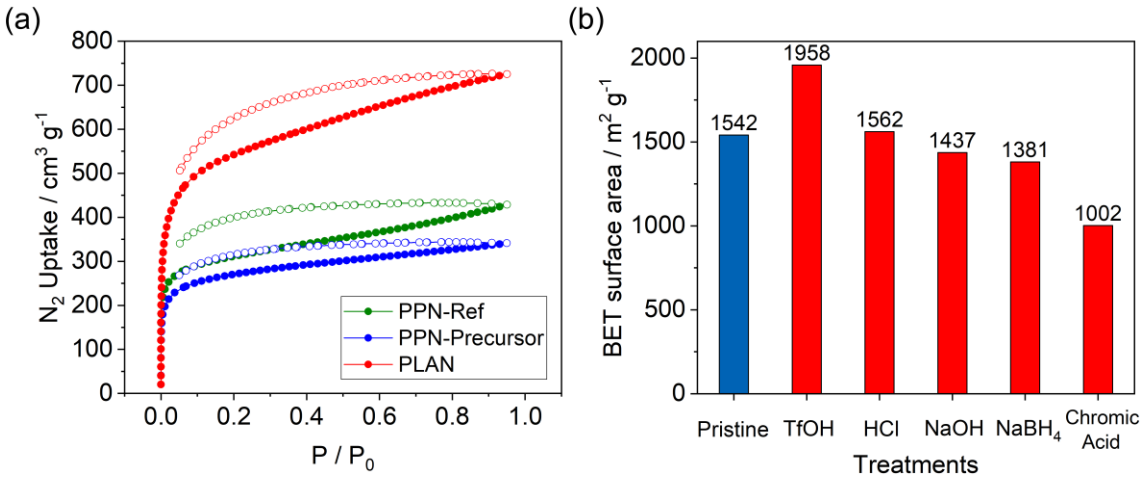

Figure 2.4. (a) N_2 adsorption isotherms (77 K) of PPN-Ref, **PPN-Precursor**, and **PLAN** after treatment with TfOH. (b) BET surface area of **PLAN** after treatment of acid (HCl, TfOH), base (NaOH), reducing agent ($NaBH_4$), or oxidant (chromic acid solution). Reproduced with permission from Fang et al.[146] Copyright 2020 American Chemical Society.

All three materials showed type I isotherms in the lower pressure region with increased adsorption at higher pressure. The hysteresis of N_2 adsorption originated from amorphous nature and irregular pore structures of PPNs, leading to a trapping effect at cryogenic temperature.[81, 175, 176] Pore size distributions calculated via nonlocal density functional theory showed primarily micropores at 1.2 nm ~ 1.5 nm, with a small population of broadly distributed mesopores (See SI). These mesopores were attributed to reaction defects formed during the Suzuki polymerization and interparticulate voids of the amorphous solid.[81] The higher surface area of **PLAN** compared to that of **PPN-Ref** was attributed to the presence of the vinyl groups in **PPN-precursor**, which acted as templates

to create latent pore volume and surface area after removal of the terminal $=CH_2$ units. In comparison, there was no such template effect for **PPN-Ref**.

2.4 Conclusion

In conclusion, we present the synthesis of a truxene-based **PLAN** through Suzuki crosslinking followed by RCM ladderization. Thermodynamically controlled ring-fusing step allowed for error-checking and proof-reading process, leading to complete ladder type backbone with minimal backbone defects. Solid state NMRs unambiguously confirmed the structural integrity, demonstrating no detectable terminal vinyl signals even with ultra-sensitive ^{13}C isotope labeling. **PLAN** possesses not only a highly stable porous structure, but also a larger BET surface area compared to its non-ladder-type counterparts. This crosslinking followed by ladderizaion method offers a universal strategy of introducing ladder-type backbone into porous system heterogeneously.

2.5 Experimental Section

2.5.1 General Methods

Starting materials, reagents, and solvents were purchased from Aldrich, Alfa Aesar, TCI, and Acros, and were used as received without further purification unless otherwise specified. Anhydrous THF was distilled with Na/benzophenone before uses. **4** (2,2'-(2,5-divinyl-1,4-phenylene)bis(4,4,5,5-tetramethyl1,3,2-dioxaborolane)) was synthesized according to reported procedures in literature.[71, 172] Analytical thin-layer chromatography (TLC) tests were performed on glass that was precoated with silica gel 60-F254 (Sorbtech).

Flash column chromatography was carried out using a Biotage® Isolera™ Prime. Solution phase ^{1}H-, ^{13}C-, HSQC, and HMBC NMR spectra were obtained on Varian Inova 500 MHz and Bruker Ascend 400 MHz spectrometers at room temperature. Chemical shifts are reported in ppm relative to the signals corresponding to the residual non-deuterated solvents (for ^{1}H NMR: $CDCl_3$ δ = 7.26 ppm; for ^{13}C NMR: $CDCl_3$ δ = 77.16 ppm). Solid-state NMR spectra were obtained on a Bruker Avance 400 MHz spectrometer with 4 mm CP/MAS probes and MAS rates of 10 kHz at room temperature. High-resolution Atmospheric Pressure Chemical Ionization (HR-APCI) mass spectra were performed using a Thermo Fisher Scientific Q Exactive Focus.

2.5.2 Synthesis

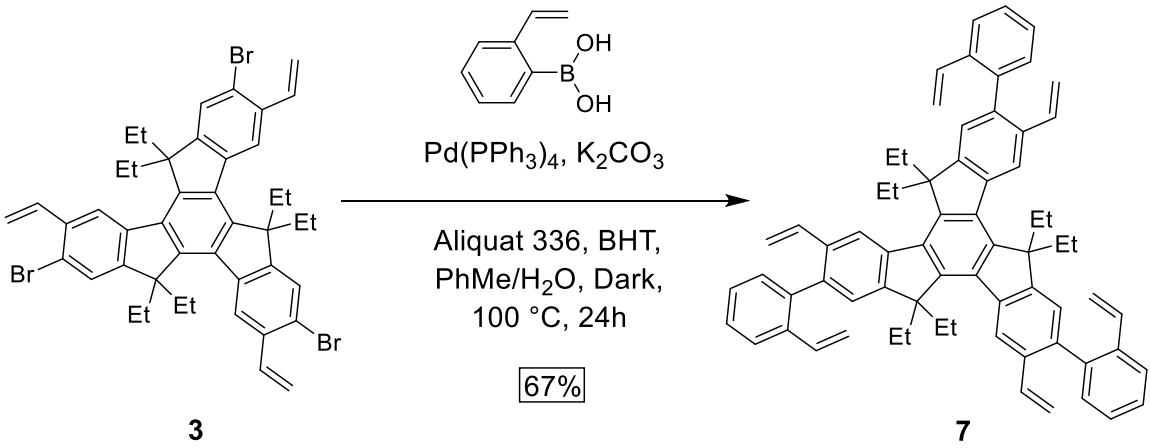

3 **7**

Compound 7: Under N_2, toluene (16 mL) and water (3.2 mL) was added to a mixture of **3** (0.2 g, 0.242 mmol), 2-Vinylphenylboronic acid (0.13 g, 0.848 mmol), K_2CO_3 (0.30 g, 2.18 mmol), aliquat 336 (0.23 mL, 0.51 mmol), several crystals of

butylated hydroxytoluene (BHT), and $Pd(PPh_3)_4$ (0.042 g, 15 mol%). The mixture was stirred at 100 °C for 24 h in dark. Then it was cooled down to room temperature, poured into water, and extracted with EtOAc. The combined organic layer was dried over Na_2SO_4, filtered, and concentrated under reduced pressure. The crude product was purified by column chromatography (SiO_2, 100% hexanes) to yield **7** as a light-yellow solid (0.15 g, 67%). ^{1}H NMR (500 MHz, Chloroform-*d*): δ 8.71 (s, 3H), 7.76 (dd, *J* = 7.8, 1.3 Hz, 3H), 7.44 (td, *J* = 7.5, 1.5 Hz, 3H), 7.39 (td, *J* = 7.4, 1.4 Hz, 3H), 7.34 (dd, *J* = 7.5, 1.5 Hz, 3H), 7.30 (s, 3H), 6.63 (ddd, *J* = 18.1, 15.4, 10.9 Hz, 6H), 5.78 (dd, *J* = 39.8, 17.5 Hz, 6H), 5.20 (dd, *J* = 13.7, 10.8 Hz, 6H), 3.13 (dh, *J* = 14.9, 7.3 Hz, 6H), 2.23 (m, 6H), 0.40 (dp, *J* = 21.5, 7.0 Hz, 18H). ^{13}C NMR (125 MHz, Chloroform-*d*): δ 152.25, 144.61, 140.07, 140.01, 138.66, 138.22, 136.51, 136.10, 135.43, 134.31, 130.89, 127.63, 127.35, 125.07, 124.58, 121.18, 114.63, 113.52, 56.82, 29.72, 29.61, 29.39, 29.27, 29.05, 8.93. HRMS (APCI): calcd for $C_{69}H_{66}$ $[M+H]^+$ *m/z*=895.5226; found *m/z*=895.5237.

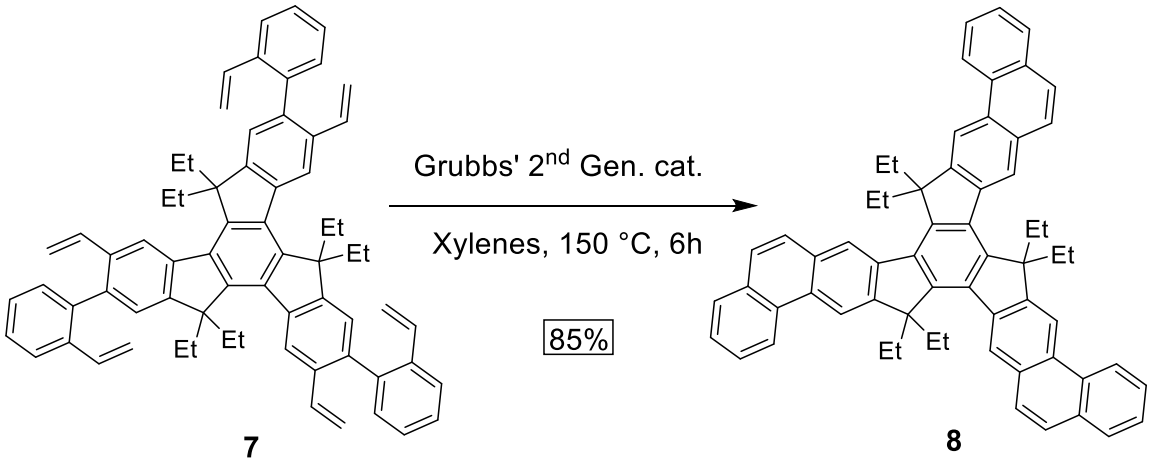

7 **8**

Compound 8: **7** (0.1 g, 0.112 mmol) and Grubbs' 2nd generation catalyst (5 mg, 5 mol%) was dissolved in degassed xylenes (10 mL). While being stirred at 150 °C under

N_2, another portion of Grubbs' 2nd generation catalyst (7 mg, 7 mol%) in degassed xylenes (10 mL) was added slowly over 4 h using a syringe pump. After that, the reaction mixture was stirred for an additional 2 h at 150 °C. Subsequently, it was cooled down to room temperature, poured into water, and extracted with EtOAc. The combined organic layer was dried over Na_2SO_4, filtered, and concentrated under reduce pressure. The crude product was purified by column chromatography (SiO_2, 100% hexanes) to yield **8** as a light-yellow solid (0.077 g, 85%). ^{1}H NMR (500 MHz, Chloroform-*d*): δ 8.98 (s, 3H), 8.90 (d, *J* = 8.2 Hz, 3H), 8.83 (s, 3H), 8.04 (d, *J* = 8.7 Hz, 3H), 7.99 (dd, *J* = 8.0, 1.4 Hz, 3H), 7.84 (d, *J* = 8.7 Hz, 3H), 7.77 (ddd, *J* = 8.3, 6.8, 1.4 Hz, 3H), 7.67 (ddd, *J* = 8.1, 6.9, 1.3 Hz, 3H), 3.43 (dq, *J* = 14.3, 7.2 Hz, 6H), 2.55 (dq, *J* = 14.5, 7.3 Hz, 6H), 0.38 (t, *J* = 7.2 Hz, 18H). ^{13}C NMR (125 MHz, Chloroform-*d*): δ 152.06, 145.93, 139.90, 138.77, 132.28, 131.33, 130.22, 129.48, 128.64, 127.95, 126.51, 126.47, 126.23, 124.40, 122.81, 115.61, 57.21, 30.30, 8.86. HRMS (APCI): calcd for $C_{63}H_{54}$ $[M+H]^+$ *m/z*=811.4287; found *m/z*=811.4298.

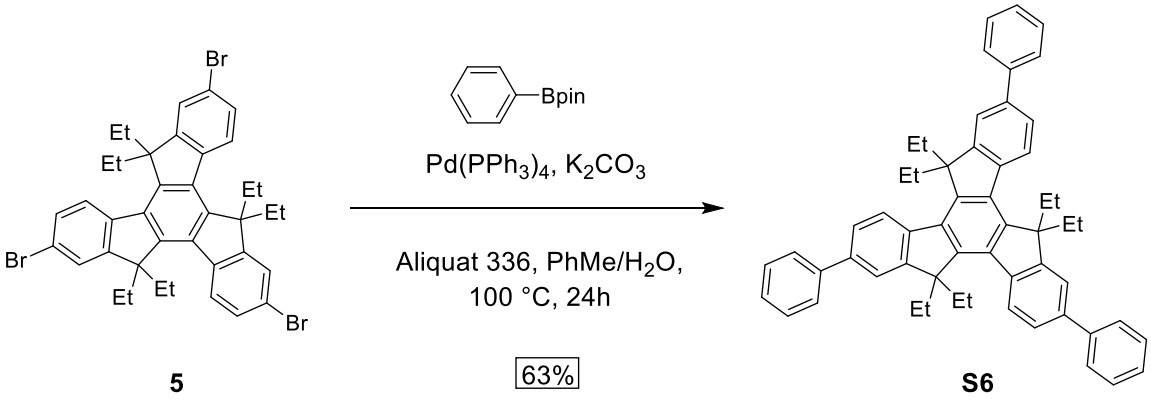

5 **S6**

Compound S6: Under N_2, toluene (16 mL) and water (3.2 mL) was added to a mixture of **5** (0.2 g, 0.268 mmol), phenylboronic acid pinacol ester (0.19 g, 0.937 mmol),

K_2CO_3 (0.33 g, 2.41 mmol), aliquat 336 (0.26 mL, 0.57 mmol), and $Pd(PPh_3)_4$ (0.046 g, 15 mol%). The reaction mixture was stirred at 100 °C for 24 h. Then it was cooled down to room temperature, poured into water, and extracted with EtOAc. The combined organic layer was dried over Na_2SO_4, filtered, and concentrated under reduced pressure. The crude product was purified by column chromatography (SiO_2, 100% hexanes) to yield **S6** as a light-yellow solid (0.12 g, 63%). ^{1}H NMR (500 MHz, Chloroform-*d*): δ 8.48 (d, *J* = 8.2 Hz, 3H), 7.80 (m, 6H), 7.75 (d, *J* = 1.8 Hz, 3H), 7.72 (dd, *J* = 8.2, 1.8 Hz, 3H), 7.55 (t, *J* = 7.6 Hz, 6H), 7.43 (m, 3H), 3.14 (dq, *J* = 14.3, 7.2 Hz, 6H), 2.30 (dq, *J* = 14.4, 7.3 Hz, 6H), 0.35 (t, *J* = 7.2 Hz, 18H). ^{13}C NMR (125 MHz, Chloroform-*d*): δ 153.57, 144.32, 141.31, 139.97, 139.44, 138.63, 128.87, 127.26, 127.16, 125.30, 124.91, 120.85, 56.97, 29.66, 8.73. HRMS (APCI): calcd for $C_{57}H_{54}$ $[M+H]^+$ *m/z*=739.4290; found *m/z*=739.4298.

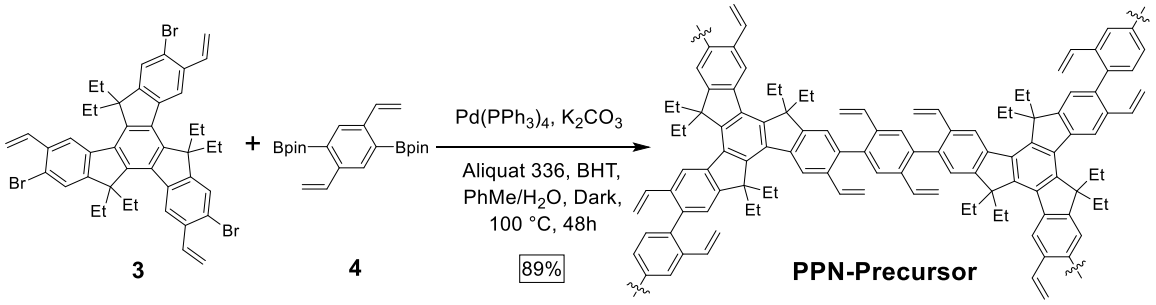

PPN-Precursor: Under N_2, toluene (8 mL) and water (1.6 mL) was added to a mixture of **3** (0.12 g, 0.142 mmol), **4** (0.082 g, 0.213 mmol), K_2CO_3 (0.18 g, 1.28 mmol), aliquat 336 (0.13 mL, 0.28 mmol), several crystals of BHT, and $Pd(PPh_3)_4$ (0.025 g, 15 mol%). The reaction mixture was stirred at 100 °C for 48 h in dark, before it was cooled down to room temperature. The precipitate was filtered, washed with DMF and H_2O, then purified by Soxhlet extraction with THF. The remaining solid was dried in vacuo to give a yellow solid (0.095 g, 89%). Solid-state ^{13}C NMR: δ 151.17, 143.35, 138.42, 134.76,

120.95, 112.17, 56.13, 28.40, 6.91. DRIFTS (cm^{-1}): 3084.18, 3062.96, 3014.74, 2964.59, 2933.73, 2875.86, 1737.86, 1693.50, 1624.06, 1604.77, 1556.55, 1492.90, 1471.69, 1415.75, 1377.17, 1355.96, 1330.88, 1305.81, 989.48, 908.47, 808.17, 779.24, 748.38.

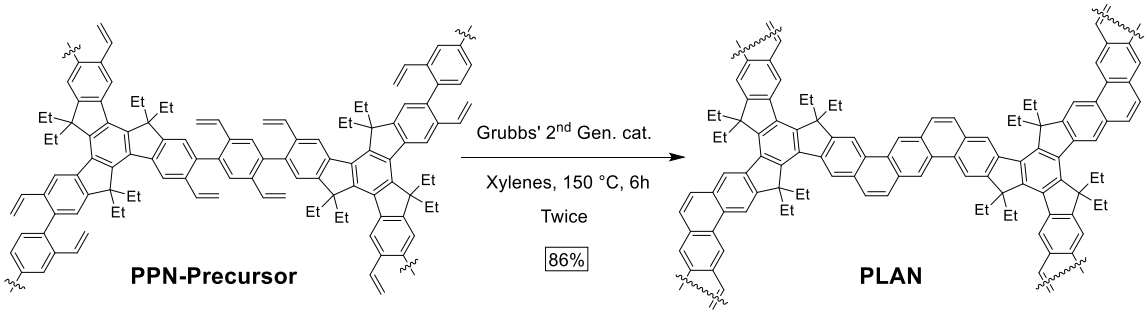

PLAN: The suspension of **PPN-Precursor** (0.1 g) in a solution of Grubbs' 2nd generation catalyst (10 mg) in degassed xylenes (10 mL) was stirred at 150 ^{o}C under N_2. Meanwhile, another portion of Grubbs' 2nd generation catalyst (20 mg) in degassed xylenes (10 mL) was added slowly over 4 h using a syringe pump. After that, the reaction mixture was stirred for an additional 2 h at 150 ^{o}C. The solid was collected by filtration, washed with DMF and H_2O, purified by Soxhlet extraction with THF, then dried in vacuo. This process was repeated one more time to give the product as a black powder (0.079 g, 86%). The lower than quantitative yield was caused by material loss during filtration and washing process. Solid-state ^{13}C NMR: δ 150.30, 143.43, 138.56, 130.06, 126.62, 120.50, 115.74, 56.87, 28.25, 5.39. DRIFTS (cm^{-1}): 3028.24, 2968.45, 2935.66, 2877.79, 1697.36, 1606.70, 1462.04, 1454.33, 1415.75, 1379.10, 1328.95, 1255.66, 1170.79, 1082.07, 881.47.

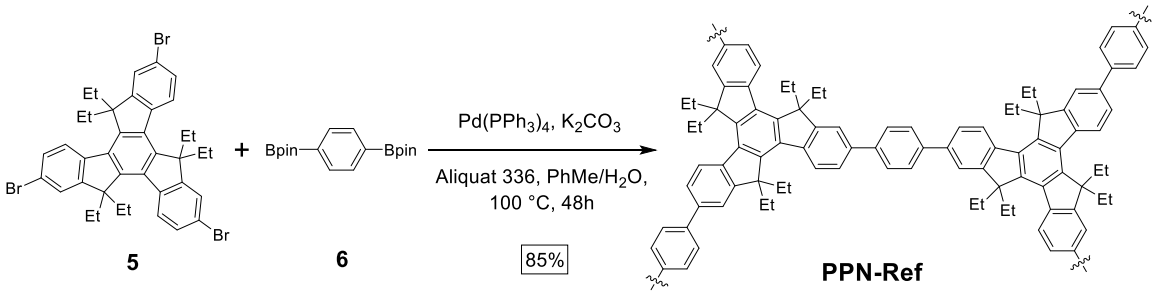

PPN-Ref: To a mixture of **5** (0.1 g, 0.134 mmol), **6** (0.066 g, 0.200 mmol), K_2CO_3 (0.17 g, 1.20 mmol), aliquat 336 (0.13 mL, 0.28 mmol), several crystals of BHT, and $Pd(PPh_3)_4$ (0.024 g, 15 mol%) were added toluene (8 mL) and water (1.6 mL) under a N_2 atmosphere. The reaction mixture was stirred at 100 ^oC for 48 h in darkness, before it was cooled down to room temperature. The precipitate was filtered, washed with DMF and H_2O, then purified by Soxhlet extraction with THF. The product was dried in vacuo to give the product as a brown solid (0.071 g, 85%). Solid-state ^{13}C NMR: δ 152.26, 142.74, 138.77, 130.88, 126.41, 123.51, 56.04, 28.61, 6.79. DRIFTS (cm^{-1}): 3057.17, 3028.24, 2966.52, 2933.73, 2875.86, 1604.77, 1492.90, 1473.62, 1436.97, 1377.17, 1184.29, 1118.71, 887.26, 694.37.

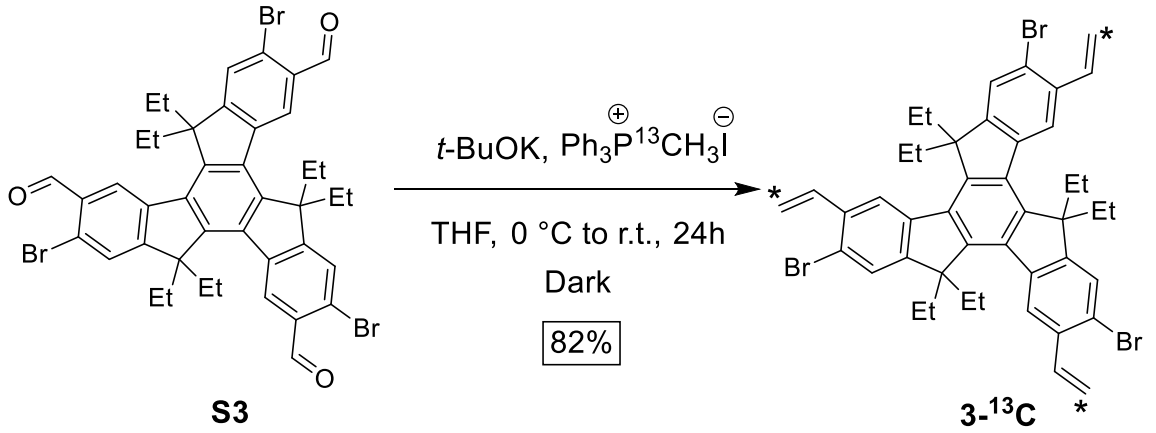

3-^{13}C: The same reaction and purification procedure for the synthesis of **3** was followed using methyl-^{13}C-triphenylphosphonium iodide as a carbon-13 source (99% ^{13}C isotope enriched, synthesized from reported literature). Yield: 0.41 g (82%). ^{1}H NMR (500 MHz, Chloroform-*d*): δ 8.52 (s, 3H), 7.62 (s, 3H), 7.22 (dd, *J* = 17.2, 10.8 Hz, 3H), 5.84 (dd, *J* = 154.2, 17.5 Hz, 3H), 5.48 (dd, *J* = 161.4, 10.8 Hz, 3H), 2.94 (dq, *J* = 14.5, 7.5 Hz, 6H), 2.16 (dq, *J* = 14.6, 7.3 Hz, 6H), 0.27 (t, *J* = 7.4 Hz, 18H). ^{13}C NMR (125 MHz, Chloroform-*d*): δ 154.34, 144.38, 139.77, 138.14, 136.89, 136.33, 135.46, 126.58, 122.72, 122.69, 122.62, 122.58, 115.93 (^{13}C enriched), 56.99, 29.36, 8.64.

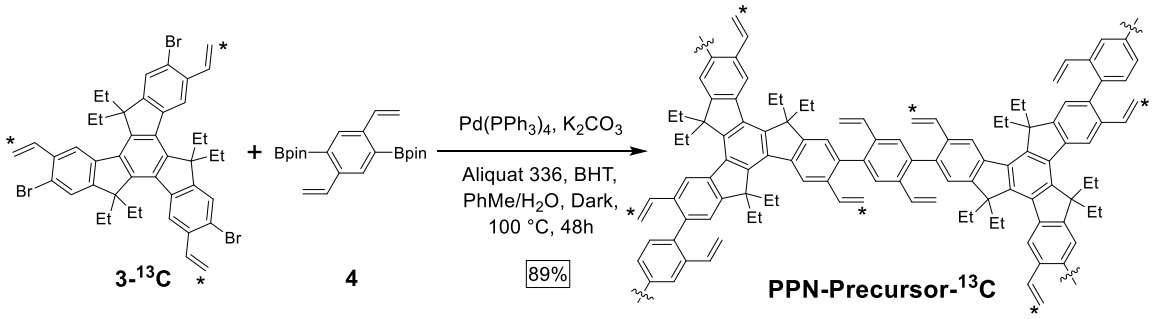

PPN-Precursor*: The same reaction and purification procedure for the synthesis of **PPN-Precursor-^{13}C** was followed. Yield: 89%.

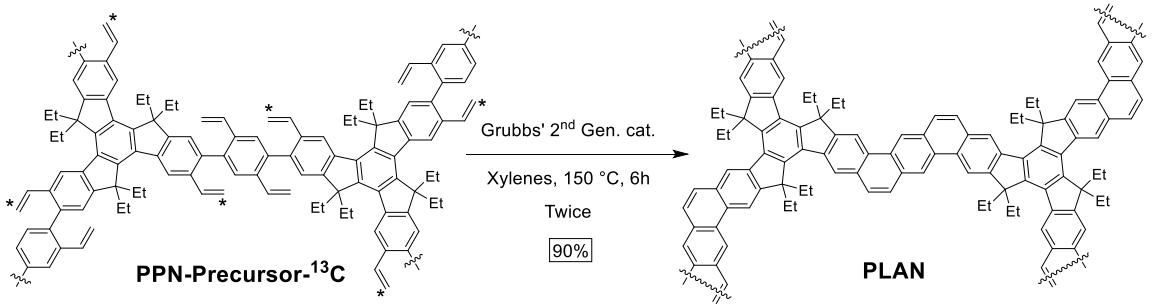

PLAN: The same reaction and purification procedure for the synthesis of normal **PLAN** was followed. Yield: 90%.

TfOH washing of PPNs: *TfOH is one of the strongest acids. Contact with skin causes severe burns with delayed tissue destruction. Please operate under full protection. 10 mL TfOH was added dropwise to 50 mg PPN inside a 20 mL vial. The suspension was sonicated for 5 minutes and stirred for 7 days at room temperature. Then it was poured into MeOH at 0 ^{o}C. The precipitate was filtered, washed with DMF, H_2O, and MeOH, purified by Soxhlet extraction with THF, then dried in vacuo.

2.5.3 BET Calculations and Pore Size Distributions

N_2 sorption isotherms at 77 K were measured with a Micromeritics ASAP 2020 surface area and pore size analyzer. Prior to the gas adsorption measurements, the sample was degassed for 10 h at 120 ^{o}C. All three materials showed type I isotherms in the lower pressure region with increased adsorption at higher pressure. The partial pressure range for the calculation of Brunauer-Emmett-Teller (BET) specific surface areas of samples was obtained from the corresponding Rouquerol plots, where the $V(1-P/P_0)$ is continuously increasing along with P/P_0.[20, 48] Pore size distribution data were calculated from the N_2 sorption isotherms based on the Nonlocal Density Functional Theory (NLDFT) method in the Micromeritics ASAP 2020 software package (assuming slit pore geometry).[20] All three materials showed primarily micropores at 1.2 nm ~ 1.5 nm, with a small population of broadly distributed mesopores. Due to the amorphous nature and possible interpenetration, the pore sizes and their distributions were not heavily dependent on their ideal crystalline structures. The mesopores were attributed to reaction defects

formed during the Suzuki polymerization and interparticulate voids of the amorphous solid.[81]

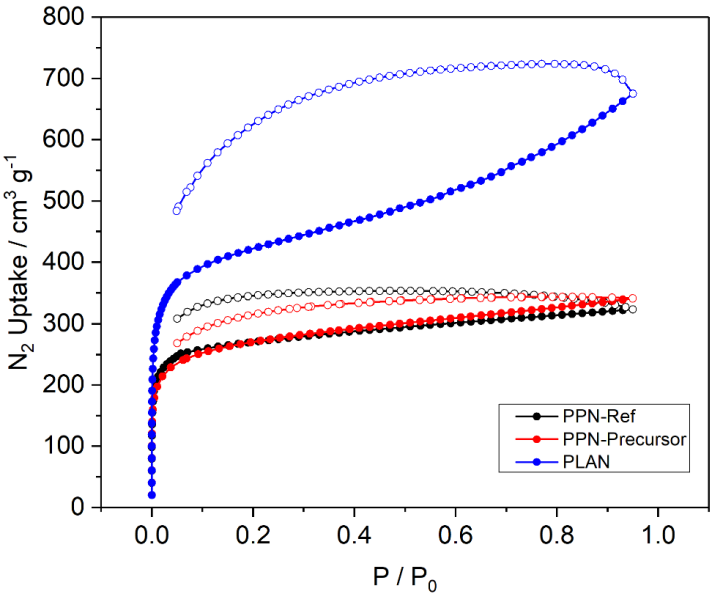

Figure 2.5. N_2 adsorption isotherms of as-synthesized **PPN-Ref**, **PPN-Precursor**, and **PLAN**.
Reproduced with permission from Fang et al.[146] Copyright 2020 American Chemical Society.

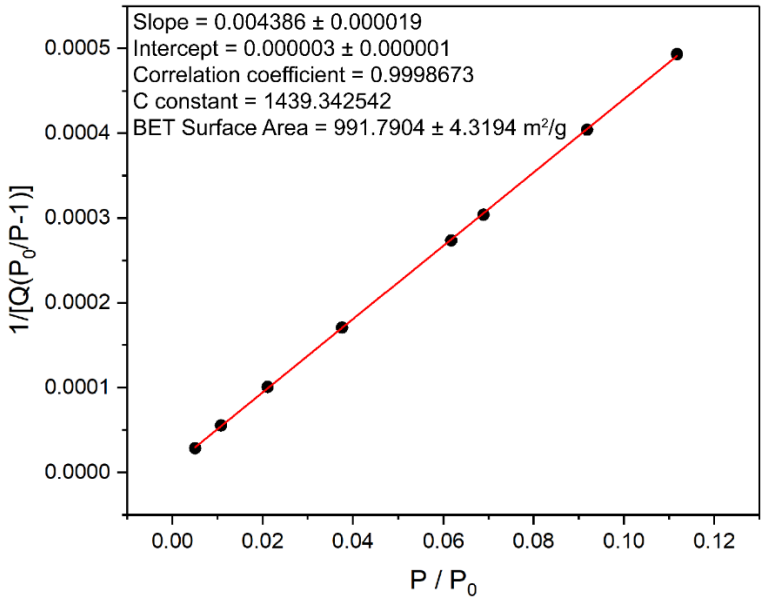

Figure 2.6. Plot of the linear region for the BET equation for **PPN-Precursor.**
Reproduced with permission from Fang et al.[146] Copyright 2020 American Chemical Society.

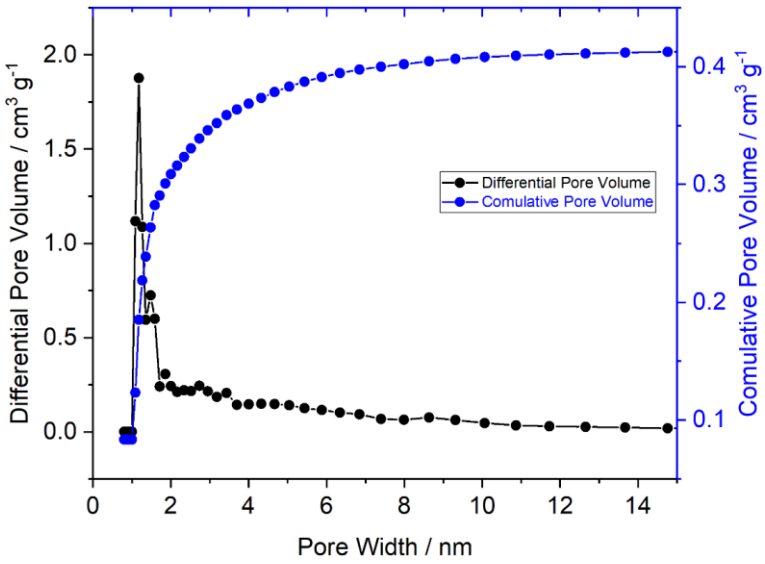

Figure 2.7. Pore size distribution of **PPN-Precursor.**
Reproduced with permission from Fang et al.[146] Copyright 2020 American Chemical Society.

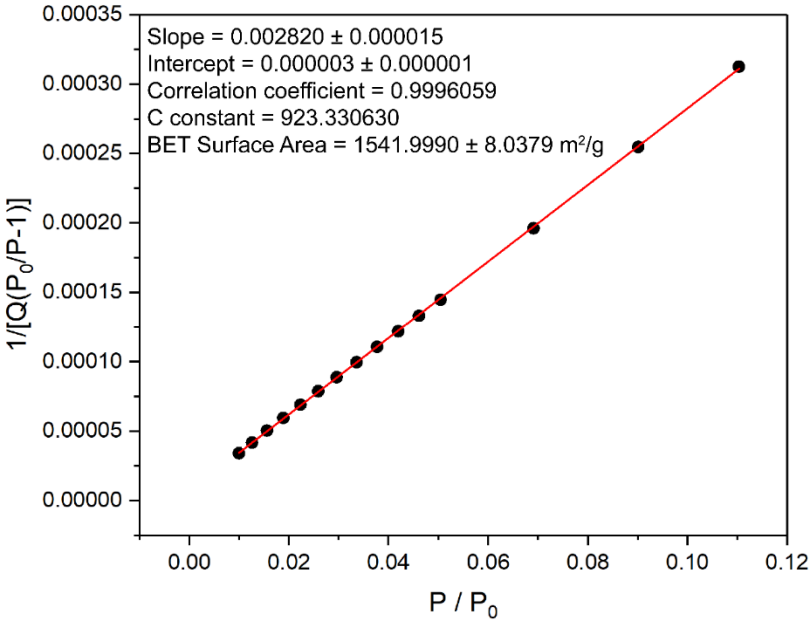

Figure 2.8. Plot of the linear region for the BET equation for **PLAN.**
Reproduced with permission from Fang et al.[146] Copyright 2020 American Chemical Society.

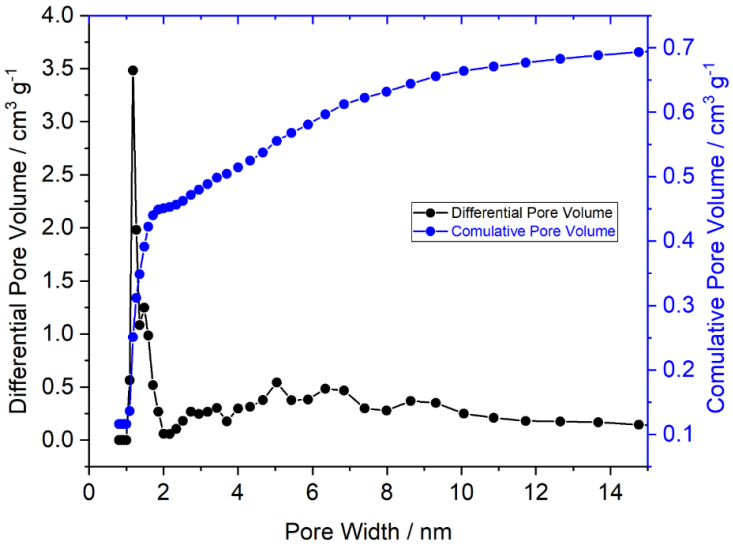

Figure 2.9. Pore size distribution of **PLAN.**
Reproduced with permission from Fang et al.[146] Copyright 2020 American Chemical Society.

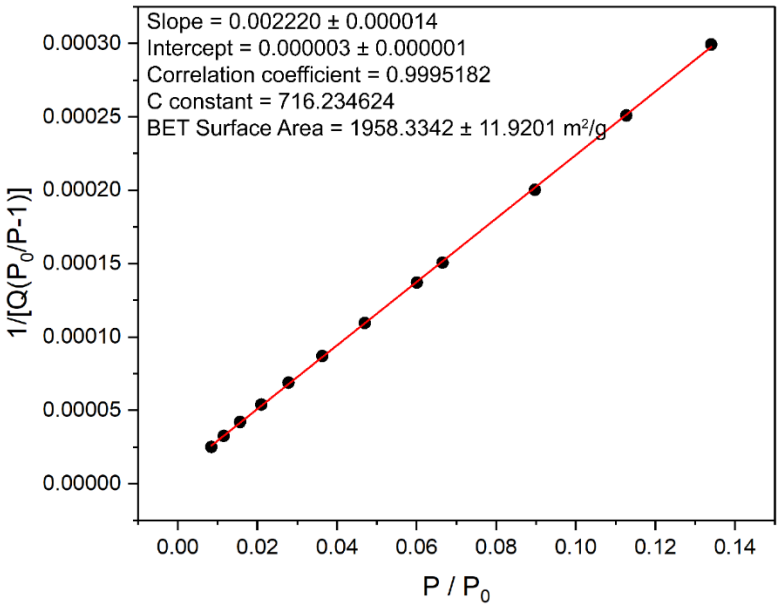

Figure 2.10. Plot of the linear region for the BET equation for **PLAN** after TfOH treatment.
Reproduced with permission from Fang et al.[146] Copyright 2020 American Chemical Society.

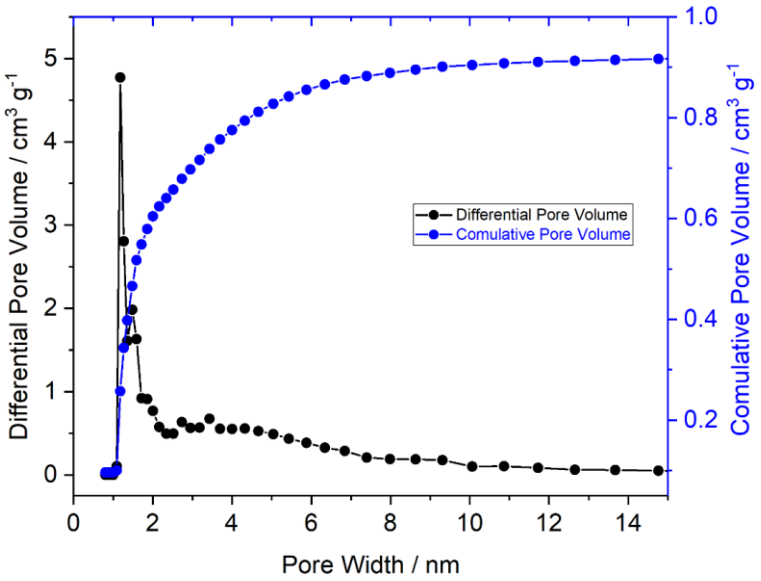

Figure 2.11. Pore size distribution of **PLAN** after TfOH treatment.
Reproduced with permission from Fang et al.[146] Copyright 2020 American Chemical Society.

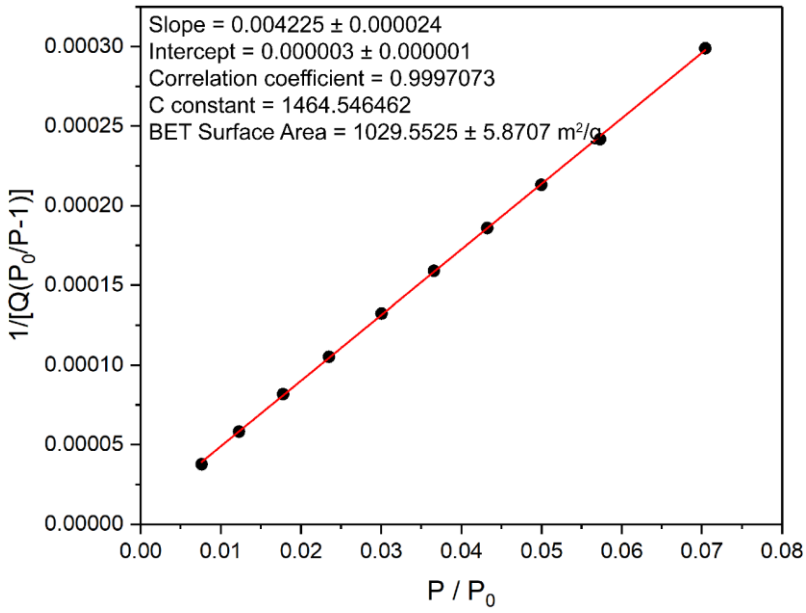

Figure 2.12. Plot of the linear region for the BET equation for **PPN-Ref.**
Reproduced with permission from Fang et al.[146] Copyright 2020 American Chemical Society.

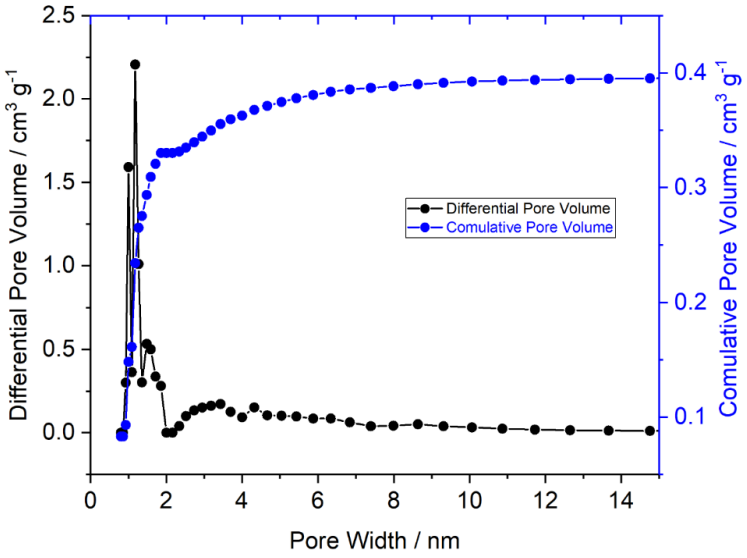

Figure 2.13. Pore size distribution of **PPN-Ref.**
Reproduced with permission from Fang et al.[146] Copyright 2020 American Chemical Society.

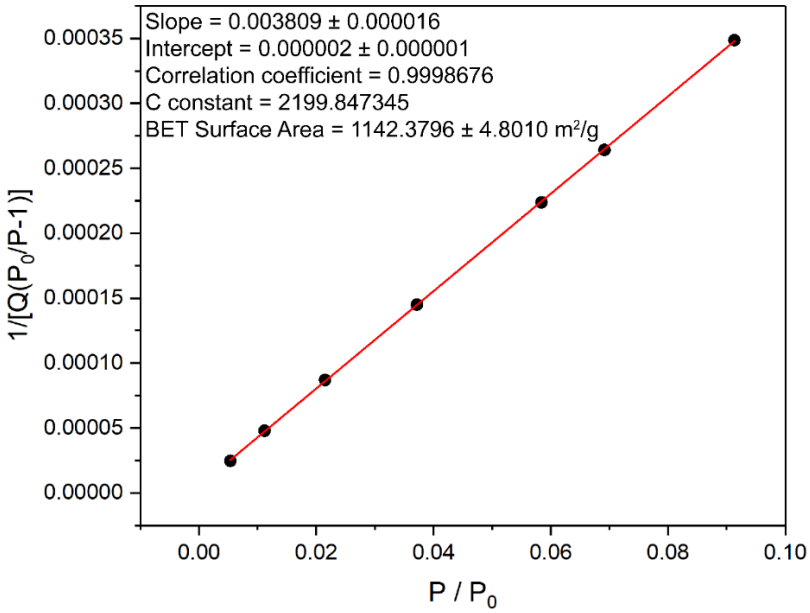

Figure 2.14. Plot of the linear region for the BET equation for **PPN-Ref** after TfOH treatment.
Reproduced with permission from Fang et al.[146] Copyright 2020 American Chemical Society.

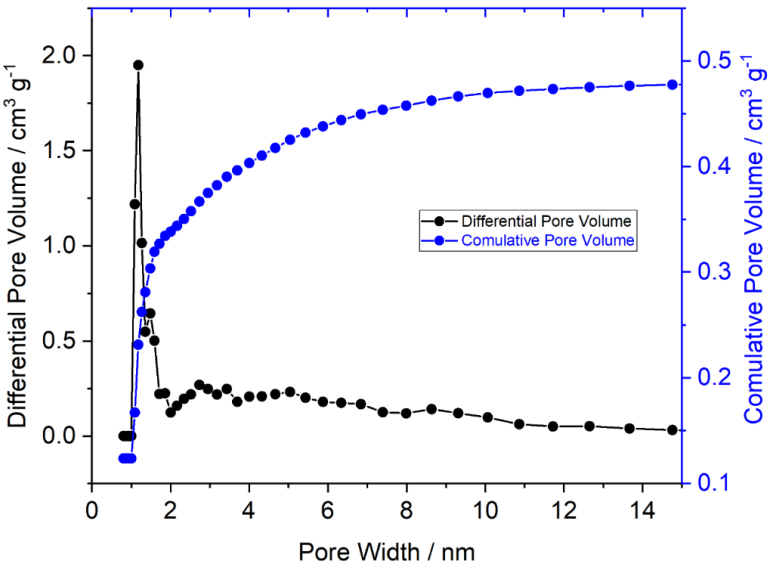

Figure 2.15. Pore size distribution of **PPN-Ref** after TfOH treatment.
Reproduced with permission from Fang et al.[146] Copyright 2020 American Chemical Society.

2.5.4 Stability tests

Standard procedure: 50 mg of **PPN-Precursor** or **PLAN** solid material was suspended in 10 mL of each following solutions (1) 12 M HCl at 80 ºC for 7 days; (2) 14 M NaOH in H_2O/MeOH at 80 ºC for 7 days; (3) 50 equiv. $NaBH_4$ in MeOH at 80 ºC for 7 days; (4) chromic acid solution (0.1 M $K_2Cr_2O_7$ in concentrated H_2SO_4) for 3 days; or (5) 98% TfOH for 7 days. Afterwards, the solid material was collected by filtration, washed with H_2O and MeOH, and dried in vacuum. Subsequently, the remaining solid was subjected to solid state CP-MAS NMR and nitrogen adsorption isotherm tests.

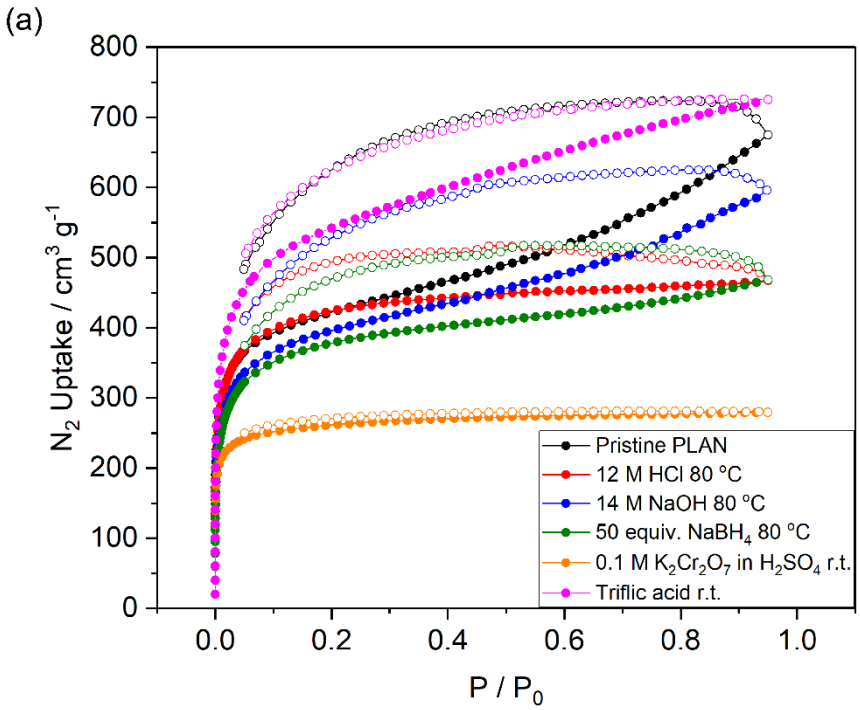

Figure 2.16. N_2 adsorption isotherms of **PLAN** (a) and **PPN-Ref** (c) after treatments. BET surface areas of **PLAN** (b) and **PPN-Ref** (d) after each treatment.
Reproduced with permission from Fang et al.[146] Copyright 2020 American Chemical Society.

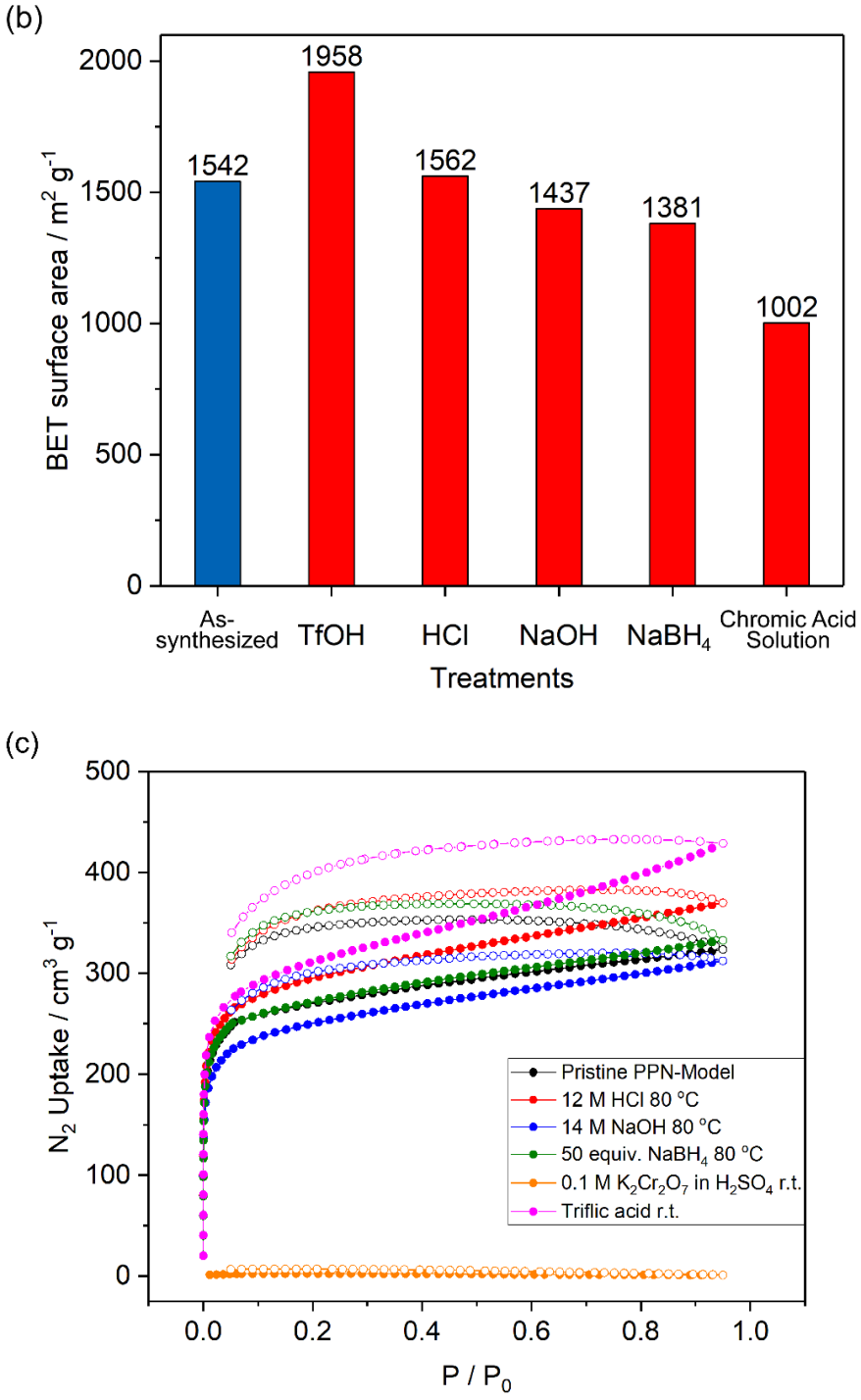

Figure 2.16. Continued.

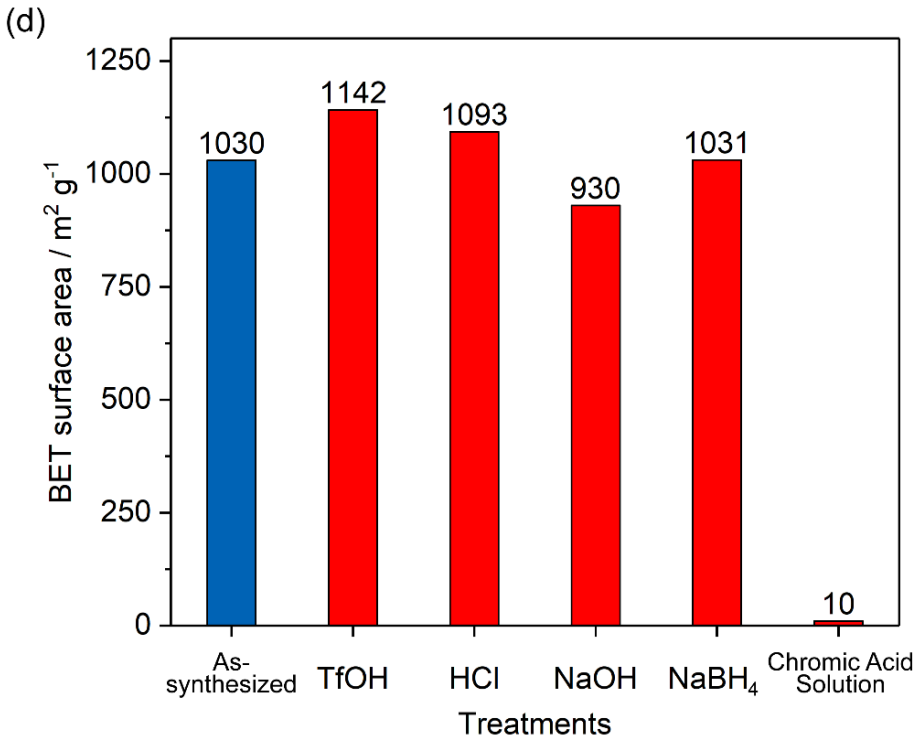

Figure 2.16. Continued.

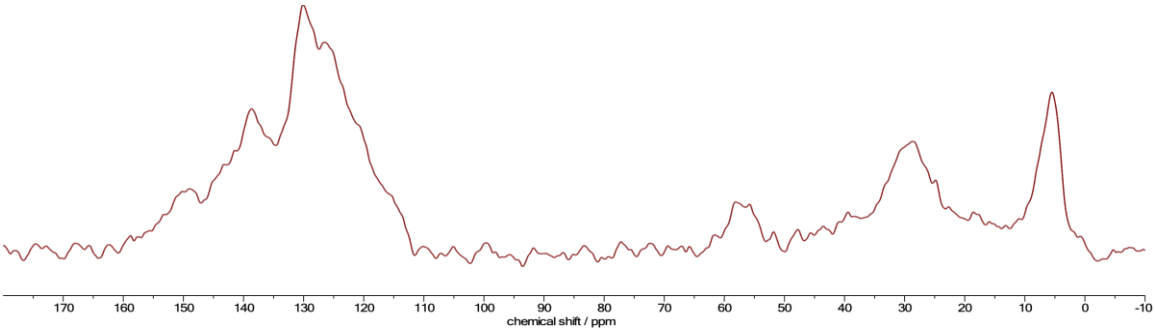

Figure 2.17. Solid-state CP-MAS 13C NMR spectra of **PLAN** after TfOH treatment. Reproduced with permission from Fang et al.[146] Copyright 2020 American Chemical Society.

2.5.5 Thermogravimetric Analysis (TGA)

Thermogravimetric analysis (TGA) data were collected on Mettle-Toledo TGA-DSC-1 at a heating rate of 20 ^{o}C min-1 from 30 ^{o}C to 900 ^{o}C under N_2 atmosphere. 5% weight loss temperature: **PPN-Ref**: 347 ^{o}C; **PPN-Precursor**: 373 ^{o}C; **PLAN**: 358 ^{o}C.

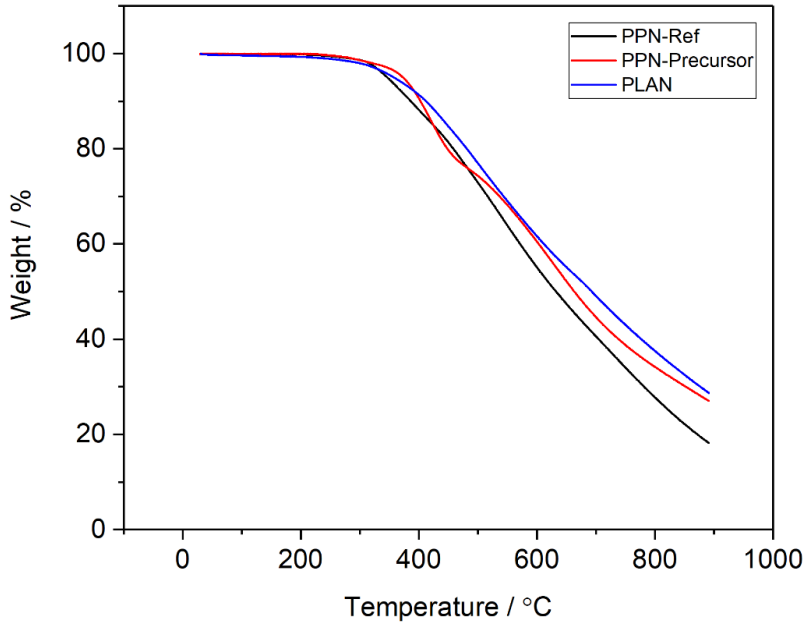

Figure 2.18. TGA plots of **PPN-Ref**, **PPN-Precursor**, and **PLAN** under N_2.
Reproduced with permission from Fang et al.[146] Copyright 2020 American Chemical Society.

2.5.6 Diffuse Reflectance Infrared Fourier Transform Spectroscopy (DRIFTS)

Diffuse Reflectance Infrared Fourier Transform Spectroscopy (DRIFTS) were recorded using a Shimadzu IRAffinity-1S spectrometer with DRIFTS accessory. The spectrum of **PPN-Precursor** exhibited the alkenyl C—H (3084.18 cm^{-1}) and C=C (1624.06 cm^{-1}) stretching peaks. These peaks disappearance on the spectrum of **PLAN** after two cycles of RCM reaction, corroborating the anticipated removal of the terminal vinyl groups.[64]

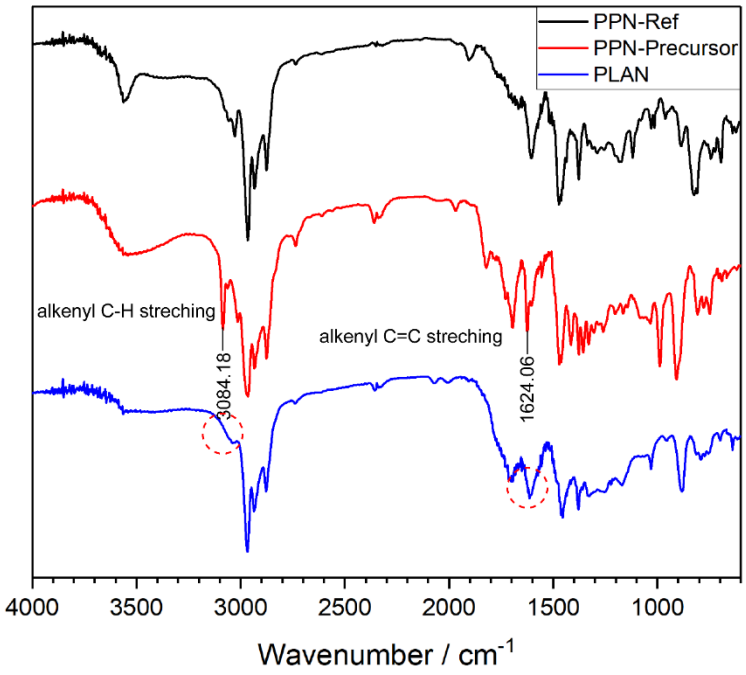

Figure 2.19. Comparison of DRIFTS of **PPN-Ref**, **PPN-Precursor**, and **PLAN**. Reproduced with permission from Fang et al.[146] Copyright 2020 American Chemical Society.

2.5.7 X-ray Photoelectron Spectroscopy (XPS)

X-ray photoelectron spectroscopy (XPS) analysis was carried out with Omicron XPS/UPS system with Argus detector using uses Omicron's DAR 400 dual Mg/Al X-ray source. Carbon and trace amount of oxygen signals were observed. The oxygen signal was attributed to partial surface oxidation. No signal was observed for the Br, B, and Pd measurements.

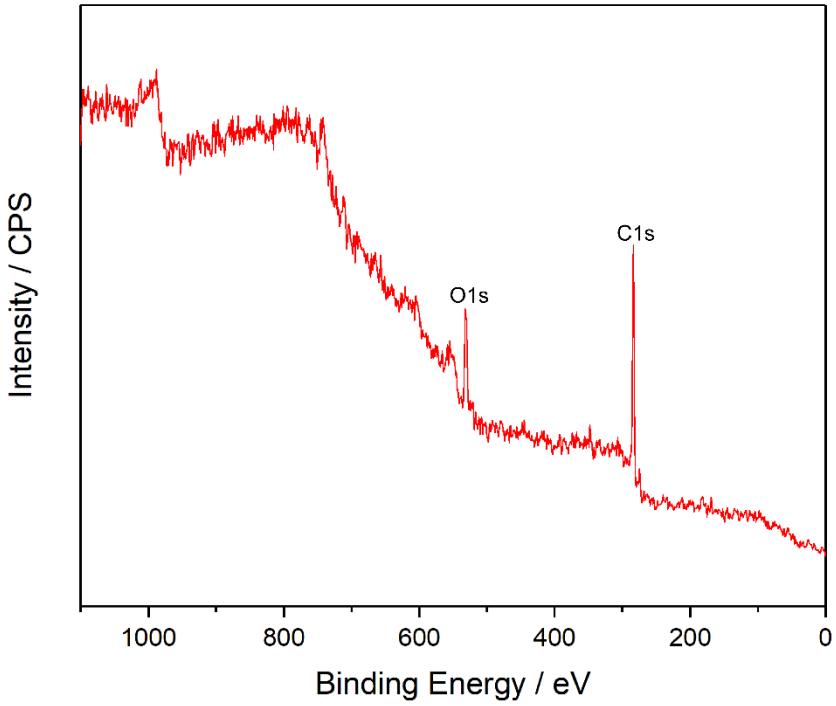

Figure 2.20. XPS survey scan of **PPN-Ref.**
Reproduced with permission from Fang et al.[146] Copyright 2020 American Chemical Society.

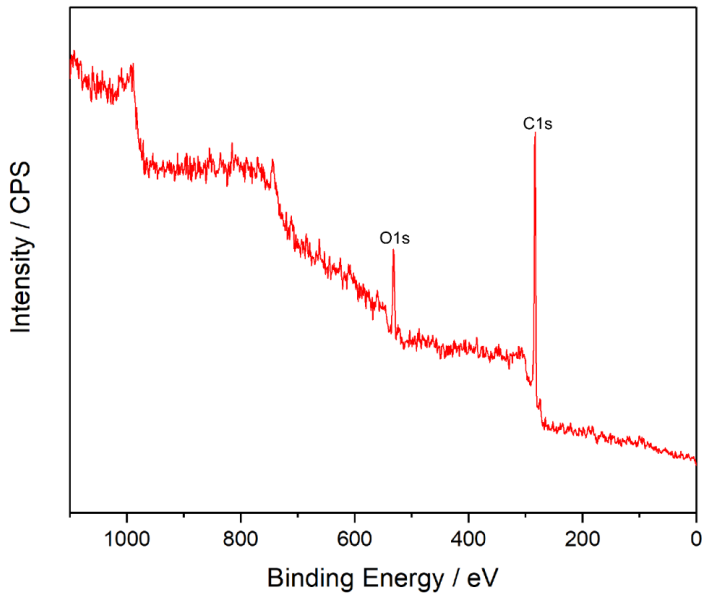

Figure 2.21. XPS survey scan of **PPN-Precursor.**
Reproduced with permission from Fang et al.[146] Copyright 2020 American Chemical Society.

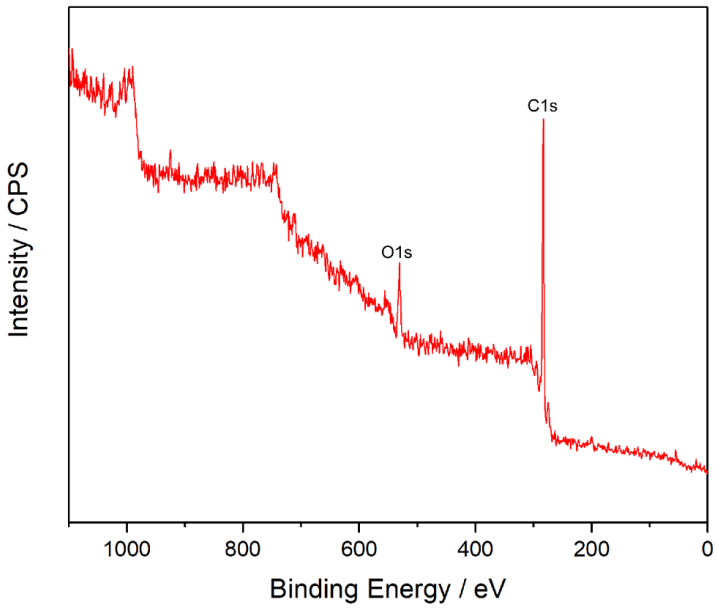

Figure 2.22. XPS survey scan of **PLAN.**
Reproduced with permission from Fang et al.[146] Copyright 2020 American Chemical Society.

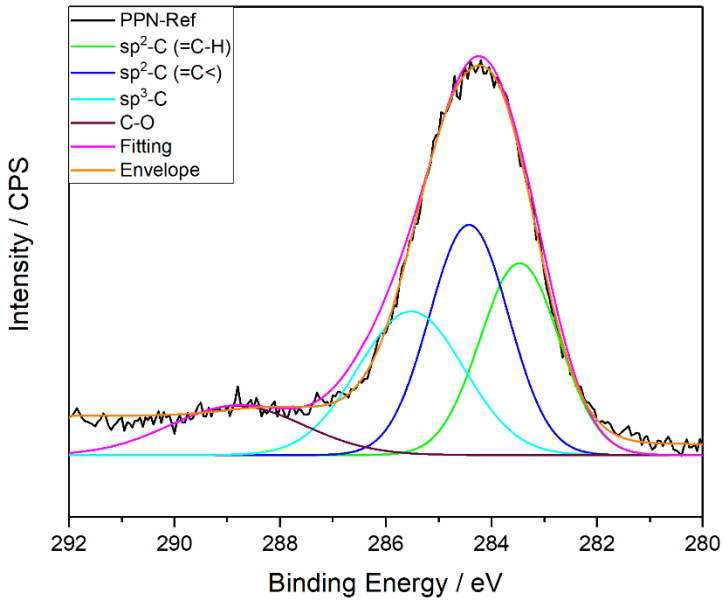

Figure 2.23. C1s XPS spectrum of **PPN-Ref.**
Reproduced with permission from Fang et al.[146] Copyright 2020 American Chemical Society.

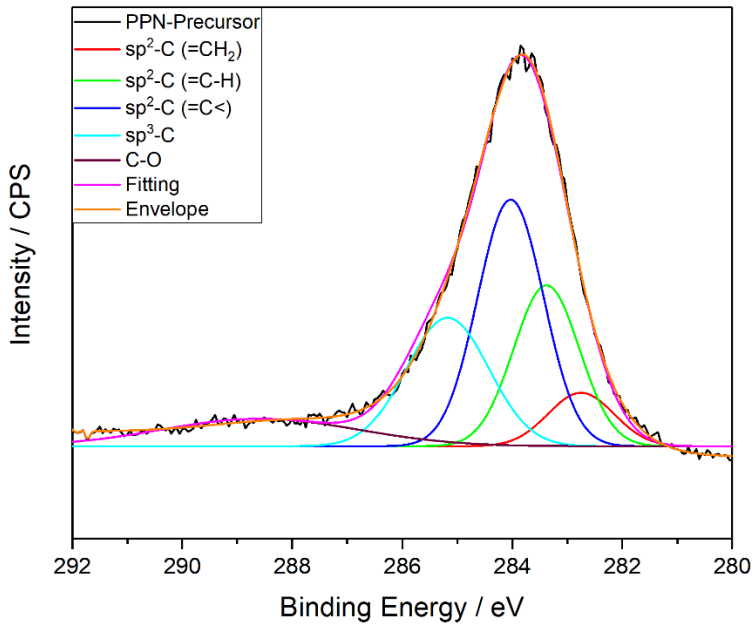

Figure 2.24. C1s XPS spectrum of **PPN-Precursor.**
Reproduced with permission from Fang et al.[146] Copyright 2020 American Chemical Society.

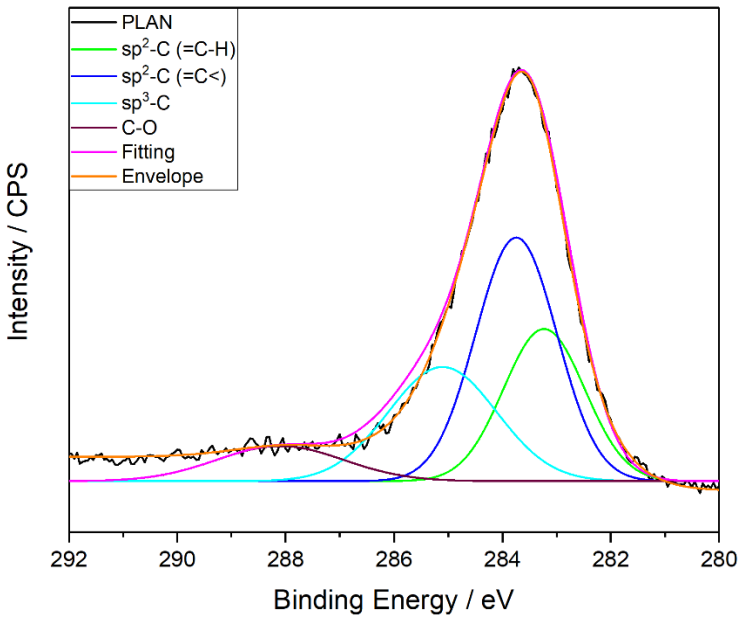

Figure 2.25. C1s XPS spectrum of **PLAN.**
Reproduced with permission from Fang et al.[146] Copyright 2020 American Chemical Society.

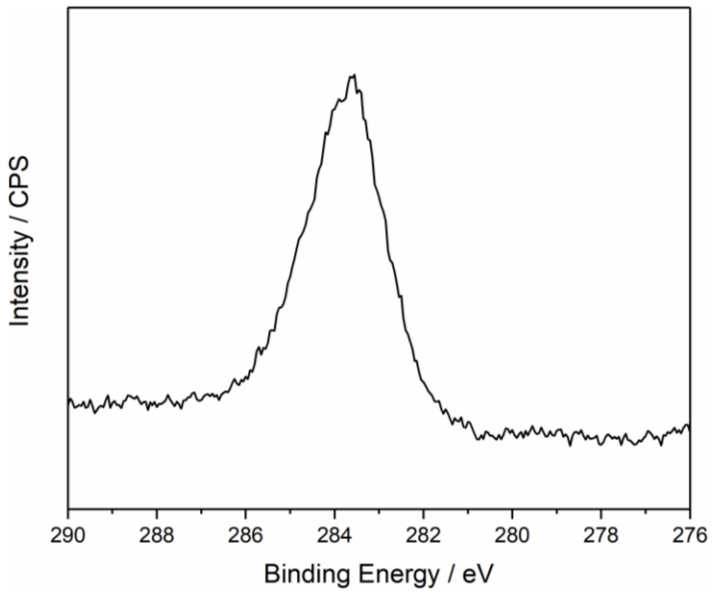

Figure 2.26. Ru3d XPS spectrum of **PLAN.**
Main signal belongs to C1s. Ru3d signal should be around 280 eV
Reproduced with permission from Fang et al.[146] Copyright 2020 American Chemical Society.

2.5.8 Powder X-Ray Diffraction (PXRD)

Powder X-ray diffraction (PXRD) was obtained with a Bruker D8-Focus Bragg-Brentano X-ray Powder Diffractometer equipped with a Cu sealed tube (λ = 1.54178 Å) at 40 kV and 40 mA. No distinct peaks were observed on powder X-ray diffraction tests of **PPN-Ref, PPN-Precursor,** and **PLAN**, confirming the expected amorphous nature of all three materials.

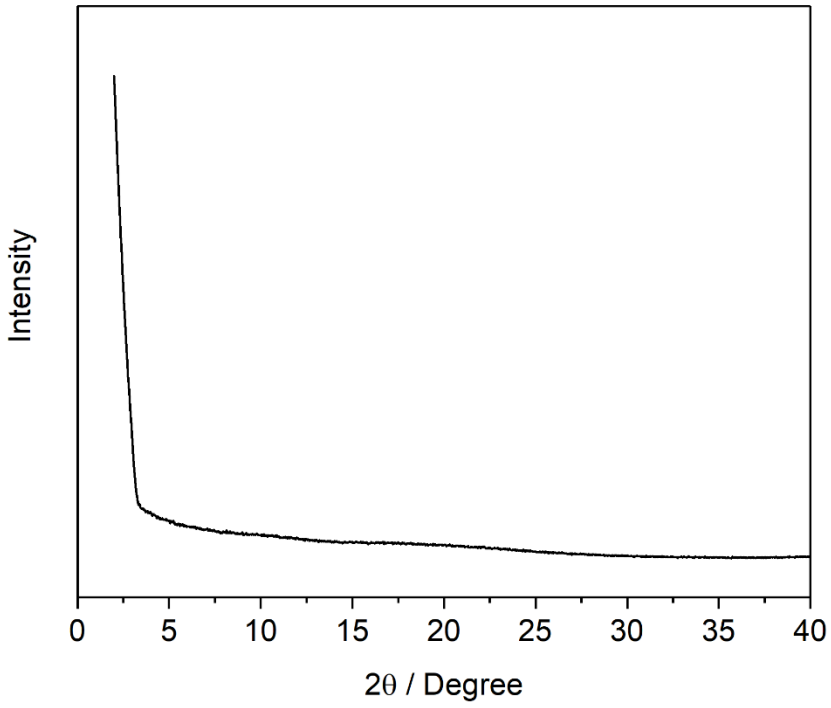

Figure 2.27. Experimental PXRD of **PPN-Ref.**
Reproduced with permission from Fang et al.[146] Copyright 2020 American Chemical Society.

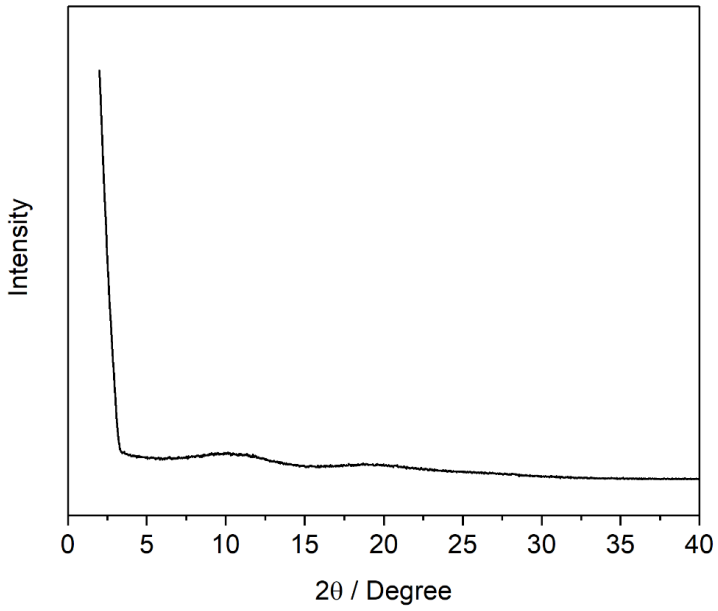

Figure 2.28. Experimental PXRD of **PPN-Precursor.**
Reproduced with permission from Fang et al.[146] Copyright 2020 American Chemical Society.

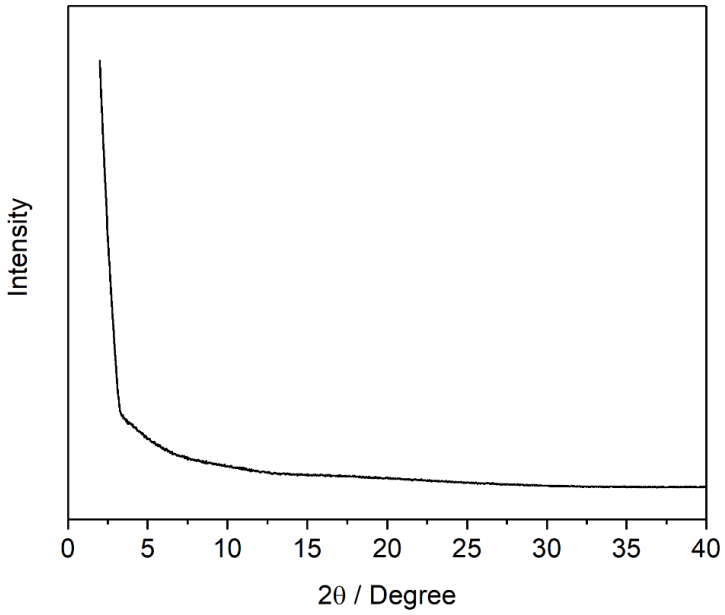

Figure 2.29. Experimental PXRD of **PLAN.**
Reproduced with permission from Fang et al.[146] Copyright 2020 American Chemical Society.

2.5.9 Optical Properties

UV-vis absorption spectra were recorded using a Shimadzu UV-2600. Fluorescence emission spectra was recorded using a Horiba Fluoromax-4 spectrometer. UV-vis absorption spectrum of **S10** was red-shifted compared with the non-ladder counterparts **S9** and **S11**, confirming the more extended π conjugation system after ring annulation. Moreover, both UV-vis absorption and fluorescence spectrum of **S10** exhibited more pronounced vibrational fine features, indicative of the more rigid backbone of **S10** arising from the fused ring consitution. Fluorescence spectrum of the suspension of **PPN-Ref**, **PPN-Precursor**, and **PLAN** in $CHCl_3$ were recorded. All three porous materials showed similar shape but more red-shifted peaks compared with their corresponding model small molecules, in accord to their similar constitutions but with more extended π conjugation system.

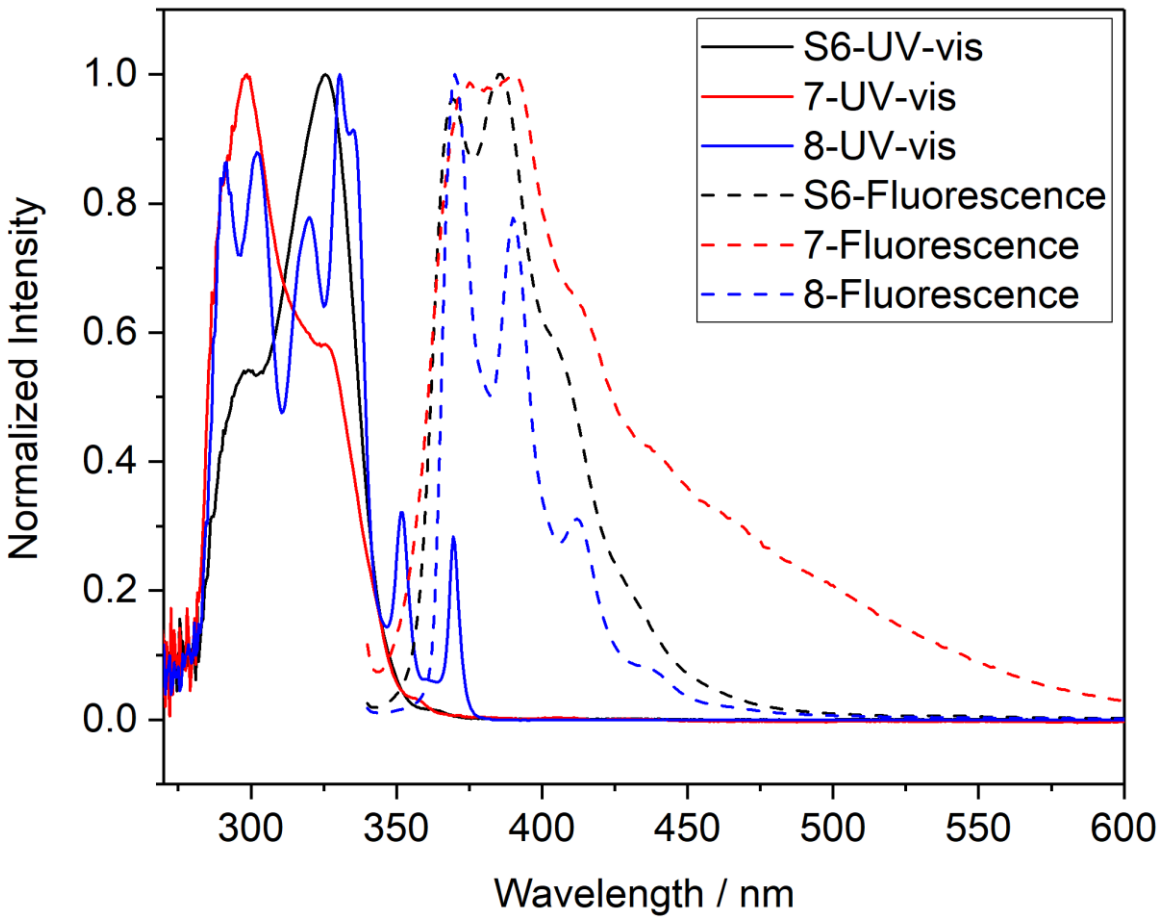

Figure 2.30. UV-vis absorption and fluorescence emission spectra of small molecular model compounds **S6**, **7**, and **8** in chloroform. Excitation: 330 nm.
Reproduced with permission from Fang et al.[146] Copyright 2020 American Chemical Society.

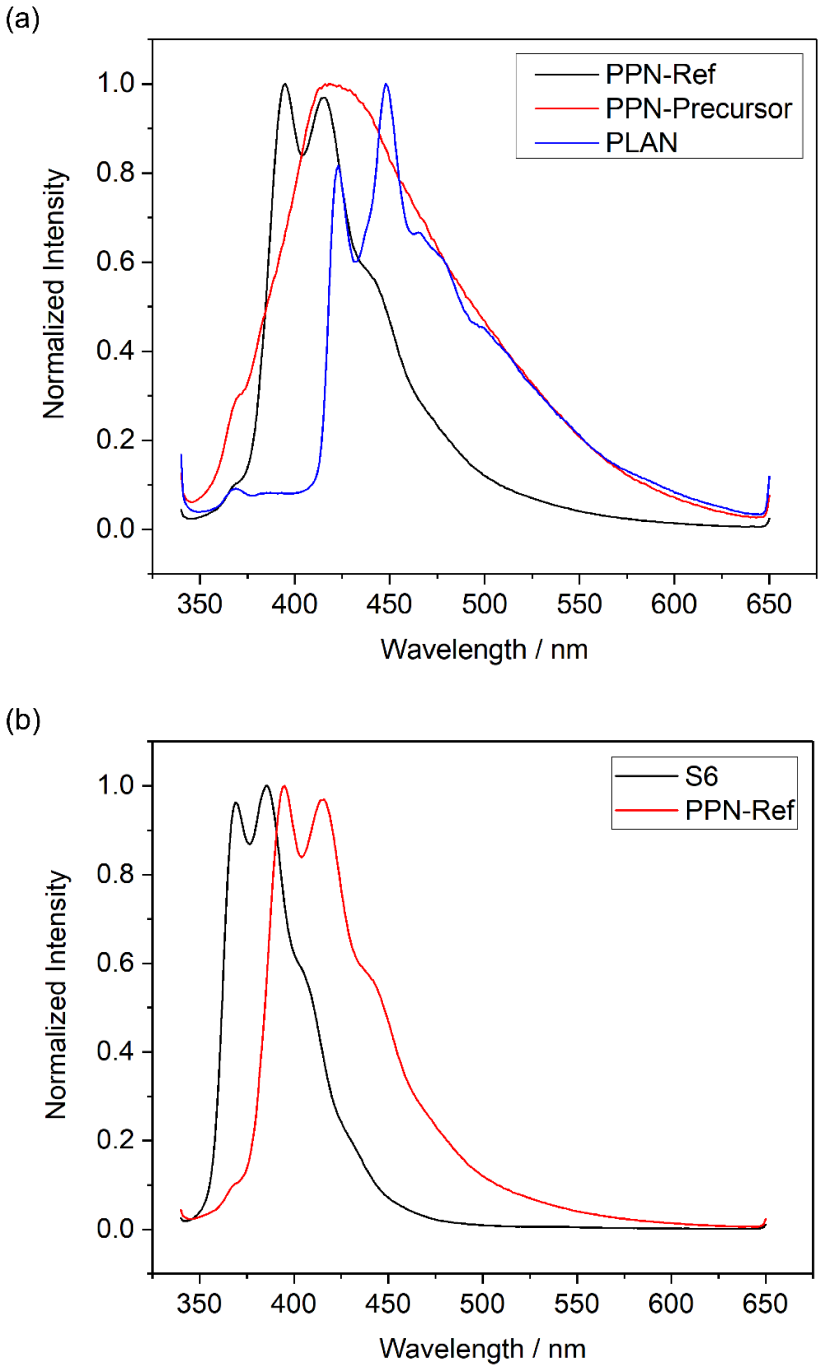

Figure 2.31. (a) Fluorescence spectrum of **PPN-Ref**, **PPN-Precursor**, and **PLAN** suspensions in chloroform. Excitation: 330 nm. (b-d) Comparison of suspension fluorescence of **PPN-Ref**, **PPN-Precursor**, and **PLAN** to their small molecular model compounds **S6**, **7**, and **8** in chloroform, respectively.
Reproduced with permission from Fang et al.[146] Copyright 2020 American Chemical Society.

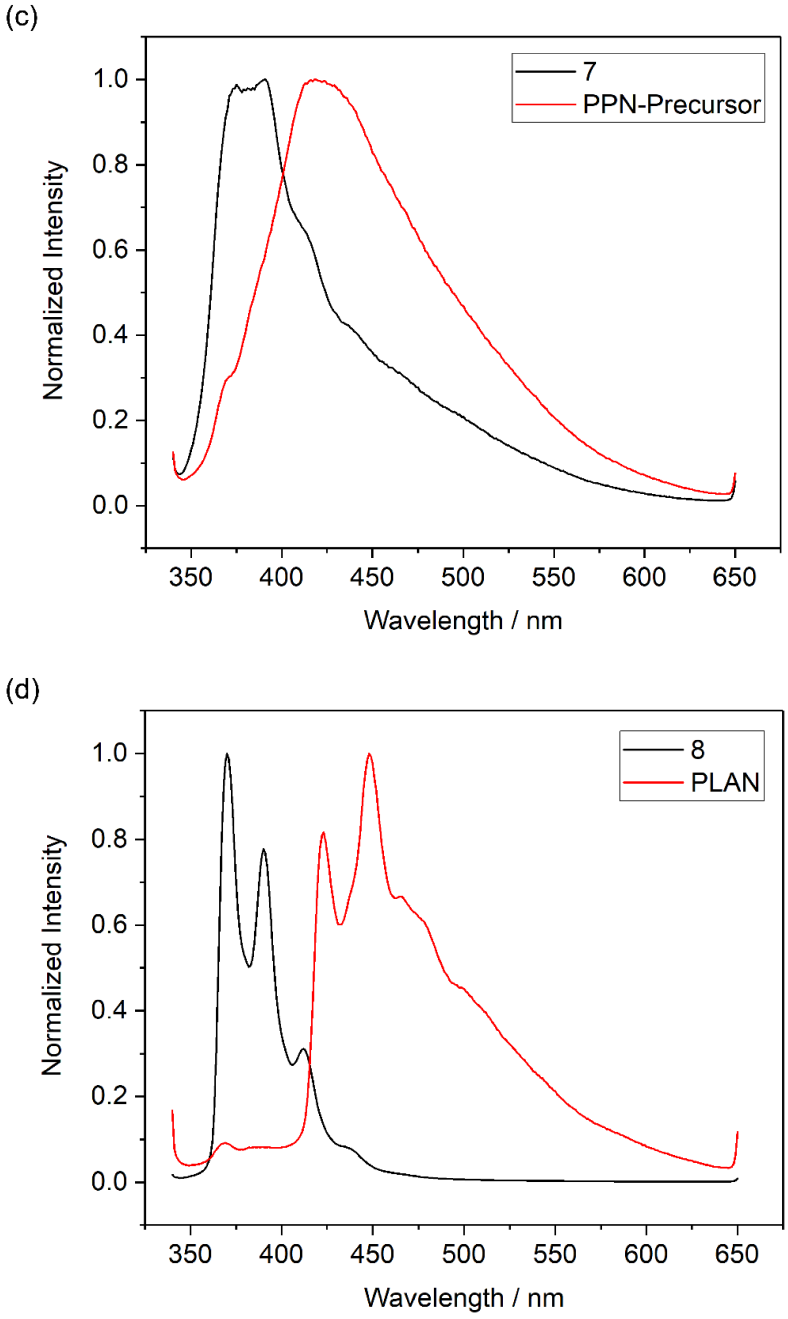

Figure 2.31. Continued.

2.5.10 SEM Images

Field-emission scanning electron microscopic (SEM) images were collected using the FEI Quanta 600 FE-SEM. All three materials showed similar morphology of sphere aggregates with diameters of ~1 μm, which is common for amorphous porous organic materials.

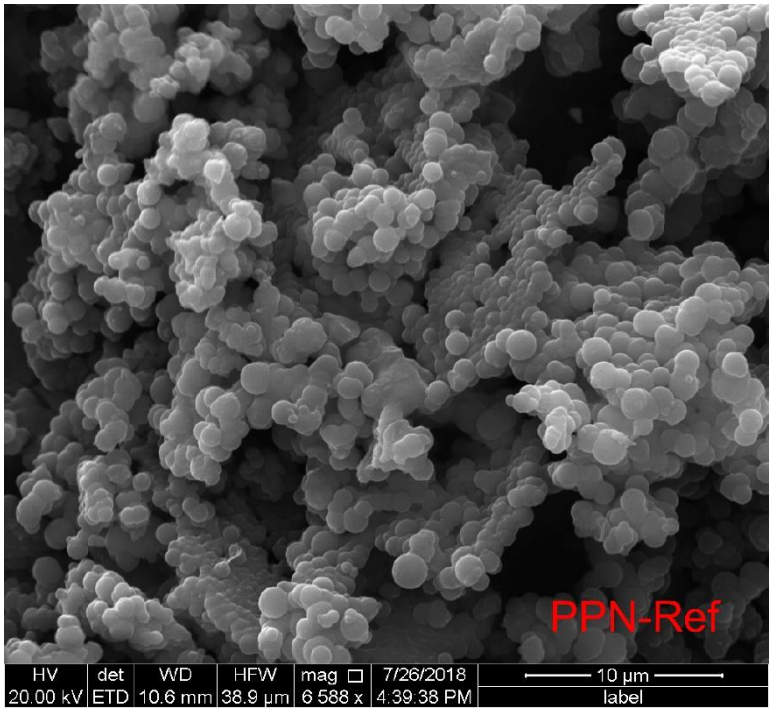

Figure 2.32. SEM images of **PPN-Ref**, **PPN-Precursor**, and **PLAN**.
Reproduced with permission from Fang et al.[146] Copyright 2020 American Chemical Society.

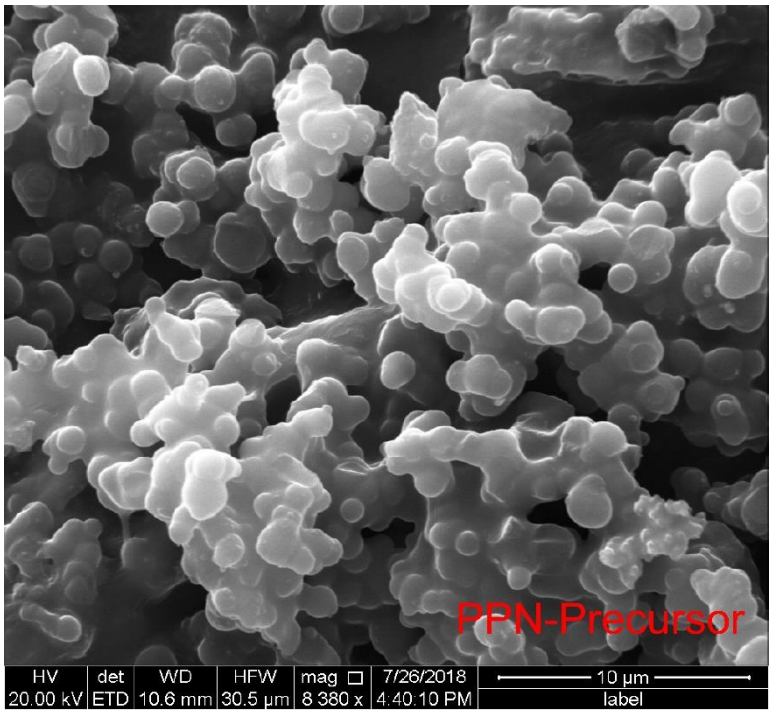

Figure 2.32. Continued.

2.5.11 ^{1}H-, ^{13}C-, HSQC, and HMBC NMR Spectra

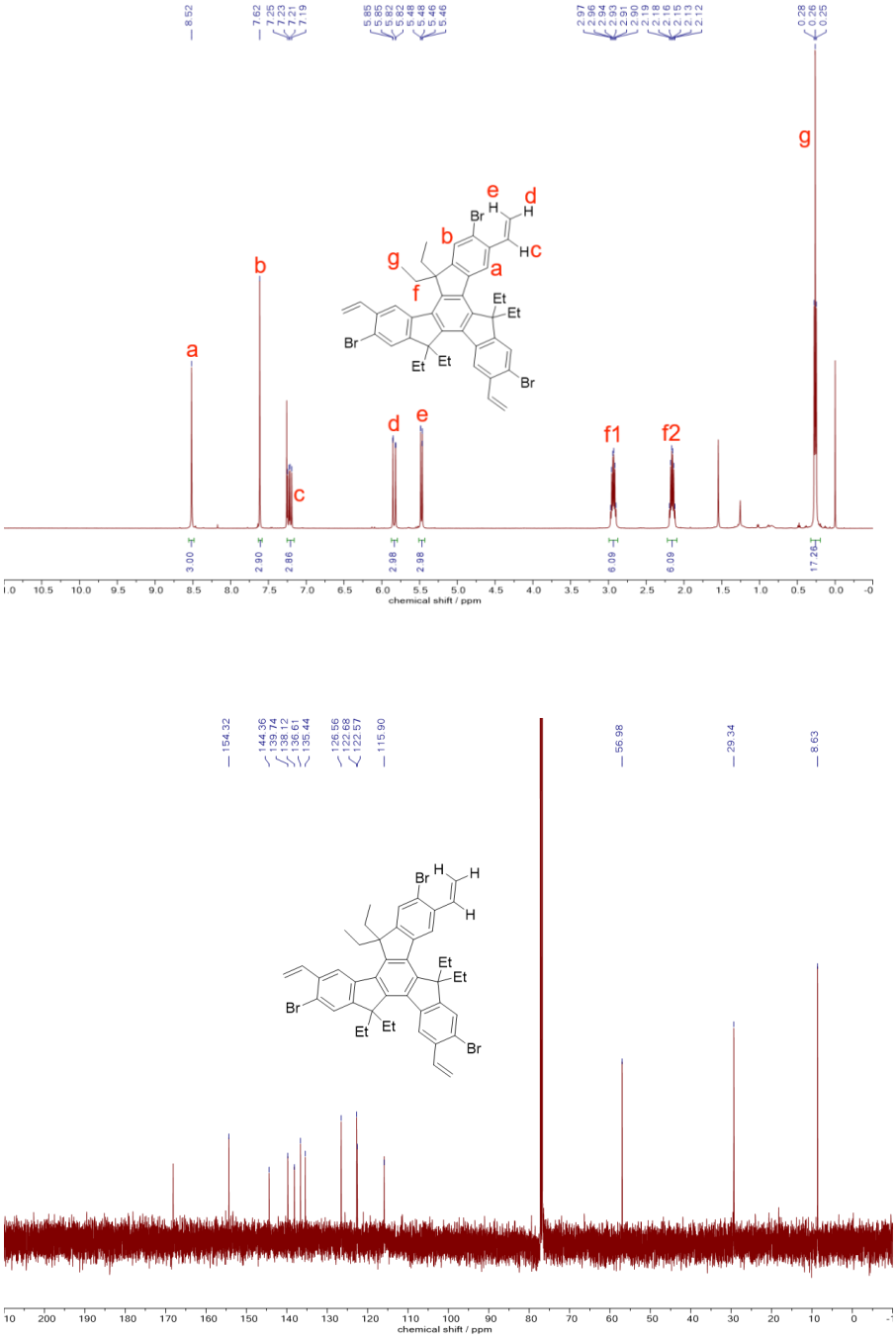

Figure 2.33. ^{1}H (500 MHz, $CDCl_3$, RT) and ^{13}C NMR (125 MHz, $CDCl_3$, RT) of **3.** Reproduced with permission from Fang et al.[146] Copyright 2020 American Chemical Society.

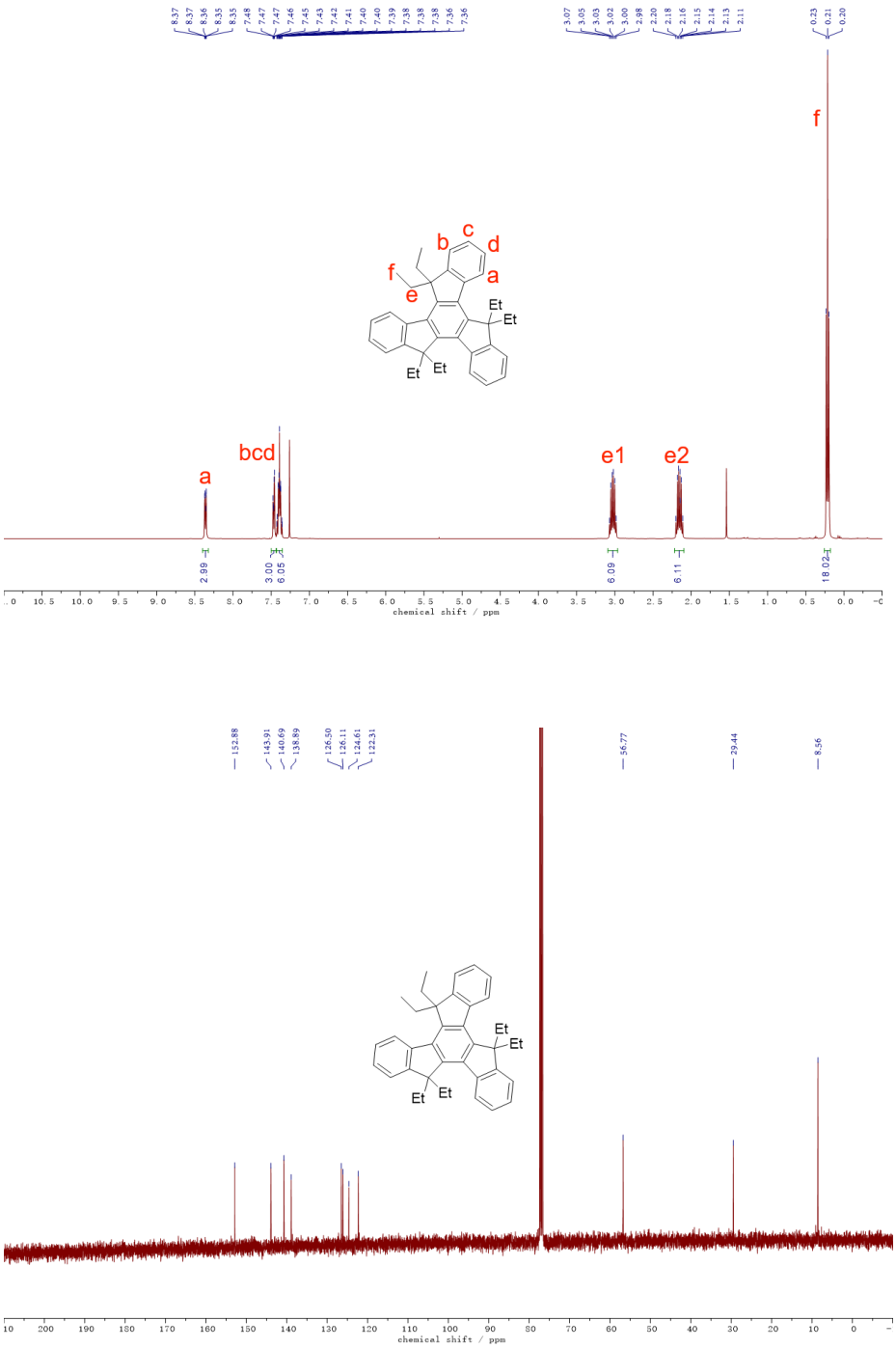

Figure 2.34. ^{1}H (500 MHz, $CDCl_3$, RT) and ^{13}C NMR (125 MHz, $CDCl_3$, RT) of **S5.** Reproduced with permission from Fang et al.[146] Copyright 2020 American Chemical Society.

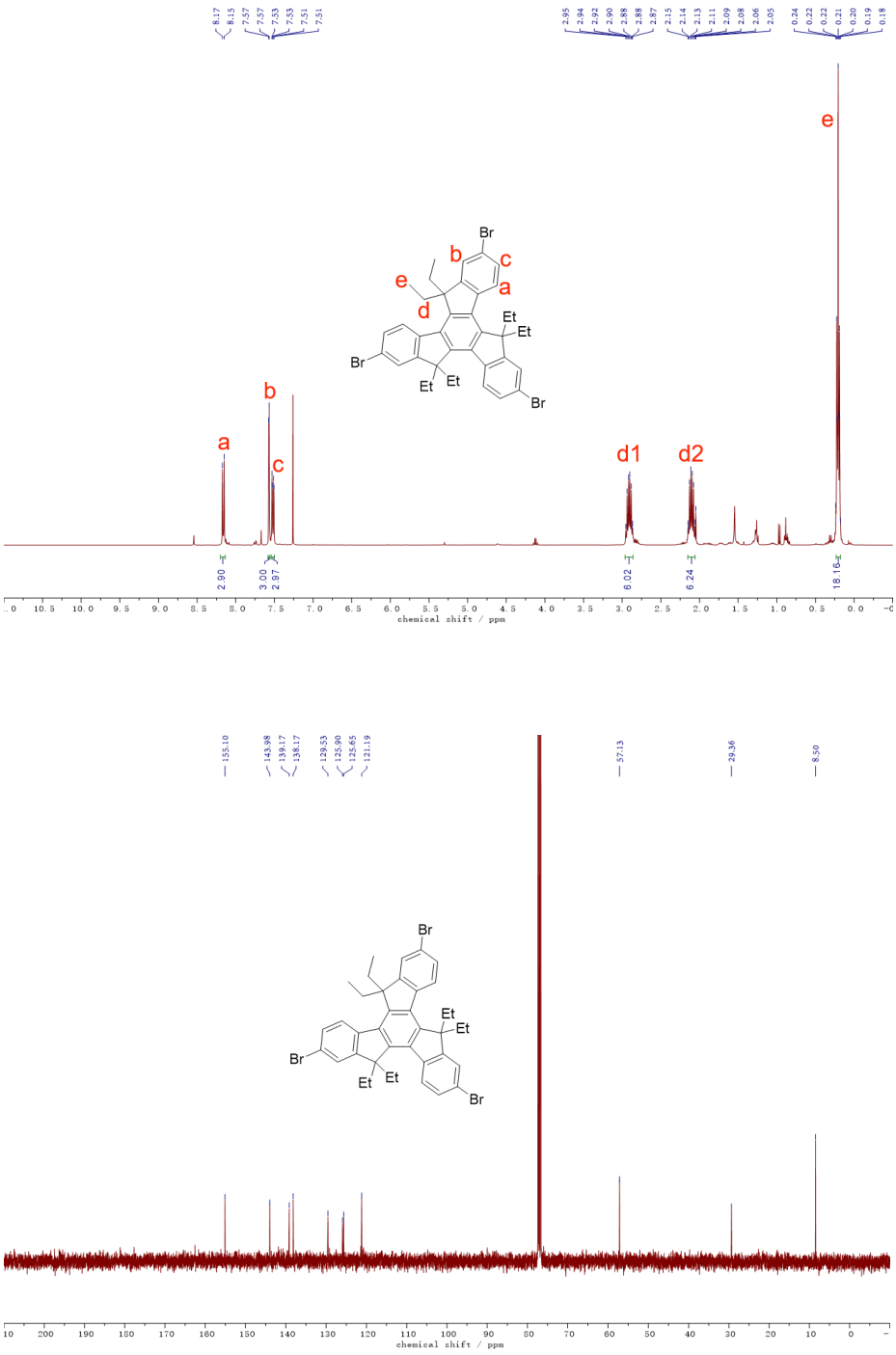

Figure 2.35. ^{1}H (500 MHz, $CDCl_3$, RT) and ^{13}C NMR (125 MHz, $CDCl_3$, RT) of **5.** Reproduced with permission from Fang et al.[146] Copyright 2020 American Chemical Society.

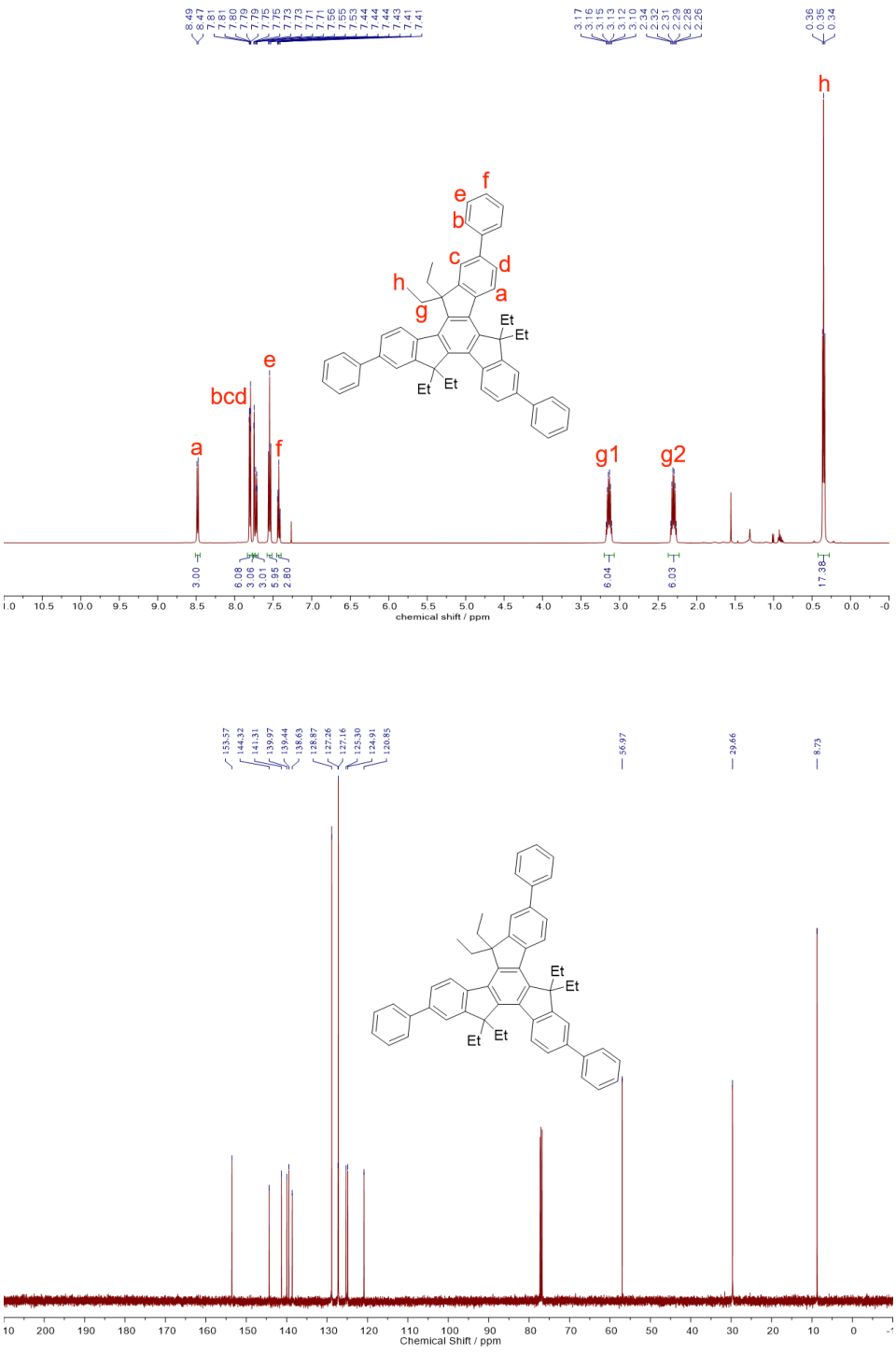

Figure 2.36. ^{1}H (500 MHz, $CDCl_3$, RT) and ^{13}C NMR (125 MHz, $CDCl_3$, RT) of **S6.** Reproduced with permission from Fang et al.[146] Copyright 2020 American Chemical Society.

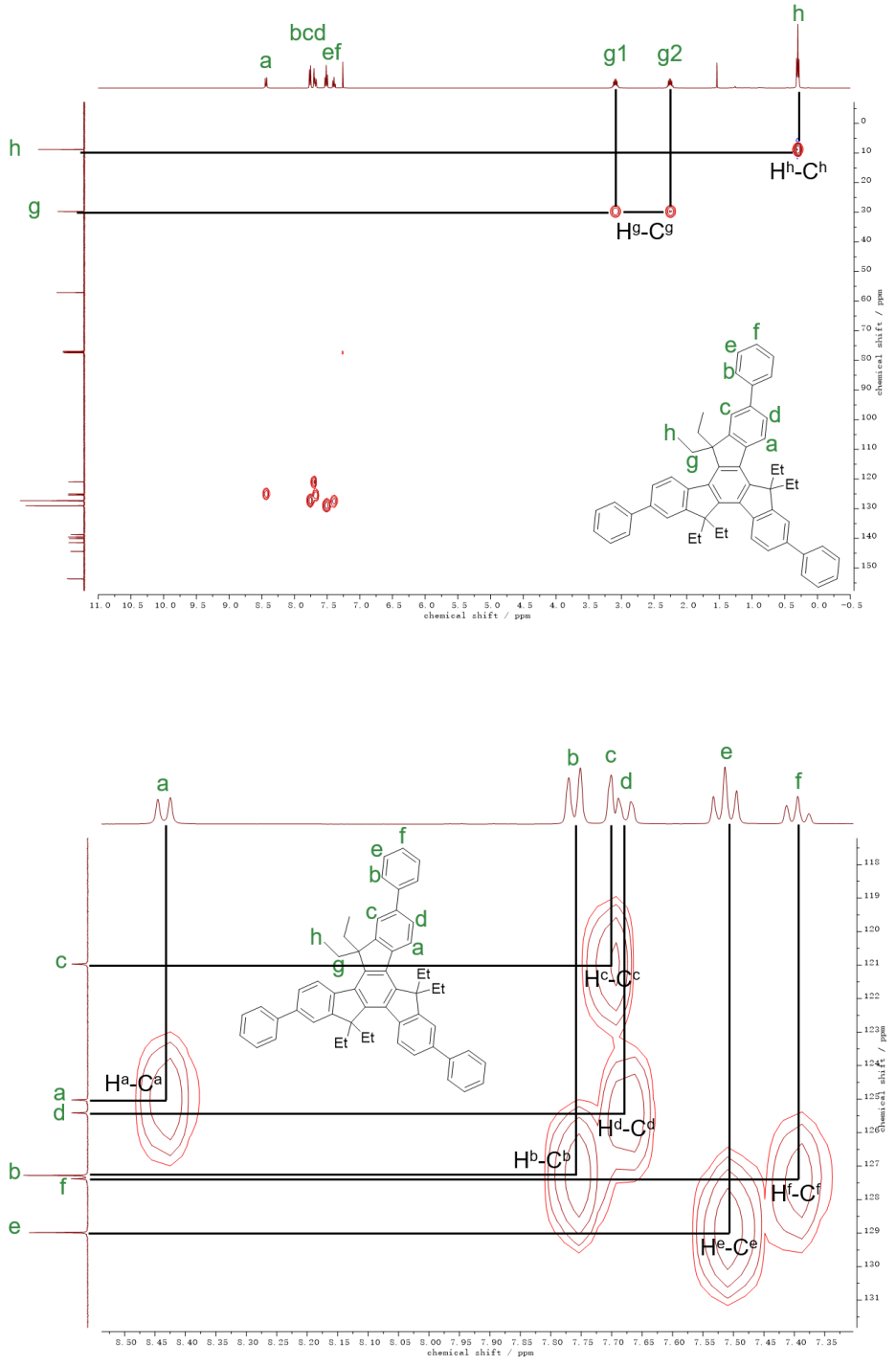

Figure 2.37. ^{1}H-^{13}C HSQC spectrum of **S6** (400 MHz, $CDCl_3$, RT).
Reproduced with permission from Fang et al.[146] Copyright 2020 American Chemical Society.

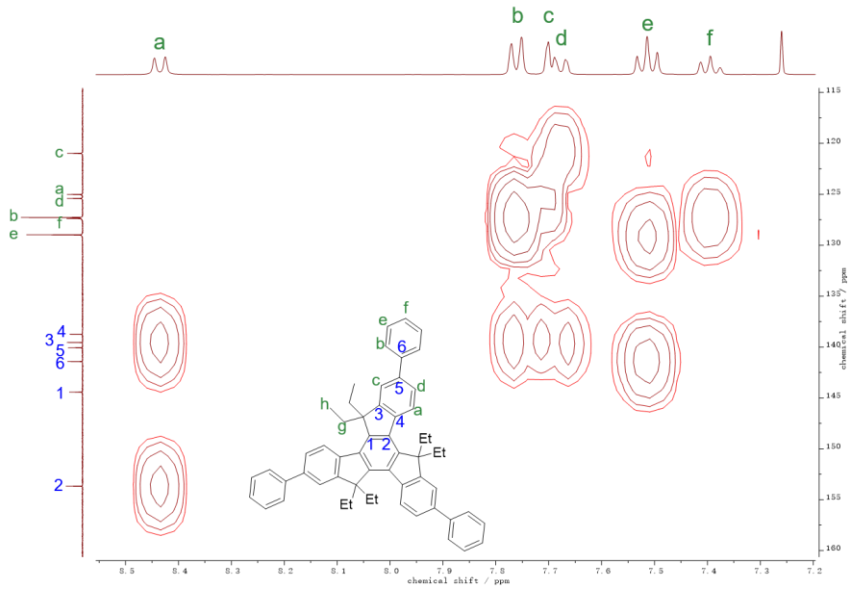

Figure 2.38. Partial ^{1}H-^{13}C HMBC spectrum of **S6** (400 MHz, $CDCl_3$, RT). Reproduced with permission from Fang et al.[146] Copyright 2020 American Chemical Society.

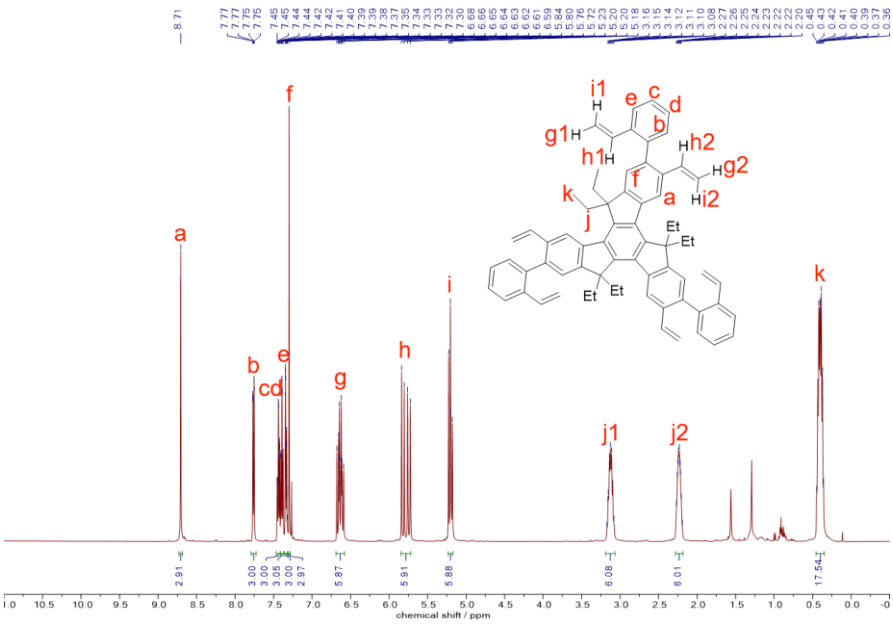

Figure 2.39. ^{1}H (500 MHz, $CDCl_3$, RT) and ^{13}C NMR (125 MHz, $CDCl_3$, RT) of **7.** Reproduced with permission from Fang et al.[146] Copyright 2020 American Chemical Society.

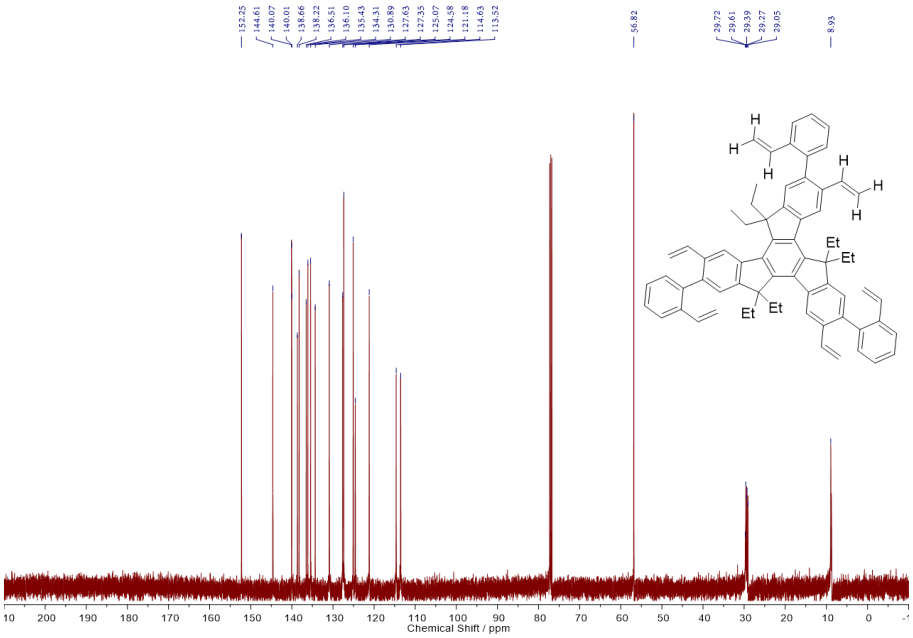

Figure 2.39. Continued.

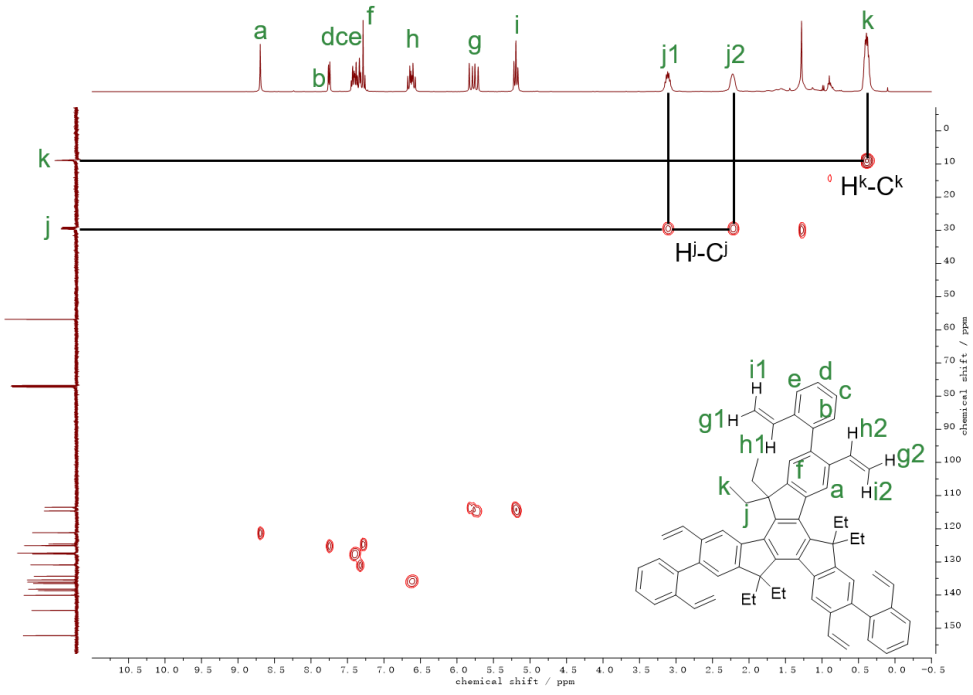

Figure 2.40. ^{1}H-^{13}C HSQC spectrum of **7** (400 MHz, $CDCl_3$, RT).
Reproduced with permission from Fang et al.[146] Copyright 2020 American Chemical Society.

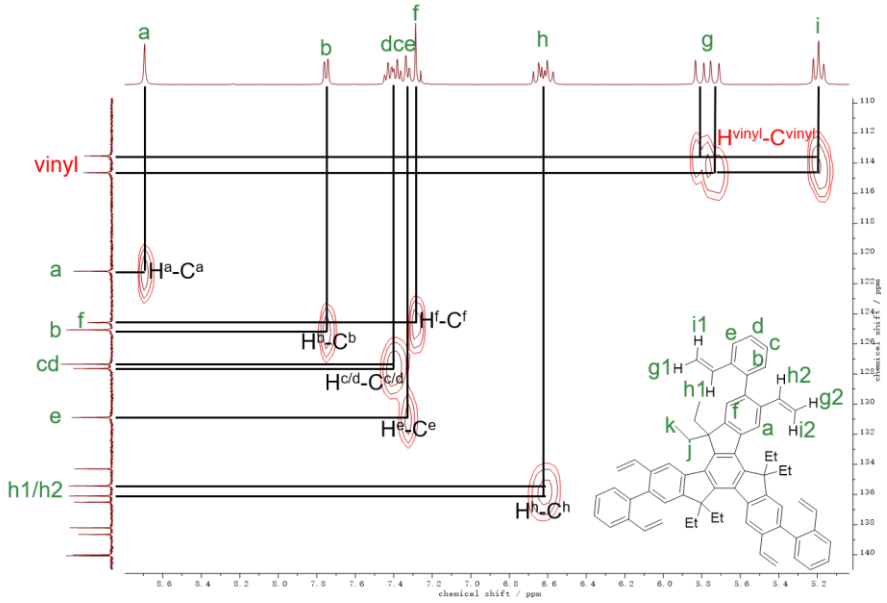

Figure 2.40. Continued.

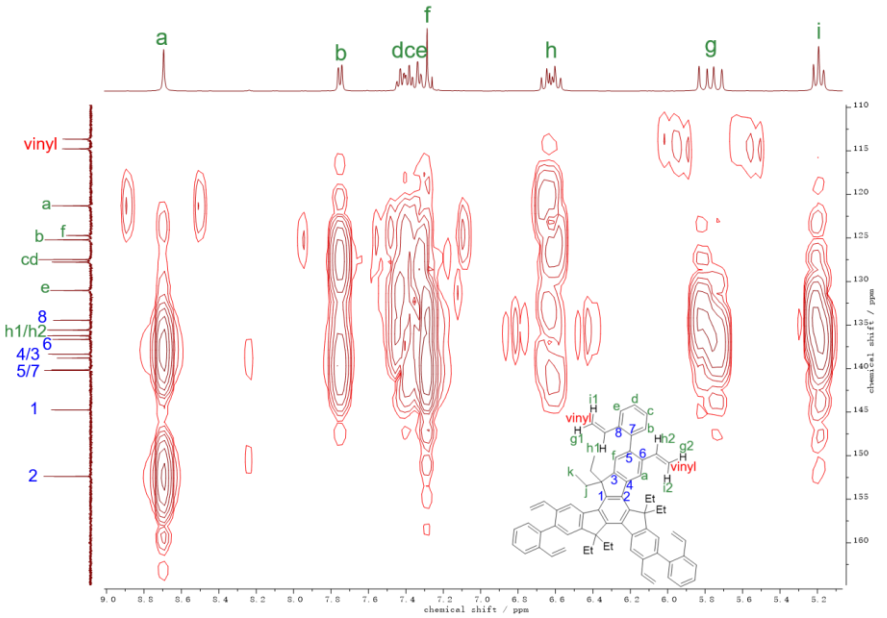

Figure 2.41. Partial ^{1}H-^{13}C HMBC spectrum of **7** (400 MHz, $CDCl_3$, RT).
Reproduced with permission from Fang et al.[146] Copyright 2020 American Chemical Society.

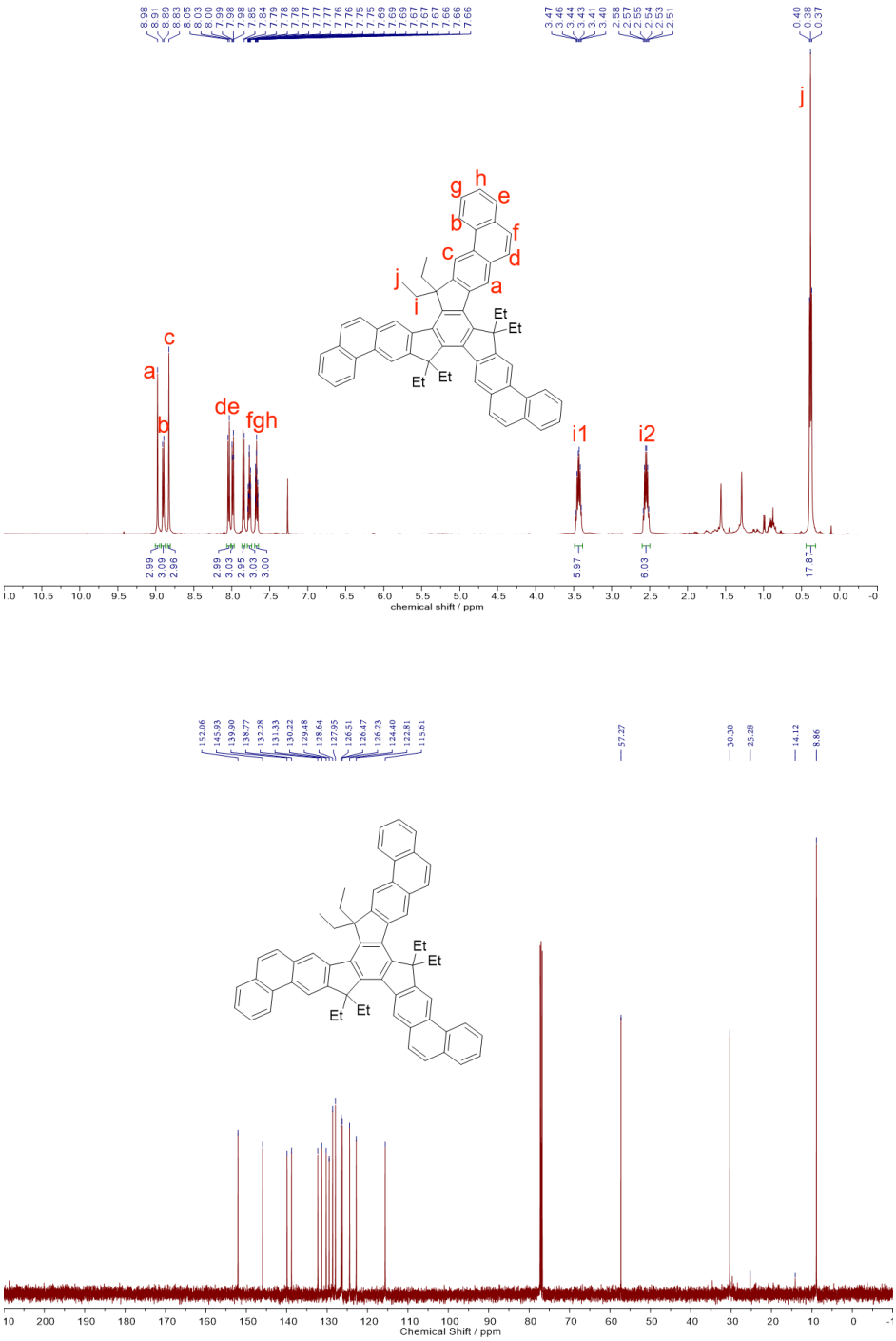

Figure 2.42. ^{1}H (500 MHz, $CDCl_3$, RT) and ^{13}C NMR (125 MHz, $CDCl_3$, RT) of **8.** Reproduced with permission from Fang et al.[146] Copyright 2020 American Chemical Society.

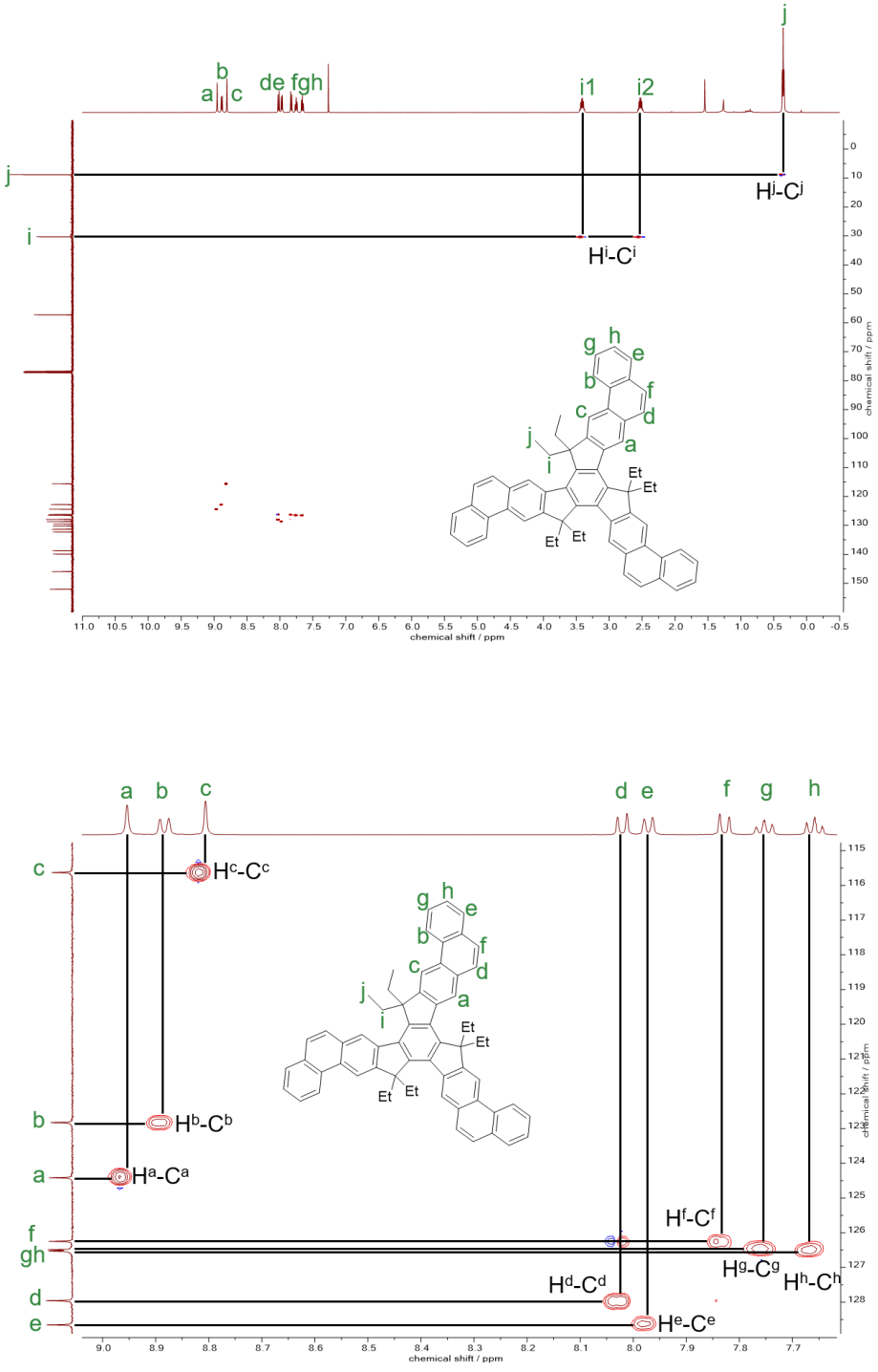

Figure 2.43. ^{1}H-^{13}C HSQC spectrum of **8** (400 MHz, $CDCl_3$, RT).
Reproduced with permission from Fang et al.[146] Copyright 2020 American Chemical Society.

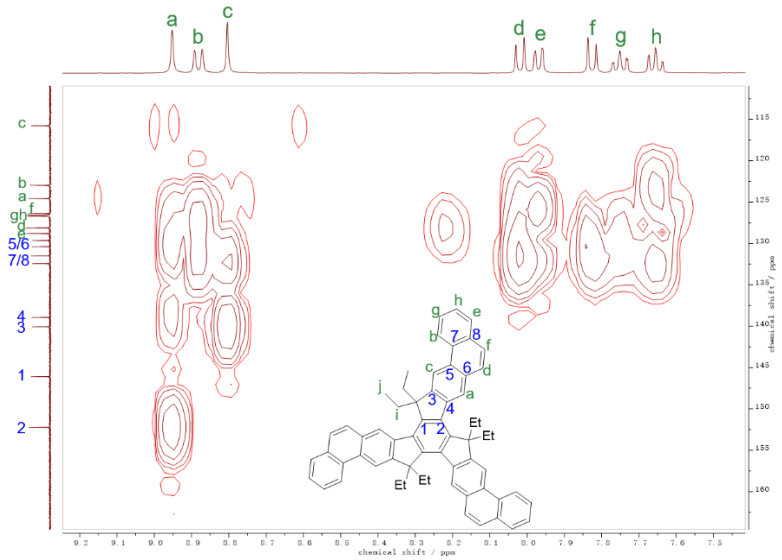

Figure 2.44. Partial ^{1}H-^{13}C HMBC spectrum of **8** (400 MHz, $CDCl_3$, RT).
Reproduced with permission from Fang et al.[146] Copyright 2020 American Chemical Society.

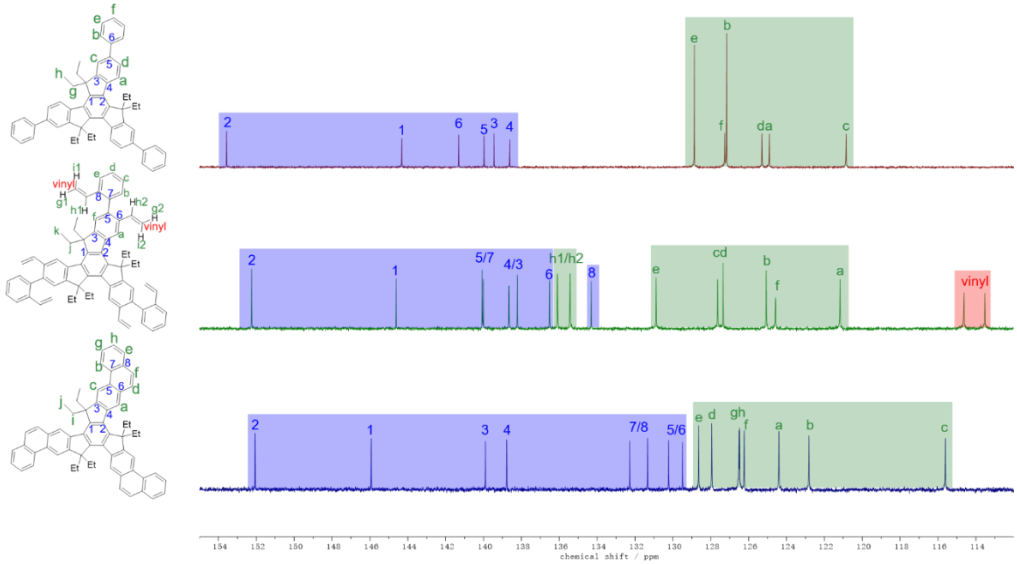

Figure 2.45. ^{13}C NMR stacking of **S6** (top), **7** (middle), and **8** (bottom) (125 MHz, $CDCl_3$, RT).
Signals were assigned with the help of HSQC and HMBC spectra (**Figure 2.37-2.38**, **2.40-2.41**, **2.43-2.44**) and color coded to distinguish =C< (blue), =CH- (green), and $=CH_2$ (red).
Reproduced with permission from Fang et al.[146] Copyright 2020 American Chemical Society.

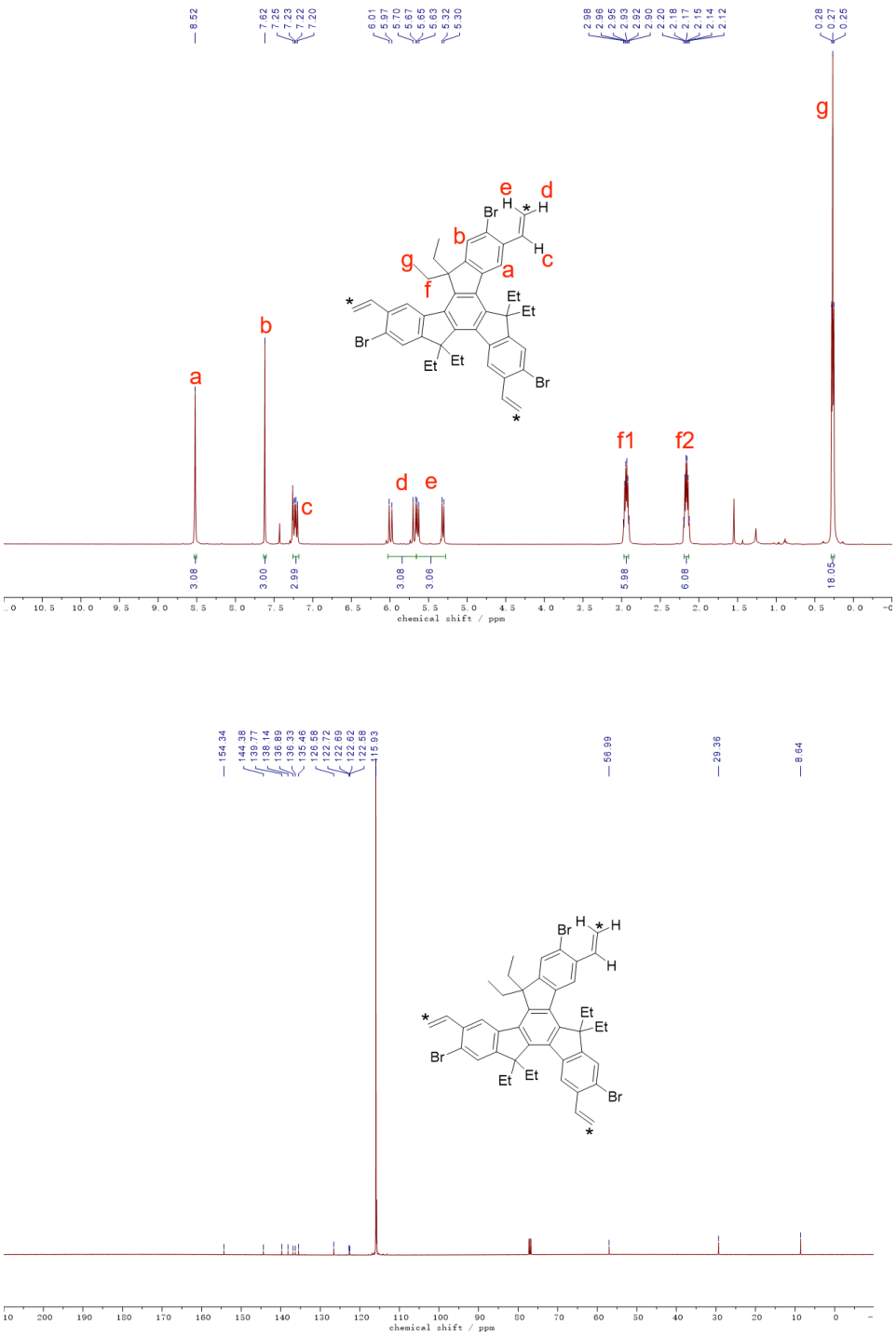

Figure 2.46. ^{1}H (500 MHz, $CDCl_3$, RT) and ^{13}C NMR (125 MHz, $CDCl_3$, RT) of **3-^{13}C.** Reproduced with permission from Fang et al.[146] Copyright 2020 American Chemical Society.

CHAPTER III

ENTROPICALLY FAVORABLE GAS ADSORPTION INDUCED BY RIGID LADDER TYPE BACKBONE*

3.1 Introduction

Adsorbed Natural Gas (ANG) in highly porous materials has emerged as an efficient and safe technology for energy storage. In order to make ANG competitive against commercial fuels, high methane storage capacity at room temperature is urgently desired.[177-182] Toward this goal, tremendous achievements have been made in increasing the surface area of various methane-adsorbing materials.[20, 48] However, an ultrahigh surface area surpassing the optimal range of 2500 - 3000 m^2 g^{-1} often results in a low material density and lowers the volumetric capacity, which is critical for volume-sensitive applications, such as powering personal vehicles.[183] Therefore, enhancing the overall methane storage capacity by increasing the uptake *per unit surface area* becomes an important strategy for practical ANG applications. To date, great research attention has been devoted to increasing the *enthalpy* gain of the methane adsorption process by strengthening the interactions between the adsorbent and methane molecules.[184] However, enthalpic interactions could also potentially lead to incomplete desorption of methane in low-pressure region, impacting the deliverable ANG capacity.[185] An alternative approach to enhance methane uptake per unit surface area is decreasing the *entropy* penalty of

*Reprinted with permission from "Rigid Ladder-Type Porous Polymer Networks for Entropically Favorable Gas Adsorption" Che, S.; Pang, J.; Kalin, A. J.; Wang, C.; Ji, X.; Lee, J.; Cole, D.; Li, J.-L.; Tu, X.; Zhang, Q.; Zhou, H.-C.; Fang, L. *ACS Materials Lett.* **2020**, *2*, 49. Copyright 2020 American Chemical Society.

adsorption, which is often significant at room temperature. However, such entropic approach has rarely been employed so far.[186]

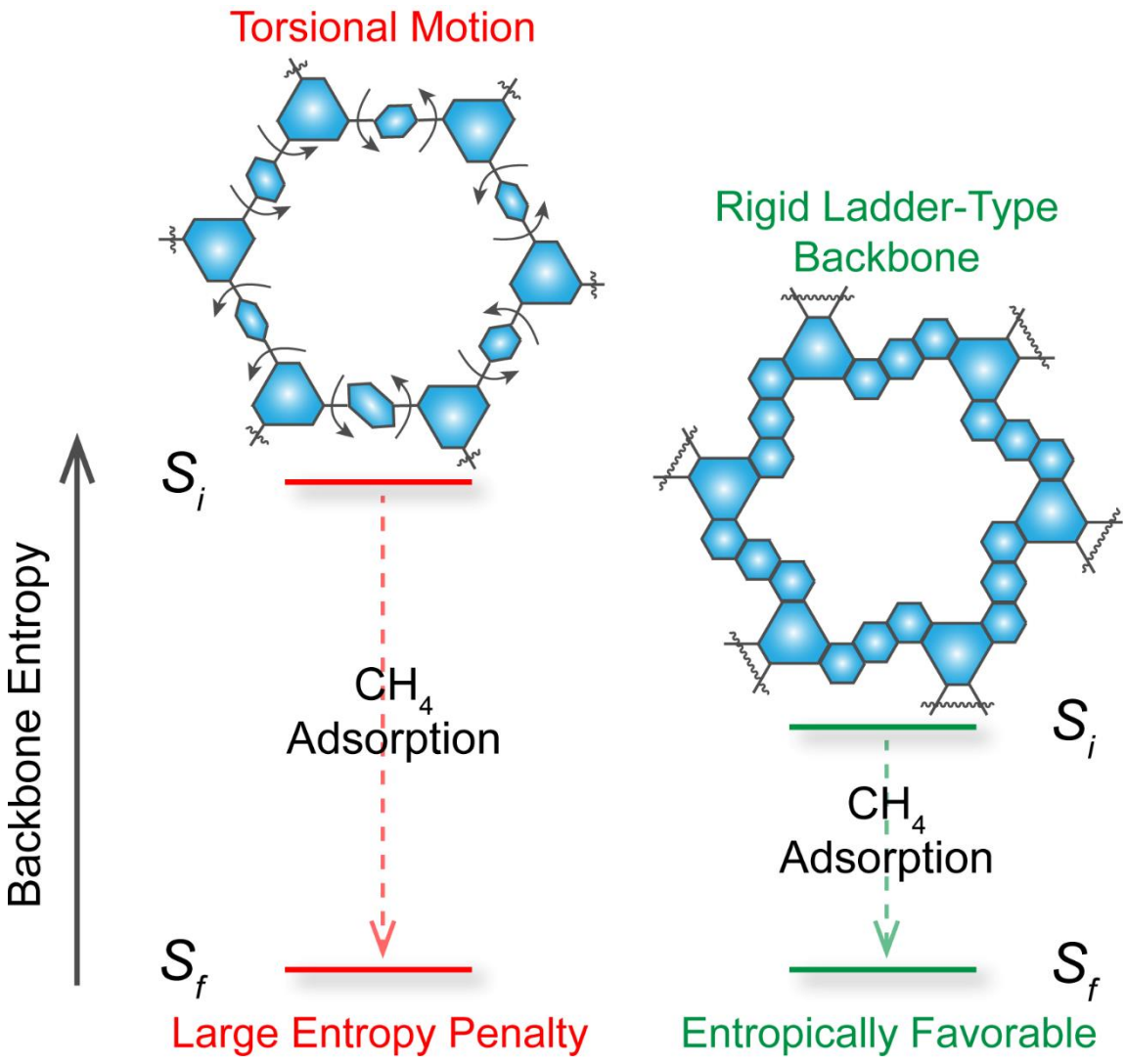

Figure 3.1. Schematic demonstration of entropically favorable methane adsorption process of **PLAN.**
Reproduced with permission from Fang et al.[146] Copyright 2020 American Chemical Society.

We envisioned that lowering the initial entropy of porous materials could be an efficient strategy to reduce the overall adsorption entropy penalty. (**Figure 3.1**) This goal

can be achieved by locking the conformation of the organic backbone via the installation of an additional strand of bonds to afford a ladder-type structure.[93] Various synthetic approaches to linear ladder polymers, including a number of scalable and inexpensive ones, have been established in the past three decades.[45, 56, 68, 74] A few porous materials with such ladder-type backbones have been reported.[100, 116, 118, 137, 187] Preliminary results indeed showed that extended ladder-type ligands in metal-organic frameworks contributed to higher methane storage performance, although these effects were attributed to enthalpic effects.[188, 189] Herein, we report the proof of the aforementioned concept on a porous ladder polymer network (**PLAN**) model system, in which a significantly less negative entropy penalty was observed during methane adsorption, leading to a remarkably high methane uptake per unit surface area.

3.2 High-pressure Methane Adsorption

High-pressure methane uptake and release of **PPN-Ref**, **PPN-Precursor**, and **PLAN** (up to 95 bar) was investigated to test the hypothesis regarding the entropically favorable adsorption with a ladder-type backbone. All three materials exhibited extremely small residue methane adsorption at low pressure and no significant hysteresis during the uptake/release cycles. The continuous increase of methane uptake at high pressure was attributed to swelling of the amorphous polymer network. **PLAN** showed a much higher methane uptake than **PPN-Ref** and **PPN-Precursor** (**Figure 3.2a**) at 298 K, partially because of its higher BET surface area. Although the absolute value is still not comparable with the top-performing materials, such as MOF-210,[190] NU-111,[177] KPOP-2,[48] which

possess much higher surface areas and/or enthalpically driven methane binding sites, PLAN exhibited a strikingly high methane uptake capacity *per unit surface area*. To contextualize these data, literature reports of porous hydrocarbons and covalent-organic

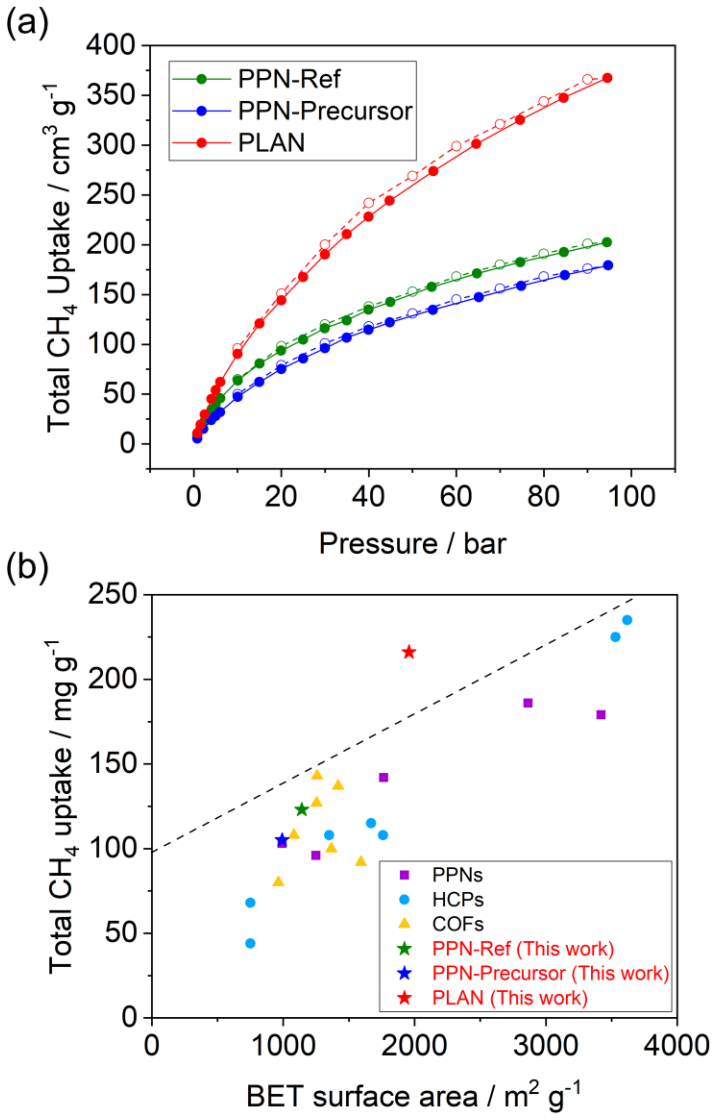

Figure 3.2. (a) Total methane uptakes and releases of **PPN-Ref**, **PPN-Precursor**, and **PLAN** at 298 K. Filled symbols: adsorption; Open symbols: desorption (b) The plot of total methane uptakes (65 bar, 298 K) versus BET surface areas of porous organic polymers without enthalpically favorable interactions with me-thane, including **PLAN**, COFs, and porous hydrocarbons.

Reproduced with permission from Fang et al.[146] Copyright 2020 American Chemical Society.

frameworks (COFs) without enthalpically favorable interactions with methane were identified. Their methane uptake capacities at 65 bar were plotted *vs* BET surface areas (**Figure 3.2b**),[18, 24, 34, 191, 192] showing a positive correlation and a clear "upper bound". These data indicated the persistent challenge of achieving a high methane uptake in porous materials without overly increasing their surface areas or introducing enthalpically favorable interactions. The data point of **PLAN**, however, appeared above the upper bound on this chart. With a surface area of 1958 $m^2 g^{-1}$, **PLAN** reached a methane uptake of 302 $cm^3 g^{-1}$ (216 mg g^{-1}) at 65 bar, comparable to the capacities of materials with almost doubled BET surface areas (> 3500 $m^2 g^{-1}$).[191] The deliverable capacity from 5 to 65 bar also showed a similar trend, with **PLAN** demonstrating highest working capacity *per unit surface area* among these materials (**Table 3.1**). This result demonstrated a significant advantage of using ladder-type backbones to enhance gas storage capacity without excessively increasing surface area.

3.3 Thermodynamic Analysis and Discussion

The unusual methane uptake performance of **PLAN** was attributed to a more favorable entropy change during adsorption. To elucidate the underlining mechanism, high-pressure methane adsorption measurements of **PPN-Ref**, **PPN-Precursor**, and **PLAN** were conducted at 273 K, 298 K, and 323 K (**Figure 3.3a**, **3.4**). It is noteworthy

that, upon raising the temperature from 298 to 323 K, adsorption capacity of **PLAN** remained at high values without much declination (*e.g.*, 301 to 286 cm g^{-1} at 65 bar),

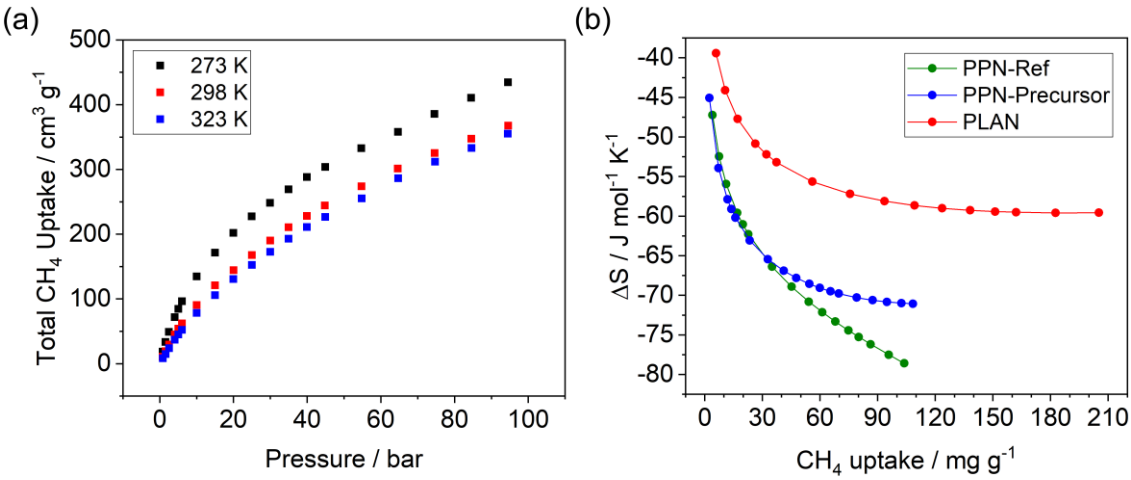

Figure 3.3. (a) Total CH_4 uptakes of **PLAN** at 273 K, 298 K, and 323 K. (b) Entropy changes derived from variable temperature high-pressure methane adsorption isotherms of **PPN-Ref**, **PPN-Precursor**, and **PLAN**.
Reproduced with permission from Fang et al.[146] Copyright 2020 American Chemical Society.

From these data, enthalpic and entropic contributions to the adsorption thermodynamics were derived (See Experimental Section) and plotted versus methane uptake.[193] **PLAN** demonstrated a significantly less negative entropy change upon the adsorption of methane molecules compared to **PPN-Ref** and **PPN-Precursor** (**Figure 3.3b**). Such difference increased at higher methane loading, reaching 19.8 J mol^{-1} K^{-1} at 100 mg g^{-1} of methane uptake. In contrast, as expected, the enthalpy change (heat of adsorption) remained similar for three porous materials (**Figure 3.5**) because none of them possesses any specific binding site to methane. The much more favorable adsorption entropy change for **PLAN** was originated from its lower initial entropy of the backbone (S_i). In all three materials, after high-pressure methane adsorption, the torsional motion of the backbone was

restricted because of the accommodation of large amount of gas molecules inside the pores, leading to a low final backbone entropy (S_f). The difference, however, came from S_i: Compared to the ladder-type rigid backbone of **PLAN** with a locked conformation, the backbones of **PPN-Ref**, **PPN-Precursor**, and most reported porous organic materials have a higher degree of freedom due to the possible torsional rotation and hence higher S_i. Consequently, **PLAN** exhibited constantly less adsorption entropy penalty than **PPN-Ref** and **PPN-Precursor**, thus a more thermodynamically favorable methane uptake process.

3.4 Conclusion

In conclusion, we present here the proof of concept of using ladder-type backbone to achieve more entropically favorable methane adsorption on PPNs. Although the absolute uptake value is not as high as the top-performing materials reported, it exhibited a remarkably high methane uptake per unit surface area without the introduction of active methane binding sites. Thermodynamic investigation revealed a significantly smaller entropy penalty of **PLAN** upon high-pressure methane uptake compared to its non-ladder-type counterpart. We envision that this entropic approach can be widely employed once integrated with the scalable synthetic methods for ladder polymers. It will serve as a promising strategy to further enhance methane storage capacity of general porous materials, including MOFs, COFs, PPNs, etc., with the following advantages. (1) It adds an orthogonal way to multiply the capacity besides the strategies of increasing surface area and increasing heat of adsorption. (2) Without introducing methane-binding functional sites, this approach benefits the high-pressure adsorption without undesired increase of the

low-pressure adsorption, thus enhancing overall deliverable working capacity. (3) The less entropy penalty renders a less temperature-sensitive methane uptake capacity, making it attractive for high temperature applications.

3.5 Experimental Section

High-pressure CH_4 adsorption isotherm measurements were carried out on an HPVA II high pressure volumetric analyzer at variable temperatures. Prior to all gas adsorption measurements, the samples were degassed for 10 h at 120 ^oC. Both isosteric heats of adsorption (Q_{st}) and Entropy change (ΔS) were calculated as functions of the methane uptakes by comparing the high-pressure total methane adsorption isotherms up to 65 bar at 273 K, 298 K, and 323 K. These data were modeled with a virial-type expression composed of temperature independent parameters a_i and b_i (Equation S1).[186, 193, 194] Q_{st} and ΔS were then calculated from the fitting parameters using Equation S2 and S3, respectively (**Figure 3.3b, 3.5**), where P is the pressure of methane gas, N is the amount adsorbed, T is the temperature, R is the universal gas constant, and m and n determine the number of terms required to adequately describe the isotherms.

$$lnP = lnN + \frac{1}{T}\sum_{i=0}^{m} a_i N^i + \sum_{i=0}^{n} b_i N^i \qquad (Equation\ S1)$$

$$Q_{st} = -R\sum_{i=0}^{m} a_i N^i \qquad (Equation\ S2)$$

$$\Delta S = R(lnP_0 - lnN - \sum_{i=0}^{n} b_i N^i) \qquad (Equation\ S3)$$

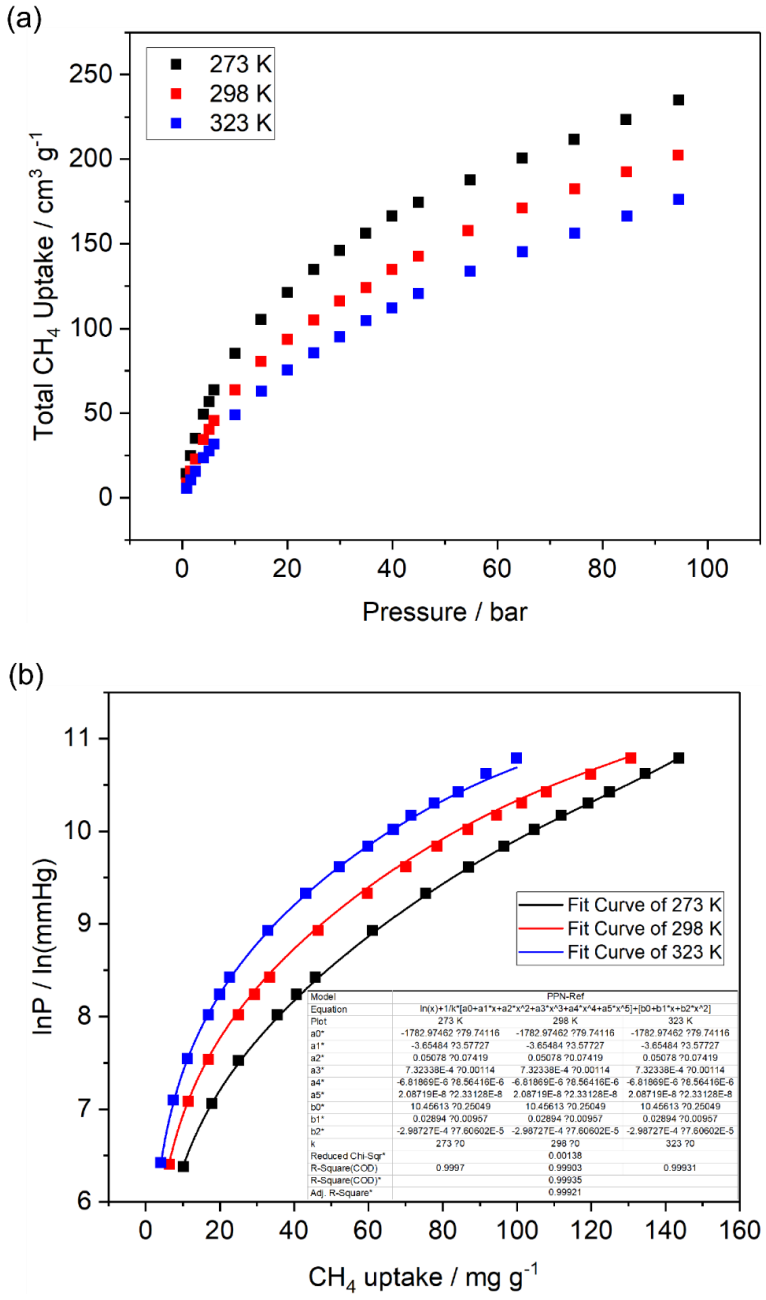

Figure 3.4. Total CH_4 uptakes of **PPN-Ref** (a), **PPN-Precursor** (c), and **PLAN** (e) at 273 K, 298 K, and 323 K. Fit curves with these data into Equation S1 of **PPN-Ref** (b), **PPN-Precursor** (d), and **PLAN** (f).
Inset: Temperature independent parameters a_i *(a_0-a_5)* and b_i *(b_0-b_2)*.
Reproduced with permission from Fang et al.[146] Copyright 2020 American Chemical Society.

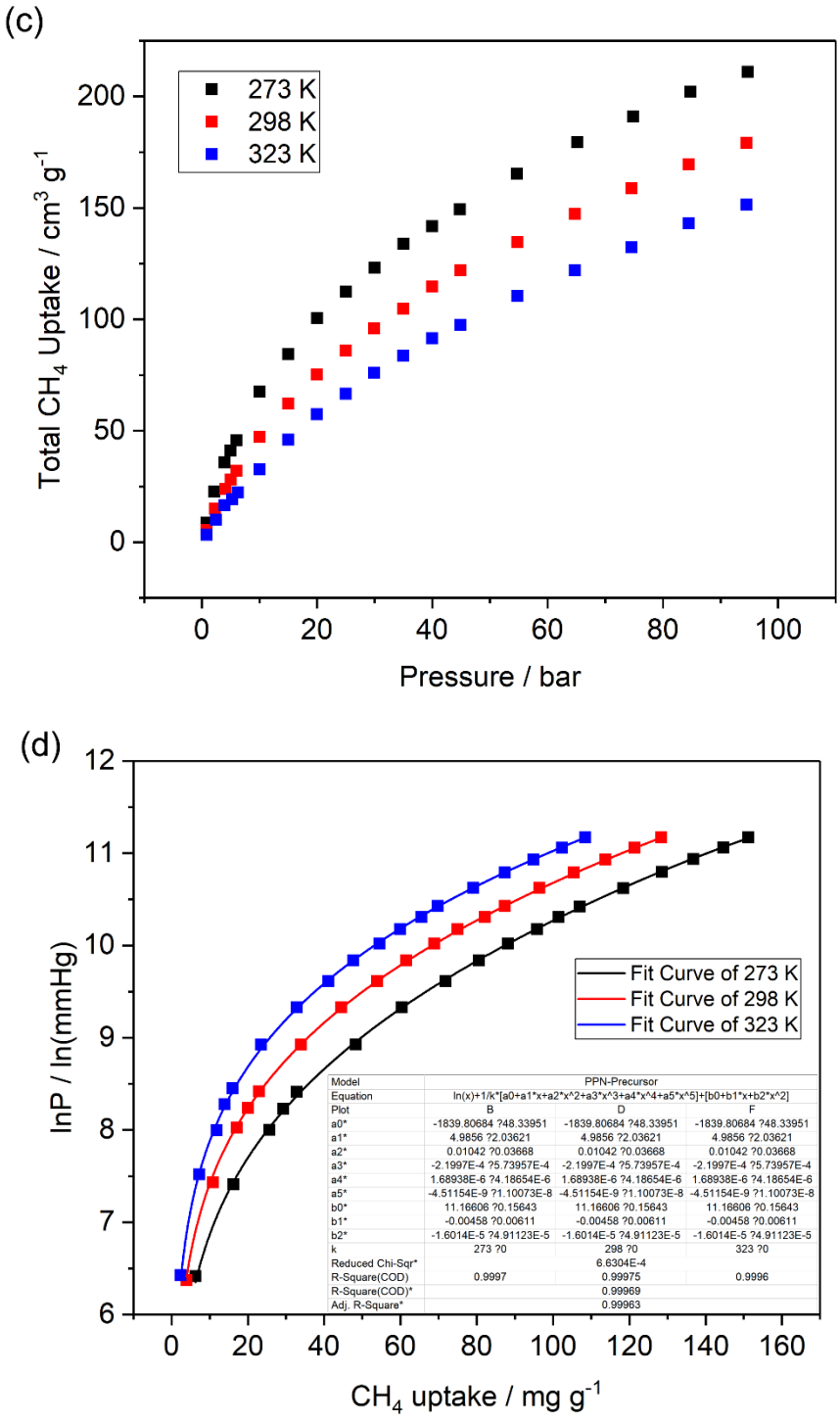

Figure 3.4. Continued.

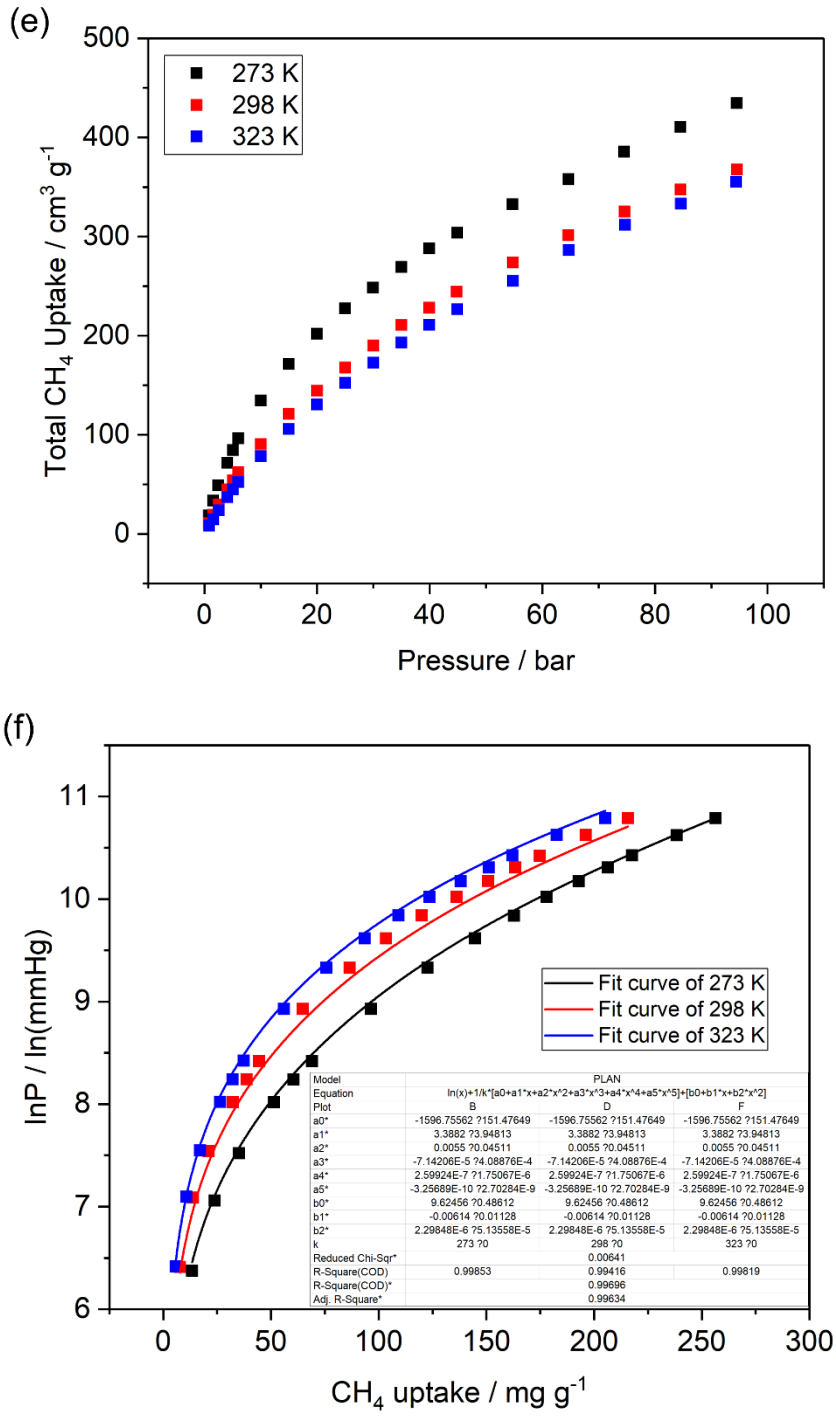

Figure 3.4. Continued.

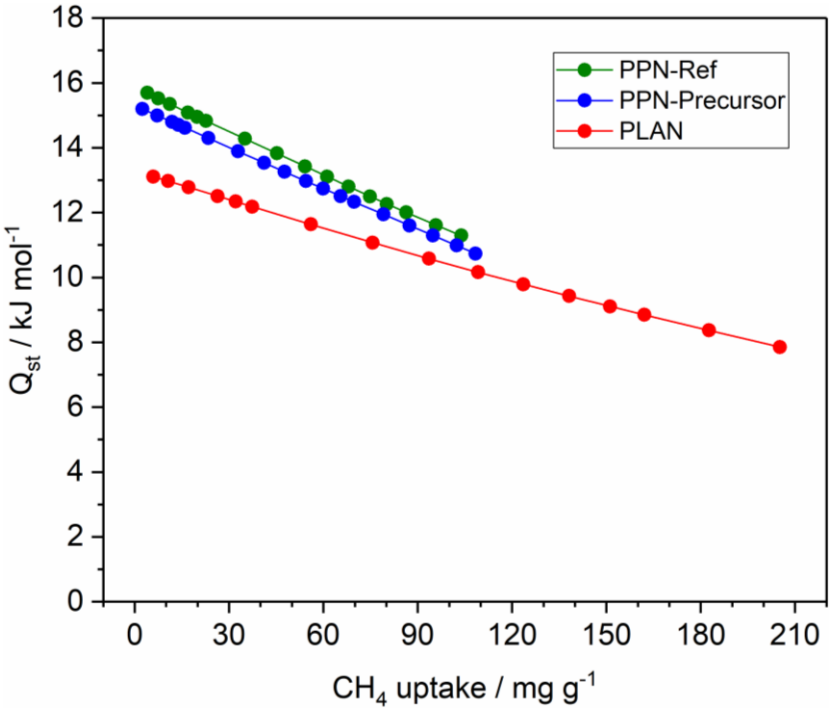

Figure 3.5. Methane heat of adsorption (Q_{st}) derived from variable temperature high-pressure methane adsorption isotherms of **PPN-Ref**, **PPN-Precursor**, and **PLAN**. Reproduced with permission from Fang et al.[146] Copyright 2020 American Chemical Society.

Table 3.1. BET surface areas, total CH_4 uptakes at 5 bar and 65 bar, 298 K, and working capacities (5-65 bar) of reported COFs and porous hydrocarbons, including PPNs, HCPs, and **PLAN**.

Category	Name	BET Surface Area/ $m^2\ g^{-1}$	Total CH_4 Uptake / mg g^{-1} at 5 bar	Total CH_4 Uptake / mg g^{-1} at 65 bar	Working Capacity / mg g^{-1} 5-65 bar	Ref
PPN	PPN-1	1249	16	96	80	[18]
PPN	PPN-2	1764	30	142	112	[18]
PPN	PPN-3	2864	38	186	148	[194]
PPN	PPN-13	3420	22	179	157	[24]
PPN	PPN-Precursor	992	18	103	85	This work
PPN	PPN-Ref	1030	18	90	72	This work
PPN	PPN-Ref-Tt	1142	25	123	98	This work
COF	COF-1	750	23	44	21	[191]
COF	COF-5	1670	29	115	86	[191]
COF	COF-6	750	25	68	43	[191]
COF	COF-8	1350	29	108	79	[191]
COF	COF-10	1760	22	108	86	[191]
COF	COF-102	3620	38	235	197	[191]
COF	COF-103	3530	38	225	187	[191]
HCP	HCP-3	963	28	80	52	[34]
HCP	HCP-4	1366	32	100	68	[34]
HCP	RUB	1258	24	143	119	[192]
HCP	STIL	1254	21	127	106	[192]
HCP	HPPh	1082	20	108	88	[192]
HCP	SPBF	1418	32	137	105	[192]
HCP	TRIP	1592	36	164	128	[192]
PLAN	PLAN	1542	30	174	144	This work
PLAN	PLAN-Tt	1958	38	216	178	This work

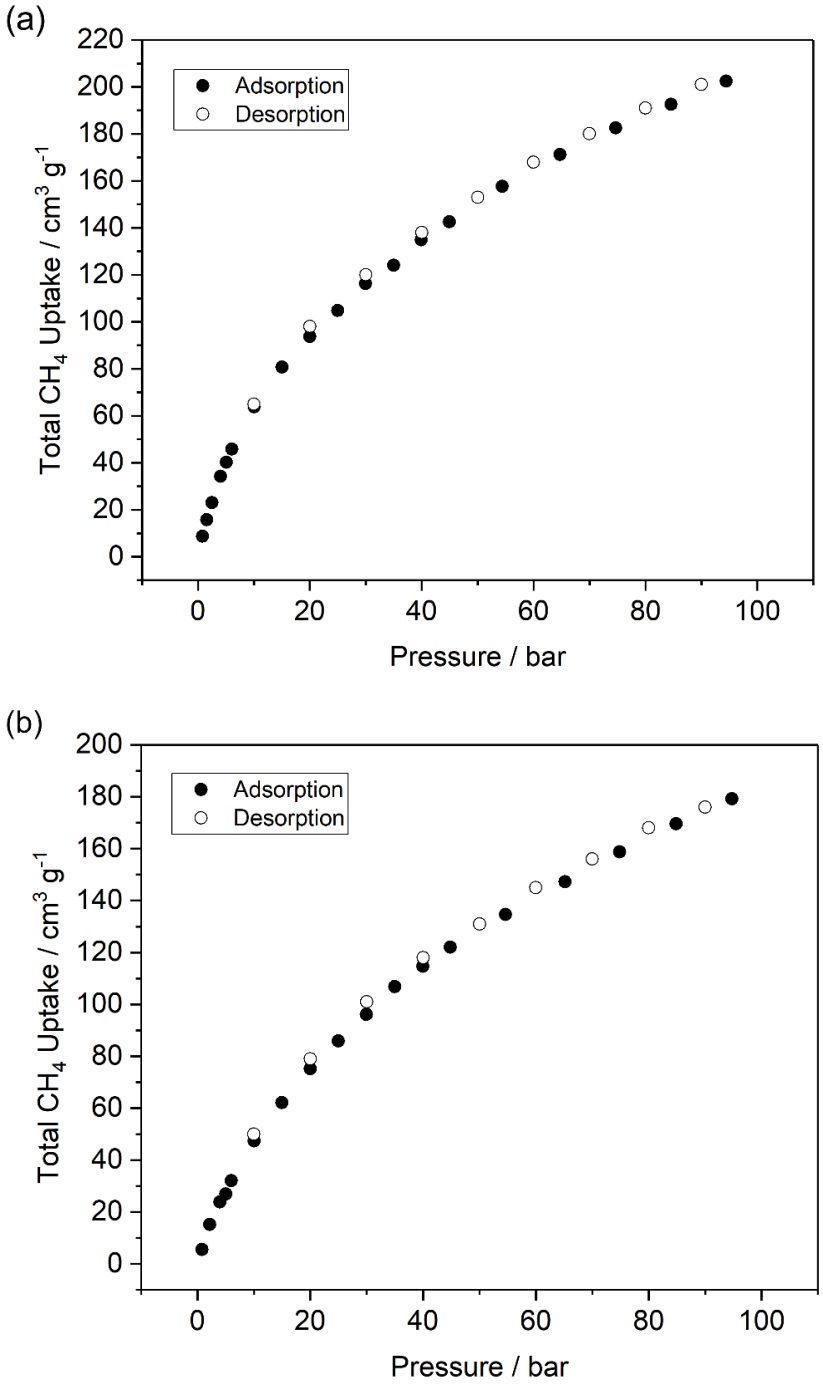

Figure 3.6. Total CH_4 adsorption and desorption of **PPN-Ref** (a), **PPN-Precursor** (b), and **PLAN** (c) at 298 K.
Reproduced with permission from Fang et al.[146] Copyright 2020 American Chemical Society.

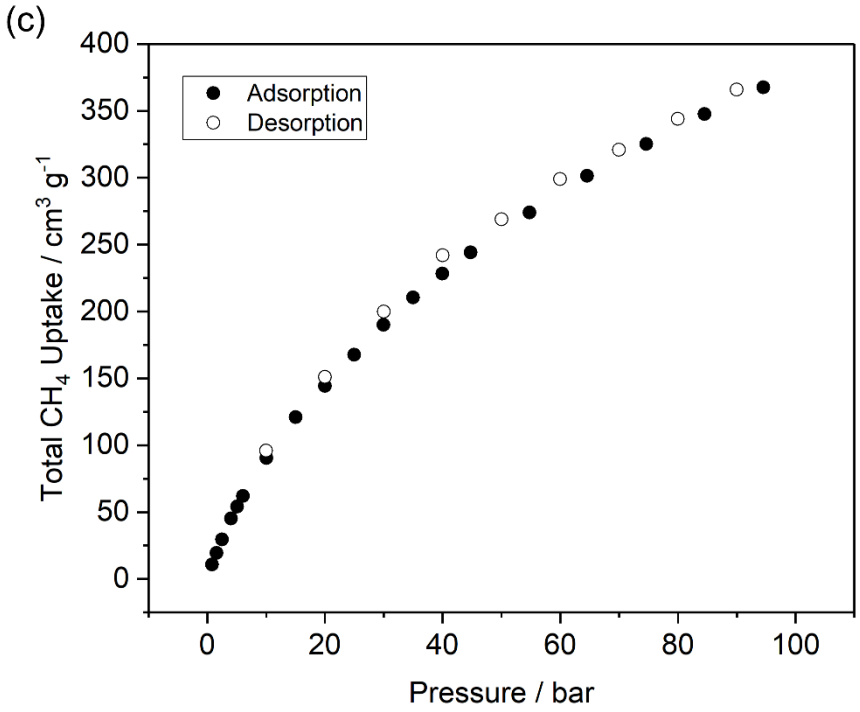

Figure 3.6. Continued.

CHAPTER IV

POROUS GRAPHITIC CARBON CONSTRUCTED BY ONE-STEP POLYMERIZATION AND GRAPHITIZATION

4.1 Introduction

Porous graphitic carbon (PGC) with regular distribution of micropores in the two-dimensional basal plane has been a research hotspot in the past decade.[195, 196] In additional to the intrinsic graphitic properties, the microporous structure imparts a number of unique properties and functions that are not available with pristine graphene: pores enables permeability towards specific molecules by rational design of pore size and functionalization;[197] high surface area leads to potential applications in storage;[198] abundant edge structures on pore periphery provides highly active catalytic sites;[199] the porous structure also opens up energy gaps to afford semiconductivity.[200] In the meantime, the graphitic structure still retains the key properties of graphene materials, such as excellent electrical and thermal conductivity, chemical stability, mechanically robustness, gas impermeability, *etc*. Combining the unique properties of the micropores and the graphitic backbone, porous graphene has been widely applied into applications in energy storage and conversion, such as supercapacitors,[201, 202] lithium ion batteries,[203, 204] field effect transistors,[205] water desalination,[206, 207] and DNA sequencing.[208, 209]

Previously, the synthesis of porous graphitic structure is typically accomplished through top-down approaches, often involving thermal or chemical etching. Template methods usually employ a sacrificial component to generate pore structures.[210-213]

Although it is able to yield regulated pores, pore sizes usually fall into mesopore or macropore region with low porosity. On the other hand, chemical etching generates high porosity with small pore sizes, but at the cost of broad pore size distributions.[214-218] It is still a significant challenge to achieve porous graphene structure with highly densed regulated micropores.

Chemical bottom-up synthesis, with a precise control at the atomic level, appears to be a promising strategy to make porous graphitic carbon. Several examples have been reported to achieve porous graphitic structure through on-surface interfacial synthesis.[219-221] Monomers were deposited and pre-aligned on certain metal lattice surface. The following heating triggered the crosslinking and cyclodehydrogenative aromatization. With delicate monomer design and temperature control, precise control of pore size and edge structure was achieved. However, most materials synthesized through this strategy still contained single-stranded bonds in their extended structures, leading to incomplete graphitization. In addition, high cost and poor scale-up ability dramatically hindered the mass production through on-surface synthesis.

To solve this problem, several porous graphitic structures were reported through mg or gram scale solution phase bottom-up synthesis. Typically, solution-phase crosslinking generated insoluble porous precursors in the first step, leading to challenges in graphitize the structure in the solid state. In order to overcome the high energy barrier to fuse the backbone into graphitic structure, high temperature annealing was usually required for such materials to reach to the thermodynamically favorable graphitized constitution.[16, 222] Due to complicated reaction pathways during pyrolysis, the exact

chemical constitutions of the backbones were usually not regulated. Therefore, mild condition graphitization with precise control and chemical versatility is of high demand. So far, such reaction approach has not been well-established yet.

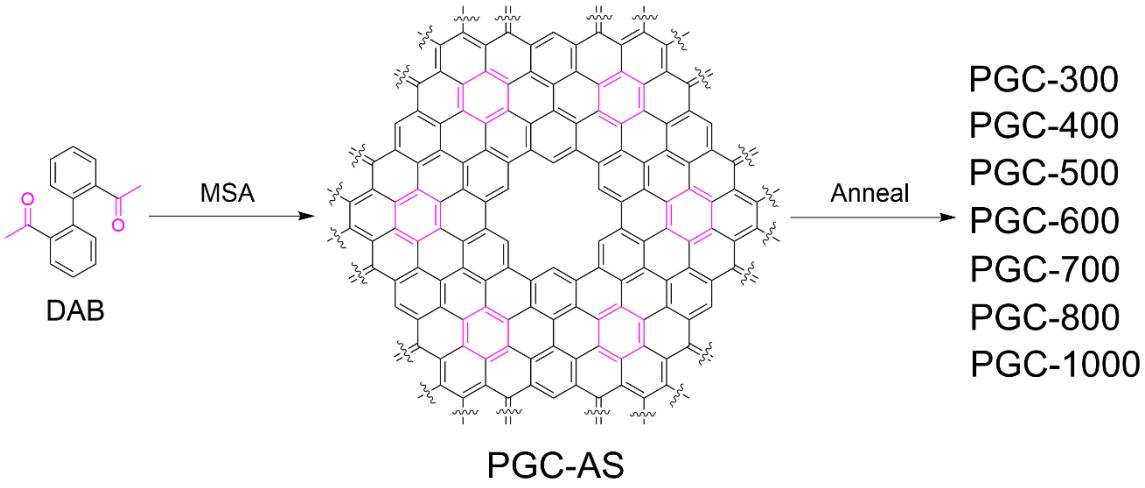

Figure 4.1. One-pot synthesis of as synthesized PGC (**PGC-AS)** from **DAB** monomer, and the subsequent annealing to afford different batches of materials (PGC-300~PGC-1000).
The number in the batch name indicate the annealing temperature.

4.2 Structure Design and Synthesis

Previously, a cost-effective aldol triple condensation (ATC) reaction was developed in our group to construct PPNs.[85, 86] In this acid-catalyzed reaction, three acetyl groups can condense together through two consecutive aldol reactions, pericyclic rearrangement, and dehydration, to form one benzene ring. This way, a diacetyl-functionalized molecule can be crosslinked to afford a network. In this method, methanesulfonic acid (MSA) was chosen to serve as both the catalyst and the solvent. The backbone is constituted with only aromatic units, enabling excellent chemical stability. In

addition, the facile reaction procedure and low cost promise potential scale-up, while the homogeneous liquid-phase reaction allowed for processability and device fabrication.

Here in this work, we employed the highly advantageous ATC strategy to synthesize a porous graphitic carbon from a diacetyl functionalized biphenyl monomer. (**Figure 4.1**) The graphitization step can take place automatically through cyclodehydrogenative aromatization on the deliberately designed network backbone on account of its favorable steric arrangement. In order to achieve the desired configuration for cyclodehydrogenative aromatization, 2,2'-diacetylbiphenyl (DAB) was chosen as the monomeric starting material. Following the ATC reaction, the network is anticipated to extend in a manner so that certain C—H groups of adjacent benzene units are in proximity to facilitate cyclodehydrogenation with minimum conformational reorganization.

The monomer DAB was synthesized through a one-step Cu-catalyzed Ullman coupling of commercially available starting material 1-(2-iodophenyl)ethan-1-one. Gram-scale was achieved with 67% yield. The ATC polymerization of DAB was carried out in MSA. Homogeneous solution of DAB in MSA was prepared by bath sonication. Upon heating the solution to 180 ^{o}C in an open vial set-up, the color of the reaction mixture rapidly changed from orange to black, indicating the formation of extended pi conjugation. After heating for 24 hours and the subsequent thorough washing, insoluble black solid was isolated in a quantitative yield. No protective procedure was required for the synthesis as the reaction is tolerable to ambient oxygen and moisture. Subsequently, the material was annealed at different temperatures to further remove defects and graphitize the backbone, to afford the PGC materials. Interestingly, characteristic D and G bands related to graphitic

structure were observed for PGC even before annealing, indicating this one-pot MSA-catalyzed crosslinking reaction was able to trigger the cyclodehydrogenation aromatization to generate a partially graphitized structure.

Although the crosslinked nature of the aromatic backbone endows PGC excellent chemical stability, it also renders the material insoluble and unmeltable, hence extremely difficult to process. In this work, however, the pristine monomer solution of DAB in MSA allows for processing the PGC thin film through an approach of casting followed by *in situ* reaction. To demonstrate this feature, the solution of reaction mixture was drop-cast onto micro cover glass and sandwiched using another micro cover glass, followed by heating at 150 ^{o}C for 72 h. The resulting black film was peeled off from the glass, thoroughly washed, and annealed at different temperatures to achieve well-defined PGC film.

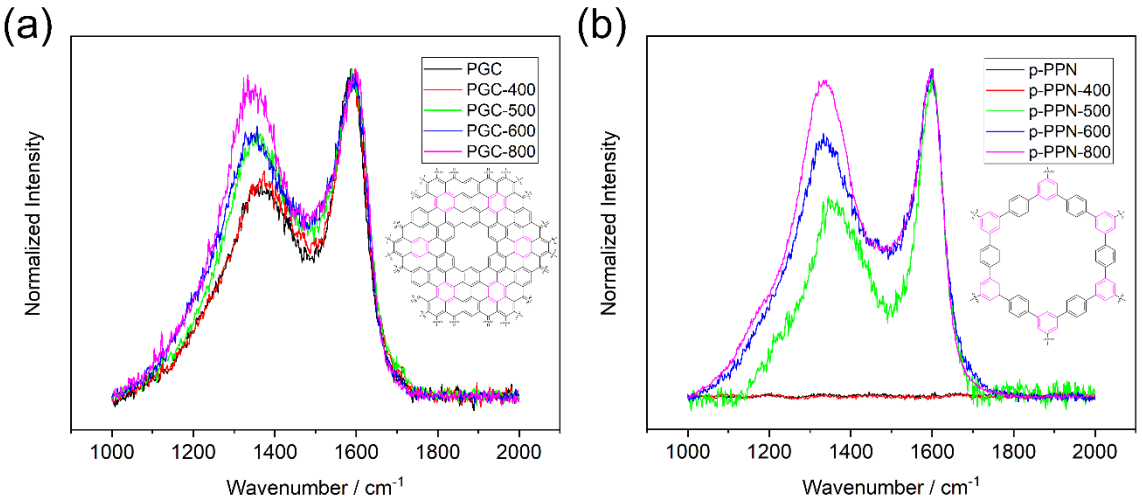

Figure 4.2. Raman spectra of (a) **PGC** film and (b) **p-PPN** film after annealing. Inset: the corresponding structures.

Raman spectroscopy was conducted to analyze the characteristic graphitic structures. G band at around 1581 cm^{-1} describes the ordered packing and extension of fused sp^2 carbons, and it is a strong evidence of presence of graphitic structure. D band, locating around 1300 to 1350 cm^{-1}, is relevant to the defects and edge structures. The as-synthesized PGC film from the MSA-mediated *in situ* crosslinking showed well-defined D and G band signals without any higher temperature annealing, indicating that cyclodehydrogenation aromatization has already been triggered in the one-pot crosslinking reaction to afford a partially graphitized structure. (**Figure 4.2a**) This unexpected graphitization can be attributed to aforementioned favorable steric arrangement of the backbone for oxidative dehydrogenation. To confirm this hypothesis, a control material p-PPN film, which is a reported PPN structure with no graphitic backbone, was also synthesized and tested. Not surprisingly, pristine p-PPN film did not show any signals in respect to D and G bands after the MSA-mediated ATC reaction, as a result of the lack of C—H groups in proximity for dehydrogenation in p-PPN. The oxidant for this reaction was attributed to the S(VI) in MSA, instead of oxygen in the air. To confirm this mechanism, an oxygen-free, sealed tube reaction of degassed mixture was conducted. It also afforded the dehydrogenated PGC product and the similar Raman signal was observed.

To remove defects and further graphitize the PGC, the as synthesized material was annealed at variable temperatures from 300 to 1000 ^{o}C. Upon annealing, the Raman spectrum exhibited a sharper and more intense G band, indicating a more dominant graphitic structure. In contrast, the control material p-PPN did not show the D- and G-

band Raman signals until the annealing temperature was set to be above 500 °C. (**Figure 4.2b**) This sharp contrast between PGC and p-PPN again demonstrated that the rational design of DAB monomer was a key to enable the efficient graphitization of PGC in relatively mild conditions.

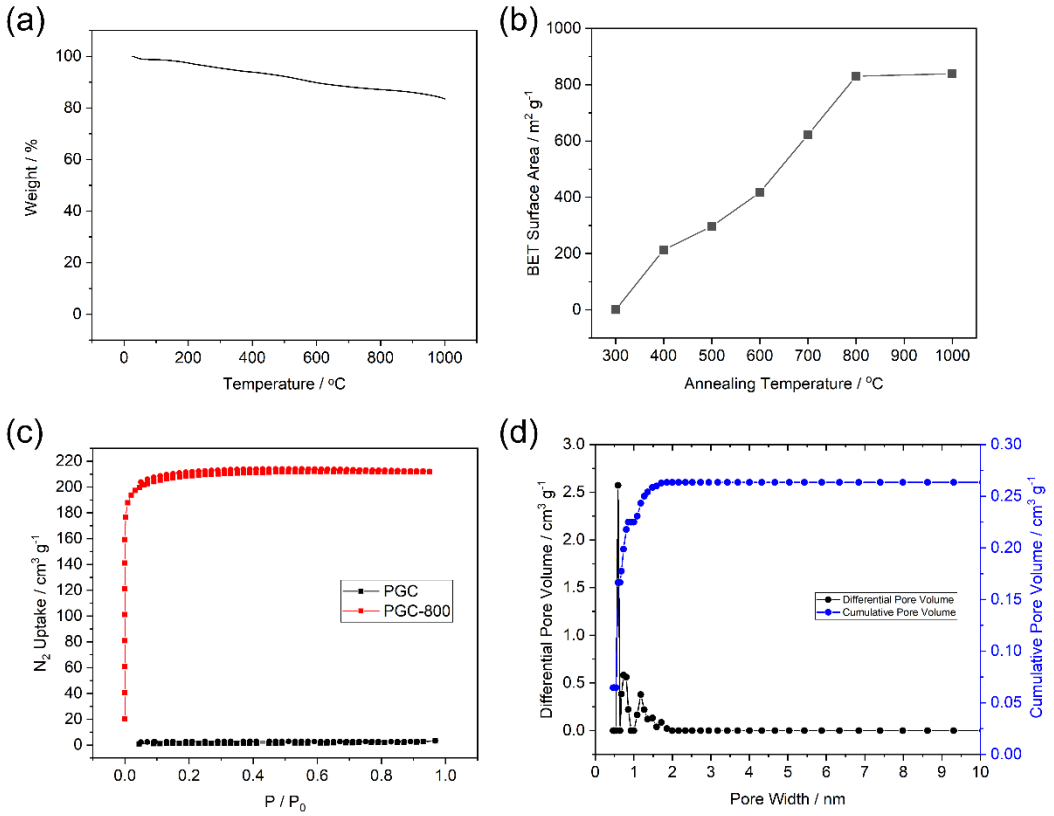

Figure 4.3. (a) TGA curve of **PGC-AS** film. (b) Relationship between BET surface areas of PGC films and annealing temperatures. (c) N_2 adsorption isotherms (77 K) of **PGC-AS** and **PGC-800**. (d) Pore size distribution of **PGC-800**.

TGA demonstrated excellent thermal stability of PGC-AS with over 80% weight remaining at 1000 °C in an oxygen free measurement. (**Figure 4.3a**) N_2 adsorption–desorption isotherm measurements at 77 K and Brunauer–Emmet–Teller (BET) surface area analysis was conducted to evaluate porosity. No distinct N_2 adsorption was observed

for PGC-AS, (**Figure 4.3c**) which was likely due to the entrapped solvent/impurity in the pores and was reported by other microporous materials as well. The annealed PGC samples started to show porosity after 300 ^{o}C annealing. The BET surface area increased with higher annealing temperatures and saturated at 800 ^{o}C, reaching 830 $m^2 g^{-1}$ for PGC-800. (**Figure 4.3b**) The nitrogen adsorption isotherms of PGC-800 showed typical type I isotherm, indicating the presence of dominant micropores. Pore size distribution revealed the major pore size of 0.6 nm with an extremely narrow distribution, which matched well with the model structure. (**Figure 4.3d**)

Graphitic structures possess good electrical conductivity. Both PGC and p-PPN film were tested for their conductivity with 2-probe set-up. (**Figure 4.4**) Neither film was conductive without annealing, presumably due to the presence of defects in the backbone that break the percolated charge transport pathways. However, PGC film started to exhibit significant conductivity after annealing at the temperature as low as 500 ^{o}C, while p-PPN film did not show any measurable conductivity until the annealing temperature was increased to 600 ^{o}C. At 600 and 700 ^{o}C annealing temperatures, PGC film exhibited 3 and 2 orders of magnitude higher conductivity than p-PPN film does, respectively. (**Figure 4.4c**) This comparison confirmed that the designed PGC constitution from DAB monomer was favorable to facilitate graphitization. It is noteworthy that both materials showed excellent conductivity after 800 ^{o}C annealing, indicating that fully graphitized backbones were achieved thermodynamically in both materials after reaching 800 ^{o}C. The lower requirement of annealing temperature by PGC, however, is critically important to achieve

a general low-energy consumption production of graphitic carbon materials, and enables procedures or applications that cannot tolerate an ultrahigh annealing temperature.

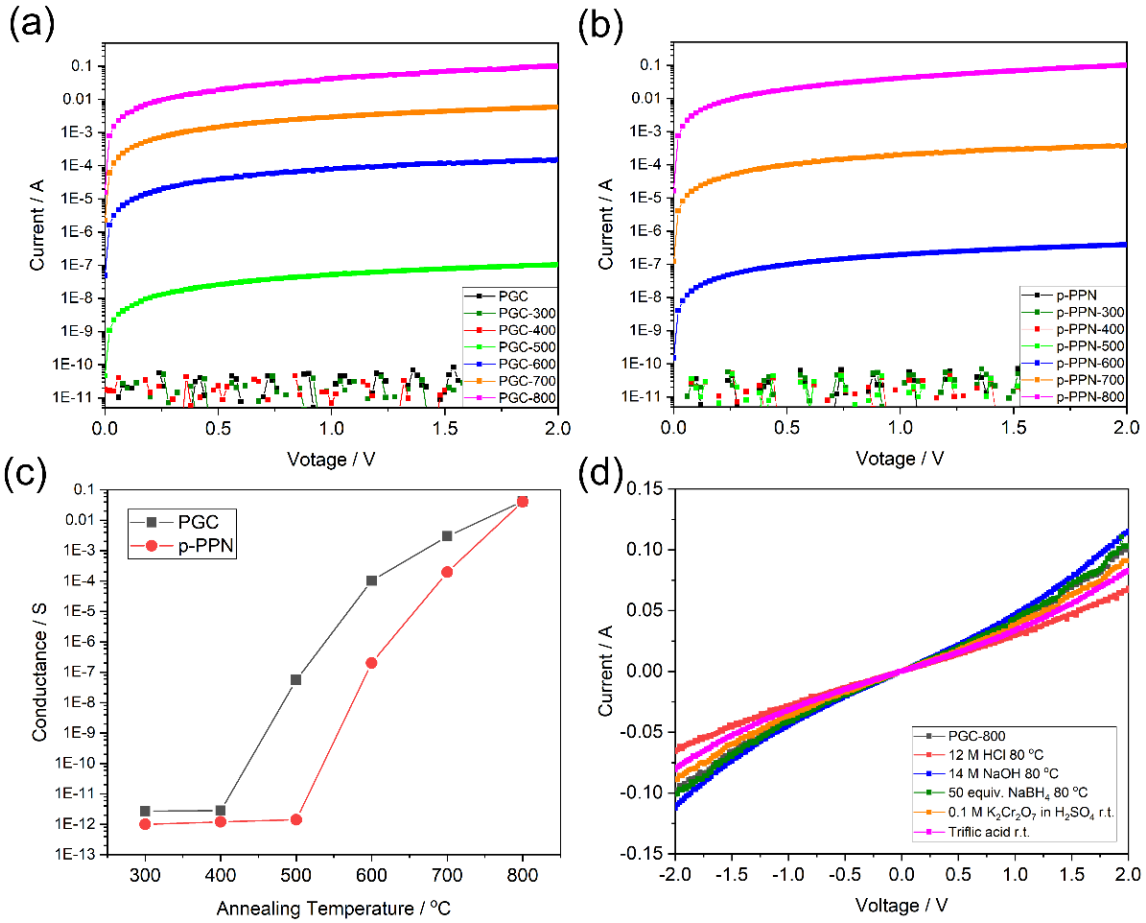

Figure 4.4. Conductivity tests of (a) **PGC** film and (b) control **p-PPN** film after annealing. (c) Comparison of conductance of **PGC** film and **p-PPN** film with different temperature annealing. (d) Conductivity tests of **PGC-800** film after treatments.

As expected for a graphitic carbon-based material, PGC-800 demonstrated excellent stability after extended treatments in harsh chemical conditions, including acids (12 M HCl at 80 °C, 7 days; or 98% TfOH, 7 days), base (14 M NaOH in H_2O/MeOH at 80 °C, 7 days), reducing agent (50 equiv. $NaBH_4$ in MeOH at 80 °C, 7 days), and oxidant(0.1 M $K_2Cr_2O_7$ in concentrated H_2SO_4). (**Figure 4.5**) BET surface area and

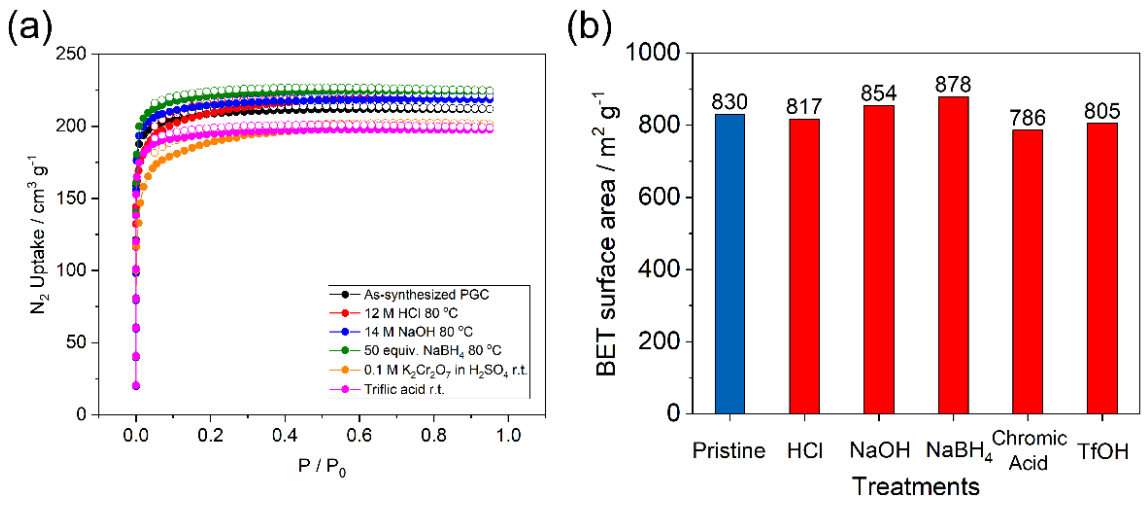

Figure 4.5. (a) N_2 adsorption isotherms (77 K) of **PGC-800** after treatments. (b) BET surface areas of **PGC-800** after treatments.

conductivity remained mostly intact through all treatments, demonstrating that the fully graphitized backbone endowed the material with exceptional chemical stability. Such remarkable robustness makes PGC able to survive extremely harsh processing/fabrication conditions and applicable in applications involving extreme environments.

4.3 Conclusion

In conclusion, chemical bottom-up synthesis of porous graphitic carbon (PGC) was achieved through a one-pot, two-step polymerization and graphitization. The framework was crosslinked by methanesulfonic acid-mediated aldol triple condensation reaction, while the pre-organized aromatic moieties allowed for cyclodehydrogenation to graphitize the backbone. This scalable method features easy starting materials preparation, inexpensive reagents, and simple reaction procedure. The pristine homogeneous reaction allowed for solution processing of this intrinsically insoluble graphitic materials, essential

for a wide range of practical applications. The PGC was equipped with dominant micropores with narrow size distributions. Both Raman spectroscopy and conductivity test confirmed the favorable and much lower temperature requirement of the graphitization process, compared to conventional conjugated polymer networks. Overall, this work establishes a promising synthetic strategy to access porous graphitic carbon in an energy-efficient manner, and paves the way for its applications in electrocatalysis, chemiresistive sensing, and sieving.

4.4 Experimental Section

4.4.1 General Information

Starting materials, reagents, and solvents were purchased from Aldrich, Alfa Aesar, TCI, and Acros, and were used as received without further purification unless otherwise specified. Analytical thin-layer chromatography (TLC) tests were performed on glass that was precoated with silica gel 60-F254 (Sorbtech). Flash column chromatography was carried out using a Biotage® Isolera™ Prime. Solution phase ^{1}H-, and ^{13}C-NMR spectra were obtained on Bruker Ascend 400 MHz spectrometers at room temperature. Chemical shifts are reported in ppm relative to the signals corresponding to the residual non-deuterated solvents (for ^{1}H NMR: $CDCl_3$ δ = 7.26 ppm; for ^{13}C NMR: $CDCl_3$ δ = 77.16 ppm). High-resolution Atmospheric Pressure Chemical Ionization (HR-APCI) mass spectra were performed using a Thermo Fisher Scientific Q Exactive Focus.

4.4.2 Synthesis

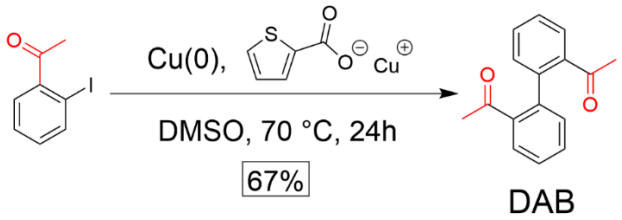

DAB synthesis: A mixture of 1-(2-iodophenyl)ethan-1-one (12.3 g, 50 mmol), Cu powder (31.8 g, 500 mol) and Copper(I) thiophene-2-carboxylate (47.7 g, 250 mmol) in DMSO (500 mL) was heated at 70 oC for 24 h. after the reaction was cooled down to room temperature, the precipitate was filtered out. The filtrate was poured into water. The white precipitate was filtered and washed with water. The crude product was purified by column chromatography (SiO_2, hexanes : EtOAc = 5:1) to yield **DAB** as a white solid (4.0 g, 67%). ^{1}H NMR (400 MHz, Chloroform-*d*): δ 7.73 (dd, *J* = 7.5, 1.7 Hz, 2H), 7.52-7.41 (m, 4H), 7.16 (dd, *J* = 7.5, 1.7 Hz, 2H), 2.25 (s, 2H). ^{13}C NMR (100 MHz, Chloroform-*d*): δ 201.68, 140.68, 138.76, 131. 11, 130.78, 128,62, 127.67. HRMS (APCI): calcd for $C_{16}H_{14}O_2$ $[M+H]^+$ *m/z*=239.1067; found *m/z*=239.1063.

PGC synthesis: A 20 mL vial was charged with 0.5 g DAB and 3 mL MSA. The reaction mixture was sonicated for 5 min. The orange solution was heated to 90 ^{o}C for 1 h. Then the temperature was increased to 150 ^{o}C and kept for 24 h. At last it was increased to 180 ^{o}C and kept for 3 h. The black solid was filtered, washed with MeOH, and purified by Soxhlet extraction with THF. The remaining solid was dried in vacuo to give a black solid **PGC-AS** (0.41 g, quantitative). Then the solid was annealed at various temperatures under N_2 to afford **PGC-T**. N_2 flow rate: 100 mL min^{-1}. Temperature ramp rate: 2 ^{o}C min^{-1}.

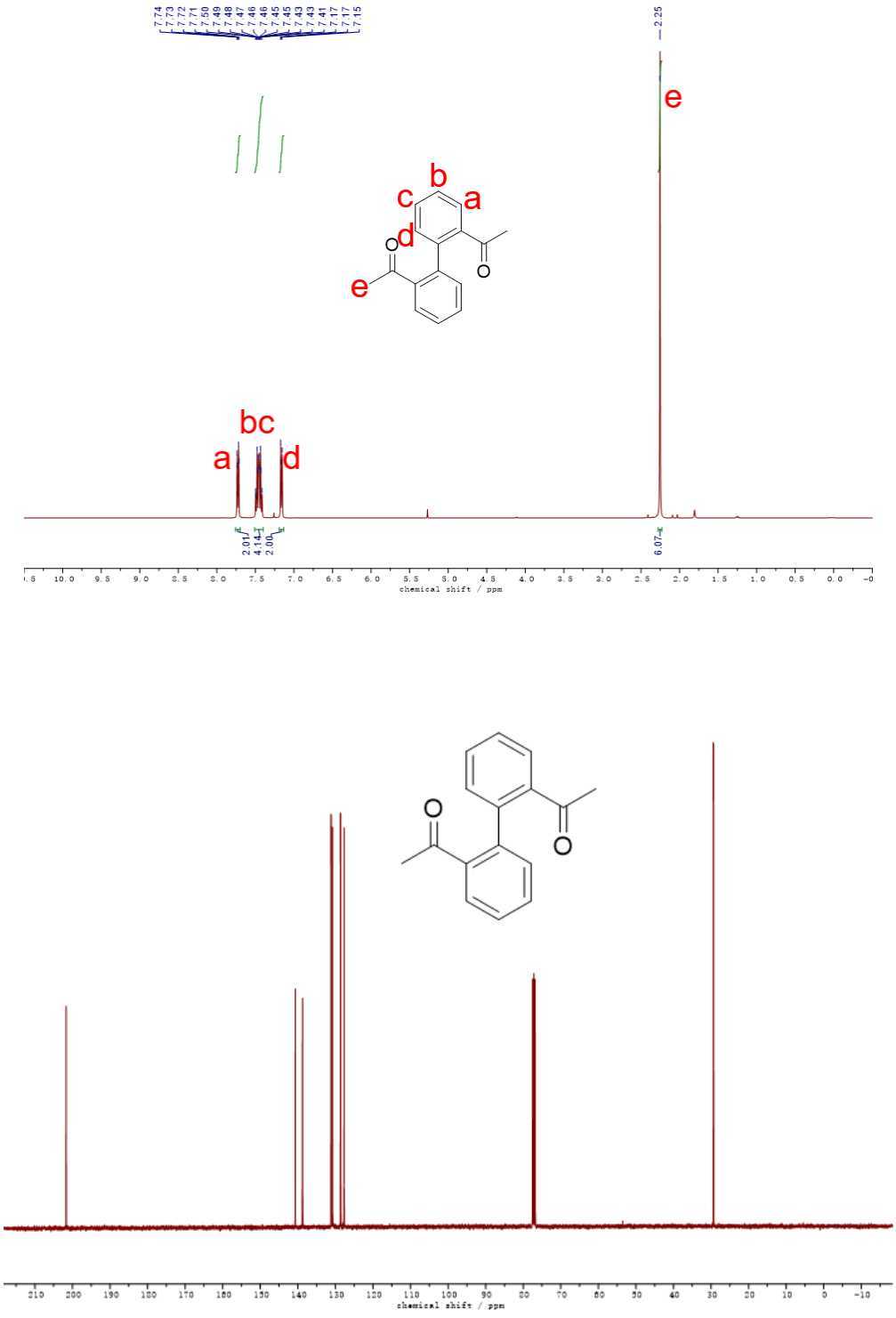

Figure 4.6. ^{1}H (400 MHz, $CDCl_3$, RT) and ^{13}C NMR (100 MHz, $CDCl_3$, RT) of DAB monomer.

CHAPTER V

CONCLUSIONS

5.1 Thermodynamically controlled ring-closing metathesis

5.1.1 Summary

A truxene-based PLAN was successfully synthesized through Suzuki crosslinking followed by RCM ladderizition. Thermodynamically controlled ring-fusing step allowed for error-checking and proof-reading process, leading to complete ladder type backbone with minimal backbone defects, which was unambiguously confirmed by solid state NMR analysis. **PLAN** possessed a larger BET surface area compared to its non-ladder-type counterparts due to the templating effect of the vinyl groups in the precursor. The rigid defect-free ladder-type backbone endowed PLAN extremely high chemical stability, leading to potential applications in harsh conditions.

Moreover, the consist conformation of ladder-type backbone achieved more entropically favorable methane adsorption. PLAN demonstrated a remarkably high methane uptake per unit surface area, which was superior to other reported porous hydrocarbons and COFs without enthalpically favorable interactions with methane. The following thermodynamic investigation under different temperatures revealed a significantly smaller entropy penalty of PLAN induced by the elimination of torsional rotation from single bonds, compared to its non-ladder-type counterparts. Entropic contribution to high-pressure gas adsorption was often overlooked, however, it could have huge impact on overall performance. The entropic approach offers a universal strategy to

increase the deliverable capacity for various types of gases while mitigating the performance decline in high temperature applications.

5.1.2 Perspective

5.1.2.1 New type of PLAN with high BET surface area

High-pressure gas adsorption is highly sensitive to porosity of the adsorbent. The current PLANs are still quite limited to 2D structure. As a comparison, 3D porous organic materials with fully ladder-type backbone has the potential to generate ultra-high porosity. However, it is still challenging to create three-dimensional extended nodes with complete ladder-type structure. Therefore, the exploration of highly porous 3D PLAN is of high demand, such as cyclooctatetraene and triptycene center.

5.1.2.2 Introduction of ladder-type backbone into reported highly porous materials

Ladder-type backbone introduced intriguing properties, such as high stability, strong structural integrity, and high coplanarity. In addition to building porous materials with complete ladder-type backbone, introducing ladder-type linkers into other already known, top-performing porous materials is a promising approach to quickly achieve the champion performance for applications. For instance, the introduction of ladder-type linker into PPN-6 UIO-68 and can dramatically increase the chemical stability and high-pressure gas adsorption.

5.2 Porous graphitic carbon through one-step aldol triple condensation and graphitization

5.2.1 Summary

Chemically bottom-up synthesis of porous graphitic structure was achieved through one-step aldol triple condensation and graphitization. The potential mass production was enabled by easy starting materials preparation, inexpensive reagents, and simple reaction procedure. Raman spectroscopy and conductivity confirmed the facile graphitization process compared to conventional PPNs, and porosity analysis revealed the regulated ultramicropore structure with narrow size distributions. The solution processability enabled potential device fabrication for various applications, such as electrocatalysis, chemiresistive sensing, and sieving.

5.2.2 Perspective

With the versatility of chemically bottom-up synthesis, this strategy stands out as a promising approach to introduce various catalytic sites into PGC backbone. Acetyl functionalized pyridine, porphyrin, phthalocyanine moieties can be blended with DAB monomer. Due to the homogeneous liquid-phase reaction system, functionalities are expected to evenly distributed across the framework. The pristine composition of the reaction precursor allowed solution processing of these insoluble graphitic materials. For instance, direct electrode fabrication with these functionalized PGC membranes enabled the electrochemical catalysis application in oxygen reduction reaction (ORR), hydrogen evolution reaction (HER), oxygen evolution reaction (OER), *etc*. (**Figure 5.1**)

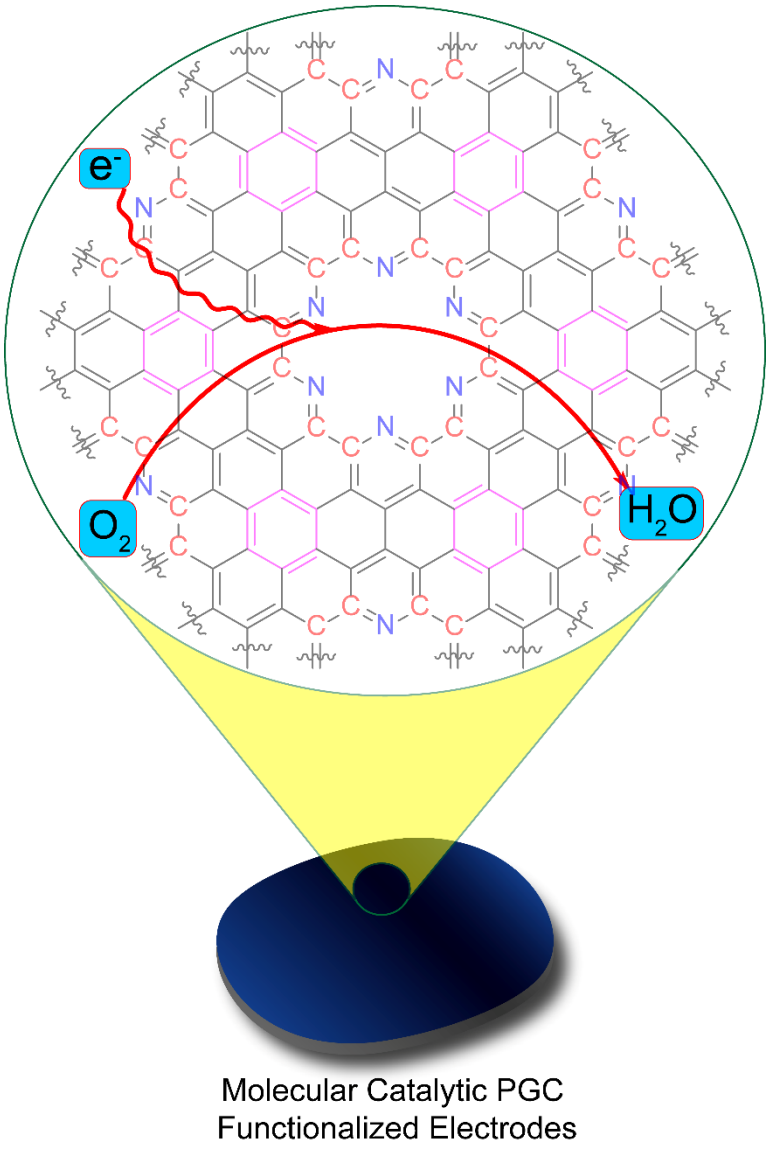

Figure 5.1. Proposed ORR catalysis scheme with pyridine-doping **PGC** functionalized electrodes.

REFERENCES

(1) Kandambeth, S.; Dey, K.; Banerjee, R., Covalent Organic Frameworks: Chemistry Beyond the Structure. *J. Am. Chem. Soc.* **2019,** *141*, 1807-1822.

(2) Chen, X.; Geng, K.; Liu, R.; Tan, K. T.; Gong, Y.; Li, Z.; Tao, S.; Jiang, Q.; Jiang, D., Covalent Organic Frameworks: Chemical Approaches to Designer Structures and Built-in Functions. *Angew. Chem. Int. Ed.* **2020,** *59*, 5050-5091.

(3) Geng, K.; He, T.; Liu, R.; Dalapati, S.; Tan, K. T.; Li, Z.; Tao, S.; Gong, Y.; Jiang, Q.; Jiang, D., Covalent Organic Frameworks: Design, Synthesis, and Functions. *Chem. Rev.* **2020**.

(4) Bisbey, R. P.; Dichtel, W. R., Covalent Organic Frameworks as a Platform for Multidimensional Polymerization. *ACS Cent. Sci.* **2017,** *3*, 533-543.

(5) Waller, P. J.; Gandara, F.; Yaghi, O. M., Chemistry of Covalent Organic Frameworks. *Acc. Chem. Res.* **2015,** *48*, 3053-3063.

(6) Ding, S. Y.; Wang, W., Covalent Organic Frameworks (COFs): From Design to Applications. *Chem. Soc. Rev.* **2013,** *42*, 548-568.

(7) Feng, X.; Ding, X.; Jiang, D., Covalent Organic Frameworks. *Chem. Soc. Rev.* **2012,** *41*, 6010-6022.

(8) Ben, T.; Ren, H.; Ma, S.; Cao, D.; Lan, J.; Jing, X.; Wang, W.; Xu, J.; Deng, F.; Simmons, J. M.; Qiu, S.; Zhu, G., Targeted Synthesis of a Porous Aromatic Framework with High Stability and Exceptionally High Surface Area. *Angew. Chem. Int. Ed.* **2009,** *48*, 9457-9460.

(9) Konstas, K.; Taylor, J. W.; Thornton, A. W.; Doherty, C. M.; Lim, W. X.; Bastow, T. J.; Kennedy, D. F.; Wood, C. D.; Cox, B. J.; Hill, J. M.; Hill, A. J.; Hill, M. R., Lithiated Porous Aromatic Frameworks with Exceptional Gas Storage Capacity. *Angew. Chem. Int. Ed.* **2012,** *51*, 6639-6642.

(10) Li, B.; Zhang, Y.; Ma, D.; Shi, Z.; Ma, S., Mercury Nano-Trap for Effective and Efficient Removal of Mercury(II) from Aqueous Solution. *Nat. Commun.* **2014,** *5*, 5537.

(11) Li, M.; Ren, H.; Sun, F.; Tian, Y.; Zhu, Y.; Li, J.; Mu, X.; Xu, J.; Deng, F.; Zhu, G., Construction of Porous Aromatic Frameworks with Exceptional Porosity Via Building Unit Engineering. *Adv. Mater.* **2018,** *30*, 1804169.

(12) Zou, J.; Trewin, A.; Ben, T.; Qiu, S., High Uptake and Fast Transportation of $LiPF_6$ in a Porous Aromatic Framework for Solid-State Li-Ion Batteries. *Angew. Chem. Int. Ed.* **2020,** *59*, 769-774.

(13) Xu, Y.; Jin, S.; Xu, H.; Nagai, A.; Jiang, D., Conjugated Microporous Polymers: Design, Synthesis and Application. *Chem. Soc. Rev.* **2013,** *42*, 8012-8031.

(14) Lee, J. M.; Cooper, A. I., Advances in Conjugated Microporous Polymers. *Chem. Rev.* **2020,** *120*, 2171-2214.

(15) Dawson, R.; Adams, D. J.; Cooper, A. I., Chemical Tuning of CO_2 Sorption in Robust Nanoporous Organic Polymers. *Chem. Sci.* **2011,** *2*, 1173-1177.

(16) Yuan, K.; Zhuang, X.; Fu, H.; Brunklaus, G.; Forster, M.; Chen, Y.; Feng, X.; Scherf, U., Two-Dimensional Core-Shelled Porous Hybrids as Highly Efficient Catalysts for the Oxygen Reduction Reaction. *Angew. Chem. Int. Ed.* **2016,** *55*, 6858-6863.

(17) Lee, J.; Buyukcakir, O.; Kwon, T. W.; Coskun, A., Energy Band-Gap Engineering of Conjugated Microporous Polymers Via Acidity-Dependent in Situ Cyclization. *J. Am. Chem. Soc.* **2018,** *140*, 10937-10940.

(18) Lu, W. G.; Yuan, D. Q.; Zhao, D.; Schilling, C. I.; Plietzsch, O.; Muller, T.; Brase, S.; Guenther, J.; Blumel, J.; Krishna, R.; Li, Z.; Zhou, H. C., Porous Polymer Networks: Synthesis, Porosity, and Applications in Gas Storage/Separation. *Chem. Mater.* **2010,** *22*, 5964-5972.

(19) Zou, L.; Sun, Y.; Che, S.; Yang, X.; Wang, X.; Bosch, M.; Wang, Q.; Li, H.; Smith, M.; Yuan, S.; Perry, Z.; Zhou, H. C., Porous Organic Polymers for Post-Combustion Carbon Capture. *Adv. Mater.* **2017,** *29*, 1700229.

(20) Yuan, D.; Lu, W.; Zhao, D.; Zhou, H. C., Highly Stable Porous Polymer Networks with Exceptionally High Gas-Uptake Capacities. *Adv. Mater.* **2011,** *23*, 3723-3725.

(21) Lu, W.; Sculley, J. P.; Yuan, D.; Krishna, R.; Wei, Z.; Zhou, H. C., Polyamine-Tethered Porous Polymer Networks for Carbon Dioxide Capture from Flue Gas. *Angew. Chem. Int. Ed.* **2012,** *51*, 7480-7484.

(22) Lu, W. G.; Verdegaal, W. M.; Yu, J. M.; Balbuena, P. B.; Jeong, H. K.; Zhou, H. C., Building Multiple Adsorption Sites in Porous Polymer Networks for Carbon Capture Applications. *Energy Environ. Sci.* **2013,** *6*, 3559-3564.

(23) Lu, W.; Bosch, M.; Yuan, D.; Zhou, H. C., Cost-Effective Synthesis of Amine-Tethered Porous Materials for Carbon Capture. *ChemSusChem* **2015,** *8*, 433-438.

(24) Lu, W.; Wei, Z.; Yuan, D.; Tian, J.; Fordham, S.; Zhou, H.-C., Rational Design and Synthesis of Porous Polymer Networks: Toward High Surface Area. *Chem. Mater.* **2014,** *26*, 4589-4597.

(25) Kuhn, P.; Thomas, A.; Antonietti, M., Toward Tailorable Porous Organic Polymer Networks: A High-Temperature Dynamic Polymerization Scheme Based on Aromatic Nitriles. *Macromolecules* **2009,** *42*, 319-326.

(26) Trewin, A.; Cooper, A. I., Porous Organic Polymers: Distinction from Disorder? *Angew. Chem. Int. Ed.* **2010,** *49*, 1533-1535.

(27) Chen, Q.; Dong, A.; Wang, D.; Qiu, L.; Ma, C.; Yuan, Y.; Zhao, Y.; Jia, N.; Guo, Z.; Wang, N., Efficient and Selective Methane Borylation through Pore Size Tuning of Hybrid Porous Organic-Polymer-Based Iridium Catalysts. *Angew. Chem. Int. Ed.* **2019,** *58*, 10671-10676.

(28) Zhang, Y.; Riduan, S. N., Functional Porous Organic Polymers for Heterogeneous Catalysis. *Chem. Soc. Rev.* **2012,** *41*, 2083-2094.

(29) Lee, J. Y.; Wood, C. D.; Bradshaw, D.; Rosseinsky, M. J.; Cooper, A. I., Hydrogen Adsorption in Microporous Hypercrosslinked Polymers. *Chem. Commun.* **2006,** 2670-2672.

(30) Xu, S.; Luo, Y.; Tan, B., Recent Development of Hypercrosslinked Microporous Organic Polymers. *Macromol. Rapid Commun.* **2013,** *34*, 471-484.

(31) Tsyurupa, M. P.; Davankov, V. A., Hypercrosslinked Polymers: Basic Principle of Preparing the New Class of Polymeric Materials. *React. Funct. Polym.* **2002,** *53*, 193-203.

(32) Xie, Z.; Wang, C.; deKrafft, K. E.; Lin, W., Highly Stable and Porous Cross-Linked Polymers for Efficient Photocatalysis. *J. Am. Chem. Soc.* **2011,** *133*, 2056-2059.

(33) Tan, L.; Tan, B., Hypercrosslinked Porous Polymer Materials: Design, Synthesis, and Applications. *Chem. Soc. Rev.* **2017,** *46*, 3322-3356.

(34) Wood, C. D.; Tan, B.; Trewin, A.; Su, F.; Rosseinsky, M. J.; Bradshaw, D.; Sun, Y.; Zhou, L.; Cooper, A. I., Microporous Organic Polymers for Methane Storage. *Adv. Mater.* **2008,** *20*, 1916-1921.

(35) Lee, J. M.; Briggs, M. E.; Hasell, T.; Cooper, A. I., Hyperporous Carbons from Hypercrosslinked Polymers. *Adv. Mater.* **2016,** *28*, 9804-9810.

(36) Dawson, R.; Stevens, L. A.; Drage, T. C.; Snape, C. E.; Smith, M. W.; Adams, D. J.; Cooper, A. I., Impact of Water Coadsorption for Carbon Dioxide Capture in Microporous Polymer Sorbents. *J. Am. Chem. Soc.* **2012,** *134*, 10741-10744.

(37) Woodward, R. T.; Stevens, L. A.; Dawson, R.; Vijayaraghavan, M.; Hasell, T.; Silverwood, I. P.; Ewing, A. V.; Ratvijitvech, T.; Exley, J. D.; Chong, S. Y.; Blanc, F.; Adams, D. J.; Kazarian, S. G.; Snape, C. E.; Drage, T. C.; Cooper, A. I., Swellable, Water- and Acid-Tolerant Polymer Sponges for Chemoselective Carbon Dioxide Capture. *J. Am. Chem. Soc.* **2014,** *136*, 9028-9035.

(38) Budd, P. M.; McKeown, N. B.; Fritsch, D., Free Volume and Intrinsic Microporosity in Polymers. *J. Mater. Chem.* **2005,** *15*, 1977-1986.

(39) McKeown, N. B.; Budd, P. M.; Msayib, K. J.; Ghanem, B. S.; Kingston, H. J.; Tattershall, C. E.; Makhseed, S.; Reynolds, K. J.; Fritsch, D., Polymers of Intrinsic Microporosity (PIMs): Bridging the Void between Microporous and Polymeric Materials. *Chem. Eur. J.* **2005,** *11*, 2610-2620.

(40) McKeown, N. B.; Budd, P. M., Polymers of Intrinsic Microporosity (PIMs): Organic Materials for Membrane Separations, Heterogeneous Catalysis and Hydrogen Storage. *Chem. Soc. Rev.* **2006,** *35*, 675-683.

(41) McKeown, N. B.; Budd, P. M., Exploitation of Intrinsic Microporosity in Polymer-Based Materials. *Macromolecules* **2010,** *43*, 5163-5176.

(42) McKeown, N. B., Polymers of Intrinsic Microporosity. *ISRN Mater. Sci.* **2012,** *2012*, 1-16.

(43) McKeown, N. B.; Hanif, S.; Msayib, K.; Tattershall, C. E.; Budd, P. M., Porphyrin-Based Nanoporous Network Polymers. *Chem. Commun.* **2002,** 2782-2783.

(44) Du, N.; Park, H. B.; Robertson, G. P.; Dal-Cin, M. M.; Visser, T.; Scoles, L.; Guiver, M. D., Polymer Nanosieve Membranes for CO_2-Capture Applications. *Nat. Mater.* **2011,** *10*, 372-375.

(45) Budd, P. M.; Ghanem, B. S.; Makhseed, S.; McKeown, N. B.; Msayib, K. J.; Tattershall, C. E., Polymers of Intrinsic Microporosity (PIMs): Robust, Solution-Processable, Organic Nanoporous Materials. *Chem. Commun.* **2004,** 230-231.

(46) Li, X.; Zhang, C.; Cai, S.; Lei, X.; Altoe, V.; Hong, F.; Urban, J. J.; Ciston, J.; Chan, E. M.; Liu, Y., Facile Transformation of Imine Covalent Organic Frameworks into Ultrastable Crystalline Porous Aromatic Frameworks. *Nat. Commun.* **2018,** *9*, 2998.

(47) Yuan, S.; Dorney, B.; White, D.; Kirklin, S.; Zapol, P.; Yu, L.; Liu, D. J., Microporous Polyphenylenes with Tunable Pore Size for Hydrogen Storage. *Chem. Commun.* **2010,** *46*, 4547-4549.

(48) Jia, J.; Chen, Z.; Jiang, H.; Belmabkhout, Y.; Mouchaham, G.; Aggarwal, H.; Adil, K.; Abou-Hamad, E.; Czaban-Jóźwiak, J.; Tchalala, M. R.; Eddaoudi, M., Extremely Hydrophobic Pops to Access Highly Porous Storage Media and Capturing Agent for Organic Vapors. *Chem* **2019,** *5*, 180-191.

(49) Jing, P.; Fang, X.; Yan, J.; Guo, J.; Fang, Y., Ultra-Low Density Porous Polystyrene Monolith: Facile Preparation and Superior Application. *J. Mater. Chem. A* **2013,** *1*, 10135-10141.

(50) Gokmen, M. T.; Du Prez, F. E., Porous Polymer Particles—a Comprehensive Guide to Synthesis, Characterization, Functionalization and Applications. *Prog. Polym. Sci.* **2012,** *37*, 365-405.

(51) Stein, A.; Wang, Z.; Fierke, M. A., Functionalization of Porous Carbon Materials with Designed Pore Architecture. *Adv. Mater.* **2009,** *21*, 265-293.

(52) International Union of Pure and Applied Chemistry. *Compendium of Polymer Terminology and Nomenclature: IUPAC Recommendations 2008* **2009**.

(53) Powell, J. W.; Chartoff, R. P., Viscoelastic Properties and Stability of BBL Ladder Polymers. *J. Appl. Polym. Sci* **1974,** *18*, 83-91.

(54) Wu, J.; Rui, X.; Wang, C.; Pei, W.-B.; Lau, R.; Yan, Q.; Zhang, Q., Nanostructured Conjugated Ladder Polymers for Stable and Fast Lithium Storage Anodes with High-Capacity. *Adv. Energy Mater.* **2015,** *5*, 1402189.

(55) Stille, J. K.; Mainen, E. L., Thermally Stable Ladder Polyquinoxalines. *Macromolecules* **1968,** *1*, 36-42.

(56) Zou, Y.; Ji, X.; Cai, J.; Yuan, T.; Stanton, D. J.; Lin, Y.-H.; Naraghi, M.; Fang, L., Synthesis and Solution Processing of a Hydrogen-Bonded Ladder Polymer. *Chem* **2017,** *2*, 139-152.

(57) Marcus, R. A., On the Theory of Oxidation‐Reduction Reactions Involving Electron Transfer. I. *J. Chem. Phys.* **1956,** *24*, 966-978.

(58) Qiu, M.; Zhu, D.; Yan, L.; Wang, N.; Han, L.; Bao, X.; Du, Z.; Niu, Y.; Yang, R., Strategy to Manipulate Molecular Orientation and Charge Mobility in D–A Type Conjugated Polymer through Rational Fluorination for Improvements of Photovoltaic Performances. *J. Phys. Chem. C* **2016,** *120*, 22757-22765.

(59) Koch, A.; Kinzel, D.; Dröge, F.; Gräfe, S.; Kupfer, S., Photochemistry and Electron Transfer Kinetics in a Photocatalyst Model Assessed by Marcus Theory and Quantum Dynamics. *J. Phys. Chem. C* **2017,** *121*, 16066-16078.

(60) Fazzi, D.; Fabiano, S.; Ruoko, T.-P.; Meerholz, K.; Negri, F., Polarons in Π-Conjugated Ladder-Type Polymers: A Broken Symmetry Density Functional Description. *J. Mater. Chem. C* **2019,** *7*, 12876-12885.

(61) Prins, P.; Grozema, F. C.; Schins, J. M.; Patil, S.; Scherf, U.; Siebbeles, L. D., High Intrachain Hole Mobility on Molecular Wires of Ladder-Type Poly(*p*-Phenylenes). *Phys. Rev. Lett.* **2006,** *96*, 146601.

(62) Samiullah, M.; Moghe, D.; Scherf, U.; Guha, S., Diffusion Length of Triplet Excitons in Organic Semiconductors. *Phys. Rev. B* **2010,** *82*, 205211.

(63) Yu, L.; Chen, M.; Dalton, L. R., Ladder Polymers: Recent Developments in Syntheses, Characterization, and Potential Applications as Electronic and Optical Materials. *Chem. Mater.* **1990,** *2*, 649-659.

(64) Lee, J.; Rajeeva, B. B.; Yuan, T.; Guo, Z. H.; Lin, Y. H.; Al-Hashimi, M.; Zheng, Y.; Fang, L., Thermodynamic Synthesis of Solution Processable Ladder Polymers. *Chem. Sci.* **2016,** *7*, 881-889.

(65) Lee, J.; Kalin, A. J.; Wang, C.; Early, J. T.; Al-Hashimi, M.; Fang, L., Donor–Acceptor Conjugated Ladder Polymer Via Aromatization-Driven Thermodynamic Annulation. *Polym. Chem.* **2018,** *9*, 1603-1609.

(66) Arnold, F. E.; Van Deusen, R. L., Preparation and Properties of High Molecular Weight, Soluble Oxobenz[De]Imidazobenzimidazoisoquinoline Ladder Polymer. *Macromolecules* **1969,** *2*, 497-502.

(67) Wilbourn, K.; Murray, R. W., The Electrochemical Doping Reactions of the Conducting Ladder Polymer Benzimidazobenzophenanthroline (BBL). *Macromolecules* **1988,** *21*, 89-96.

(68) Scherf, U.; Müllen, K., A Soluble Ladder Polymer Via Bridging of Functionalized Poly(P-Pheny1ene)-Precursor. *Makromol. Chem., Rapid Commun.* **1991,** *12*, 489-497.

(69) Zhu, C.; Fang, L., Locking the Coplanar Conformation of π-Conjugated Molecules and Macromolecules Using Dynamic Noncovalent Bonds. *Macromol. Rapid Commun.* **2018,** *39*, 1700241.

(70) Lee, J.; Kalin, A. J.; Yuan, T.; Al-Hashimi, M.; Fang, L., Fully Conjugated Ladder Polymers. *Chem. Sci.* **2017,** *8*, 2503-2521.

(71) Lee, J.; Li, H.; Kalin, A. J.; Yuan, T.; Wang, C.; Olson, T.; Li, H.; Fang, L., Extended Ladder-Type Benzo[K]Tetraphene-Derived Oligomers. *Angew. Chem. Int. Ed.* **2017,** *56*, 13727-13731.

(72) Corrado, T.; Guo, R., Macromolecular Design Strategies toward Tailoring Free Volume in Glassy Polymers for High Performance Gas Separation Membranes. *Mol. Syst. Des. Eng.* **2020,** *5*, 22-48.

(73) Abdulhamid, M. A.; Lai, H. W. H.; Wang, Y.; Jin, Z.; Teo, Y. C.; Ma, X.; Pinnau, I.; Xia, Y., Microporous Polyimides from Ladder Diamines Synthesized by Facile Catalytic Arene–Norbornene Annulation as High-Performance Membranes for Gas Separation. *Chem. Mater.* **2019,** *31*, 1767-1774.

(74) Liu, S.; Jin, Z.; Teo, Y. C.; Xia, Y., Efficient Synthesis of Rigid Ladder Polymers Via Palladium Catalyzed Annulation. *J. Am. Chem. Soc.* **2014,** *136*, 17434-17437.

(75) Watson, M. D.; Fechtenkotter, A.; Mullen, K., Big Is Beautiful--"Aromaticity" Revisited from the Viewpoint of Macromolecular and Supramolecular Benzene Chemistry. *Chem. Rev.* **2001,** *101*, 1267-1300.

(76) Durban, M. M.; Kazarinoff, P. D.; Segawa, Y.; Luscombe, C. K., Synthesis and Characterization of Solution-Processable Ladderized N-Type Naphthalene Bisimide Copolymers for OFET Applications. *Macromolecules* **2011,** *44*, 4721-4728.

(77) Germain, J.; Fréchet, J. M. J.; Svec, F., Hypercrosslinked Polyanilines with Nanoporous Structure and High Surface Area: Potential Adsorbents for Hydrogen Storage. *J. Mater. Chem.* **2007,** *17*, 4989-4997.

(78) Germain, J.; Frechet, J. M.; Svec, F., Nanoporous, Hypercrosslinked Polypyrroles: Effect of Crosslinking Moiety on Pore Size and Selective Gas Adsorption. *Chem. Commun.* **2009,** 1526-1528.

(79) Carothers, W. H., Polymers and Polyfunctionality. *J. Chem. Soc. Faraday Trans.* **1936,** *32*, 39-49.

(80) Chen, Y.; Sun, H.; Yang, R.; Wang, T.; Pei, C.; Xiang, Z.; Zhu, Z.; Liang, W.; Li, A.; Deng, W., Synthesis of Conjugated Microporous Polymer Nanotubes with Large Surface Areas as Absorbents for Iodine and CO_2 Uptake. *J. Mater. Chem. A* **2015,** *3*, 87-91.

(81) Kamcev, J.; Taylor, M. K.; Shin, D. M.; Jarenwattananon, N. N.; Colwell, K. A.; Long, J. R., Functionalized Porous Aromatic Frameworks as High-Performance Adsorbents for the Rapid Removal of Boric Acid from Water. *Adv. Mater.* **2019,** *31*, 1808027.

(82) Chen, Q.; Liu, D. P.; Luo, M.; Feng, L. J.; Zhao, Y. C.; Han, B. H., Nitrogen-Containing Microporous Conjugated Polymers Via Carbazole-Based Oxidative Coupling Polymerization: Preparation, Porosity, and Gas Uptake. *Small* **2014,** *10*, 308-315.

(83) Liao, Y.; Wang, H.; Zhu, M.; Thomas, A., Efficient Supercapacitor Energy Storage Using Conjugated Microporous Polymer Networks Synthesized from Buchwald-Hartwig Coupling. *Adv. Mater.* **2018,** *30*, 1705710.

(84) Sprick, R. S.; Thomas, A.; Scherf, U., Acid Catalyzed Synthesis of Carbonyl-Functionalized Microporous Ladder Polymers with High Surface Area. *Polym. Chem.* **2010,** *1*, 283-285.

(85) Guo, Z. H.; Wang, C. X.; Zhang, Q.; Che, S.; Zhou, H. C.; Fang, L., Cost-Effective Synthesis and Solution Processing of Porous Polymer Networks through Methanesulfonic Acid-Mediated Aldol Triple Condensation. *Mater. Chem. Front.* **2018,** *2*, 396-401.

(86) Wang, C.; Li, C.; Rutledge, E. R. C.; Che, S.; Lee, J.; Kalin, A. J.; Zhang, C.; Zhou, H.-C.; Guo, Z.-H.; Fang, L., Aromatic Porous Polymer Network Membranes for Organic Solvent Nanofiltration under Extreme Conditions. *J. Mater. Chem. A* **2020,** DOI: 10.1039/c9ta10190j.

(87) Troschke, E.; Gratz, S.; Lubken, T.; Borchardt, L., Mechanochemical Friedel-Crafts Alkylation-a Sustainable Pathway Towards Porous Organic Polymers. *Angew. Chem. Int. Ed.* **2017,** *56*, 6859-6863.

(88) Puthiaraj, P.; Cho, S.-M.; Lee, Y.-R.; Ahn, W.-S., Microporous Covalent Triazine Polymers: Efficient Friedel–Crafts Synthesis and Adsorption/Storage of CO_2 and CH_4. *J. Mater. Chem. A* **2015,** *3*, 6792-6797.

(89) Li, H.; Meng, B.; Chai, S. H.; Liu, H.; Dai, S., Hyper-Crosslinked Beta-Cyclodextrin Porous Polymer: An Adsorption-Facilitated Molecular Catalyst Support for Transformation of Water-Soluble Aromatic Molecules. *Chem. Sci.* **2016,** *7*, 905-909.

(90) Xie, X.; Wang, J.; Zheng, J.; Huang, J.; Ni, C.; Cheng, J.; Hao, Z.; Ouyang, G., Low-Cost Scholl-Coupling Microporous Polymer as an Efficient Solid-Phase Microextraction Coating for the Detection of Light Aromatic Compounds. *Anal. Chim. Acta* **2018,** *1029*, 30-36.

(91) Teo, Y. C.; Lai, H. W. H.; Xia, Y., Synthesis of Ladder Polymers: Developments, Challenges, and Opportunities. *Chem. Eur. J.* **2017,** *23*, 14101-14112.

(92) Kalin, A. J.; Lee, J.; Fang, L., Annulation Reactions for Conjugated Ladder-Type Oligomers. *Synlett* **2018,** *29*, 993-998.

(93) Zhu, C.; Kalin, A. J.; Fang, L., Covalent and Noncovalent Approaches to Rigid Coplanar Pi-Conjugated Molecules and Macromolecules. *Acc. Chem. Res.* **2019,** *52*, 1089-1100.

(94) Zhang, B.; Wei, M.; Mao, H.; Pei, X.; Alshmimri, S. A.; Reimer, J. A.; Yaghi, O. M., Crystalline Dioxin-Linked Covalent Organic Frameworks from Irreversible Reactions. *J. Am. Chem. Soc.* **2018,** *140*, 12715-12719.

(95) Mahmood, J.; Lee, E. K.; Jung, M.; Shin, D.; Jeon, I. Y.; Jung, S. M.; Choi, H. J.; Seo, J. M.; Bae, S. Y.; Sohn, S. D.; Park, N.; Oh, J. H.; Shin, H. J.; Baek, J. B., Nitrogenated Holey Two-Dimensional Structures. *Nat. Commun.* **2015,** *6*, 6486.

(96) Wang, M.; Ballabio, M.; Wang, M.; Lin, H. H.; Biswal, B. P.; Han, X.; Paasch, S.; Brunner, E.; Liu, P.; Chen, M.; Bonn, M.; Heine, T.; Zhou, S.; Canovas, E.; Dong, R.; Feng, X., Unveiling Electronic Properties in Metal-Phthalocyanine-Based Pyrazine-Linked Conjugated Two-Dimensional Covalent Organic Frameworks. *J. Am. Chem. Soc.* **2019,** *141*, 16810-16816.

(97) Mahmood, J.; Anjum, M. A. R.; Shin, S. H.; Ahmad, I.; Noh, H. J.; Kim, S. J.; Jeong, H. Y.; Lee, J. S.; Baek, J. B., Encapsulating Iridium Nanoparticles inside a 3D Cage-Like Organic Network as an Efficient and Durable Catalyst for the Hydrogen Evolution Reaction. *Adv. Mater.* **2018,** *30*, 1805606.

(98) Mahmood, J.; Anjum, M. A. R.; Baek, J. B., Fused Aromatic Network Structures as a Platform for Efficient Electrocatalysis. *Adv. Mater.* **2018,** 1805062.

(99) Talapaneni, S. N.; Kim, J.; Je, S. H.; Buyukcakir, O.; Oh, J.; Coskun, A., Bottom-up Synthesis of Fully Sp2 Hybridized Three-Dimensional Microporous Graphitic Frameworks as Metal-Free Catalysts. *J. Mater. Chem. A* **2017,** *5*, 12080-12085.

(100) Kou, Y.; Xu, Y.; Guo, Z.; Jiang, D., Supercapacitive Energy Storage and Electric Power Supply Using an Aza-Fused π-Conjugated Microporous Framework. *Angew. Chem. Int. Ed.* **2011,** *50*, 8753-8757.

(101) Meng, Z.; Aykanat, A.; Mirica, K. A., Proton Conduction in 2D Aza-Fused Covalent Organic Frameworks. *Chem. Mater.* **2018,** *31*, 819-825.

(102) Meng, Z.; Stolz, R. M.; Mirica, K. A., Two-Dimensional Chemiresistive Covalent Organic Framework with High Intrinsic Conductivity. *J. Am. Chem. Soc.* **2019,** *141*, 11929-11937.

(103) Li, X.; Wang, H.; Chen, H.; Zheng, Q.; Zhang, Q.; Mao, H.; Liu, Y.; Cai, S.; Sun, B.; Dun, C.; Gordon, M. P.; Zheng, H.; Reimer, J. A.; Urban, J. J.; Ciston, J.; Tan, T.; Chan, E. M.; Zhang, J.; Liu, Y., Dynamic Covalent Synthesis of Crystalline Porous Graphitic Frameworks. *Chem* **2020,** *6*, 933-944.

(104) Mendoza-Cortes, J. L.; Han, S. S.; Furukawa, H.; Yaghi, O. M.; Goddard, W. A. I., Adsorption Mechanism and Uptake of Methane in Covalent Organic Frameworks: Theory and Experiment. *J. Phys. Chem. A* **2010,** *114*, 10824-10833.

(105) Mahmood, J.; Kim, S. J.; Noh, H. J.; Jung, S. M.; Ahmad, I.; Li, F.; Seo, J. M.; Baek, J. B., A Robust 3D Cage-Like Ultramicroporous Network Structure with High Gas-Uptake Capacity. *Angew. Chem. Int. Ed.* **2018,** *57*, 3415-3420.

(106) Budd, P. M.; Ghanem, B.; Msayib, K.; McKeown, N. B.; Tattershall, C., A Nanoporous Network Polymer Derived from Hexaazatrinaphthylene with Potential as an Adsorbent and Catalyst Support. *J. Mater. Chem.* **2003,** *13*, 2721-2726.

(107) McKeown, N. B.; Makhseed, S.; Budd, P. M., Phthalocyanine-Based Nanoporous Network Polymers. *Chem. Commun.* **2002,** 2780-2781.

(108) Maffei, A. V.; Budd, P. M.; McKeown, N. B., Adsorption Studies of a Microporous Phthalocyanine Network Polymer. *Langmuir* **2006,** *22*, 4225-4229.

(109) McKeown, N. B.; Gahnem, B.; Msayib, K. J.; Budd, P. M.; Tattershall, C. E.; Mahmood, K.; Tan, S.; Book, D.; Langmi, H. W.; Walton, A., Towards Polymer-Based Hydrogen Storage Materials: Engineering Ultramicroporous Cavities within Polymers of Intrinsic Microporosity. *Angew. Chem. Int. Ed.* **2006,** *45*, 1804-1807.

(110) Budd, P. M.; Butler, A.; Selbie, J.; Mahmood, K.; McKeown, N. B.; Ghanem, B.; Msayib, K.; Book, D.; Walton, A., The Potential of Organic Polymer-Based Hydrogen Storage Materials. *Phys. Chem. Chem. Phys.* **2007,** *9*, 1802-1808.

(111) Ghanem, B. S.; Msayib, K. J.; McKeown, N. B.; Harris, K. D.; Pan, Z.; Budd, P. M.; Butler, A.; Selbie, J.; Book, D.; Walton, A., A Triptycene-Based Polymer of Intrinsic Microposity That Displays Enhanced Surface Area and Hydrogen Adsorption. *Chem. Commun.* **2007,** 67-69.

(112) Mackintosh, H. J.; Budd, P. M.; McKeown, N. B., Catalysis by Microporous Phthalocyanine and Porphyrin Network Polymers. *J. Mater. Chem.* **2008,** *18*, 573-578.

(113) Ghanem, B. S.; Hashem, M.; Harris, K. D. M.; Msayib, K. J.; Xu, M.; Budd, P. M.; Chaukura, N.; Book, D.; Tedds, S.; Walton, A.; McKeown, N. B., Triptycene-Based Polymers of Intrinsic Microporosity: Organic Materials That Can Be Tailored for Gas Adsorption. *Macromolecules* **2010,** *43*, 5287-5294.

(114) Wang, L.; Zhang, Y., Advances in Polyarylethers: Opening New Opportunities. *J. Mater. Chem. C* **2019,** *7*, 14767-14770.

(115) Skala, L. P.; Yang, A.; Klemes, M. J.; Xiao, L.; Dichtel, W. R., Resorcinarene Cavitand Polymers for the Remediation of Halomethanes and 1,4-Dioxane. *J. Am. Chem. Soc.* **2019,** *141*, 13315-13319.

(116) Guan, X.; Li, H.; Ma, Y.; Xue, M.; Fang, Q.; Yan, Y.; Valtchev, V.; Qiu, S., Chemically Stable Polyarylether-Based Covalent Organic Frameworks. *Nat. Chem.* **2019,** *11*, 587-594.

(117) Zhang, M.; Lu, M.; Lang, Z. L.; Liu, J.; Liu, M.; Chang, J. N.; Li, L. Y.; Shang, L. J.; Wang, M.; Li, S. L.; Lan, Y. Q., Semiconductor/Covalent-Organic-Framework Z-Scheme Heterojunctions for Artificial Photosynthesis. *Angew. Chem. Int. Ed.* **2020,** *59*, 6500-6506.

(118) Ong, W. J.; Swager, T. M., Dynamic Self-Correcting Nucleophilic Aromatic Substitution. *Nat. Chem.* **2018,** *10*, 1023-1030.

(119) Ghosh, S.; Gueskine, V.; Berggren, M.; Zozoulenko, I. V., Electronic Structures and Optical Absorption of N-Type Conducting Polymers at Different Doping Levels. *J. Phys. Chem. C* **2019,** *123*, 15467-15476.

(120) Hong, S. Y.; Kertesz, M.; Lee, Y. S.; Kim, O. K., Geometrical and Electronic Structures of a Benzimidazobenzophenanthroline-Type Ladder Polymer (BBL). *Macromolecules* **1992,** *25*, 5424-5429.

(121) Shin, S.-H.; Noh, H.-J.; Kim, Y.-H.; Im, Y.-K.; Mahmood, J.; Baek, J.-B., Forming Layered Conjugated Porous BBL Structures. *Polym. Chem.* **2019,** *10*, 4185-4193.

(122) Noh, H. J.; Im, Y. K.; Yu, S. Y.; Seo, J. M.; Mahmood, J.; Yildirim, T.; Baek, J. B., Vertical Two-Dimensional Layered Fused Aromatic Ladder Structure. *Nat. Commun.* **2020,** *11*, 2021.

(123) Kissel, P.; Murray, D. J.; Wulftange, W. J.; Catalano, V. J.; King, B. T., A Nanoporous Two-Dimensional Polymer by Single-Crystal-to-Single-Crystal Photopolymerization. *Nat. Chem.* **2014,** *6*, 774-778.

(124) Kissel, P.; Erni, R.; Schweizer, W. B.; Rossell, M. D.; King, B. T.; Bauer, T.; Gotzinger, S.; Schluter, A. D.; Sakamoto, J., A Two-Dimensional Polymer Prepared by Organic Synthesis. *Nat. Chem.* **2012,** *4*, 287-291.

(125) Bhola, R.; Payamyar, P.; Murray, D. J.; Kumar, B.; Teator, A. J.; Schmidt, M. U.; Hammer, S. M.; Saha, A.; Sakamoto, J.; Schluter, A. D.; King, B. T., A Two-Dimensional Polymer from the Anthracene Dimer and Triptycene Motifs. *J. Am. Chem. Soc.* **2013,** *135*, 14134-14141.

(126) Payamyar, P.; Kaja, K.; Ruiz-Vargas, C.; Stemmer, A.; Murray, D. J.; Johnson, C. J.; King, B. T.; Schiffmann, F.; Vandevondele, J.; Renn, A.; Gotzinger, S.; Ceroni, P.; Schutz, A.; Lee, L. T.; Zheng, Z.; Sakamoto, J.; Schluter, A. D., Synthesis of a Covalent Monolayer Sheet by Photochemical Anthracene Dimerization at the Air/Water Interface and Its Mechanical Characterization by Afm Indentation. *Adv. Mater.* **2014,** *26*, 2052-2058.

(127) Murray, D. J.; Patterson, D. D.; Payamyar, P.; Bhola, R.; Song, W.; Lackinger, M.; Schluter, A. D.; King, B. T., Large Area Synthesis of a Nanoporous Two-Dimensional Polymer at the Air/Water Interface. *J. Am. Chem. Soc.* **2015,** *137*, 3450-3453.

(128) Gupta, H. K.; Reginato, N.; Ogini, F. O.; Brydges, S.; McGlinchey, M. J., $SiCl_4$–Ethanol as a Trimerization Agent for Organometallics: Convenient Syntheses of the Symmetrically Substituted Arenes 1,3,5- $C_6H_3R_3$ Where R = $(C_5H_4)Mn(Co)_3$ and $(C_5H_4)Fe(C_5H_5)$. *Can. J. Chem.* **2002,** *80*, 1546-1554.

(129) Elmorsy, S. S.; Pelter, A.; Smith, K., The Direct Production of Tri- and Hexa-Substituted Benzenes from Ketones under Mild Conditions. *Tetrahedron Lett.* **1991,** *32*, 4175-4176.

(130) Cherioux, F.; Guyard, L., Synthesis and Electrochemical Properties of Novel 1,3,5-Tris(Oligothienyl)Benzenes: A New Generation of 3d Reticulating Agents. *Adv. Funct. Mater.* **2001,** *11*, 305-309.

(131) Pei, J.; Wang, J. L.; Cao, X. Y.; Zhou, X. H.; Zhang, W. B., Star-Shaped Polycyclic Aromatics Based on Oligothiophene-Functionalized Truxene: Synthesis, Properties, and Facile Emissive Wavelength Tuning. *J. Am. Chem. Soc.* **2003,** *125*, 9944-9945.

(132) Huang, C.; Fu, W.; Li, C. Z.; Zhang, Z.; Qiu, W.; Shi, M.; Heremans, P.; Jen, A. K.; Chen, H., Dopant-Free Hole-Transporting Material with a C_{3h} Symmetrical Truxene Core for Highly Efficient Perovskite Solar Cells. *J. Am. Chem. Soc.* **2016,** *138*, 2528-2531.

(133) Rose, M.; Klein, N.; Senkovska, I.; Schrage, C.; Wollmann, P.; Böhlmann, W.; Böhringer, B.; Fichtner, S.; Kaskel, S., A New Route to Porous Monolithic Organic Frameworks Via Cyclotrimerization. *J. Mater. Chem.* **2011,** *21*, 711-716.

(134) Zhao, Y.-C.; Zhou, D.; Chen, Q.; Zhang, X.-J.; Bian, N.; Qi, A.-D.; Han, B.-H., Thionyl Chloride-Catalyzed Preparation of Microporous Organic Polymers through Aldol Condensation. *Macromolecules* **2011,** *44*, 6382-6388.

(135) Wisser, F. M.; Eckhardt, K.; Wisser, D.; Böhlmann, W.; Grothe, J.; Brunner, E.; Kaskel, S., Tailoring Pore Structure and Properties of Functionalized Porous Polymers by Cyclotrimerization. *Macromolecules* **2014,** *47*, 4210-4216.

(136) Walczak, R.; Kurpil, B.; Savateev, A.; Heil, T.; Schmidt, J.; Qin, Q.; Antonietti, M.; Oschatz, M., Template- and Metal-Free Synthesis of Nitrogen-Rich Nanoporous "Noble" Carbon Materials by Direct Pyrolysis of a Preorganized Hexaazatriphenylene Precursor. *Angew. Chem. Int. Ed.* **2018,** *57*, 10765-10770.

(137) Buyukcakir, O.; Yuksel, R.; Jiang, Y.; Lee, S. H.; Seong, W. K.; Chen, X.; Ruoff, R. S., Synthesis of Porous Covalent Quinazoline Networks (CQNs) and Their Gas Sorption Properties. *Angew. Chem. Int. Ed.* **2019,** *58*, 872-876.

(138) Abel, M.; Clair, S.; Ourdjini, O.; Mossoyan, M.; Porte, L., Single Layer of Polymeric Fe-Phthalocyanine: An Organometallic Sheet on Metal and Thin Insulating Film. *J. Am. Chem. Soc.* **2011,** *133*, 1203-1205.

(139) Koudia, M.; Abel, M., Step-by-Step on-Surface Synthesis: From Manganese Phthalocyanines to Their Polymeric Form. *Chem. Commun.* **2014,** *50*, 8565-8567.

(140) Anandhababu, G.; Abbas, S. C.; Lv, J.; Ding, K.; Liu, Q.; Babu, D. D.; Huang, Y.; Xie, J.; Wu, M.; Wang, Y., Highly Exposed Fe-N_4 Active Sites in Porous Poly-Iron-Phthalocyanine Based Oxygen Reduction Electrocatalyst with Ultrahigh Performance for Air Cathode. *Dalton Trans.* **2017,** *46*, 1803-1810.

(141) Xue, Q.; Xu, Z.; Jia, D.; Li, X.; Zhang, M.; Bai, J.; Li, W.; Zhang, W.; Zhou, B., Solid‐Phase Synthesis Porous Organic Polymer as Precursor for Fe/Fe_3C‐Embedded Hollow Nanoporous Carbon for Alkaline Oxygen Reduction Reaction. *ChemElectroChem* **2019,** *6*, 4491-4496.

(142) Abdel-Razik, H. H.; Mahmoud, K. H., Novel Fully Conjugated 2H- and Metal-Phthalocyanine Network Polymers: Synthesis, Characterization, and Dielectric Spectra Analysis. *J. Appl. Polym. Sci* **2012,** *123*, 1329-1339.

(143) Byun, Y.; Coskun, A., Epoxy-Functionalized Porous Organic Polymers Via the Diels-Alder Cycloaddition Reaction for Atmospheric Water Capture. *Angew. Chem. Int. Ed.* **2018,** *57*, 3173-3177.

(144) Byun, Y.; Xie, L. S.; Fritz, P.; Ashirov, T.; Dinca, M.; Coskun, A., A Three-Dimensional Porous Organic Semiconductor Based on Fully Sp(2) -Hybridized Graphitic Polymer. *Angew. Chem. Int. Ed.* **2020**. *59*, 1-6

(145) Byun, Y.; Coskun, A., Bottom-up Approach for the Synthesis of a Three-Dimensional Nanoporous Graphene Nanoribbon Framework and Its Gas Sorption Properties. *Chem. Mater.* **2015,** *27*, 2576-2583.

(146) Che, S.; Pang, J.; Kalin, A. J.; Wang, C.; Ji, X.; Lee, J.; Cole, D.; Li, J.-L.; Tu, X.; Zhang, Q.; Zhou, H.-C.; Fang, L., Rigid Ladder-Type Porous Polymer Networks for Entropically Favorable Gas Adsorption. *ACS Materials Lett.* **2020,** *2*, 49-54.

(147) Peurifoy, S. R.; Russell, J. C.; Sisto, T. J.; Yang, Y.; Roy, X.; Nuckolls, C., Designing Three-Dimensional Architectures for High-Performance Electron Accepting Pseudocapacitors. *J. Am. Chem. Soc.* **2018,** *140*, 10960-10964.

(148) Byun, Y.; Cho, M.; Kim, D.; Jung, Y.; Coskun, A., Edge-Functionalized Graphene Nanoribbon Frameworks for the Capture and Separation of Greenhouse Gases. *Macromolecules* **2017,** *50*, 523-533.

(149) Veber, G.; Diercks, C. S.; Rogers, C.; Perkins, W. S.; Ciston, J.; Lee, K.; Llinas, J. P.; Liebman-Peláez, A.; Zhu, C.; Bokor, J.; Fischer, F. R., Reticular Growth of Graphene Nanoribbon 2d Covalent Organic Frameworks. *Chem* **2020,** *6*, 1125-1133.

(150) Zhang, Y.; Wan, Q.; Yang, N., Recent Advances of Porous Graphene: Synthesis, Functionalization, and Electrochemical Applications. *Small* **2019,** *15*, 1903780.

(151) Xu, P.; Yang, J.; Wang, K.; Zhou, Z.; Shen, P., Porous Graphene: Properties, Preparation, and Potential Applications. *Chinese Sci. Bull.* **2012,** *57*, 2948-2955.

(152) Jiang, L.; Fan, Z., Design of Advanced Porous Graphene Materials: From Graphene Nanomesh to 3d Architectures. *Nanoscale* **2014,** *6*, 1922-1945.

(153) Guirguis, A.; Maina, J. W.; Zhang, X.; Henderson, L. C.; Kong, L.; Shon, H.; Dumée, L. F., Applications of Nano-Porous Graphene Materials – Critical Review on Performance and Challenges. *Mater. Horiz* **2020,** *7*, 1218-1245.

(154) Hooch Antink, W.; Choi, Y.; Seong, K.-d.; Kim, J. M.; Piao, Y., Recent Progress in Porous Graphene and Reduced Graphene Oxide-Based Nanomaterials for Electrochemical Energy Storage Devices. *Adv. Mater. Interfaces* **2018,** *5*, 1701212.

(155) Sivasankar, K.; Pal, S.; Thiruppathi, M.; Lin, C. H., Carbonization and Preparation of Nitrogen-Doped Porous Carbon Materials from Zn-Mof and Its Applications. *Materials* **2020,** *13*, 264-276.

(156) Ren, Q.; Wang, H.; Lu, X. F.; Tong, Y. X.; Li, G. R., Recent Progress on MOF-Derived Heteroatom-Doped Carbon-Based Electrocatalysts for Oxygen Reduction Reaction. *Adv. Sci.* **2018,** *5*, 1700515.

(157) Chen, Y.-Z.; Zhang, R.; Jiao, L.; Jiang, H.-L., Metal–Organic Framework-Derived Porous Materials for Catalysis. *Coord. Chem. Rev.* **2018,** *362*, 1-23.

(158) Duan, J.; Chen, S.; Jaroniec, M.; Qiao, S. Z., Heteroatom-Doped Graphene-Based Materials for Energy-Relevant Electrocatalytic Processes. *ACS Catal.* **2015,** *5*, 5207-5234.

(159) Miner, E. M.; Gul, S.; Ricke, N. D.; Pastor, E.; Yano, J.; Yachandra, V. K.; Van Voorhis, T.; Dincă, M., Mechanistic Evidence for Ligand-Centered Electrocatalytic Oxygen Reduction with the Conductive MOF Ni_3(hexaiminotriphenylene)$_2$. *ACS Catal.* **2017,** *7*, 7726-7731.

(160) Sheberla, D.; Bachman, J. C.; Elias, J. S.; Sun, C. J.; Shao-Horn, Y.; Dinca, M., Conductive MOF Electrodes for Stable Supercapacitors with High Areal Capacitance. *Nat. Mater.* **2017,** *16*, 220-224.

(161) Phillips, B.; Banerjee, S.; Tu, X.; Fang, L., Electrical Vapour Sensing with Macrocyclic Molecular Receptors. *Supramol. Chem.* **2020,** 1-13.

(162) Guo, J.; Xu, Y.; Jin, S.; Chen, L.; Kaji, T.; Honsho, Y.; Addicoat, M. A.; Kim, J.; Saeki, A.; Ihee, H.; Seki, S.; Irle, S.; Hiramoto, M.; Gao, J.; Jiang, D., Conjugated Organic Framework with Three-Dimensionally Ordered Stable Structure and Delocalized π Clouds. *Nat. Commun.* **2013,** *4*, 2736.

(163) Kim, J.; Gwon, O.; Kwon, O.; Mahmood, J.; Kim, C.; Yang, Y.; Lee, H.; Lee, J. H.; Jeong, H. Y.; Baek, J. B.; Kim, G., Synergistic Coupling Derived Cobalt Oxide with Nitrogenated Holey Two-Dimensional Matrix as an Efficient Bifunctional Catalyst for Metal-Air Batteries. *ACS Nano* **2019,** *13*, 5502-5512.

(164) Ahmad, I.; Li, F.; Kim, C.; Seo, J.-M.; Kim, G.; Mahmood, J.; Jeong, H. Y.; Baek, J.-B., Robust Fused Aromatic Pyrazine-Based Two-Dimensional Network for Stably Cocooning Iron Nanoparticles as an Oxygen Reduction Electrocatalyst. *Nano Energy* **2019,** *56*, 581-587.

(165) Kim, S. J.; Mahmood, J.; Kim, C.; Han, G. F.; Kim, S. W.; Jung, S. M.; Zhu, G.; De Yoreo, J. J.; Kim, G.; Baek, J. B., Defect-Free Encapsulation of Fe(0) in 2D Fused Organic Networks as a Durable Oxygen Reduction Electrocatalyst. *J. Am. Chem. Soc.* **2018,** *140*, 1737-1742.

(166) Mahmood, J.; Jung, S.-M.; Kim, S.-J.; Park, J.; Yoo, J.-W.; Baek, J.-B., Cobalt Oxide Encapsulated in C_2N-*h*2D Network Polymer as a Catalyst for Hydrogen Evolution. *Chem. Mater.* **2015,** *27*, 4860-4864.

(167) Mahmood, J.; Li, F.; Jung, S. M.; Okyay, M. S.; Ahmad, I.; Kim, S. J.; Park, N.; Jeong, H. Y.; Baek, J. B., An Efficient and Ph-Universal Ruthenium-Based Catalyst for the Hydrogen Evolution Reaction. *Nat. Nanotechnol.* **2017,** *12*, 441-446.

(168) Kuehl, V. A.; Yin, J.; Duong, P. H. H.; Mastorovich, B.; Newell, B.; Li-Oakey, K. D.; Parkinson, B. A.; Hoberg, J. O., A Highly Ordered Nanoporous, Two-Dimensional

Covalent Organic Framework with Modifiable Pores, and Its Application in Water Purification and Ion Sieving. *J. Am. Chem. Soc.* **2018,** *140*, 18200-18207.

(169) Marco, A. B.; Cortizo-Lacalle, D.; Perez-Miqueo, I.; Valenti, G.; Boni, A.; Plas, J.; Strutynski, K.; De Feyter, S.; Paolucci, F.; Montes, M.; Khlobystov, A. N.; Melle-Franco, M.; Mateo-Alonso, A., Twisted Aromatic Frameworks: Readily Exfoliable and Solution-Processable Two-Dimensional Conjugated Microporous Polymers. *Angew. Chem. Int. Ed.* **2017,** *56*, 6946-6951.

(170) Zhu, Y.; Yang, H.; Jin, Y.; Zhang, W., Porous Poly(Aryleneethynylene) Networks through Alkyne Metathesis. *Chem. Mater.* **2013,** *25*, 3718-3723.

(171) Ma, L.; Liu, Y.; Liu, Y.; Jiang, S.; Li, P.; Hao, Y.; Shao, P.; Yin, A.; Feng, X.; Wang, B., Ferrocene-Linkage-Facilitated Charge Separation in Conjugated Microporous Polymers. *Angew. Chem. Int. Ed.* **2019,** *58*, 4221-4226.

(172) Bonifacio, M. C.; Robertson, C. R.; Jung, J. Y.; King, B. T., Polycyclic Aromatic Hydrocarbons by Ring-Closing Metathesis. *J. Org. Chem.* **2005,** *70*, 8522-8526.

(173) Vermeulen, N. A.; Karagiaridi, O.; Sarjeant, A. A.; Stern, C. L.; Hupp, J. T.; Farha, O. K.; Stoddart, J. F., Aromatizing Olefin Metathesis by Ligand Isolation inside a Metal-Organic Framework. *J. Am. Chem. Soc.* **2013,** *135*, 14916-14919.

(174) Wu, X. L.; Zilm, K. W., Complete Spectral Editing in Cpmas Nmr. *J. Magn. Reson., Ser A* **1993,** *102*, 205-213.

(175) Echeverri, M.; Gamez-Valenzuela, S.; Gonzalez-Cano, R. C.; Guadalupe, J.; Cortijo-Campos, S.; Navarrete, J. T. L.; Iglesias, M.; Delgado, M. C. R.; Gomez-Lor, B., Effect of the Linkage Position on the Conjugation Length of Truxene-Based Porous Polymers: Implications for Their Sensing Performance of Nitroaromatics. *Chem. Mater.* **2019,** *31*, 6971-6978.

(176) Makhseed, S.; Samuel, J., Microporous Organic Polymers Incorporating Dicarboximide Units for H2 Storage and Remarkable CO_2 Capture. *J. Mater. Chem. A* **2013,** *1*, 13004–13010.

(177) Peng, Y.; Krungleviciute, V.; Eryazici, I.; Hupp, J. T.; Farha, O. K.; Yildirim, T., Methane Storage in Metal-Organic Frameworks: Current Records, Surprise Findings, and Challenges. *J. Am. Chem. Soc.* **2013,** *135*, 11887-11894.

(178) Li, B.; Wen, H.-M.; Zhou, W.; Xu, Jeff Q.; Chen, B., Porous Metal-Organic Frameworks: Promising Materials for Methane Storage. *Chem* **2016,** *1*, 557-580.

(179) Mason, J. A.; Oktawiec, J.; Taylor, M. K.; Hudson, M. R.; Rodriguez, J.; Bachman, J. E.; Gonzalez, M. I.; Cervellino, A.; Guagliardi, A.; Brown, C. M.; Llewellyn, P. L.; Masciocchi, N.; Long, J. R., Methane Storage in Flexible Metal-Organic Frameworks with Intrinsic Thermal Management. *Nature* **2015,** *527*, 357-361.

(180) Zhang, Y. B.; Furukawa, H.; Ko, N.; Nie, W.; Park, H. J.; Okajima, S.; Cordova, K. E.; Deng, H.; Kim, J.; Yaghi, O. M., Introduction of Functionality, Selection of Topology, and Enhancement of Gas Adsorption in Multivariate Metal-Organic Framework-177. *J. Am. Chem. Soc.* **2015,** *137*, 2641-2650.

(181) Rowland, C. A.; Lorzing, G. R.; Gosselin, E. J.; Trump, B. A.; Yap, G. P. A.; Brown, C. M.; Bloch, E. D., Methane Storage in Paddlewheel-Based Porous Coordination Cages. *J. Am. Chem. Soc.* **2018,** *140*, 11153-11157.

(182) Rozyyev, V.; Thirion, D.; Ullah, R.; Lee, J.; Jung, M.; Oh, H.; Atilhan, M.; Yavuz, C. T., High-Capacity Methane Storage in Flexible Alkane-Linked Porous Aromatic Network Polymers. *Nat. Energy* **2019,** *4*, 604-611.

(183) Wilmer, C. E.; Leaf, M.; Lee, C. Y.; Farha, O. K.; Hauser, B. G.; Hupp, J. T.; Snurr, R. Q., Large-Scale Screening of Hypothetical Metal-Organic Frameworks. *Nat. Chem.* **2011,** *4*, 83-89.

(184) Guo, Z.; Wu, H.; Srinivas, G.; Zhou, Y.; Xiang, S.; Chen, Z.; Yang, Y.; Zhou, W.; O'Keeffe, M.; Chen, B., A Metal-Organic Framework with Optimized Open Metal Sites and Pore Spaces for High Methane Storage at Room Temperature. *Angew. Chem. Int. Ed.* **2011,** *50*, 3178-3181.

(185) Jiang, J.; Furukawa, H.; Zhang, Y. B.; Yaghi, O. M., High Methane Storage Working Capacity in Metal-Organic Frameworks with Acrylate Links. *J. Am. Chem. Soc.* **2016,** *138*, 10244-10251.

(186) Savage, M.; da Silva, I.; Johnson, M.; Carter, J. H.; Newby, R.; Suyetin, M.; Besley, E.; Manuel, P.; Rudic, S.; Fitch, A. N.; Murray, C.; David, W. I.; Yang, S.; Schroder, M., Observation of Binding and Rotation of Methane and Hydrogen within a Functional Metal-Organic Framework. *J. Am. Chem. Soc.* **2016,** *138*, 9119-9127.

(187) DeBlase, C. R.; Dichtel, W. R., Moving Beyond Boron: The Emergence of New Linkage Chemistries in Covalent Organic Frameworks. *Macromolecules* **2016,** *49*, 5297-5305.

(188) Düren, T.; Sarkisov, L.; Yaghi, O. M.; Snurr, R. Q., Design of New Materials for Methane Storage. *Langmuir* **2004,** *20*, 2683-2689.

(189) Ma, S.; Sun, D.; Simmons, J. M.; Collier, C. D.; Yuan, D.; Zhou, H. C., Metal-Organic Framework from an Anthracene Derivative Containing Nanoscopic Cages Exhibiting High Methane Uptake. *J. Am. Chem. Soc.* **2008,** *130*, 1012-1016.

(190) Furukawa, H.; Ko, N.; Go, Y. B.; Aratani, N.; Choi, S. B.; Choi, E.; Yazaydin, A. O.; Snurr, R. Q.; O'Keeffe, M.; Kim, J.; Yaghi, O. M., Ultrahigh Porosity in Metal-Organic Frameworks. *Science* **2010,** *329*, 424-428.

(191) Furukawa, H.; Yaghi, O. M., Storage of Hydrogen, Methane, and Carbon Dioxide in Highly Porous Covalent Organic Frameworks for Clean Energy Applications. *J. Am. Chem. Soc.* **2009,** *131*, 8875-8883.

(192) Bracco, S.; Piga, D.; Bassanetti, I.; Perego, J.; Comotti, A.; Sozzani, P., Porous 3d Polymers for High Pressure Methane Storage and Carbon Dioxide Capture. *J. Mater. Chem. A* **2017,** *5*, 10328-10337.

(193) Czepirski, L.; JagieŁŁo, J., Virial-Type Thermal Equation of Gas—Solid Adsorption. *Chem. Eng. Sci.* **1989,** *44*, 797-801.

(194) Rowsell, J. L.; Yaghi, O. M., Effects of Functionalization, Catenation, and Variation of the Metal Oxide and Organic Linking Units on the Low-Pressure Hydrogen Adsorption Properties of Metal-Organic Frameworks. *J. Am. Chem. Soc.* **2006,** *128*, 1304-15.

(195) West, C.; Elfakir, C.; Lafosse, M., Porous Graphitic Carbon: A Versatile Stationary Phase for Liquid Chromatography. *J. Chromatogr. A* **2010,** *1217*, 3201-16.

(196) Wang, D. W.; Li, F.; Liu, M.; Lu, G. Q.; Cheng, H. M., 3d Aperiodic Hierarchical Porous Graphitic Carbon Material for High-Rate Electrochemical Capacitive Energy Storage. *Angew. Chem. Int. Ed.* **2008,** *47*, 373-6.

(197) Shibukawa, M.; Unno, A.; Miura, T.; Nagoya, A.; Oguma, K., On-Column Derivatization Using Redox Activity of Porous Graphitic Carbon Stationary Phase: An Approach to Enhancement of Separation Selectivity of Liquid Chromatography. *Anal. Chem.* **2003,** *75*, 2775-83.

(198) Sun, L.; Tian, C.; Wang, L.; Zou, J.; Mu, G.; Fu, H., Magnetically Separable Porous Graphitic Carbon with Large Surface Area as Excellent Adsorbents for Metal Ions and Dye. *J. Mater. Chem.* **2011,** *21*.

(199) Wu, X.; Xie, Z.; Sun, M.; Lei, T.; Zuo, Z.; Xie, X.; Liang, Y.; Huang, Q., Edge-Rich and (N, S)-Doped 3D Porous Graphene as an Efficient Metal-Free Electrocatalyst for the Oxygen Reduction Reaction. *RSC Adv.* **2016,** *6*, 90384-90387.

(200) Sinitskii, A.; Tour, J. M., Patterning Graphene through the Self-Assembled Templates: Toward Periodic Two-Dimensional Graphene Nanostructures with Semiconductor Properties. *J. Am. Chem. Soc.* **2010,** *132*, 14730-2.

(201) Zhang, X.; Zhang, H.; Li, C.; Wang, K.; Sun, X.; Ma, Y., Recent Advances in Porous Graphene Materials for Supercapacitor Applications. *RSC Adv.* **2014,** *4*, 45862-45884.

(202) Zheng, C.; Zhou, X.; Cao, H.; Wang, G.; Liu, Z., Synthesis of Porous Graphene/Activated Carbon Composite with High Packing Density and Large Specific Surface Area for Supercapacitor Electrode Material. *J. Power Sources* **2014,** *258*, 290-296.

(203) Xiao, J.; Mei, D.; Li, X.; Xu, W.; Wang, D.; Graff, G. L.; Bennett, W. D.; Nie, Z.; Saraf, L. V.; Aksay, I. A.; Liu, J.; Zhang, J. G., Hierarchically Porous Graphene as a Lithium-Air Battery Electrode. *Nano Lett.* **2011,** *11*, 5071-8.

(204) Fan, Z.; Yan, J.; Ning, G.; Wei, T.; Zhi, L.; Wei, F., Porous Graphene Networks as High Performance Anode Materials for Lithium Ion Batteries. *Carbon* **2013,** *60*, 558-561.

(205) Some, S.; Kim, J.; Lee, K.; Kulkarni, A.; Yoon, Y.; Lee, S.; Kim, T.; Lee, H., Highly Air-Stable Phosphorus-Doped N-Type Graphene Field-Effect Transistors. *Adv. Mater.* **2012,** *24*, 5481-6.

(206) Surwade, S. P.; Smirnov, S. N.; Vlassiouk, I. V.; Unocic, R. R.; Veith, G. M.; Dai, S.; Mahurin, S. M., Water Desalination Using Nanoporous Single-Layer Graphene. *Nat. Nanotechnol.* **2015,** *10*, 459-64.

(207) Celebi, K.; Buchheim, J.; Wyss, R. M.; Droudian, A.; Gasser, P.; Shorubalko, I.; Kye, J. I.; Lee, C.; Park, H. G., Ultimate Permeation across Atomically Thin Porous Graphene. *Science* **2014,** *344*, 289-92.

(208) Schneider, G. F.; Dekker, C., DNA Sequencing with Nanopores. *Nat. Biotechnol.* **2012,** *30*, 326-8.

(209) Postma, H. W., Rapid Sequencing of Individual DNA Molecules in Graphene Nanogaps. *Nano Lett.* **2010,** *10*, 420-5.

(210) Liang, X.; Jung, Y. S.; Wu, S.; Ismach, A.; Olynick, D. L.; Cabrini, S.; Bokor, J., Formation of Bandgap and Subbands in Graphene Nanomeshes with Sub-10 Nm Ribbon Width Fabricated Via Nanoimprint Lithography. *Nano Lett.* **2010,** *10*, 2454-60.

(211) Chen, Z.; Ren, W.; Gao, L.; Liu, B.; Pei, S.; Cheng, H. M., Three-Dimensional Flexible and Conductive Interconnected Graphene Networks Grown by Chemical Vapour Deposition. *Nat. Mater.* **2011,** *10*, 424-8.

(212) Chen, C. M.; Zhang, Q.; Huang, C. H.; Zhao, X. C.; Zhang, B. S.; Kong, Q. Q.; Wang, M. Z.; Yang, Y. G.; Cai, R.; Sheng Su, D., Macroporous 'Bubble' Graphene Film Via Template-Directed Ordered-Assembly for High Rate Supercapacitors. *Chem. Commun.* **2012,** *48*, 7149-51.

(213) Wang, Z. L.; Xu, D.; Wang, H. G.; Wu, Z.; Zhang, X. B., In Situ Fabrication of Porous Graphene Electrodes for High-Performance Energy Storage. *ACS Nano* **2013,** *7*, 2422-30.

(214) Bai, J.; Zhong, X.; Jiang, S.; Huang, Y.; Duan, X., Graphene Nanomesh. *Nat. Nanotechnol.* **2010,** *5*, 190-4.

(215) Zhao, X.; Hayner, C. M.; Kung, M. C.; Kung, H. H., Flexible Holey Graphene Paper Electrodes with Enhanced Rate Capability for Energy Storage Applications. *ACS Nano* **2011,** *5*, 8739-49.

(216) Fan, Z.; Zhao, Q.; Li, T.; Yan, J.; Ren, Y.; Feng, J.; Wei, T., Easy Synthesis of Porous Graphene Nanosheets and Their Use in Supercapacitors. *Carbon* **2012,** *50*, 1699-1703.

(217) Zhang, L. L.; Zhao, X.; Stoller, M. D.; Zhu, Y.; Ji, H.; Murali, S.; Wu, Y.; Perales, S.; Clevenger, B.; Ruoff, R. S., Highly Conductive and Porous Activated Reduced Graphene Oxide Films for High-Power Supercapacitors. *Nano Lett.* **2012,** *12*, 1806-12.

(218) Zhou, D.; Cui, Y.; Xiao, P. W.; Jiang, M. Y.; Han, B. H., A General and Scalable Synthesis Approach to Porous Graphene. *Nat. Commun.* **2014,** *5*, 4716.

(219) Moreno, C.; Vilas-Varela, M.; Kretz, B.; Garcia-Lekue, A.; Costache, M. V.; Paradinas, M.; Panighel, M.; Ceballos, G.; Valenzuela, S. O.; Pena, D.; Mugarza, A., Bottom-up Synthesis of Multifunctional Nanoporous Graphene. *Science* **2018,** *360*, 199-203.

(220) Bieri, M.; Treier, M.; Cai, J.; Ait-Mansour, K.; Ruffieux, P.; Groning, O.; Groning, P.; Kastler, M.; Rieger, R.; Feng, X.; Mullen, K.; Fasel, R., Porous Graphenes: Two-Dimensional Polymer Synthesis with Atomic Precision. *Chem. Commun.* **2009,** 6919-21.

(221) Xu, K.; Urgel, J. I.; Eimre, K.; Di Giovannantonio, M.; Keerthi, A.; Komber, H.; Wang, S.; Narita, A.; Berger, R.; Ruffieux, P.; Pignedoli, C. A.; Liu, J.; Mullen, K.; Fasel, R.; Feng, X., On-Surface Synthesis of a Nonplanar Porous Nanographene. *J. Am. Chem. Soc.* **2019,** *141*, 7726-7730.

(222) Yuan, K.; Lutzenkirchen-Hecht, D.; Li, L.; Shuai, L.; Li, Y.; Cao, R.; Qiu, M.; Zhuang, X.; Leung, M. K. H.; Chen, Y.; Scherf, U., Boosting Oxygen Reduction of Single Iron Active Sites Via Geometric and Electronic Engineering: Nitrogen and Phosphorus Dual Coordination. *J. Am. Chem. Soc.* **2020**.